Theoretical methods for femtomagnetism and ultrafast spintronics

Citation for published version (APA):
Beens, M. (2022). *Theoretical methods for femtomagnetism and ultrafast spintronics.* [Phd Thesis 1 (Research TU/e / Graduation TU/e), Applied Physics and Science Education]. Eindhoven University of Technology.

Document status and date:
Published: 25/10/2022

Document Version:
Publisher’s PDF, also known as Version of Record (includes final page, issue and volume numbers)

Please check the document version of this publication:

• A submitted manuscript is the version of the article upon submission and before peer-review. There can be important differences between the submitted version and the official published version of record. People interested in the research are advised to contact the author for the final version of the publication, or visit the DOI to the publisher's website.
• The final author version and the galley proof are versions of the publication after peer review.
• The final published version features the final layout of the paper including the volume, issue and page numbers.

Link to publication

General rights
Copyright and moral rights for the publications made accessible in the public portal are retained by the authors and/or other copyright owners and it is a condition of accessing publications that users recognise and abide by the legal requirements associated with these rights.

- Users may download and print one copy of any publication from the public portal for the purpose of private study or research.
- You may not further distribute the material or use it for any profit-making activity or commercial gain
- You may freely distribute the URL identifying the publication in the public portal.

If the publication is distributed under the terms of Article 25fa of the Dutch Copyright Act, indicated by the “Taverne” license above, please follow below link for the End User Agreement:

www.tue.nl/taverne

Take down policy
If you believe that this document breaches copyright please contact us at:

openaccess@tue.nl

providing details and we will investigate your claim.

Download date: 05. Oct. 2023

Theoretical methods for femtomagnetism and ultrafast spintronics

PROEFSCHRIFT

ter verkrijging van de graad van doctor aan de Technische Universiteit
Eindhoven, op gezag van de rector magnificus prof.dr.ir. F.P.T. Baaijens,
voor een commissie aangewezen door het College voor Promoties, in het
openbaar te verdedigen op dinsdag 25 oktober om 13:30 uur

door

Maarten Beens

geboren te Kampen

Dit proefschrift is goedgekeurd door de promotoren en de samenstelling van de promotiecommissie is als volgt:

voorzitter: prof.dr. C. Storm
1e promotor: prof.dr. B. Koopmans
2e promotor: prof.dr. R.A. Duine
leden: prof.dr. P.A. Bobbert
dr. O. Chubykalo-Fesenko (Instituto de Ciencia de Materiales de Madrid, CSIC)
prof.dr. G. Woltersdorf (Martin-Luther-Universität Halle-Wittenberg)
adviseur: dr.ir. J.H. Mentink (Radboud Universiteit Nijmegen)

Het onderzoek dat in dit proefschrift wordt beschreven is uitgevoerd in overeenstemming met de TU/e Gedragscode Wetenschapsbeoefening.

Theoretical methods for femtomagnetism and ultrafast spintronics

Maarten Beens

A catalogue record is available from the Eindhoven University of Technology Library

ISBN: 978-90-386-5569-7

This work is part of the research programme of the Foundation for Fundamental Research on Matter (FOM), which is part of the Netherlands Organisation for Scientific Research (NWO).

Cover design by André Beens.

To my mother,

CONTENTS

1

GENERAL INTRODUCTION

The aim of this chapter is to present a general overview of the topics discussed in this thesis. First, the fields of femtomagnetism and ultrafast spintronics are introduced. Then, the most relevant physical concepts are briefly reviewed, such as ultrafast demagnetization, laser-induced spin transport, and all-optical switching. The corresponding sections include an overview of the relevant theoretical descriptions, with a focus on the models that are the basis of the work in this thesis. The final section includes an outline of the thesis and a brief summary of the theoretical research presented in the main chapters.

1.1 MAGNETISM AND SPINTRONICS

Magnetism is all around us, playing a visible role in modern society through applications such as electric cars, wind turbines, medical imaging, and data storage. In the latter case, the recent developments in information technology drive the need for nonvolatile and efficient ways to store binary data. Magnetic materials come into play, since data can be imprinted within the orientation of tiny magnetic domains. The most common example of a device that uses this technique is the hard disk drive, where the data is written on a rotating magnetic disk, as schematically depicted in Fig. 1.1(a). The inset shows the magnetoresistive read head and inductive write head used for the sensing and control of the recorded magnetic data [1, 2]. Due to the ever-growing amount of data, and the excessive energy usage of the digital society, it is essential to search for innovative magnetic storage devices. A key ingredient for this development is to better understand the control and design of magnetic materials. For that reason, magnetism remains a topic of ongoing research, both from a fundamental and engineering perspective.

From a fundamental point of view, the dynamical connection between magnetism, electricity, and light, was already well understood from 19th-century classical physics. Nevertheless, the microscopic mechanism that creates the magnetic property of materials remained unidentified until the development of Quantum mechanics in the 20th century. It turned out that magnetism is closely connected to the fundamental characteristics of the electron. Besides its negative electric charge that is responsible for electricity, an electron carries an intrinsic angular momentum known as 'spin.' The latter is associated with a tiny magnetic dipole. In a ferromagnetic material,[1] unpaired electron spins favor to be aligned and collectively create magnetic domains. This is a result of the so-called exchange interaction, as was explained by Werner Heisenberg in 1928 [3], and is of a purely quantum mechanical nature.

As electrons play a fundamental role in ferromagnetism, it is clear that the knowledge we have on electronics is a stepping stone for the development of innovative magnetic technologies. Typically, electronics refers to the branch of physics and technology that addresses the behavior and transport of electrons, specifically, as a carrier of electric charge. In case the focus is on the spin degree of freedom of the electron, the research field is referred to as **spintronics**. The latter addresses the transport of spin, through so-called spin currents, and the connection to the local magnetization dynamics. The most famous discovery in spintronics is Giant magnetoresistance (GMR), independently discovered by 2007 Nobel laureates Albert Fert and Peter Grünberg in the eighties [5, 6]. GMR corresponds to the effect that a spin valve structure consisting of two ferromagnetic metallic layers has a varying electrical resistance dependent on the relative magnetic orientation, as visually represented in Fig. 1.1(b). Since the orientation can be sensitive to nearby magnetic fields, GMR is implemented in the read heads of hard disk drives to translate the magnetic domain structure to an electrical signal. Another essential discovery in spintronics was the spin-transfer torque (STT) [7, 8], which corresponds to the effect that an injected spin current can manipulate the magnetization direction of the absorption layer. The STT can be used as a writing mechanism in magnetic memory devices and is schematically depicted in Fig. 1.1(c). A current is sent through a fixed magnetic layer and becomes spin polarized. Subsequently, the resulting net

---

[1] 'Ferro' refers to iron, which is the most common example of this type of magnetic material.

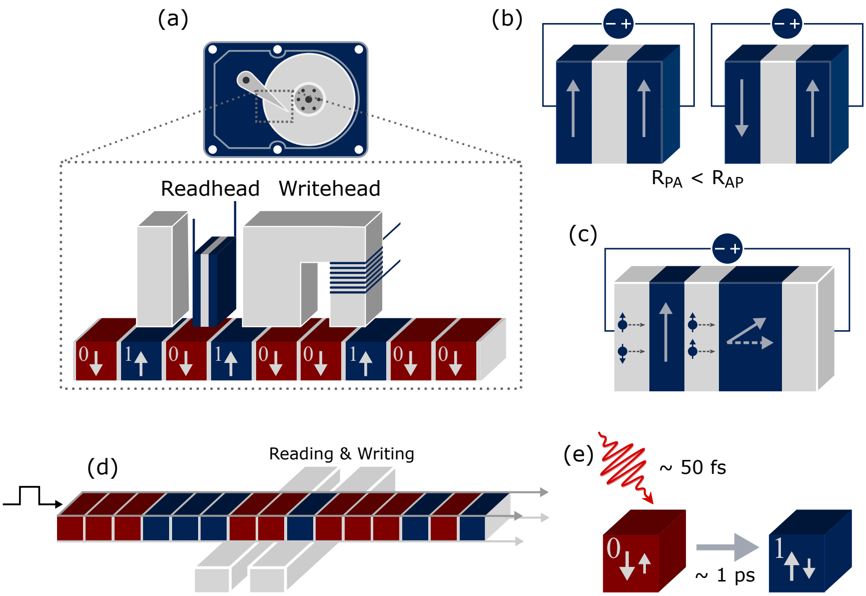

Figure 1.1: (a) Simplified schematic overview of the hard disk drive based on perpendicular magnetic recording. The bottom part presents a side view showing the bits of data being stored within the orientation of magnetic domains. (b) Giant magnetoresistance corresponds to the effect where the parallel and antiparallel orientation of a magnetic spin valve structure have a distinct electrical resistance. (c) Schematic overview of the spin-transfer torque. An electric current is sent through a fixed magnetic layer (left) and becomes spin polarized. Subsequently, the spin current exerts a torque on the perpendicular magnetic layer (right). (d) Schematic representation of the racetrack memory. The magnetic domains carrying the data are transported through the track by applying current pulses. (e) Femtosecond laser pulses can be used to deterministically switch magnetic domains in multisublattice magnetic materials such as GdFeCo. The figures are based on images in Refs. [1, 2, 4].

spin current exerts a torque on the secondary (perpendicular) magnetic layer and effectively manipulates its magnetization direction.

A promising candidate for the next generation of spintronic devices is the so-called magnetic racetrack memory [9]. A schematic representation is given in Fig. 1.1(d). In this case, the data is stored on a magnetic track where the domains can be moved by applying current pulses. The racetrack memory is expected to be beneficial in terms of energy efficiency and data density, without the requirement of mechanically moving parts. To pave the way towards a fully functional device with an optimized efficiency, current research focuses on the various aspects of (chiral) magnetic domain structures, current-induced domain-wall motion, and methods for the readout and control of the magnetization. In direct connection with the work presented in this thesis, one proposed mechanism for future data-writing techniques is the switching of the magnetic domains with ultrashort laser pulses [10–12], as schematically depicted in Fig. 1.1(e). This so-called all-optical switching was first demonstrated in GdFeCo alloys [10], a material that consists of multiple magnetic subsystems. The switching mechanism is very fast compared to conventional methods and is one of the various discoveries that show the relevance of using ultrashort laser pulses as a tool to control magnetic order.

The theoretical research discussed in this thesis focuses on the intriguing magnetic phenomena that are observed when a magnetic system is excited with an ultrashort laser pulse. The corresponding field of research is typically called **femtomagnetism**, where its naming refers to the duration of the laser pulse. A defining moment in the field was the experimental observation of the subpicosecond quenching of the magnetization, a process now known as ultrafast demagnetization [13]. Another interesting phenomenon is that the pulsed-laser excitation scheme results in the rapid generation of spin currents [14–16], thus reaching the regime of **ultrafast spintronics**. The idea is that understanding how to control magnetism on the timescale of a picosecond, which corresponds to one trillionth of a second, paves the way towards future magnetic technologies that are faster and more efficient than the conventional devices. In the following sections, we sum up the experimental pinnacles of femtomagnetism and discuss the state-of-the-art theoretical approaches. Special attention is given to the theoretical models directly related to the work presented in the research chapters of this thesis.

1.2 ULTRAFAST DEMAGNETIZATION

The field of femtomagnetism emerged in the late nineties, following the pioneering experiments by Beaurepaire et al. [13]. The study involved the excitation of a Nickel thin film with an ultrashort laser pulse of 60 femtoseconds. The authors were able to probe the response of the magnetization on a subpicosecond timescale. The main result is presented in Fig. 1.2, showing that the remanent magnetization is quenched in less than a picosecond. This was a very surprising result at the time, as it was not known that the magnetization could be manipulated on such a short timescale. Despite more than 25 years of fundamental research on this phenomenon, the microscopic origin of the observed ultrafast demagnetization is not completely understood and remains heavily debated.

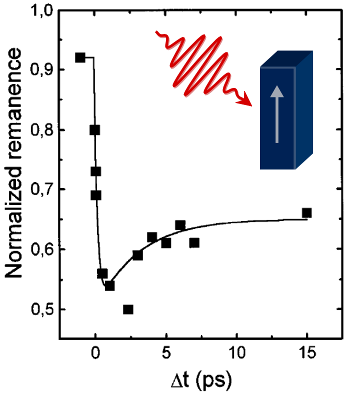

Figure 1.2: The famous measurements of ultrafast demagnetization as published by Beaurepaire et al. [13]. The plot shows the remanent magnetization as a function of time for a Ni thin film that is excited with a femtosecond laser pulse at $\Delta t = 0$.

Although identifying the microscopic magnetic processes at a subpicosecond timescale was an unprecedented challenge, Beaurepaire et al. managed to introduce a phenomenological description that could adequately model the observations [13]. The latter was inspired by the two-temperature model, which describes the heating of a (nonmagnetic) metal by laser-pulse excitation [17]. The extension to ferromagnetic metals is known as the phenomenological three-temperature model (3TM). It describes three interacting subsystems, each in internal thermal equilibrium, the electrons with temperature T_e, the phonons (lattice vibrations) with temperature T_p, and the spins with temperature T_s. The electron system is assumed to absorb the laser-pulse energy. Subsequently, the excess energy is redistributed between the subsystems. A schematic overview of the 3TM is given in Fig. 1.3(a). Furthermore, an example calculation is presented in Fig. 1.3(c), showing the transient response of T_e (blue), T_p (gray), and T_s (red), as a function of time after laser-pulse excitation at $t = 0$. Intuitively, the laser-induced heating leads to a partially quenching of the magnetization through an increase of thermal fluctuations in the magnetic system, modeled by a transient increase of the spin temperature. Despite that the 3TM can be well fitted to the experiments, it contains numerous free parameters and does not provide a full explanation of the microscopic processes that lead to the loss of spin angular momentum on a subpicosecond timescale.

Over the course of the past decades, various microscopic theories have been pro-

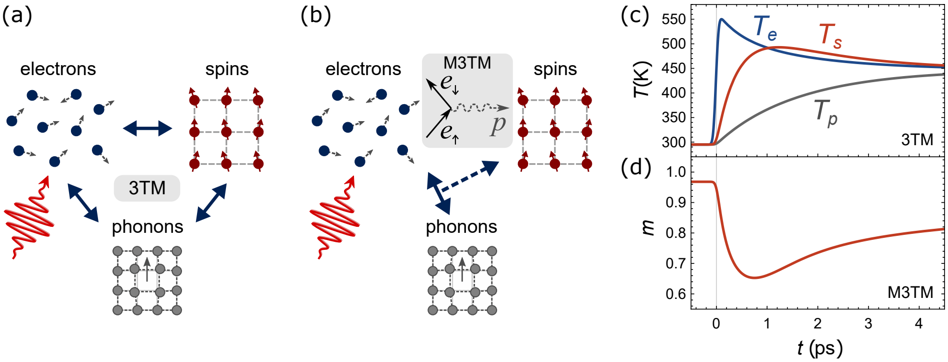

Figure 1.3: Two examples of models that describe ultrafast demagnetization. (a) The three-temperature model (3TM) describes the energy exchange between three subsystems, parametrized by the electron temperature, phonon temperature, and spin temperature. (b) The microscopic three-temperature model (M3TM) describes the magnetization dynamics driven by spin-flip electron-phonon scattering. (c) Example calculation using the 3TM. The plot indicates the three temperatures as a function of time after laser-pulse excitation at $t = 0$. The transient increase of the spin temperature T_s is associated with the decrease of the magnetization. (d) Example calculation using the M3tM. The plot indicates the solution to Eq. (1.1), giving the magnetization as a function of time after laser-pulse excitation at $t = 0$, and showing its subpicosecond quenching. The figures are based on images in Refs. [4, 13, 18].

posed to explain ultrafast demagnetization. Typically, the theories can be categorized in three groups depending on the physical ingredients [4, 19, 20]: (i) the direct coherent interaction between the laser pulse and the spin degree of freedom [21, 22], (ii) local spin dynamics as triggered by laser heating or excitation [13, 18, 23–38], and (iii) nonlocal transfer of angular momentum such as superdiffusive spin transport [39]. Typically, the direct processes from category (i) are assumed to play a minor role. One naive argument can be that the dominant magnetization dynamics happens on a timescale larger than the duration of the laser pulse. An additional argument is that it has been shown experimentally that the demagnetization is not affected by the pump helicity [40], i.e., the direct transfer of angular momentum from the photons to the ferromagnet is expected to be negligible and can not be the main driving force for ultrafast demagnetization.

The second category focuses on the local spin dynamics indirectly triggered by excitation of the electronic system [13, 18, 23–38]. The resulting magnetization dynamics can be calculated within various theoretical models. Examples include the atomistic Landau-Lifshitz-Gilbert (LLG) equation [24, 41], the Landau-Lifshitz-Bloch (LLB) equation [27, 30, 35], Time-dependent density functional theory [37], and multiple other implementations. Microscopically, exciting the electron system yields an increased rate of various scattering processes that may involve spin flips, such as electron-phonon scattering [18, 30], electron-magnon scattering [25, 31, 36, 42], and electron-electron scattering [26]. The general consensus is that multiple types of those spin-flip scattering processes contribute to the observed large demagnetization rates [19, 34, 43]. Moreover, it has been claimed that it is required to implement a modified electronic band structure [44, 45], including a dynamical exchange splitting that responds to the changed magnetization [32, 33, 36, 44, 46]. The latter is typically described by a thermodynamical approach where, besides an increased electron temperature, the equilibration of the spin-dependent chemical potentials plays a critical role [29, 33, 36].

In this thesis, we repeatedly make use of the microscopic three-temperature model (M3TM) [18]. A schematic overview of this description is given in Fig. 1.3(b). In the M3TM, it is assumed that the demagnetization process is driven by Elliott-Yafet electron-phonon scattering [18, 23]. Generally, the Elliott-Yafet mechanism refers to the fact that in the presence of spin-orbit coupling any scattering event involving electrons has a nonvanishing probability to result in an effective spin flip [26, 47–53]. In that scenario, Elliott-Yafet electron-phonon scattering enables the demagnetization process, since it provides a channel for the loss of spin angular momentum. The scattering rate is typically calculated using Fermi's golden rule. In the case of a spin one-half system, the dynamics of the normalized magnetization m is described by the well-known formula [18]

$$\frac{dm}{dt} = Rm\frac{T_p}{T_C}\left[1 - m\coth\left(\frac{mT_C}{T_e}\right)\right], \tag{1.1}$$

where T_C corresponds to the Curie temperature, and R is a coefficient determined by the electron-phonon scattering rate and spin-flip probability [18]. To model the laser-induced magnetization dynamics, the response of the temperatures T_e and T_p is typically calculated using the original two-temperature model. Subsequently, Eq. (1.1) is solved for m. An example calculation is presented in Fig. 1.3(d), showing the normalized magnetization m as a function of time after laser-pulse excitation at $t = 0$. The plot represents a typical demagnetization curve in accordance with the experiments (e.g., Fig. 1.2). As it is assumed that this process is driven by the Elliott-Yafet mechanism, which originates from spin-orbit coupling, the lost spin angular momentum is eventually transferred to the lattice degrees of freedom [23, 26]. This transfer has recently been observed experimentally [54, 55]

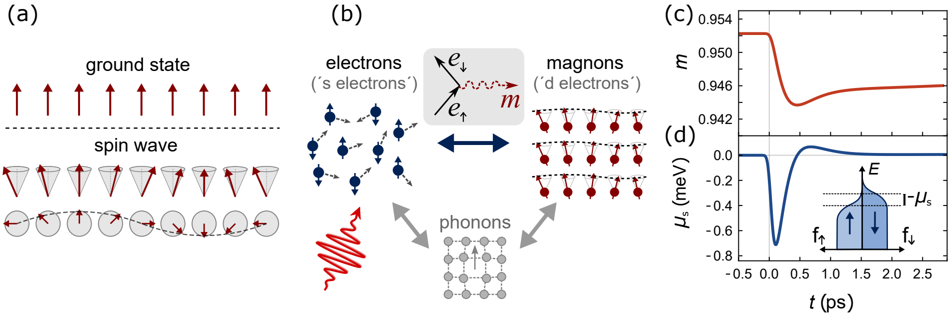

Figure 1.4: (a) Schematic representation of spin waves, where the arrows indicate the spin at a lattice site. Spin waves (magnons) correspond to collective spin excitations, and yield a decrease of the net spin of the system compared to the ground state. (b) Schematic overview of the model for ultrafast demagnetization based on electron-magnon scattering. The latter transfers angular momentum between the itinerant spin system and the magnon system. In gray, we note the *s*-*d* model terminology and an eventual coupling to the phonon system. (c) Example calculation of ultrafast demagnetization driven by electron-magnon scattering. The red curve indicates the magnetization as a function of time after laser-pulse excitation at $t = 0$. (d) The spin accumulation generated within the itinerant spin system. The inset indicates the distribution of the spin up and down electrons, where the spin accumulation μ_s is defined as the difference in chemical potential [36].

An alternative theoretical approach that plays an important role in this thesis, is based on the *s*-*d* interaction [31, 56–58]. It describes the coupling between local and itinerant spin degrees of freedom.[2] When the system is rapidly heated, the *s*-*d* interaction enables the spin transfer from the relatively localized *d* spins to the itinerant *s* electrons and drives the (local) demagnetization process. Typically, this process requires additional spin dissipation channels that efficiently remove the built-up spin accumulation from the itinerant system [36, 56]. The framework of the *s*-*d* model was originally applied to describe the laser-induced spin dynamics in semiconductors [56], and ferrimagnetic alloys [58]. For ferromagnetic transition metals, the validity of the *s*-*d* model is less pronounced due to the absence of a clear separation of 'local' 3*d* and 'nonlocal' 4*s* electrons. Hence, the *s*-*d* model should be interpreted as a phenomenological treatment of the effective local and nonlocal spin degrees of freedom. As discussed in this thesis, the *s*-*d* model is of particular interest, since it provides a transparent and simple description to qualitatively address the relation between ultrafast demagnetization and laser-induced spin transport.

A different view on the *s*-*d* interaction, that better suits the magnetic properties of

---

[2] Depending on the specific material, the naming should actually refer to coupling of *s*, *p*, *d* or *f* electrons.

transition metal ferromagnets, is based on taking into account magnon excitations. To clarify, a magnon corresponds to the quantum of a collective 'spin-wave' excitation. The creation of a magnon yields a decrease of the net spin of the magnetic system, as schematically depicted in Fig. 1.4(a). Importantly, the abovementioned *s*-*d* interaction leads to electron-magnon scattering processes. When the magnet is heated, electron-magnon scattering results in an increase of the magnon density, i.e., a decrease of the magnetization [31, 36]. A schematic overview of the corresponding model for ultrafast demagnetization is presented in Fig. 1.4(b), where the dark arrow indicates the transfer of spin angular momentum through electron-magnon scattering processes. A typical calculation of the laser-induced magnetization dynamics is depicted in Fig. 1.4(c). The latter shows the magnetization as a function of time after laser-pulse excitation at $t = 0$. Simultaneously, a spin accumulation is built up in the itinerant spin system, which corresponds to a spin-split chemical potential $\mu_s = \mu_\uparrow - \mu_\downarrow$ and is plotted in Fig. 1.4(d) as a function of time. This approach was introduced by Tveten et al. [36], and its importance will be discussed in more detail in the following section about spin transport. Finally, we note that in the case that magnon-phonon coupling is taken into account, this approach can produce a microscopic equivalent of the original three-temperature model [13], where the previously introduced spin temperature corresponds to the magnon temperature of an instantaneously thermalized magnon system [31, 59].

Up to this point, we only discussed the models based on the local spin dynamics. Another possible mechanism for ultrafast demagnetization in a magnetic thin film is the loss of spin into adjacent metallic layers, driven by spin transport [39, 60]. Quantifying the relative significance of local and nonlocal spin processes is one of the major challenges of femtomagnetism. Some experiments showed that it can not be solely spin transport that drives the rapid quenching of the magnetization, e.g., by comparing the demagnetization rates for samples with respectively an insulating or conducting substrate [61]. Nevertheless, it is widely accepted in literature that both local spin dynamics and spin transport can significantly contribute to ultrafast demagnetization [60, 62, 63], where the relative importance strongly depends on the specific magnetic system and its environment. The physical origin of laser-induced spin transport, and its role in femtomagnetism in general, are discussed in the next section.

1.3 LASER-INDUCED SPIN TRANSPORT

The first evidence of laser-induced spin transport was found in 2008 by Malinowski et al. [14]. The authors probed the magnetization dynamics of a collinear magnetic heterostructure, consisting of two out-of-plane magnetic layers with a conductive spacer layer in between. A comparison of the demagnetization rate for the parallel and antiparallel configuration was carried out. The results are shown in Fig. 1.5(a), where the inset gives a schematic overview of the collinear system and the specific configurations. The red and blue lines indicate the magnetization as a function of time after laser-pulse excitation at $t = 0$, for the parallel (red) and antiparallel (blue) configuration, respectively. The clear difference in the demagnetization rate was attributed to the presence of interlayer spin transport, which provides an additional channel for spin angular momentum transfer.

Optically-induced spin currents provide a potential tool to efficiently control the magnetic orientation within multilayered spin structures. For instance, experiments in noncollinear magnetic heterostructures showed that the laser-induced spin currents exert a spin-transfer torque onto the magnetization of a secondary magnetic layer [64, 65]. Interestingly, the absorption layer is excited inhomogeneously due to the short penetration depth of the injected spins, leading to the generation of standing spin waves [66, 67]. The particular magnetic structure and the spin-wave excitation scheme are visually represented by the insets in Fig. 1.5(b). This phenomenon was demonstrated experimentally by multiple groups [66, 67], and one of the measurements is presented in the main part of Fig. 1.5(b). The plot shows the magneto-optical signal determined by the transverse magnetization in the top region of the in-plane layer, given as a function of time after laser-pulse excitation. The oscillatory characteristics indicate the presence of coherent standing spin waves. Specifically, the homogeneous precession (10.23 GHz) and the first normal mode (0.55 THz) are clearly observed.

Although the abovementioned experiments proved the existence of laser-induced spin transport, they do not give direct information on the temporal profile of the spin current. The latter can be probed by using THz spectroscopy [68–70]. Figure 1.6(a) shows an example, and corresponds to very recent measurements [70]. The experiments were performed using three types of magnetic heterostructures, all containing a transition metal ferromagnet and a platinum layer. Figure 1.6(b) gives a schematic representation of the magnetic system, including the injected

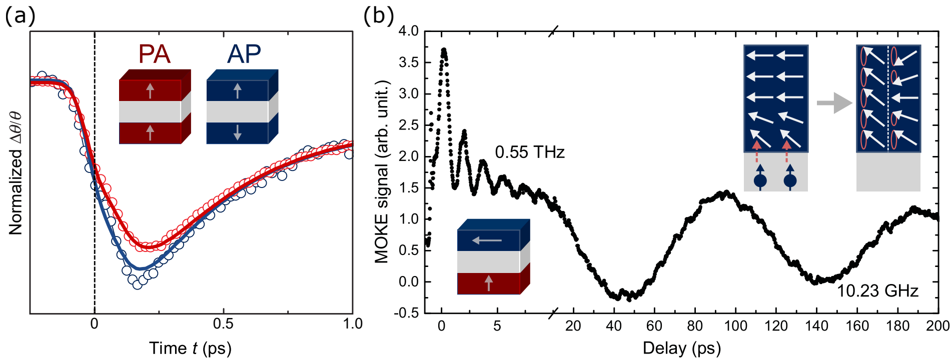

Figure 1.5: (a) The measurements by Malinowski et al. [14]. The plotted magneto-optical signals show the distinct demagnetization rates of a parallel (red) and antiparallel (blue) configuration of a collinear magnetic heterostructure. Here, t indicates the time after laser-pulse excitation. The observed different rates indicate the presence of interlayer spin transport. The inset shows a schematic overview of the two configurations. (b) The experimental results of Lalieu et al. [67], indicating the excitation of THz standing spin waves. The left inset shows the particular system, corresponding to a noncollinear magnetic heterostructure. The presented magneto-optical signal gives the out-of-plane magnetization of the top layer and is plotted as a function of time after laser-pulse excitation. The right inset indicates the spin-wave excitation mechanism. The incoming spins are absorbed near the interface, resulting in the excitation of both a homogeneous precession (10.23 GHz) and a first-order standing spin wave (0.55 THz). The figures are adapted from Refs. [14, 67].

spin current $j_s(t)$. In Fig. 1.6(a), the blue lines indicate the temporal behavior of the injected spin current as a function of time after laser-pulse excitation at $t = 0$, and clearly show the ultrashort transient behavior of the spin-current pulses. The red curves indicate the derivative of the magnetization for the specific magnetic layers. Importantly, the figure indicates that the temporal profile of spin current and the derivative of magnetization are closely connected. The latter is an important observation in relation to identifying the underlying microscopic mechanism of optically-generated spin currents. However, it does not exclusively point to one specific theory and can be interpreted with multiple models [36, 39, 65, 70–72].

Similar to ultrafast demagnetization, the physical origin of laser-induced spin transport is not yet unanimously identified. A commonly used theoretical approach for laser-induced spin currents is based on the model for superdiffusive spin transport [39]. The laser pulse generates a population of highly energetic electrons that through a spin-dependent excitation rate and mobility yield spin-polarized hot electron currents. Because of the generated cascades of secondary hot electrons, it is an efficient scheme of spin-current generation [39, 73]. This characteristic transport

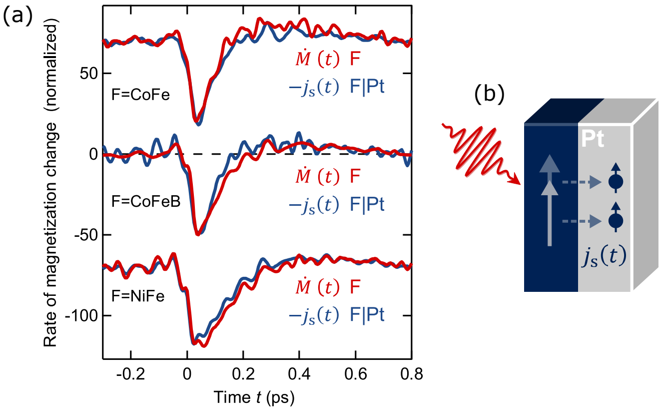

Figure 1.6: (a) THz spectroscopy experiments indicating the relation between the spin current and the demagnetization in three types of magnetic heterostructures (given in the figure), as presented by Rouzegar et al. [70]. The blue lines indicate the spin current, and the red lines correspond to the temporal derivative of the magnetization, both plotted as a function of time t after laser-pulse excitation at $t = 0$. (b) A schematic overview of the corresponding magnetic heterostructure, showing the demagnetization in the ferromagnetic layer (blue) and a spin current $j_s(t)$ flowing into the Pt layer (gray). Figure (a) is taken from Ref. [70].

type is dubbed 'superdiffusive', since the corresponding mean-free path qualifies between the diffusive and ballistic regime.

Another recently supported view is related to the results shown in Fig. 1.6(a), the close connection between the spin current and the change of the magnetization. Choi et al. [65] proposed that the source of the laser-induced spin currents is directly related to the temporal derivative of the magnetization. The authors performed experiments where they simultaneously probed the magnetization in a Co thin film and the built-up spin accumulation in an adjacent Cu layer. The measurements were compared to a calculation using the spin diffusion equation, including a source term proportional to the derivative of the (experimentally-retrieved) magnetization. The calculated spin accumulation was in fair agreement with the experiments.

The choice of this spin source is motivated by the conservation of angular momentum, assuming that the spin loss during the local demagnetization process is converted to itinerant spins [65]. This coupling between local and nonlocal spin degrees of freedom is clearly related to an *s*-*d* type of interaction, as discussed in the previous section. In that sense, the authors claimed that laser-induced spin transport is governed by local electron-magnon scattering processes as a spin source [65]. The source term was later confirmed by a microscopic calculation performed by Tveten et al. [36], who derived the rate equation describing the temporal derivative of the spin accumulation as a result of bulk and interfacial electron-magnon scattering. A typical calculation of the bulk contribution was presented in the previous section, in Fig. 1.3(d), showing the bipolar transient behavior of the generated spin accumulation. The qualitative similarities between the latter and the measurements in Fig. 1.6(a) support the view that the local accumulation of spin is possibly the dominant driving force for ultrafast spin transport. However, it should be noted that these observations, including the direct relation between the spin current and the derivative of the magnetization, could be demonstrated within other theoretical approaches [39, 70].

The third type of models for laser-induced spin transport is related to the spin-dependent Seebeck effect [74, 75]. It describes the mechanism in ferromagnetic systems that thermal gradients in the bulk, or across an interface, generate a net spin current carried by conduction electrons. In case an instantaneously thermalized electron system is assumed, the spin current is directly proportional to the temperature gradient. Obviously, heating through laser-pulse excitation creates such an imbalance in the thermal state of the system. It is shown that the contribution of the spin-dependent Seebeck effect to laser-induced spin transport is relatively small in the subpicosecond regime, however, it can be significant on the timescale of a few picoseconds [74]. At short timescales, the nonthermal nature of the hot electron distribution function is proposed to play an important role, and yields the so-called nonthermal spin-dependent Seebeck effect [75]. Here, the spin current stems directly from a significant difference in the interfacial transmittance of majority and minority hot electrons [75].

Some of the theoretical interpretations discussed in this chapter, especially the mechanism related to electron-magnon scattering, provide a complete picture of local and nonlocal spin dynamics in laser-excited magnetic heterostructures. Nevertheless, a joint theoretical description of ultrafast demagnetization and laser-induced spin transport has not been fully carried out and is one of the main topics of this thesis. Here, an additional goal is to investigate systems that include a ferrimagnetic component. These materials are exceptionally interesting, as they allow the magnetization direction to be controlled with femtosecond laser pulses. In the following section, we focus on this process in detail and shortly discuss the interplay with laser-induced spin transport.

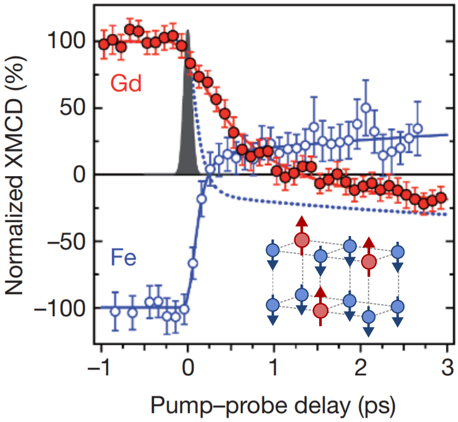

Figure 1.7: (a) The element-specific time-resolved measurements of all-optical switching in GdFeCo, as published by Radu et al. [11]. The plotted signals represent the magnetization of Gd (red) and Fe (blue), as a function of time after the laser-pulse excitation. The gray area indicates the temporal profile of the laser pulse. The inset gives a simplified representation of the microscopic structure of the GdFeCo system, showing the antiparallel orientation of the Gd (red) and FeCo (blue) magnetic sublattices. Taken from Ref. [11].

1.4 ALL-OPTICAL SWITCHING

The previous sections already showed the versatility of using femtosecond laser pulses as a tool to manipulate magnetic order. The final example we discuss in this introductory chapter is that ultrashort laser pulses can induce magnetization reversal in ferrimagnetic materials. This so-called all-optical switching (AOS) was first observed in ferrimagnetic GdFeCo alloys by Stanciu et al. [10]. Although it was originally believed that circularly polarized laser pulses were required, it was later demonstrated that the use of a linearly-polarized pulse is sufficient for deterministically switching the magnetization [11, 12]. Surprisingly, the results indicate that the magnetic order in GdFeCo can be toggled with ultrafast heating as the only stimulus. It is obvious that such a simple and efficient mechanism for controlling magnetization is interesting from a technological point of view. For that reason, single-pulse AOS is one of the most popular themes of recent research in femtomagnetism.

A breakthrough in the field was obtaining the element-specific time-resolved measurements of AOS in GdFeCo alloys, as presented by Radu et al. [11]. The result is depicted in Fig. 1.7, where the inset presents a schematic representation of the equilibrium state of ferrimagnetic GdFeCo. The material consists of two magnetic sublattices that are antiferromagnetically coupled. The main figure indicates the element-specific magnetization as a function of time after laser-pulse excitation. Upon excitation, the two sublattices demagnetize at distinct rates. The Fe magnetization reverses rapidly and crosses zero within a picosecond, resulting in a transient ferromagnetic state. Subsequently, the Gd magnetization changes sign around 1.5 ps. Ultimately, the combined system remagnetizes and reaches the new (reversed) equilibrium state.

The element-specific measurements elucidated the essential physical properties of the switchable material, such as the antiferromagnetically coupled magnetic sublattices and the distinct demagnetization rates. This insight helped to develop the theoretical models for the underlying physical mechanism. A phenomenological theoretical framework was proposed by Mentink et al. [76, 77]. The authors claimed the essential role of the antiferromagnetic exchange and the resulting intersublattice transfer of angular momentum. The latter has been implemented within a microscopic approach by Schellekens et al. [78], by introducing exchange scattering processes in a multisublattice extension of the microscopic three-temperature model [78]. Other successful theoretical methods include the atomistic Landau-Lifshitz-Gilbert equation [79–84], and the Landau-Lifshitz-Bloch equation [85, 86], applied for the ferrimagnetic systems. A different approach was proposed by Gridnev et al. [58, 87, 88], and involves the *s*-*d* exchange interaction. Here, the model describes two independent local spin systems that can exchange angular momentum with a single itinerant spin system. The combination of the *s*-*d* exchange and efficient spin dissipation to the lattice yields an adequate pathway for switching a ferrimagnetic alloy.

From an engineering point of view, it is essential to search for the optimal material for the integration of AOS in future data storage devices. Single-pulse AOS has been demonstrated in various material systems such as GdFeCo alloys [10, 11], Co/Gd bilayers [89], Co/Tb multilayers [90], and Heusler alloys [91]. Note that we only listed the materials in which helicity-independent single-pulse AOS is demonstrated, meaning that we do not discuss the helicity-dependent variant [92]. Although the latter is interesting in itself, it is beyond the scope of this thesis. Similarly, single-pulse AOS in Heusler alloys is not discussed in detail. We should, however, mention its relevance for spintronic applications [91].

Although the materials that allow single-pulse AOS are mostly based on transition-metal and rare-earth components, the precise composition and structure strongly affect the applicability of the specific system. For instance, the ferrimagnetic alloys are only switchable in a small concentration range near the magnetization compensation point and thereby require a specific composition [93, 94]. On top of that, Co/Gd and Co/Tb stacks are more practical in terms of the fabrication process and tuning the precise magnetic properties of the systems. Other factors to take into account are the minimal stable (all-optically written) domain size and the achievable domain wall velocity. In the case of the size of the domains, the use a Tb component is favorable [90, 95]. On the other hand, in the Gd-based systems, both for alloys [96, 97], and recently multilayers [98], experiments on current-induced domain-wall motion demonstrated relatively high velocities in the order of kilometers per second. In that sense, multilayers including Co/Gd components are a promising candidate for the integration of single-pulse AOS in a racetrack memory device [99]. Hence, it is not a coincidence that these material systems are studied theoretically in this thesis.

Finally, recent experiments show fascinating physics regarding laser-induced spin transport in magnetic heterostructures that include a ferrimagnetic layer. For instance, Iihama et al. [100, 101] showed that in [Co/Pt]/Cu/GdFeCo stacks the ferromagnetic layer ([Co/Pt]) can be indirectly switched by exciting the multilayer with a single laser pulse. Here, the laser pulse toggles the GdFeCo layer magnetization and simultaneously generates an interlayer spin current. The switching of the ferromagnetic Co/Pt layer arises from the combination of its ultrafast demagnetization and the absorbed interlayer spin current [100, 102, 103]. Similar experiments were performed in GdFeCo/Cu/GdFeCo stacks [104], showing that the interlayer spin transport strongly affects the requirements for switching the individual ferrimagnetic layers. Hence, tuning the composition of magnetic multilayers is an essential advantage and can be used to functionalize the material for optimal AOS properties. This has been shown in [Gd/Co]/Cu/[Co/Ni]$_N$ multilayers [105], where the ferromagnetic [Co/Ni] component is used as a reference layer. Interlayer spin transport either enhances or hinders the AOS process, dependent on the orientation of the reference layer. Because of this effect, the laser pulses can be tuned to write a predetermined magnetization direction, regardless of the initial state of the system. In that way, single-pulse AOS evolves from a toggle mechanism to a method for deterministic magnetization writing [105].

All the listed experiments reveal the complex interplay between demagnetization, spin-current generation, and magnetization reversal. To determine the critical material parameters for the optimization of the underlying mechanisms, an insightful theoretical model would be helpful. Although such a complete description is still lacking, the models discussed in this thesis could be a possible starting point.

1.5 THESIS OUTLINE

In this introductory chapter, we gave an overview of the main topics of femtomagnetism and ultrafast spintronics. In the research of the thesis, we build on the theoretical fundaments that have been developed over the past decades and present new insights regarding the mechanisms underlying ultrafast magnetism. The main goal of our work is to develop an intuitive theoretical framework that includes all dominant physical concepts, without the loss of simplicity.

We start with providing a firm theoretical basis in **Chapter 2**. Here, we introduce the physical concepts that are essential for the main chapters. This includes a detailed derivation of the models like the M3TM, the *s*-*d* model, and other theoretical descriptions. Importantly, the chapter gives an overview of the various models we use and we specifically discuss their applicability and validity in the context of the relevant physical regimes.

The following five chapters present the main results. In **Chapter 3**, we discuss a joint description of ultrafast demagnetization and laser-induced spin transport. By connecting the *s*-*d* model for the local spin dynamics, to the diffusive description of spin transport, we show that the typical experiments can be simulated within a single microscopic implementation. In **Chapter 4**, we extend this theory by including thermal magnons. Here, spin-dependent electron transport and magnon transport are treated on equal footing. The model is compared to recent experiments, and an analysis is presented that formulates the relation between the ultrafast spin currents and the derivative of the magnetization. Furthermore, it is shown that the role of magnon transport can not be neglected.

In **Chapter 5**, we develop a toy model that includes both the spin current resulting from the laser-excited hot electrons and the spin current triggered by electron-magnon scattering. Based on an analytical relation, we show that the latter contribution is generally large.

The two subsequent research chapters are focused on modeling AOS in Co/Gd bilayers. In **Chapter 6**, we develop a model that simulates AOS in these synthetic-ferrimagnetic systems. Here, we identify the switching mechanism as a front of reversed Co magnetization that nucleates near the Co/Gd interface and propagates through the bilayer to establish the full switch. The latter emphasizes the robustness of the AOS mechanism in synthetic ferrimagnets. **Chapter 7** includes a discussion on the role of intermixing of the Co/Gd interface. We show calculations that predict that intermixing enhances the AOS process and helps to reduce the threshold fluence.

Finally, **Chapter 8** presents additional research that corresponds either to preliminary results, or extensions of the work in the main chapters. Furthermore, this final chapter includes a general outlook on the research field.

2

THEORETICAL BACKGROUND

Since all models are wrong the scientist must be alert to what is importantly wrong. It is inappropriate to be concerned about mice when there are tigers abroad.

George E.P. Box [106]

In this chapter, we introduce the theoretical tools that are used in the remaining part of the thesis. First, we discuss several models that describe the local spin dynamics driven by laser-pulse excitation, including the microscopic three-temperature model and the s-d model. Secondly, we review the implementation of spin transport, specifically, spin-dependent electron transport and diffusive magnon transport. Finally, we focus on the description of ferrimagnetic systems and the modeling of all-optical switching. We stress that the majority of the derivations presented here have been introduced before in literature. Therefore, experts in the field may skip this introductory chapter. Nevertheless, as some extensions and interpretations deviate from the standard approaches, this chapter functions as an additional reference for the work in the remainder of the thesis.

2.1 INTRODUCTION

Over the course of the past decades, a wide variety of theoretical models have been developed that address the spin dynamics in rapidly heated magnets. A brief overview of the most common approaches was presented in Chapter 1. As the long list of interpretations exemplifies, laser-induced spin dynamics is intrinsically difficult to understand at a microscopic level. Although it might be possible to implement all degrees of freedom and interactions within a single theory, such an extensive description is (practically) too complex to describe numerically, and overcomplicates the process of identifying the essential physics. The latter is the reason we generally take a simplified approach and choose a theoretical treatment that only captures specific, presumably dominant, physical concepts. Here, we generally aim for a compact mathematical framework to investigate the physics underlying ultrafast magnetism. Hopefully, this approach clarifies the inclusion of the quote at the beginning of this chapter.

This background chapter presents a step-by-step derivation of several models for laser-induced spin dynamics that are developed with the above mindset. We gently introduce the basic underlying concepts, including references to the original works, and motivate every subsequent extension or simplification. Furthermore, the chapter includes multiple illustrative examples of modeling the standard experiments. Below we give a detailed outline of the chapter.

In Sec. 2.2, the Weiss model is shortly reviewed, which will be useful as a simple description for the magnetization in equilibrium. Then, Sections 2.3-2.5 focus on the local magnetization dynamics driven by rapid heating. Here, the discussed models are all analogously derived from a microscopic Hamiltonian, and require the calculation of spin-flip scattering rates using Fermi's golden rule. This standard method is the basis of the microscopic three-temperature model, which is the main subject of Sec. 2.3. Using the same mathematical tools, the magnetization dynamics driven by the *s*-*d* interaction is described in Sec. 2.4. The resulting *s*-*d* model is an essential step towards modeling nonlocal spin dynamics, as it includes an itinerant spin system [56, 57]. In close connection to the *s*-*d* model, the role of thermal magnons and electron-magnon scattering processes is discussed in Sec. 2.5. The latter results in a more comprehensive description of spin dynamics in metallic ferromagnets [31, 36], as both magnons and electrons may contribute to nonlocal spin transfer.

The second part of the chapter, Section 2.6, focuses on the standard description of diffusive spin transport [107]. We subsequently discuss spin-dependent electron transport and thermal magnon transport. Both contributions are analogously derived from the Boltzmann equation and equivalently expressed in terms of gradients of a chemical potential and temperature. Importantly, the overview does not include any other types of descriptions for nonlocal spin transfer, such as the superdiffusive spin transport model [39]. A very brief comparison between the latter and the diffusive approach is presented in Chapter 5.

Finally, in Sec. 2.7, the focus is redirected towards ferrimagnetic systems and the modeling of all-optical switching. Two models for the local spin dynamics in ferrimagnetic alloys are discussed. The first one represents an extension of the microscopic three-temperature model [4, 78], and requires calculating the intersublattice spin-transfer rate as a result of exchange scattering processes. The second one is a straightforward extension of the *s*-*d* model to ferrimagnetic alloys [58]. Similar to multiple other models in this chapter, the equilibrium conditions are determined by a simple Weiss model. The latter is the subject of the following paragraph.

2.2 The Weiss model

In the first part of this chapter, several theoretical approaches for describing laser-induced spin dynamics are introduced. Before analyzing the behavior of the excited spin systems, we first address the thermodynamic properties of the magnetization in equilibrium. Specifically, the Weiss model is introduced, which is a statistical description that gives the magnetization as a function of temperature. The presented framework will provide the initial (and final) conditions for multiple dynamical models discussed later in this chapter.

The starting point to introduce the Weiss mean-field approach is the standard Heisenberg model for a lattice of spins. The corresponding Hamiltonian is given by [1, 3, 108]

$$\hat{H} = -J \sum_{i,j} \hat{\mathbf{S}}_i \cdot \hat{\mathbf{S}}_j. \tag{2.1}$$

where $\hat{\mathbf{S}}_j$ corresponds to the spin operator at lattice site j (in units of $\hbar$). The summation is carried over the nearest neighbors and J is the exchange coupling constant. We employ a mean-field approach. Here, we define that the ensemble average of the spin in our system is pointing along the z direction, i.e., the mean field is given by $\langle \mathbf{S} \rangle = \langle \hat{S}^z \rangle \hat{z}$. We omitted the lattice index j, as we assume a homogeneous system. The Hamiltonian now reads

$$\hat{H} = \Delta \sum_j \hat{S}_j^z, \tag{2.2}$$

where $\Delta = -Jz\langle \hat{S}^z \rangle$ is the exchange splitting, with z the number of nearest neighbors. Focusing on a single spin $\hat{S}_j^z$ with spin quantum number S, the Hamiltonian in Eq. (2.2) describes a system of $2S+1$ spin levels separated by the exchange splitting Δ. The possible states are labeled by the azimuthal spin quantum number $m_s \in \{-S, -S+1, .., S-1, S\}$. The statistical state of the spin system is described by the occupation probability f_{m_s} of the state m_s. In equilibrium, f_{m_s} is determined by Boltzmann statistics [1, 4, 109]

$$f_{m_s} = \frac{e^{-\Delta m_s/(k_B T)}}{\sum_{m_s} e^{-\Delta m_s/(k_B T)}}, \tag{2.3}$$

where T is the temperature. The ensemble average of the z component of the spin is given by

$$\langle \hat{S}^z \rangle = \sum_{m_s=-S}^{S} m_s f_{m_s}. \tag{2.4}$$

We define the order parameter $m = -\langle \hat{S}^z \rangle / S$, which is equivalent to the normalized magnetization. Combining the equations above gives a self-consistent equation for the normalized magnetization

$$m = B_S\left(\frac{S\Delta}{k_B T}\right), \tag{2.5}$$

where $B_S(x)$ is the Brillouin function [1, 35]. An analysis of Eq. (2.5) near the critical point, which is by definition given by the Curie temperature T_C, yields that the exchange splitting is given by $\Delta = 3k_B T_C m/(S+1)$ [4]. For a $S = 1/2$ system, the magnetization is then described by the standard formula $m = \tanh(mT_C/T)$. To further clarify the meaning of Eq. (2.5), Figure 2.1 gives its solution for multiple values of S. The plot presents the normalized magnetization as a function of temperature, and clearly shows the magnetization abruptly vanishes above the critical point T_C.

The Weiss model provides an intuitive description of the equilibrium magnetization and describes the temperature dependence relatively well. Although the approach

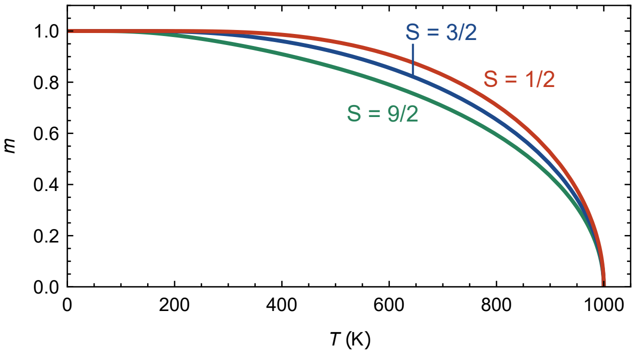

Figure 2.1: The Weiss model for varying spin quantum number S. The normalized magnetization m is plotted as a function of the temperature T, for $S = 1/2$ (red), $S = 3/2$ (blue), and $S = 9/2$ (green). The Curie temperature is set to $T_C = 1000$ K.

has certain loopholes, its simpleness makes it a practical starting point for the development of microscopic models that describe the out-of-equilibrium spin dynamics. In that case, the occupation probability $f_{m_s}(t)$ becomes time dependent and deviates from the probability given by Boltzmann statistics. In the following sections, we discuss what processes are involved and how the temporal behavior of spin system can be calculated.

2.3 The microscopic three-temperature model

In this section, we discuss the physical concepts related to the microscopic three-temperature model (M3TM). First, we review the Elliott-Yafet mechanism for spin relaxation. Second, we present the calculation of the spin-flip scattering rate. For the latter, we first focus on spin-flip impurity scattering and later discuss the role of the electron-phonon interaction. At that point, we shortly discuss the connection to the two-temperature model for laser heating.

2.3.1 The Elliott-Yafet mechanism

In the M3TM, a central role is played by Elliott-Yafet spin-flip scattering. In this paragraph, we introduce the underlying mechanism in a general context [47]. In the presence of spin-orbit coupling, the spin up and spin down electron states are not eigenstates of the Hamiltonian. Instead, the eigenstates are given by spin-mixed states of the form [47, 51, 53]

$$|\mathbf{k},\Uparrow\rangle = a_{\mathbf{k}}^{+}\,|\mathbf{k},\uparrow\rangle + b_{\mathbf{k}}^{+}\,|\mathbf{k},\downarrow\rangle\,, \tag{2.6}$$

$$|\mathbf{k},\Downarrow\rangle = a_{\mathbf{k}}^{-}\,|\mathbf{k},\downarrow\rangle + b_{\mathbf{k}}^{-}\,|\mathbf{k},\uparrow\rangle\,. \tag{2.7}$$

The labels $\Uparrow$ and $\Downarrow$ refer to predominantly spin up or spin down states [53], as it is typically imposed that $|a_{\mathbf{k}}^{\pm}| \gg |b_{\mathbf{k}}^{\pm}|$.

Now we assume that the electron is subject to an additional interaction with the environment, by definition described by an operator $\hat{V}$. To arrive at the Elliott-Yafet mechanism, we write the operator $\hat{V}$ in second quantization. It is expressed in terms of creation and annihilation operators $c_{\mathbf{k}\alpha}^{\dagger}$ and $c_{\mathbf{k},\alpha}$ with $\alpha \in \{\Uparrow,\Downarrow\}$ and momentum $\mathbf{k}$. In second quantization, the interaction Hamiltonian is given by

$$\hat{H}_{\text{int}} = \sum_{\mathbf{k}\mathbf{k}'\alpha\alpha'} \langle\mathbf{k},\alpha|\,\hat{V}\,|\mathbf{k}',\alpha'\rangle\, c_{\mathbf{k}\alpha}^{\dagger}c_{\mathbf{k}'\alpha'} = \sum_{\mathbf{k}\mathbf{k}'\alpha\alpha'} V_{\mathbf{k}\mathbf{k}'\alpha\alpha'}c_{\mathbf{k}\alpha}^{\dagger}c_{\mathbf{k}'\alpha'}. \tag{2.8}$$

Even if the operator $\hat{V}$ is completely spin independent, the Hamiltonian might include terms for $\alpha \neq \alpha'$ due to the nonvanishing $\langle\mathbf{k},\Uparrow|\,\hat{V}\,|\mathbf{k}',\Downarrow\rangle \neq 0$ as a result of the spin mixing [53]. These terms describe transitions between majority and minority spin states. In other words, these processes correspond to spin-flip scattering and yield a net change of the spin component along the z axis. We stress that the Elliott-Yafet mechanism is present regardless of the origin of $\hat{V}$ and thereby might involve various scattering events, such as impurity scattering, electron-phonon scattering, or other contributions. As the scattering rate is proportional to the square of the corresponding matrix element, the spin-flip probability is determined by $|b_{\mathbf{k}}^{\pm}|^2$ [51].

In the remainder of this chapter, the spin-flip scattering resulting from the Elliott-Yafet mechanism is either treated phenomenologically or by hand introduced in a microscopic Hamiltonian.

2.3.2 SPIN DYNAMICS AND THE M3TM APPROXIMATION

In this section, we calculate the spin dynamics driven by Elliott-Yafet spin-flip scattering within the framework of the microscopic three-temperature model (M3TM). With the latter we mean imposing three critical approximations: (i) spin dynamics is exclusively driven by Elliott-Yafet spin-flip scattering, (ii) the spin degree of freedom is treated as a localized system of spins and in equilibrium described by the Weiss model, (iii) the additional electronic degrees of freedom are described by a separate system of free and spinless electrons. In the remainder of the thesis, we refer to this list of assumptions as the "M3TM approximation". Typically, a fourth assumption is made that only considers a spin one-half system. We discuss this specific case at the end of the section. First, we present the results for a system with an arbitrary spin quantum number, since the derivation is used later in the thesis.

For illustrative purposes, we focus on spin-flip impurity scattering [23]. In essence, the discussed method is applicable for other Elliott-Yafet spin-flip scattering processes, such as electron-phonon scattering. Within the M3TM approximation, where the electrons are treated as spinless, the Hamiltonian for spin-flip impurity scattering would be of the form [23]

$$\hat{H} = \frac{\lambda}{N} \sum_{j} \sum_{\mathbf{k}\mathbf{k}'} \left[\hat{S}_j^+ c_{\mathbf{k}'}^\dagger c_{\mathbf{k}} + \hat{S}_j^- c_{\mathbf{k}}^\dagger c_{\mathbf{k}'} \right], \tag{2.9}$$

where N is defined as the number of lattice sites, λ is a phenomenological constant that determines the scattering rate, and $\hat{S}_j^\pm$ represent the spin ladder operators for the spin located at site j. Obviously, the first term in the Hamiltonian describes the scattering process in which the spin quantum number m_s is increased, whereas the second term corresponds to an opposite transition.

We are mainly interested in the spin dynamics as a result of the scattering events described by Eq. (2.9). The physical model requires calculating the corresponding scattering rates using Fermi's golden rule. Although the latter is a standard formalism, its application to multiple coupled subsystems requires some extra comments. Therefore, Appendix A includes an introduction to Fermi's golden rule and its relation to the Boltzmann equation. The discussion includes the derivation within a density matrix formalism and is only meant for readers interested in the underlying theoretical assumptions.

Applying Fermi's golden rule to the interaction Hamiltonian in Eq. (2.9) yields the transition rate for spin state $|m_s\rangle$ to $|m_s \pm 1\rangle$. It is defined as $W^\pm_{m_s \pm 1, m_s}$ and given by

$$W^\pm_{m_s \pm 1, m_s} = \frac{2\pi}{\hbar} \lambda^2 S^\pm_{m_s} \frac{1}{N^2} \sum_{\mathbf{k}\mathbf{k}'} \delta(\epsilon_{\mathbf{k}} \mp \Delta - \epsilon_{\mathbf{k}'}) f_{\mathbf{k}} (1 - f_{\mathbf{k}'}). \tag{2.10}$$

The prefactor includes $S^{\pm}_{m_s} = S(S+1) - m_s(m_s \pm 1)$, which comes from the spin ladder operators. The terms in the summation have a simple physical meaning in relation to the scattering process. The Dirac delta function imposes energy conservation. Moreover, the electron distribution function $f_{\mathbf{k}}$ determines the occupation of the initial electron state with momentum $\mathbf{k}$. Finally, the factor $(1 - f_{\mathbf{k}'})$ depends on the occupation of the final state and is a manifestation of Pauli's exclusion principle. The remainder of this section describes a number of mathematical simplifications of the transition rate.

First, we take the continuum limit and replace the summations over the $\mathbf{k}$ vectors by integrals

$$\sum_{\mathbf{k}} \to \frac{V}{(2\pi)^3} \int d\mathbf{k}, \tag{2.11}$$

where V is the volume of the system. Secondly, the expression is written in terms of integrals over the energy. We substitute

$$\frac{V}{(2\pi)^3} \int d\mathbf{k} \to V \int d\epsilon \left[\int \frac{d\mathbf{k}}{(2\pi)^3} \delta(\epsilon - \epsilon_{\mathbf{k}}) \right] = V \int d\epsilon D(\epsilon). \tag{2.12}$$

Here, we used the definition of the density of states $D(\epsilon)$ in units per energy per volume. The resulting expression for the transition rate is

$$W^{\pm}_{m_s \pm 1, m_s} = \frac{2\pi}{\hbar} \lambda^2 S^{\pm}_{m_s} V_{\text{at}}^2 \int d\epsilon \int d\epsilon' D(\epsilon) D(\epsilon') \delta(\epsilon \mp \Delta - \epsilon') f(\epsilon)(1 - f(\epsilon')). \tag{2.13}$$

For convenience, we defined the atomic volume $V_{\text{at}} = V/N$. Since the Dirac delta function eliminates one integral, it automatically follows that

$$W^{\pm}_{m_s \pm 1, m_s} = \frac{2\pi}{\hbar} \lambda^2 S^{\pm}_{m_s} V_{\text{at}}^2 \int d\epsilon D(\epsilon) D(\epsilon \mp \Delta) f(\epsilon)(1 - f(\epsilon \mp \Delta)). \tag{2.14}$$

As a standard assumption in the two or three-temperature model, we impose that the distribution function $f(\epsilon)$ describes an (instantaneously) thermalized electron system. Specifically, the distribution function $f(\epsilon)$ is equal to the Fermi-Dirac distribution

$$f(\epsilon) = \frac{1}{e^{(\epsilon - \epsilon_F)/(k_B T_e)} + 1}, \tag{2.15}$$

where ϵ_F is the Fermi energy and T_e is the electron temperature. By substituting the Fermi-Dirac distribution in Eq. (2.14), the transition rate can be further simplified.

In order to do this, we have to calculate an integral of the form

$$\int d\epsilon\, F(\epsilon) f(\epsilon - a)(1 - f(\epsilon - b)) = \frac{1}{e^{(b-a)/(k_B T)} - 1} \int d\epsilon F(\epsilon)(f(\epsilon - b) - f(\epsilon - a)), \tag{2.16}$$

where a and b (in units of energy) correspond to an arbitrary shift of the Fermi-Dirac distribution. The form on the right-hand side can be proven algebraically using the definition of the Fermi-Dirac distribution. The integral is evaluated and is given by

$$\int d\epsilon\, F(\epsilon) f(\epsilon - a)(1 - f(\epsilon - b)) = \frac{(b-a)}{e^{(b-a)/(k_B T)} - 1} F(\epsilon_F). \tag{2.17}$$

For this expression to be valid it is required that the energy dependence of the function $F(\epsilon)$ is relatively weak in the vicinity of the Fermi energy. In our context that would mean that we impose that $D(\epsilon_F \pm \Delta) \approx D(\epsilon_F)$. This approximation heavily relies on the assumption that the electrons are represented by a free electron system. Here, we note that a realistic density of states for a (ferromagnetic) transition metal would strongly deviate from this free electron character, due to the presence of relatively flat d bands. The interpretation we use here will become more sophisticated in the following sections, where we discuss the separation of the d and s character of the electrons.

In the context of this section, the integral in Eq. (2.14) can be expressed in terms of Eq. (2.17), under the condition that all energy scales remain much smaller than the Fermi energy $\Delta, k_B T \ll \epsilon_F$. The transition rate is now written in the compact form [56–58]

$$W^{\pm}_{m_s \pm 1, m_s} = \frac{2\pi}{\hbar} \Delta \lambda^2 S^{\pm}_{m_s} D_F^2 \frac{e^{\mp \Delta/(2k_B T_e)}}{2\sinh(\Delta/(2k_B T_e))}. \tag{2.18}$$

For convenience, we defined the density of states at the Fermi energy in the units per energy per atom $D_F = V_{\mathrm{at}} D(\epsilon_F)$. Now that we have a compact expression for the transition rate, the spin dynamics can be calculated by determining the derivative of the occupation number f_{m_s}. Taking into account all the allowed transitions, this yields [56]

$$\frac{df_{m_s}}{dt} = -(W^{+}_{m_s+1, m_s} + W^{-}_{m_s-1, m_s}) f_{m_s} + W^{+}_{m_s, m_s-1} f_{m_s-1} + W^{-}_{m_s, m_s+1} f_{m_s+1}. \tag{2.19}$$

Importantly, in case the occupation probability is given by Boltzmann statistics

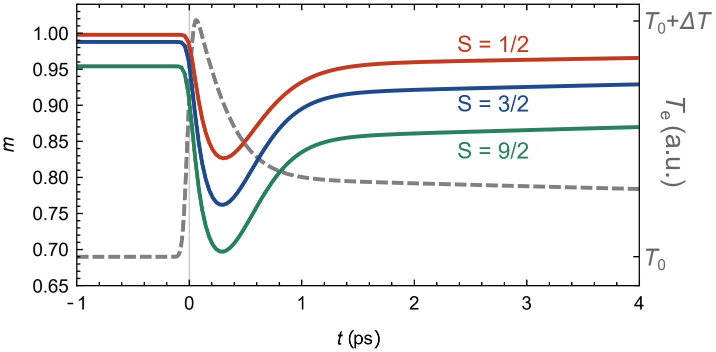

Figure 2.2: Laser-induced magnetization dynamics as calculated with the model based on spin-flip impurity scattering. The latter is implemented by using the M3TM approximation. The plot shows the normalized magnetization as a function of time after laser-pulse excitation at $t = 0$. As given in the figure, the calculation is performed for various values of the spin quantum number S. The other magnetic parameters are given in the main text. The dashed gray line in the background schematically depicts the transient increase in the electron temperature that drives the demagnetization process (details given in Sec. 2.3.3).

$f_{m_s} \propto e^{-\Delta m_s/(k_B T_e)}$, the right-hand side of Eq. (2.19) vanishes and the system is in equilibrium. Finally, the temporal derivative of the normalized magnetization results from calculating the ensemble average

$$\frac{dm}{dt} = -\frac{1}{S} \sum_{m_s=-S}^{S} m_s \frac{df_{m_s}}{dt}. \tag{2.20}$$

Figure 2.2 shows an example calculation for various values of the spin quantum number S. The plot indicates the magnetization as a function of time after laser-pulse excitation at $t = 0$. It visualizes the response of Eq. (2.20) to a transient increase of the electron temperature. The latter is schematically depicted by the gray line.[1] For simplicity, we defined the rate constant $\tau^{-1} = 4\pi\lambda^2 D_F^2 (k_B T_C)/\hbar$ to replace the prefactor in the transition rate Eq. (2.18). In the example calculation it is set to $\tau^{-1} = 5\ \text{ps}^{-1}$. Furthermore, we used a Curie temperature of 1000 K, such that the calculations in Fig. 2.2 correspond to the same spin system as the one represented in Fig. 2.1.

Finally, to find a closed expression for the magnetization, it is convenient to focus on a $S = 1/2$ system. Moreover, this is the simplification that is used in the microscopic three-temperature model [18, 23]. For spin half we can use that

---

[1] The electron temperature is calculated with the two-temperature model, which is discussed in the next section.

$\langle S^z \rangle = (f_{1/2} - f_{-1/2})/2$ and $f_{1/2} + f_{-1/2} = 1$. We retrieve the well-known formula for the magnetization dynamics of a spin one-half system [23, 35]

$$\frac{dm}{dt} = \frac{m}{\tau}\left(1 - m \coth\left(\frac{mT_C}{T_e}\right)\right). \tag{2.21}$$

Obviously, the equilibrium condition corresponds to the $m = \tanh(mT_c/T_e)$, as follows from the Weiss model.

In this section, we have purely focused on spin-flip impurity scattering. Later in this thesis, we will show that the scattering rates of other (Elliott-Yafet) spin-flip processes can be calculated analogously. Moreover, it turns out that the extension to an *s*-*d* model is relatively straightforward to derive and requires the same mathematical steps as presented in this section. Before diving into other contributions to the spin dynamics, we shortly address the energy transfer driven by electron-phonon scattering. It is the microscopic process underlying the two-temperature model, which was already used to model the temperature dynamics underlying Fig. 2.2.

2.3.3 The two-temperature model

In this intermezzo, we discuss the microscopic mechanism that is the basis of the two-temperature model for describing laser heating in (nonmagnetic) metals. The underlying driving force is the interaction between electrons and the lattice [17]. Here, phonons come into play as the quasiparticles associated with the vibrational modes of the lattice. The interaction with electrons corresponds to electron-phonon scattering processes, where phonons are effectively created or absorbed. The Hamiltonian is of the form [4, 18, 23]

$$\hat{H}_{\mathrm{ep}} = \frac{\lambda_{\mathrm{ep}}}{N} \sum_{\mathbf{k}\mathbf{k}'\mathbf{q}} c^\dagger_{\mathbf{k}} c_{\mathbf{k}'} (a^\dagger_{\mathbf{q}} + a_{\mathbf{q}}). \tag{2.22}$$

where $a^\dagger_{\mathbf{q}}$ and $a_{\mathbf{q}}$ are the creation and annihilation operator of a phonon with momentum $\mathbf{q}$. Hence, the two processes described by the Hamiltonian correspond to the generation and absorption of a phonon, resulting in the energy exchange between the electrons and the lattice. The goal of the following paragraph is to calculate the resulting energy transfer rate. We use here a very general approach, independent of the exact implementation of the phonon dynamics. For a detailed discussion on modeling the phonon system we refer to Refs. [4, 18].

Using Fermi's golden rule, it can easily be shown that the temporal derivative of the energy density E_e in the electronic system can be written as

$$\begin{aligned} \frac{dE_e}{dt} &= -\int d\epsilon_p \int d\epsilon \int d\epsilon' \, \epsilon_p \, \delta(\epsilon - \epsilon' - \epsilon_p) \Gamma_{\text{ep}}(\epsilon_p, \epsilon, \epsilon') \\ &\quad \times \Big[(1 + n(\epsilon_p)) f(\epsilon)(1 - f(\epsilon')) - n(\epsilon_p)(1 - f(\epsilon)) f(\epsilon') \Big]. \end{aligned} \tag{2.23}$$

For notational purposes, we defined the function $\Gamma_{\text{ep}}(\epsilon_p, \epsilon, \epsilon')$ which contains all the information regarding the (phonon and electron) density of states and the prefactors. Analogous to the previous section, $f(\epsilon)$ corresponds to a Fermi-Dirac distribution with electron temperature T_e. Hence, it is again imposed that the electronic system is thermalized instantaneously. Similarly, the phonon distribution function is given by a Bose-Einstein distribution

$$n(\epsilon_p) = \frac{1}{e^{\epsilon_p/(k_B T_p)} - 1}, \tag{2.24}$$

with phonon temperature T_p. We simplify the term between square brackets in Eq. (2.23) by substituting the thermal distribution functions. Using the algebraic identity as given in Eq. (2.16), and evaluating the integral over ϵ', yields

$$\begin{aligned} \frac{dE_e}{dt} &= \int d\epsilon \int d\epsilon_p \, \epsilon_p \Gamma_{\text{ep}}(\epsilon_p, \epsilon, \epsilon - \epsilon_p)(f(\epsilon - \epsilon_p) - f(\epsilon)) \\ &\quad \times \frac{1}{2} \left[\coth\left(\frac{\epsilon_p}{2k_B T_p} \right) - \coth\left(\frac{\epsilon_p}{2k_B T_e} \right) \right]. \end{aligned} \tag{2.25}$$

The term on the second line is further simplified by introducing a cutoff energy for the phonon system, such that ϵ_p remains relatively small compared to the temperatures $\epsilon_p \ll k_B T_e, \, k_B T_p$.[2] In this regime, the term between the square brackets will be dominated by a factor linear in the temperatures

$$\frac{1}{2} \left[\coth\left(\frac{\epsilon_p}{2k_B T_p} \right) - \coth\left(\frac{\epsilon_p}{2k_B T_e} \right) \right] \approx \frac{k_B}{\epsilon_p}(T_p - T_e). \tag{2.26}$$

It is used that $\coth(x) \approx 1/x$ for $x \ll 1$. The energy transfer rate is written in the

---

[2] In the context of Refs. [4, 18, 109], the cutoff energy is the Debye energy. Although the inequality $\epsilon_p \ll k_B T_{e,p}$ is not necessarily satisfied, the relation leads to reasonable approximations for ferromagnetic transition metals [4].

simple form

$$\frac{dE_e}{dt} = g_{\mathrm{ep}}(T_p - T_e), \tag{2.27}$$

where the rate constant g_{ep} is determined by the evaluation of the integrals in Eq. (2.25). Note that an expression of the form Eq. (2.27) could similarly be deduced from a linearization procedure, assuming the temperatures remain close to the initial (ambient) temperature. To arrive at the two-temperature model, a few more steps are required. First, the change in the electron energy density is expressed in terms of heat capacity and the change in the temperature. Second, an equivalent equation for the energy in the phonon system is deduced. The resulting coupled set of differential equations is known as the two-temperature model [17]

$$\gamma T_e \frac{dT_e}{dt} = g_{ep}(T_p - T_e) + P(t), \tag{2.28}$$

$$C_p \frac{dT_p}{dt} = -g_{ep}(T_p - T_e) - C_p \frac{T_p - T_{\mathrm{amb}}}{\tau_D}. \tag{2.29}$$

where C_p is the phonon heat capacity and $\gamma T_e = C_e(T_e)$ is the electron heat capacity. Within the free electron model the prefactor is given by $\gamma = \pi^2 k_B^2 D(\epsilon_F)/3$ [108]. Furthermore, two additional phenomenological terms are introduced. First, the function $P(t)$ is an energy source that represents the absorbed laser pulse energy. Second, the additional term on the right-hand side of Eq. (2.29) is included to cover heat dissipation out of the combined system, where a typical timescale τ_D is introduced. Here, the term is included in the expression for the phonon temperature, assuming the neighboring material is an insulator.

To model laser heating the coupled set of differential equations for T_e and T_p is solved using a given function $P(t)$ for the laser pulse. Typically, the temporal profile of the laser pulse is described by a Gaussian function

$$P(t) = \frac{P_0}{\sigma\sqrt{\pi}} e^{-(t-t_0)^2/\sigma^2}, \tag{2.30}$$

where P_0 is the absorbed laser pulse energy density, σ is the pulse duration, and t_0 is the time of incidence. Fig. 2.3 shows the resulting dynamics of the temperatures, where we used the thermal system parameters for a typical ferromagnetic transition metal that are listed in Table 6.1. The plot indicates the electron temperature T_e and T_p as a function of time after laser-pulse excitation at $t = 0$. It shows the abrupt increase of the electron temperature upon absorption of the laser pulse energy.

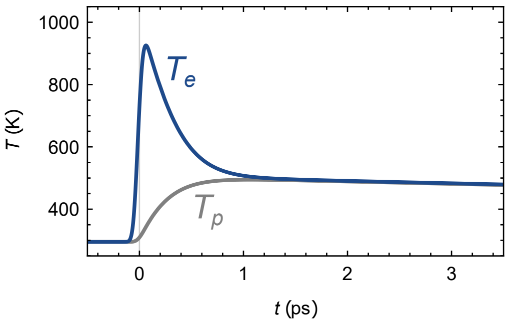

Figure 2.3: The response of the temperatures to laser heating, calculated with the two-temperature model. The electron temperature T_e and phonon temperature T_p, plotted as a function of time after laser-pulse excitation at $t = 0$. The used parameters are given in Table 6.1, with $P_0 = 10 \cdot 10^8$ Jm^{-3}.

Subsequently, the electron temperature equilibrates with the phonon temperature due to electron-phonon scattering.

Here ends the intermezzo on the energy transfer between the electrons and the lattice. The discussed two-temperature model will be frequently used later in the thesis, as a relevant and simple approach to model the typical behavior of the electron temperature, and therefore as an input to the models for laser-induced spin dynamics. As noted before, the underlying electron-phonon scattering processes contribute to spin relaxation due to the Elliott-Yafet mechanism. In the following paragraph, we specify the corresponding formula for the magnetization dynamics.

2.3.4 SPIN-FLIP ELECTRON-PHONON SCATTERING AND THE M3TM FORMULA

The M3TM in its most common form is based on the assumption that the magnetization dynamics is dominated by Elliott-Yafet electron-phonon scattering. We shortly recall that in the M3TM approximation, as discussed in Section 2.3.2, the associated spin flips are described separately from the electronic degrees of freedom. In this context, the Hamiltonian for Elliott-Yafet electron-phonon scattering is given by [4, 18, 109]

$$\hat{H} = \sqrt{a_{\mathrm{sf}}}\frac{\lambda'_{\mathrm{ep}}}{N}\sum_{\mathbf{k}\mathbf{k}'\mathbf{q}} c^{\dagger}_{\mathbf{k}}c_{\mathbf{k}'}(a^{\dagger}_{\mathbf{q}}+a_{\mathbf{q}})(\hat{S}^{+}_{j}+\hat{S}^{-}_{j}), \tag{2.31}$$

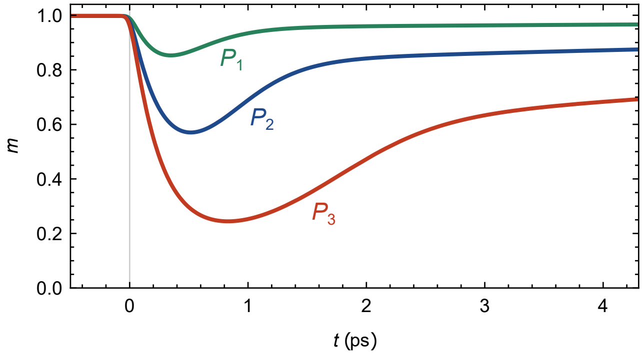

Figure 2.4: M3TM calculation for multiple values of the absorbed laser pulse energy density. The lines indicate the normalized magnetization m as a function of time after laser-pulse excitation at $t = 0$. The calculations correspond to the absorbed laser-pulse energy densities $P_1 = 10 \cdot 10^8$ Jm^{-3} (green), $P_2 = 20 \cdot 10^8$ Jm^{-3} (blue), and $P_3 = 30 \cdot 10^8$ Jm^{-3} (red). The other used parameters are given in the main text.

where a_{sf} is the spin-flip probability and λ'_{ep} is the coupling constant associated with the represented processes. Note that λ'_{ep} is directly proportional to the previously introduced constant λ_{ep}, however, additional scaling factors are typically introduced to phenomenologically address the fact that the spin per atom in a magnetic metal is not a half-integer [18]. For convenience, we keep using the constant λ'_{ep}.

The calculation of the transition rate resulting from the spin-flip electron-phonon scattering processes is a straightforward extension of the analogous derivation for impurity scattering. Hence, we closely follow the mathematical steps that led to the expression in Eq. (2.18) for $W^{\pm}_{m_s \pm 1, m_s}$. The extension involves the fact that now every spin-flip process is accompanied by either the absorption or creation of a phonon. First, this means that the scattering process is now associated with an energy transfer of $\Delta \pm \epsilon_p$, with ϵ_p the energy of the phonon. Second, the phonon distribution function $n(\epsilon_p)$ will appear in the expressions, specifically, a factor $(1 + n(\epsilon_p))$ for phonon creation and a factor $n(\epsilon_p)$ for absorption. The third step would be to impose the condition that $\epsilon_p \ll k_B T_{e,p}$ (see Sec. 2.3.3), and only take into account the terms to lowest order in $\epsilon_p/(k_B T_{e,p})$. For the details on all these intermediate steps we refer to Refs. [4, 109]. In fact, it is straightforward to show that the transition rate is now given by

$$W^{\pm}_{m_s \pm 1, m_s} = R \frac{T_p}{T_C} \frac{\Delta}{2 k_B T_C} S^{\pm}_{m_s} \frac{e^{\mp \Delta/(2 k_B T_e)}}{2 \sinh(\Delta/(2 k_B T_e))}, \tag{2.32}$$

where R depends on the various parameters that characterize the specific implementation of the spin, phonon, and electron subsystems [18]. R is typically treated as an effective parameter and can be determined by fitting the model to experimental data. Its typical order of magnitude for transition metal ferromagnets is $R \sim 10\ \mathrm{ps}^{-1}$ [18], yielding demagnetization times around hundreds of femtoseconds.

In analogy with the section on impurity scattering, the standard M3TM formula can be found by assuming a $S = 1/2$ system. Then, the temporal derivative of the normalized magnetization reduces to

$$\frac{dm}{dt} = Rm\frac{T_p}{T_C}\left(1 - m\coth\left(\frac{mT_C}{T_e}\right)\right). \tag{2.33}$$

The main difference with the equation for impurity scattering, as was presented in Eq. (2.21), is that the prefactor is now explicitly dependent on the phonon temperature T_p.

For illustrative purposes, we use the M3TM to calculate the demagnetization traces for varying laser fluences. The latter is implemented by using the two-temperature model to derive the relevant traces of the electron temperature for different values of P_0. The magnetization is calculated by numerically solving the M3TM formula in Eq. (2.33). The result is depicted in Fig. 2.4, showing the magnetization as a function of time after laser-pulse excitation at $t = 0$. The corresponding values for P_0 are given in the figure. The used values for the other thermal parameters are identical to the ones used for Figs. 2.2 and 2.3, and are given in Table 6.1. The magnetic parameters are given by the typical values $R = 10\ \mathrm{ps}^{-1}$ and $T_C = 1000$ K.

The example illustrates, as shown by the experimental study in Ref. [110], that the M3TM nicely describes the magnetization dynamics over a large range of fluences. Other interesting experimental studies that presented a comparison with the M3TM include the demagnetization for a varying ambient temperature [110], and investigations of demagnetization in rare-earth ferromagnets [18]. Although the M3TM is widely used in the field of femtomagnetism, it has certain limitations. One important example is that the itinerant property of spins in ferromagnetic metals is completely lost by treating the free electrons as spinless. Hence, spin transport can not be included in the standard way. This is one of the motivations to go beyond the M3TM approximation and move to an approach that includes the itinerant character of the spin degree of freedom. Such an approach is discussed in the next section.

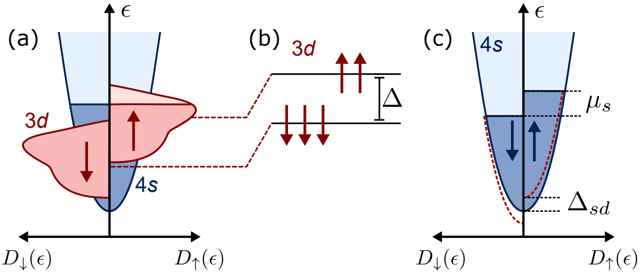

Figure 2.5: (a) Schematic overview of the spin-polarized density of states of a typical transition-metal ferromagnet. (b)-(c) The simplifications underlying the *s*-*d* model. (b) The *d* electron system is described by a local spin system characterized by exchange splitting Δ. (c) The occupation of the *s* electron states. The out-of-equilibrium spin density is determined by a spin-dependent shift of the chemical potentials, defined as the spin accumulation μ_s, and an additional shift originating from the *s*-*d* exchange splitting [36].

2.4 THE s-d MODEL

In this section, we present the *s*-*d* model for laser-induced spin dynamics [36, 56, 57]. Before diving into detail, we want to emphasize the motivation for the discussed approach. Specifically, we are interested in a compact model that describes: (i) ultrafast demagnetization in rapidly-heated magnetic thin films, and (ii) laser-induced spin transport in magnetic heterostructures. In the previous section, we noted that case (i) can be described by a simple $S = 1/2$ Weiss model and, additionally, an efficient spin-flip scattering mechanism. To describe case (ii), we choose the model that is one of the pillars of theoretical spintronics, the model for spin-dependent diffusive electron transport [107]. To implement the latter, it is required to introduce an itinerant spin system. In order to cover both cases (i) and (ii), the local spin description of the previous sections is now extended and accompanied by an itinerant spin system. In this section, we specifically discuss how the combined spin system responds to rapid heating, as is described by the *s*-*d* model. The presented derivation closely resembles the work in Refs. [36, 56, 57, 111, 112]. Later in this chapter, we discuss how spin transport can be introduced.

To substantiate the description with a separate local and itinerant spin system, we shortly discuss the band structure of a typical transition metal ferromagnet. Figure 2.5(a) shows a schematic representation of the spin-dependent density of states [1]. In red, one can identify the relatively narrow (local) *d* bands, and observe an effective exchange splitting between the spin up and spin down bands. In blue, the relatively wide bands are of an *s* character. These two properties are the basis of the *s*-*d* model, in which the system is described as a combination of perfectly flat (*d*) bands, and parabolic (*s*) bands. A schematic representation of this approach is presented in Figs. 2.5(b) and 2.5(c). The additional parameters in the itinerant spin system, as indicated in Fig. 2.5(b), are discussed below.

We note here that the nomenclature of the *s*-*d* model, implying a perfect separation between the *d* and *s* subsystems, should be used carefully. For instance, *s*-*d* mixing disallows the exact separation. Hence, the naming of the *s*-*d* model should be purely interpreted as the separation of local and itinerant spin degrees of freedom within an effective treatment.

In addition to defining two separate spin subsystems, the *s*-*d* model is based on the presence of a nonnegligible *s*-*d* interaction. Specifically, the *s* and *d* electrons will be subject to a mutual exchange coupling. The corresponding Hamiltonian is given by [36, 56]

$$\hat{H}_{sd} = J_{sd} V_{\mathrm{at}} \sum_j \hat{\mathbf{S}}_j^d \cdot \hat{\mathbf{s}}(r_j), \tag{2.34}$$

where J_{sd} determines the *s*-*d* coupling strength. Furthermore, $\hat{\mathbf{S}}_j^d$ corresponds to the spin operator for the localized (*d*) spin at lattice site j. The operator $\hat{\mathbf{s}}(\mathbf{r}_j)$ is the spin density of the itinerant electrons at the position $\mathbf{r}_j$ of lattice site j. To have all the terms in the convenient units, a factor of the atomic volume V_{at} is included.

In analogy with the previous sections, the *s*-*d* interaction Hamiltonian will be rewritten to identify the underlying scattering mechanism. In order to do so, we use the definition of the spin ladder operators

$$\hat{S}_j^{\pm} = \hat{S}_j^x \pm i\hat{S}_j^y, \tag{2.35}$$

expressed in terms of the transverse components of the spin operator. For convenience, we omitted the superscript *d*. Furthermore, the spin density operator needs to be specified and is expressed in terms of field operators [113]

$$\hat{\mathbf{s}}(\mathbf{r}) = \frac{1}{2} \sum_{\sigma\sigma'} \hat{\psi}_\sigma^\dagger(\mathbf{r}) \boldsymbol{\tau}_{\sigma\sigma'} \hat{\psi}_{\sigma'}(\mathbf{r}), \tag{2.36}$$

where the indices $\sigma \in \{\uparrow,\downarrow\}$ indicate the spin polarization. Furthermore, $\hat{\psi}_\sigma(\mathbf{r})$ corresponds to the field operator for the electrons at spatial position $\mathbf{r}$. Importantly, $\boldsymbol{\tau}_{\sigma\sigma'}$ is a vector containing the three Pauli matrices as its components. We switch to momentum space and map the field operators to creation and annihilation operators by using

$$\hat{\psi}^\dagger_\sigma(\mathbf{r}) = \frac{1}{\sqrt{V}} \sum_{\mathbf{k}} c^\dagger_{\mathbf{k}\sigma} e^{-i\mathbf{k}\cdot\mathbf{r}}. \tag{2.37}$$

Implementing this in the H_{sd}, and substituting the Pauli matrices, gives the expression

$$\begin{aligned} \hat{H}_{sd} &= \sum_{j\mathbf{k}\mathbf{k}'} \left[V^*_{j\mathbf{k}\mathbf{k}'} c^\dagger_{\mathbf{k}'\downarrow} c_{\mathbf{k}\uparrow} \hat{S}^+_j + V_{j\mathbf{k}\mathbf{k}'} c^\dagger_{\mathbf{k}\uparrow} c_{\mathbf{k}'\downarrow} \hat{S}^-_j \right] \\ &\quad + \sum_{j\mathbf{k}\mathbf{k}'} V_{j\mathbf{k}\mathbf{k}'} \left[\hat{S}^z_j (c^\dagger_{\mathbf{k}\uparrow} c_{\mathbf{k}'\uparrow} - c^\dagger_{\mathbf{k}\downarrow} c_{\mathbf{k}'\downarrow}) \right], \end{aligned} \tag{2.38}$$

where the first part of the Hamiltonian corresponds to spin-flip scattering processes and is clearly similar to the Hamiltonians we discussed in the previous sections. In this case, the associated matrix element $V_{j\mathbf{k}\mathbf{k}'}$ is given by

$$V_{j\mathbf{k}\mathbf{k}'} = \frac{J_{sd}}{2N} e^{-i(\mathbf{k}-\mathbf{k}')\cdot\mathbf{r}_j}. \tag{2.39}$$

In the expression for $\hat{H}_{sd}$ in Eq. (2.38), the last term does not contribute to spin-flip scattering. As schematically depicted in Fig. 2.6(c), the contribution is typically treated as a mean-field shift by substituting $\hat{S}^z_j \to \langle \hat{S}^z \rangle$, and is included in the Hamiltonian for the *s* electrons [36]. Note that the similar energy shift for the *d* electrons is neglected, since it is expected to play a minor role compared to the exchange splitting Δ.

To clarify, we repeat that a Weiss mean-field approach is used to describe the *d* electron system. In combination with the free electron description for the itinerant *s* spins, the complete model is specified by the three Hamiltonians

$$\hat{H}_d = \Delta \sum_j \hat{S}^z_j, \tag{2.40}$$

$$\hat{H}_s = \sum_{\mathbf{k}\sigma} \epsilon_{\mathbf{k}\sigma} c^\dagger_{\mathbf{k}\sigma} c_{\mathbf{k}\sigma}, \tag{2.41}$$

$$\hat{H}_{sd} = \sum_{j\mathbf{k}\mathbf{k}'} (V^*_{j\mathbf{k}\mathbf{k}'} c^\dagger_{\mathbf{k}'\downarrow} c_{\mathbf{k}\uparrow} \hat{S}^+_j + \text{h.c.}), \tag{2.42}$$

where $\hat{H}_d$ is the Hamiltonian for the *d* electrons with exchange splitting Δ, and is equivalent to the description for the local spin system in the previous sections.

Furthermore, $\hat{H}_s$ describes the s electron system, where the single-particle energy is given by $\epsilon_{\mathbf{k}\sigma} = \epsilon_{\mathbf{k}} \pm J_{sd}\langle \hat{S}_z \rangle /2$, including the abovementioned mean-field shift. Lastly, H_{sd} describes the exchange scattering processes that stem from the *s*-*d* interaction and is our main interest. The remaining part of this section shows the calculation for the transition rate of the d electron spin states driven by the scattering processes associated with the *s*-*d* interaction. In analogy with the previous sections, the transition rate is calculated using Fermi's golden rule. However, a crucial difference is that the spin degree of freedom of the itinerant (s) electrons is taken into account. The transition rates are given by

$$W^{+}_{m_s+1,m_s} = \frac{\pi}{2\hbar}\left(\frac{J_{sd}}{N}\right)^2 S^{+}_{m_s} \sum_{\mathbf{k}\mathbf{k}'} \delta(\epsilon_{\mathbf{k}\uparrow} - \Delta - \epsilon_{\mathbf{k}'\downarrow}) f_{\mathbf{k}\uparrow}(1 - f_{\mathbf{k}'\downarrow}), \tag{2.43}$$

$$W^{-}_{m_s-1,m_s} = \frac{\pi}{2\hbar}\left(\frac{J_{sd}}{N}\right)^2 S^{-}_{m_s} \sum_{\mathbf{k}\mathbf{k}'} \delta(\epsilon_{\mathbf{k}\uparrow} - \Delta - \epsilon_{\mathbf{k}'\downarrow}) f_{\mathbf{k}'\downarrow}(1 - f_{\mathbf{k}\uparrow}). \tag{2.44}$$

Here, $f_{\mathbf{k}\sigma}$ corresponds to the spin-dependent distribution function of the itinerant electrons with momentum $\mathbf{k}$ and spin σ. Typically, the expression for the transition rate is simplified by replacing the summation over the momenta for integrals over the energies and substituting an exact form of the distribution function $f_\sigma(\epsilon)$. Again, the crucial step is the assumption that the electron system is rapidly thermalized. In this case, the spin-specific distribution functions are given by Fermi-Dirac distributions with a spin-dependent chemical potential

$$f_{\uparrow}(\epsilon) = \frac{1}{e^{(\epsilon-\mu_\uparrow)/(k_B T_e)} + 1}, \tag{2.45}$$

$$f_{\downarrow}(\epsilon) = \frac{1}{e^{(\epsilon-\mu_\downarrow)/(k_B T_e)} + 1}, \tag{2.46}$$

where $\mu_\uparrow$ and $\mu_\downarrow$ correspond to the chemical potential for the spin up and spin down electrons, respectively. In equilibrium, we have $\mu_\uparrow = \mu_\downarrow$ and both are effectively equal to the Fermi energy ϵ_F. It is obvious that in the case $\mu_\uparrow \neq \mu_\downarrow$, an out-of-equilibrium spin density is built up in the s electron system, mathematically determined by the spin-specific shift of the distribution function (and spin-dependent density of states). For that reason, the difference in chemical potential is defined as the spin accumulation $\mu_s = \mu_\uparrow - \mu_\downarrow$. Implementing the spin-specific distribution functions, and using the definition for the spin accumulation μ_s, the final expression for the spin transition rate in the d system is [56–58]

$$W^{\pm}_{m_s\pm 1,m_s} = \frac{\pi}{2\hbar} J_{sd}^2 S^{\pm}_{m_s} D_\uparrow D_\downarrow (\Delta - \mu_s) \frac{\exp\left(\mp \dfrac{\Delta - \mu_s}{2k_B T_e}\right)}{2\sinh\left(\dfrac{\Delta - \mu_s}{2k_B T_e}\right)}, \tag{2.47}$$

where $D_{\uparrow\downarrow}$ is the spin-dependent density of states evaluated at the Fermi energy in units per energy per atom.[3] Note that the transition rate $W^{\pm}_{m_s\pm 1,m_s}$ has a similar mathematical form as the expressions in M3TM approximation, with the essential difference that the spin accumulation μ_s is subtracted from the exchange splitting Δ.

The spin dynamics is found by substituting the transition rate in the formula for the derivative of $f_{m_s}(t)$, as given in Eq. (2.19), and calculating the change of the ensemble average $\langle \hat{S}^z \rangle(t)$. Here, we define the normalized magnetization of d electron spin system as $m_d = -\langle \hat{S}^z \rangle / S$. For illustrative purposes, we focus on a $S = 1/2$ system, where the exchange splitting is given by $\Delta = 2k_B T_C m_d$, and the formula that determines the magnetization dynamics reads

$$\frac{dm_d}{dt} = \frac{1}{\tau_{sd}} \left(m_d - \frac{\mu_s}{2k_B T_C} \right) \left[1 - m_d \coth\left(\frac{2m_d k_B T_C - \mu_s}{2k_B T_e} \right) \right]. \tag{2.48}$$

The timescale associated with the s-d interaction is defined as $\tau_{sd}^{-1} = (\pi/\hbar) J_{sd}^2 D_\uparrow D_\downarrow k_B T_C$. The equation has the same form as the original M3TM, with the additional variable μ_s. Hence, to finalize the formulation of the s-d model, we should determine the dynamics of the spin accumulation itself. Before focusing on the latter, we write down the expression for the number density of the s electrons with spin σ [112]

$$n_\sigma = \int d\epsilon D_\sigma(\epsilon \mp \Delta_{sd}) f_\sigma(\epsilon). \tag{2.49}$$

As noted before, the spin up and spin down band are shifted due to the presence of the s-d interaction, here indicated as $\Delta_{sd} = J_{sd} \langle \hat{S}^z \rangle / 2$. In the expression for the electron density n_σ, this is implemented as a shift in the density of states [112]. The integral in Eq. (2.49) can be approximated using the Sommerfeld expansion [108].

---

[3] To avoid confusion, we use various conventions for the units of the density of states throughout this chapter. In the case we specifically note the energy dependence, as in $D_\sigma(\epsilon)$, it is in units per energy per volume. However, in case we use the notation D_σ, the density of states is defined in units per energy per atom, and by definition evaluated at ϵ_F.

Here, we are mostly interested in how the itinerant spin density responds to small changes in the spin-dependent chemical potential μ_σ and *s*-*d* splitting Δ_{sd}. As long as all energy scales remain much smaller than the Fermi energy, and the density of states is only weakly energy dependent in the vicinity of the Fermi level, the change in the spin-dependent electron density is given by

$$\frac{dn_\sigma}{dt} = D_\sigma(\epsilon_F)\left[\frac{d\mu_\sigma}{dt} \mp \frac{d\Delta_{sd}}{dt}\right]. \tag{2.50}$$

Since the *s*-*d* spin-flip scattering processes conserve the total spin angular momentum, the temporal derivative of $n_\uparrow - n_\downarrow$ can straightforwardly be expressed in terms of the local magnetization m_d. Moreover, using that the total number of electrons $n_\uparrow + n_\downarrow$ remains constant, and substituting the definition of Δ_{sd}, results in a simple expression for the temporal derivative of the spin accumulation [36, 112]

$$\frac{d\mu_s}{dt} = \rho_{sd}\frac{dm_d}{dt} - \frac{\mu_s}{\tau_s}, \tag{2.51}$$

where we used the definition $\rho_{sd} = D^{-1} - J_{sd}/2$ for $S = 1/2$, with the spin-averaged density of states $D = 2D_\uparrow D_\downarrow/(D_\uparrow + D_\downarrow)$ [36]. Importantly, an extra spin relaxation term is included that depends on the phenomenological timescale τ_s [36, 56]. The latter includes all additional spin-flip scattering processes, such as the ones resulting from the Elliott-Yafet mechanism.

To illustrate the use of the *s*-*d* model, we present a standard calculation in Fig. 2.6, which shows response of the combined *s*-*d* spin system to a transient increase of the electron temperature. The figure corresponds to a calculation presented in Chapter 3, where all parameters are specified. Importantly, the spin systems are characterized by $\tau_{sd} = 0.2$ ps, $\tau_s = 0.1$ ps, and $T_C = 1000$K. Figure 2.6(a) shows the normalized magnetization m_d (the solid red curve) of the *d* electron system as a function of time after laser-pulse excitation at $t = 0$. Analogous to the modeling in the previous sections, the ultrafast demagnetization process is clearly visible. However, one should be careful with directly comparing the theoretical magnetization m_d with the magnetic signal from the experiments, since in the *s*-*d* model the additional *s* subsystem contributes to the spin dynamics. Generally, it is safe to say that the experimentally-probed magnetic signal is a linear combination of the contributions by the theoretical *s* and *d* spin subsystems, and the precise relation with the magnetization m_d is dependent on the specific probing method.

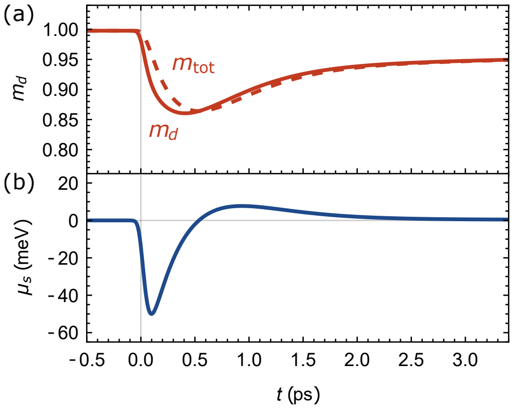

Figure 2.6: Illustrative calculation of laser-induced spin dynamics in the *s*-*d* model. (a) The normalized magnetization m_d of the d electron system as a function of time after laser-pulse excitation at $t = 0$. The dashed line indicates the normalized magnetization of the combined *s*-*d* spin system. (b) The generated spin accumulation μ_s in the s electron system plotted as a function of time.

To elucidate the spin dynamics of the combined spin system, and shortly address the relation with the M3TM, we plotted the normalized magnetization $m_{\rm tot}$ of the total spin system, indicated by the dashed red line in Fig. 2.6(a). For $m_{\rm tot}$ the demagnetization rate is critically determined by the additional processes that transfer spin out of the combined *s*-*d* system and strongly depends on the timescale τ_s. Here, the correspondence with the M3TM is evident, as the spin-flip scattering time τ_s includes the Elliott-Yafet processes. Importantly, in this interpretation the *s*-*d* interaction mediates the indirect spin transfer from the local magnetization to the lattice. One could argue that the presence of a strong *s*-*d* interaction is a (partial) justification of the model-specific implementation of Elliott-Yafet processes in the M3TM. The relation between the two approaches, the *s*-*d* model and the M3TM, will be further discussed in Chapter 3.

As mentioned at the beginning of this section, the primary goal of using the *s*-*d* model is to understand how an additional itinerant spin system responds to a rapidly changing temperature and local magnetization. The resulting dynamics of the spin accumulation is depicted in Fig. 2.6(b). The plot shows the characteristic bipolar behavior of μ_s, resembling the spin-current pulses measured in rapidly heated magnetic heterostructures (Introduction Fig. 1.6). Obviously, the latter is not a surprise, since the spin accumulation is the essential variable in the standard models for spin transport [107].

Before we move on to the implementation of spin transport, we discuss one more extension of the description for the local spin dynamics. The principal limitation of the *s*-*d* model in the presented form is that it only considers single-spin excitations. Specifically, the model neglects excitations that are distributed over the spin system. These collective spin excitations, and their relevance for the thermodynamic description of ferromagnets, are the main subject of the next section.

2.5 THERMAL MAGNONS AND ELECTRON-MAGNON SCATTERING

In this section, we introduce magnons, which are the quasiparticles associated with collective spin-wave excitations. To introduce magnons properly, we discuss the mathematical framework that leads to a simple derivation of the magnon dispersion relation. The starting point is the Hamiltonian [114]

$$\hat{H} = -J \sum_{i,j=i+\delta} \hat{\mathbf{S}}_i \cdot \hat{\mathbf{S}}_j + \hbar\omega_0 \sum_i \hat{S}^z_j. \tag{2.52}$$

The first term describes the Heisenberg exchange, where i labels the lattice site and δ the nearest neighbors. The second term corresponds to a Zeeman contribution resulting from an external field along the z direction. For convenience, the field is expressed in terms of an angular frequency ω_0. The first step in the derivation is to map the spin operators to bosonic creation and annihilation operators, using the Holstein-Primakoff transformation [115]

$$\hat{S}^+_j = a^\dagger_j \sqrt{2S - a^\dagger_j a_j}, \tag{2.53}$$

$$\hat{S}^-_j = \sqrt{2S - a^\dagger_j a_j}\, a_j, \tag{2.54}$$

$$\hat{S}^z_j = a^\dagger_j a_j - S, \tag{2.55}$$

where $a^\dagger_j$ creates and a_j annihilates a local spin deviation at lattice site j. The terms involving the square root are typically expanded using the condition that $\langle a^\dagger_j a_j \rangle \ll S$. The latter essentially means that the magnetization remains close to the saturation value. Applying the Holstein-Primakoff transformation to the Hamiltonian in Eq. (2.52), and collecting the terms up to first order in the bosonic operators, results in the expression

$$\hat{H} = -JS\sum_i\sum_\delta \left[a_i^\dagger a_{i+\delta} + a_i a_{i+\delta}^\dagger - a_i^\dagger a_i - a_{i+\delta}^\dagger a_{i+\delta}\right] + \hbar\omega_0 \sum_i a_i^\dagger a_i. \tag{2.56}$$

Here, we omitted the constant terms. To arrive at a Hamiltonian for magnons the expression is rewritten in terms of the Fourier transform of the local bosonic operators, using

$$a_j^\dagger = \frac{1}{\sqrt{N}}\sum_{\mathbf{q}} a_{\mathbf{q}}^\dagger e^{-i\mathbf{q}\cdot\mathbf{r}_j}, \tag{2.57}$$

where $a_{\mathbf{q}}^\dagger$ is the bosonic creation operator of a magnon with momentum $\mathbf{q}$. Its hermitian conjugate $a_{\mathbf{q}}$ corresponds to the magnon annihilation operator. After simplification, the Hamiltonian reads [114]

$$\hat{H} = -2JS\sum_\delta\sum_{\mathbf{q}} a_{\mathbf{q}}^\dagger a_{\mathbf{q}}\left[\cos(\mathbf{q}\cdot\delta) - 1\right] + \hbar\omega_0\sum_i a_{\mathbf{q}}^\dagger a_{\mathbf{q}}. \tag{2.58}$$

In the argument of the cosine function, δ corresponds to the vector pointing from a lattice site to its nearest neighbor (labeled by index δ in the summation). We consider the limit $\mathbf{q}\cdot\delta \ll 1$, i.e., the magnon wavelength is much larger than the lattice spacing. The cosine is Taylor expanded using $\cos(x) \approx 1 - x^2/2$ for small x. The result is a quadratic magnon dispersion relation, which is further simplified by assuming a simple cubic lattice with lattice constant a. We arrive at the final diagonal Hamiltonian

$$\hat{H} = \sum_{\mathbf{q}}(\epsilon_0 + Aq^2)a_{\mathbf{q}}^\dagger a_{\mathbf{q}} \equiv \sum_{\mathbf{q}}\epsilon_{\mathbf{q}} a_{\mathbf{q}}^\dagger a_{\mathbf{q}}. \tag{2.59}$$

Here, the dispersion relation is determined by $\epsilon_{\mathbf{q}} = \epsilon_0 + Aq^2$, with the spin-wave stiffness $A = 2JSa^2$ and the magnon gap $\epsilon_0 = \hbar\omega_0$. The final diagonal form of the Hamiltonian in Eq. (2.59) can generally be reached for a magnon system, even if the initial Hamiltonian involves additional contributions. For instance, including dipolar interactions, or any additional anisotropic terms, is a relatively straightforward extension. The Hamiltonian can typically be diagonalized using the so-called Bogoliubov transformation [114]. In the context of our work, where the excited magnons are mainly characterized by energies of the order of k_BT, the dispersion is dominated by the exchange contribution. Hence, we use the simple quadratic dispersion as defined in Eq. (2.59). In the following section, we discuss the properties of the magnon system in thermal equilibrium.

Thermal magnons in (quasi) equilibrium

Before we characterize the dynamical properties of the magnon system, we first focus on the equilibrium state. The main interest is to find the magnetization as a function of temperature. The latter is determined by the magnon density

$$n_d = \int d\epsilon D(\epsilon) n(\epsilon), \tag{2.60}$$

where $n(\epsilon)$ is the magnon distribution function and $D(\epsilon)$ is the density of states. The energy dependence of the density of states is deduced from the dispersion relation $\epsilon_{\mathbf{q}} = \epsilon_0 + Aq^2$, resulting in [36, 116]

$$D(\epsilon) = \frac{\sqrt{\epsilon - \epsilon_0}}{4\pi^2 A^{3/2}}. \tag{2.61}$$

In thermal equilibrium, the distribution function is given by the Bose-Einstein distribution

$$n_{\mathrm{BE}}(\epsilon) = \frac{1}{e^{(\epsilon - \mu_m)/(k_B T_m)} - 1}, \tag{2.62}$$

where μ_m is the magnon chemical potential and T_m is the magnon temperature. The magnon number density now follows from the integral

$$n_d = \frac{1}{4\pi^2 A^{3/2}} \int_{\epsilon_0}^{\infty} d\epsilon \frac{\sqrt{\epsilon - \epsilon_0}}{e^{(\epsilon - \mu_m)/(k_B T_m)} - 1}, \tag{2.63}$$

where the upper bound of the integral is set to infinity using the condition that the temperature remains far below the Curie temperature. The integral can be expressed in terms of the polylogarithm function [117]

$$\mathrm{Li}_s(e^x) = \frac{1}{\Gamma(s)} \int_0^{\infty} dt \frac{t^{s-1}}{e^t / e^x - 1}, \tag{2.64}$$

where $\Gamma(s)$ is the Gamma function. A change of the integration variable in Eq. (2.63) leads to the following expression for the magnon density

$$n_d = \frac{(k_B T_m)^{3/2}}{4\pi^2 A^{3/2}} \Gamma(3/2) \mathrm{Li}_{3/2}\Big(e^{(\mu_m - \epsilon_0)/(k_B T_m)} \Big). \tag{2.65}$$

For reasons discussed below, we set the chemical potential to zero $\mu_m = 0$. Furthermore, we impose that the magnon gap satisfies $\epsilon_0 \ll k_B T_m$, which is a reasonable assumption for a ϵ_0 that corresponds to a typical FMR frequency of $\sim$ 10 GHz and a temperature T_m close to room temperature. Then, the argument of the polylogarithm is approximately equal to one, such that the polylogarithm becomes equivalent to the zeta function $\mathrm{Li}_{3/2}(1) = \zeta(3/2)$. The magnon density reduces to

$$n_d = \frac{(k_B T_m)^{3/2}}{4\pi^2 A^{3/2}} \Gamma(3/2)\zeta(3/2). \tag{2.66}$$

The reduction of the normalized magnetization is given by $\Delta m = -n_d/s$, with s the saturation spin density (in units of $\hbar$), and scales as $T_m^{3/2}$. This is the famous Bloch law and results in an observable reduction of the magnetization even at low temperatures. The latter is a consequence of the relatively small energy cost of exciting collective spin excitations. As a final remark regarding the Bloch law, we stress that it is only valid far below the Curie point and fails as the ratio T_m/T_C becomes significant. In that regime, the single-magnon energy relation is reduced due to a significant magnon density present in its environment. Although this can straightforwardly be implemented in the description [31, 114], it is not of critical importance in the regime we will apply the model.

As an important final note, we want to discuss the relevance of introducing a nonzero magnon chemical potential. As the magnon number is not conserved due to interactions with the environment, the chemical potential vanishes in equilibrium. Nevertheless, a quasi-equilibrium state with a nonzero chemical potential can be reached in a dynamical system. For instance, it can be accomplished in a transport scenario by the injection of an externally-generated spin current. In relation to that, it was shown that the magnon chemical was a relevant ingredient for the description of spin transport in magnetic insulators [114, 118]. Moreover, the magnon chemical potential plays an essential role in the context of magnon Bose-Einstein condensates [119, 120]. Although the examples typically require an efficient thermalization process of the magnon system, the mathematical role of the chemical potential can be defined for the general case. We briefly discuss this approach below.

The magnon system has two degrees of freedom, the number of magnons and the total energy. Hence, two parameters are required to fully describe the system. The two parameters are conveniently denoted as a generalized chemical potential μ_m and temperature T_m. In the case that we consider a dynamical scenario, the change in magnon density δn_d and magnon energy density δU_d can be parametrized as

$$\begin{pmatrix} \delta n_d \\ \delta U_d \end{pmatrix} = \begin{pmatrix} C_{n,\mu} & C_{n,T} \\ C_{U,\mu} & C_{U,T} \end{pmatrix} \begin{pmatrix} \delta \mu_m \\ \delta T_m \end{pmatrix}. \tag{2.67}$$

where the coefficients typically involve integrals over the density of states and the distribution function.

In the case that the thermalization process is faster than all other timescales, the parameters μ_m and T_m are equal to the thermodynamic chemical potential and temperature. As an example, now the coefficient $C_{n,T} = \partial n_d / \partial T$ is given by the partial derivative of Eq. (2.66). The other coefficients can be calculated analogously [121], as will be done in Chapter 4. In the opposite case, where the magnon system is temporarily characterized by a nonthermal distribution, the parameters correspond to a generalized chemical potential and temperature. Then, μ_m and T_m are simply mathematical tools for bookkeeping the variation in the number of magnons and the total energy. This approach is similar to how one can define the generalized spin accumulation and electron temperature for a nonthermal electron distribution.

In the following section, we discuss the dynamics of the magnon system driven by the interaction with itinerant electrons. The result will be expressed in terms of the parametrization presented above.

THE ELECTRON-MAGNON SCATTERING RATE

In a ferromagnetic metal, magnons interact with the surrounding itinerant electrons. The coupling is closely connected to the *s-d* interaction discussed previously. Using the Holstein-Primakoff transformation, the *s-d* interaction Hamiltonian is rewritten

$$\hat{H}_{sd} = \sum_{\mathbf{qkk'}} \left[V^*_{\mathbf{qkk'}} c^\dagger_{\mathbf{k'}\downarrow} c_{\mathbf{k}\uparrow} a^\dagger_{\mathbf{q}} + V_{\mathbf{qkk'}} c^\dagger_{\mathbf{k}\uparrow} c_{\mathbf{k'}\downarrow} a_{\mathbf{q}} \right]. \tag{2.68}$$

The Hamiltonian describes electron-magnon scattering processes, where the spin-flip of an itinerant electron yields either the creation or annihilation of a magnon. The process transfers spin and energy between the two populations, where the rate of transfer is determined by the electron-magnon scattering rate. In analogy with the previous sections, the transfer rate is calculated using Fermi's golden rule. It results in an expression for the time derivative of the magnon density [36, 116, 117]

$$\begin{aligned}\frac{dn_d}{dt} &= \frac{2\pi}{\hbar V}\sum_{\mathbf{qkk'}}|V_{\mathbf{kk'q}}|^2\delta(\epsilon_{\mathbf{k}\uparrow}-\epsilon_{\mathbf{k'}\downarrow}-\epsilon_{\mathbf{q}})f_{\mathbf{k}\uparrow}(1-f_{\mathbf{k'}\downarrow})(1+n_{\mathbf{q}}) \\ &\quad -\frac{2\pi}{\hbar V}\sum_{\mathbf{qkk'}}|V_{\mathbf{kk'q}}|^2\delta(\epsilon_{\mathbf{k}\uparrow}-\epsilon_{\mathbf{k'}\downarrow}-\epsilon_{\mathbf{q}})f_{\mathbf{k'}\downarrow}(1-f_{\mathbf{k}\uparrow})n_{\mathbf{q}}\,,\end{aligned} \tag{2.69}$$

where $n_{\mathbf{q}}$ is the (nonequilibrium) magnon distribution function. Furthermore, $f_{\mathbf{k}\uparrow}$ and $f_{\mathbf{k'}\downarrow}$ correspond to the spin-dependent distribution functions for the electrons. Simplifying the expression in Eq. (2.69) requires the same mathematical steps as previously used for the *s*-*d* model. First, the summations are rewritten in terms of integrals over the energy. Second, the electron distribution functions are assumed to be given by Fermi-Dirac distributions with a spin-dependent chemical potential. Following the standard algebraic steps, the spin-transfer rate is expressed as [36, 117]

$$\frac{dn_d}{dt} \equiv I_{sd} = \int d\epsilon_q \Gamma(\epsilon_q)D(\epsilon_q)(\epsilon_q-\mu_s)\Big[n_{\mathrm{BE}}(\epsilon_q-\mu_s)-n(\epsilon_q)\Big]. \tag{2.70}$$

By definition, I_{sd} describes the spin-transfer rate between the itinerant (s) electrons and magnons (d electrons) per unit volume. Note that $n(\epsilon_q)$ corresponds to the magnon distribution function, for which no specific form has been assumed yet. In contrast, the Bose-Einstein function $n_{\mathrm{BE}}(\epsilon_q-\mu_s)$, is a result of evaluating the integrals involving Fermi-Dirac distributions (as seen previously in Eq. (2.17)). Using the same definition as Ref. [117], all the remaining parameters that determine the electron-magnon scattering rate are defined within the energy-dependent function $\Gamma(\epsilon_q)$ [117]

$$\Gamma(\epsilon_q) = \frac{2\pi V^2}{\hbar D(\epsilon_q)}\int\frac{d\mathbf{k}}{(2\pi)^2}\int\frac{d\mathbf{k'}}{(2\pi)^3}\int\frac{d\mathbf{q}}{(2\pi)^3}\delta(\epsilon_{\mathbf{k}}-\epsilon_F)\delta(\epsilon_{\mathbf{k'}}-\epsilon_F)\delta(\epsilon_{\mathbf{q}}-\epsilon_q)|V_{\mathbf{kk'q}}|^2. \tag{2.71}$$

In the remainder of this thesis, the function $\Gamma(\epsilon_q)$ is treated phenomenologically. In analogy with the spin-transfer rate, the rate of energy transfer per unit volume is given by [116]

$$U_{sd} = \int d\epsilon_q \Gamma(\epsilon_q)\epsilon_q D(\epsilon_q)(\epsilon_q-\mu_s)\Big[n_{\mathrm{BE}}(\epsilon_q-\mu_s)-n(\epsilon_q)\Big], \tag{2.72}$$

which includes an additional factor of energy in the integral.

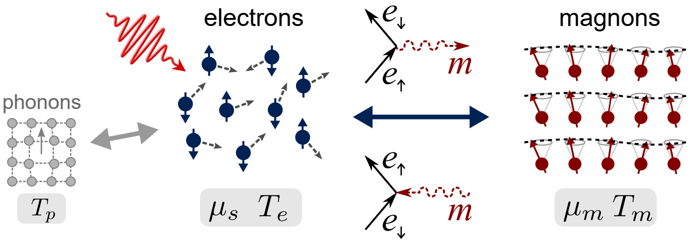

Figure 2.7: Schematic overview of the model based on electron-magnon scattering. The latter mediates the spin transfer between thermal magnons and spin-polarized electrons. Itinerant spins and thermal magnons are treated on equal footing, by parametrizing both systems in terms of a chemical potential and a temperature. Additionally, the electronic system exchanges energy and spin with the lattice.

Using the expressions for the spin transfer I_{sd} and energy transfer U_{sd}, a complete model for the dynamics in the magnon system can be formulated. Before introducing our specific approach, we discuss two examples from the literature of how electron-magnon scattering is implemented in models for ultrafast demagnetization. First, Manchon et al. [31] assumed an instantaneously thermalized magnon system parametrized by the magnon temperature T_m (and a vanishing chemical potential). By calculating the energy transfer rate U_{sd}, the authors formulated a microscopic equivalent of the three-temperature model. A contrasting approach was introduced by Tveten et al. [36], who assumed a nonthermal magnon distribution. The authors carried out the explicit evaluation of the spin-transfer rate I_{sd}, and included the spin accumulation as an additional parameter that describes the generation of an out-of-equilibrium spin density in the itinerant system.

The formulation we use combines the two approaches of Refs. [31, 36], such that we are able to model both energy transfer and spin transfer in an effective way. A schematic overview of the model is given in Fig. 2.7. The method relies on the parametrization discussed in the previous section, i.e., we express the dynamical equation for the magnon system in terms of the generalized chemical potential and temperature. In matrix notation

$$\begin{pmatrix} C_{n,\mu} & C_{n,T} \\ C_{U,\mu} & C_{U,T} \end{pmatrix} \begin{pmatrix} \partial_t \mu_m \\ \partial_t T_m \end{pmatrix} = \frac{1}{\hbar} \begin{pmatrix} g_{n,\mu} & g_{n,T} \\ g_{U,\mu} & g_{U,T} \end{pmatrix} \begin{pmatrix} \mu_s - \mu_m \\ T_e - T_m \end{pmatrix}, \tag{2.73}$$

where the coefficients on the right-hand side are directly determined by the spin and energy transfer rates. All the coefficients are estimated by substituting a ther-

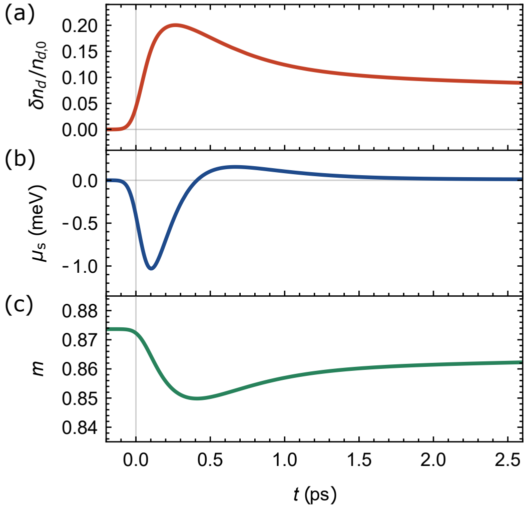

Figure 2.8: Spin dynamics as a result of electron-magnon scattering in a rapidly heated ferromagnet expressed as a function of time t after laser-pulse excitation at $t = 0$. (a) The increase of the magnon density δn_d, normalized compared to the initial value $n_{d,0}$. (b) The generated spin accumulation μ_s. (c) The normalized magnetization of the combined spin system.

malized magnon distribution in the corresponding integrals. Since the model will only be applied for situations close to equilibrium, all terms are expanded up to first order in perturbations of the chemical potential and temperatures. As some subtleties arise within this method, we refer to Chapter 5 for more details on the final expressions for the coefficients.

The essence of the discussed implementation of electron-magnon scattering is that magnons and itinerant spins are treated on equal footing. Expressed in terms of the spin accumulation μ_s and electron temperature T_e, the itinerant system is described by

$$\begin{pmatrix} 1 & 0 \\ 0 & C_e \end{pmatrix} \begin{pmatrix} \partial_t \mu_s \\ \partial_t T_e \end{pmatrix} = -\begin{pmatrix} 2\rho_{sd} I_{sd} \\ U_{sd} \end{pmatrix} - \begin{pmatrix} 1/\tau_s & 0 \\ 0 & g_{ep} \end{pmatrix} \begin{pmatrix} \mu_s \\ T_e - T_p \end{pmatrix}, \tag{2.74}$$

where the term corresponding to electron-phonon scattering is introduced by hand and follows from the standard two-temperature model. We note that the coefficient $\rho_{sd} = 1/\tilde{\nu} - J_{sd}a^3/2$ is defined in different units compared to last Sec. 2.4, where we used the notation $\tilde{\nu} = 2D_\uparrow D_\downarrow/(D_\uparrow + D_\downarrow)$ for the spin-averaged density of states in units per energy per volume [36].

To illustrate the use of the discussed implementation of electron-magnon scattering, Fig. 2.8 visualizes the dynamics of the magnons and electrons upon rapid heating. The calculation uses the assumptions and coefficients as presented in Chapter 4. Figure 2.8(a) indicates the change of the magnon density δn_d, and clearly shows the rapid generation of thermal magnons. Figure 2.8(b) indicates the spin accumulation μ_s as a function of time. Finally, Fig. 2.8(c) depicts the normalized magnetization of the combined spin system. The latter is defined as $m = (s - n_d - n_s/2)/s$, with n_d the magnon density and $n_s = n_\uparrow - n_\downarrow$ the spin density of the itinerant electrons.

In comparison to the *s*-*d* model, the implementation of electron-magnon scattering has two major advantages. First, it includes the magnons as elemental spin excitations and thereby provides a better microscopic representation of a ferromagnet. Secondly, it allows for a straightforward extension to a more complete description of spin transport, one that includes both itinerant electrons and thermal magnons as a spin-current carrier. This brings us to the end of the first part of this background chapter, as we have now introduced all the essential tools for the description of the local spin dynamics. In the second part, the focus redirects towards the theoretical model for diffusive spin transport. We start with a general review of the underlying transport description.

2.6 DIFFUSIVE SPIN TRANSPORT

In this section, we discuss the basic theoretical description of diffusive spin transport. We closely follow the standard derivation based on Boltzmann transport theory, as presented in Refs. [107, 108, 122, 123]. The formalism will be introduced for a general system of particles, and later specifically applied to spin-polarized electrons and thermal magnons. Additionally, this overview also includes the description of heat transport, which will be used in Chapter 4.

Without the loss of generality, the system is characterized by the distribution function $f_{\mathbf{k}} = f_{\mathbf{k}}(\mathbf{r})$, which is now explicitly dependent on the position $\mathbf{r}$. The distribution function satisfies the Boltzmann equation [108]

$$\frac{\partial f_{\mathbf{k}}}{\partial t} + \mathbf{v} \cdot \nabla f_{\mathbf{k}} = I\{f_{\mathbf{k}}\}, \tag{2.75}$$

where $\mathbf{v} = \partial \omega_{\mathbf{k}} / \partial \mathbf{k}$ is the group velocity corresponding to the dispersion relation

$\omega_{\mathbf{k}}$. The term on the right-hand side $I\{f_{\mathbf{k}}\}$ is a functional describing the full Boltzmann collision integral and includes all possible scattering processes. In principle, the typical form of the collision integral can be deduced from the microscopic calculations presented in the previous sections. For now, our main interest is calculating the modified distribution function in the presence of (small) gradients of the chemical potential and the temperature. In order to do this, it is convenient to write

$$f_{\mathbf{k}}(\mathbf{r}) = f_{\mathbf{k}}^0 + \delta f_{\mathbf{k}}, \tag{2.76}$$

where $f_{\mathbf{k}}^0$ describes the distribution function in the local equilibrium and $\delta f_{\mathbf{k}}$ describes a small deviation. The latter determines the particle current density $\mathbf{j}$ and heat current density $\mathbf{j}_Q$, as given by

$$\mathbf{j} = \int \frac{d\mathbf{k}}{(2\pi)^3} \mathbf{v} \delta f_{\mathbf{k}}, \tag{2.77}$$

$$\mathbf{j}_Q = \int \frac{d\mathbf{k}}{(2\pi)^3} (\epsilon_{\mathbf{k}} - \mu) \mathbf{v} \delta f_{\mathbf{k}}. \tag{2.78}$$

The next step is to determine an expression for $\delta f_{\mathbf{k}}$ using the Boltzmann equation, where the collision term is rewritten using the relaxation time approximation. To linear order in the gradients of the driving fields, $\delta f_{\mathbf{k}}$ satisfies

$$\frac{\partial \delta f_{\mathbf{k}}}{\partial t} + \mathbf{v} \cdot \nabla f_{\mathbf{k}}^0 = -\frac{\delta f_{\mathbf{k}}}{\tau}. \tag{2.79}$$

where τ is the relaxation time, which is assumed to be independent of $\mathbf{k}$, and is determined by all scattering processes that contribute to the decay of $\delta f_{\mathbf{k}}$. Furthermore, it is assumed that τ is much shorter than the timescale at which (gradients of) the driving field vary. In that case, the temporal derivative can be omitted and $\delta f_{\mathbf{k}}$ is given by

$$\delta f_{\mathbf{k}}(\mathbf{r}) = -\tau \mathbf{v} \cdot \nabla f_{\mathbf{k}}^0(\mathbf{r}). \tag{2.80}$$

Substituting this relation in the particle current density gives

$$\mathbf{j} = -\tau \int \frac{d\mathbf{k}}{(2\pi)^3} \mathbf{v} (\mathbf{v} \cdot \nabla f_{\mathbf{k}}^0), \tag{2.81}$$

and a similar expression is found for the heat current density. Generally, the local equilibrium distribution function is parametrized by the chemical potential and temperature $f_{\mathbf{k}}^0 = f(\epsilon_{\mathbf{k}}, \mu(\mathbf{r}, t), T(\mathbf{r}, t))$, and is given by either a Bose-Einstein or

Fermi-Dirac distribution. For simplicity, we consider the situation that the gradients are only nonzero along the x-axis. The current is written in terms of the driving fields and an integral over the energy

$$j = -\tau \int d\epsilon D(\epsilon) \frac{|\mathbf{v}|^2}{3} \frac{\partial f^0}{\partial \epsilon} \left[-\frac{\partial \mu}{\partial x} - \frac{(\epsilon - \mu)}{T} \frac{\partial T}{\partial x} \right], \tag{2.82}$$

where $D(\epsilon)$ is the density of states. Here, a quadratic dispersion relation is assumed and $|\mathbf{v}|^2$ is linear in the energy. A similar expression can be determined for the heat current density. Therefore, we generally define the coefficient L_{ij} that fully specifies the current densities

$$L_{ij} = \tau \int d\epsilon D(\epsilon) (|\mathbf{v}|^2/3)(\epsilon - \mu)^{i+j-2} \frac{\partial f^0}{\partial \epsilon}. \tag{2.83}$$

In summary, the particle current density and heat current density are given by

$$\begin{pmatrix} j \\ j_Q \end{pmatrix} = \begin{pmatrix} L_{11} & L_{12} \\ L_{21} & L_{22} \end{pmatrix} \begin{pmatrix} \partial_x \mu \\ \partial_x T/T \end{pmatrix}. \tag{2.84}$$

Evaluating the coefficients is a relatively straightforward exercise. However, the calculation method depends on whether $f^0_{\mathbf{k}}$ is given by a Bose-Einstein or Fermi-Dirac distribution. Therefore, spin-dependent electron transport and diffusive magnon transport are separately discussed in the following sections.

2.6.1 SPIN-DEPENDENT ELECTRON TRANSPORT

Since electrons correspond to spin one-half particles, the first step to introduce spin-polarized electron transport is to define two separate electron systems, one for each spin polarization. Furthermore, one should take into account that the electrons carry electric charge and the Boltzmann equation includes an additional term in the presence of an electric field. The latter can easily be implemented by introducing the electrochemical potential $\tilde{\mu}_\sigma = \mu_\sigma - eV$ for $\sigma \in \{\uparrow, \downarrow\}$ [71, 107], where V is the electric potential. Applying the framework of Eq. (2.84) to both spin populations and substituting the definition of the electrochemical potential yields a complete description of spin-dependent electron transport in linear response.

The main interests are the spin-specific current densities $j_\uparrow$ and $j_\downarrow$, and the total heat current density $j_{Q,\uparrow} + j_{Q,\downarrow}$. They are given by [124, 125]

$$\begin{pmatrix} j_\uparrow \\ j_\downarrow \\ j_{Q,\uparrow} + j_{Q,\downarrow} \end{pmatrix} = -\begin{pmatrix} \sigma_\uparrow/e^2 & 0 & \sigma_\uparrow S_\uparrow/e^2 \\ 0 & \sigma_\downarrow/e^2 & \sigma_\downarrow S_\downarrow/e^2 \\ \sigma_\uparrow \Pi_\uparrow/e^2 & \sigma_\downarrow \Pi_\downarrow/e^2 & \kappa_\uparrow + \kappa_\downarrow \end{pmatrix} \begin{pmatrix} \partial_x \tilde{\mu}_\uparrow \\ \partial_x \tilde{\mu}_\downarrow \\ \partial_x T_e \end{pmatrix}, \tag{2.85}$$

where the spin-dependent coefficients are expressed in terms of the conductivity σ_σ, Seebeck coefficient S_σ, Peltier coefficient Π_σ, and heat conductivity κ_σ. The corresponding L_{ij} can straightforwardly be evaluated by employing the Sommerfeld expansion and collecting the dominant terms for $k_B T_e \ll \epsilon_F$.

Our main interest is thermal spin transport, specifically, in the absence of a charge current. In the context of a time-dependent excitation mechanism, it is assumed that any transfer of charge that may arise upon excitation, is effectively screened within an extremely short timescale [71]. In that way, one can impose that the charge current vanishes instantaneously. Then, the spin current density $j_{s,e} = j_\uparrow - j_\downarrow$ and (total) heat current density $j_{Q,e} = j_{Q,\uparrow} + j_{Q,\downarrow}$ can be simplified. Specifically, by using Eq. (2.85) under the condition that $j_\uparrow + j_\downarrow = 0$ and eliminating the electric field (included in $\tilde{\mu}_\sigma$) yields

$$\begin{pmatrix} j_{s,e} \\ j_{Q,e} \end{pmatrix} = -\begin{pmatrix} \tilde{\sigma}/e^2 & \tilde{\sigma} S_s/e^2 \\ \tilde{\sigma}\Pi_s/(2e^2) & \kappa_e \end{pmatrix} \begin{pmatrix} \partial_x \mu_s \\ \partial_x T_e \end{pmatrix}, \tag{2.86}$$

which is now expressed in terms of the spin accumulation $\mu_s = \mu_\uparrow - \mu_\downarrow$, the spin-dependent Seebeck coefficient $S_s = S_\uparrow - S_\downarrow$, and the spin-dependent Peltier coefficient $\Pi_s = TS_s$.

The goal is to calculate the transport in the itinerant spin system in response to laser heating. The full dynamics of the itinerant spin system follows from the conservation laws for spin and energy. The corresponding continuity equations can equivalently be deduced from integrating the Boltzmann equation over the momentum. The interactions with a magnon and phonon bath are included in the collision integral and reduce to the local spin and energy transfer rates as derived in the previous section. The resulting continuity equations are given by

$$\tilde{\nu}\frac{\partial \mu_s}{\partial t} + \frac{\partial j_{s,e}}{\partial x}, = -\frac{\tilde{\nu}\mu_s}{\tau_s} - 2I_{sd}, \tag{2.87}$$

$$C_e \frac{\partial T_e}{\partial t} + \frac{\partial j_{Q,e}}{\partial x} = g_{ep}(T_p - T_e) - U_{sd} + P(t,x), \tag{2.88}$$

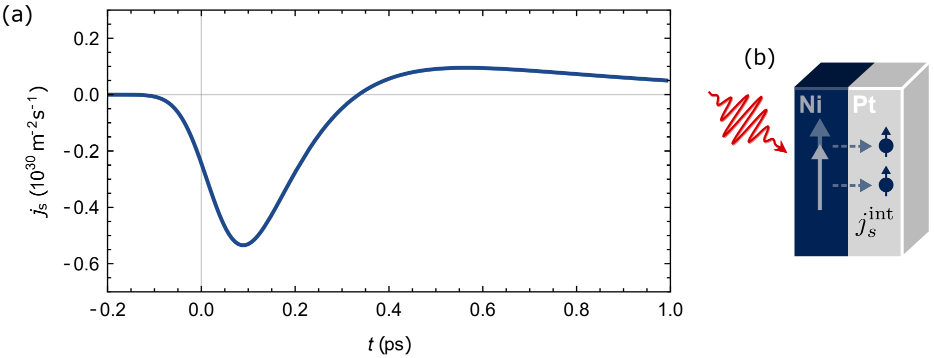

Figure 2.9: (a) The interfacial spin current (blue) as a function of time after laser-pulse excitation at $t = 0$. (b) Schematic overview of the Ni/Pt magnetic heterostructure and the excited interfacial spin current $j_s^{\rm int}$.

which is equivalent to Eq. (2.74) with an additional divergence term for the spin and heat current densities.[4]

To illustrate the presented approach for laser-induced spin transport, we explicitly calculate the interfacial spin current in a Ni/Pt heterostructure. Here, the magnon system is treated as a local system, described by the parametrization introduced in Section 2.5. In other words, all the generated spin transport is carried by the itinerant electrons. Figure 2.9(a) shows the result, where the blue line indicates the interfacial spin current as a function of time after laser-pulse excitation at $t = 0$. The plot shows the typical transient spin-current pulse as expected from the experiments [65, 70]. A detailed discussion on the presented model for laser-induced spin transport in magnetic heterostructures, including all the used system parameters, is presented in Chapter 4. Furthermore, in that chapter, we discuss the close similarity between the spin current and the time derivative of the magnetization.

In contrast to the research presented in Chapter 4, the calculation visualized in Fig. 2.9(a) does not include the transport of magnons. Interestingly, introducing the diffusive transport of magnons is a straightforward extension, and can be formulated in analogy with the implementation of electron transport.

---

[4] For simplicity, we assumed that $\rho_{sd} = \tilde{\nu}^{-1}$, meaning that the mean-field shift induced by the s-d interaction is neglected.

2.6.2 Diffusive magnon transport

In this final section on spin transport, we discuss an intuitive implementation of diffusive magnon transport following the results of Ref. [118]. Equivalent to the previous section, the magnon current density and magnon heat current density are calculated by employing the Boltzmann transport theory to linear order in gradients of the chemical potential and temperature. The corresponding transport coefficients are given by Eq. (2.83). The calculation involves evaluating Bose-Einstein integrals and may be expressed in terms of polylogarithms. To further simplify, it is assumed that the magnon temperature T_m remains close to the ambient temperature, and the magnon gap and chemical potential satisfy $\epsilon_0, \mu_m \ll k_B T_0$. The resulting transport coefficients are given in Ref. [118, 121], and are summarized in Chapter 4. Finally, the magnon current density j_m and magnon heat current density $j_{m,Q}$ are formulated as [118]

$$\begin{pmatrix} j_m \\ j_{Q,m} \end{pmatrix} = -\begin{pmatrix} \sigma_m/e^2 & L/T_0 \\ L & \kappa_m \end{pmatrix} \begin{pmatrix} \partial_x \mu_m \\ \partial_x T_m \end{pmatrix}, \tag{2.89}$$

where the transport coefficients are defined in terms of the magnon conductivity σ_m, the spin Seebeck coefficient L, and the magnon heat conductivity κ_m. Furthermore, T_0 is the ambient temperature. For illustrative purposes, we state the final expression for the magnon conductivity

$$\sigma_m = \frac{e^2 \tau_{\mathrm{tr},m} (k_B T_0)^{3/2} \Gamma(3/2) \zeta(3/2)}{2\pi^2 \hbar^2 A^{1/2}}. \tag{2.90}$$

Using the expression for the magnon density n_d in Eq. (2.66), it is straightforward to show that the magnon conductivity is given by the Drude-like formula $\sigma_m = e^2 n_d \tau / m_m$ [121]. Here, the effective magnon mass is $m_m = \hbar^2 (\partial^2 \epsilon_q / \partial q^2)^{-1} = \hbar^2/(2A)$. Although it was shown in magnetic insulators that σ_m is an order of magnitude smaller than the typical values for the electrical conductivity [118], the magnonic system responds differently to thermal gradients. To compare it to thermoelectric effects, we note that the resulting expression for L gives the relation $L/(\sigma_m T) \sim k_B$ [118]. In contrast, in the free electron model the Seebeck coefficient scales as $(T/T_F) k_B$, and thermoelectric effects are generally weak. The comparison suggests that in ferromagnetic metals, where both electrons and magnons contribute to spin transport, the spin current as a result of a temperature bias may be dominated by the transport of magnons. In the case of a metallic magnetic heterostructure with a constant temperature gradient, the magnonic and electronic contribution to thermal spin injection were calculated explicitly in Ref. [126]. It was shown that the ratio of the distinct contributions to the injected spin current j_s^{int} scales as

$$\frac{j_s^{\mathrm{int}}\big|_{\mathrm{magnons}}}{j_s^{\mathrm{int}}\big|_{\mathrm{electrons}}} \propto \left(\frac{T_F}{T_C}\right)\sqrt{\frac{T}{T_C}}, \tag{2.91}$$

which is strongly in favor of the magnonic contribution due to the fact that generally $T_F \gg T_C$. Although this is a different context than the time-dependent scenarios discussed in this thesis, the observation hints that thermal magnons may play a significant role in the spin transport driven by laser heating. The role of magnon transport is extensively discussed in Chapter 4.

As we have now introduced the two types of spin transport that will be investigated in the main chapters, we arrived at the end of the second part of this introductory chapter. In the remaining part, we switch back to describing local spin dynamics, specifically, the dynamics in ferrimagnetic materials.

2.7 SPIN DYNAMICS IN MULTISUBLATTICE MAGNETS

In the final sections of this chapter, two models for the local spin dynamics in multisublattice magnets are discussed. Specifically, the focus is on rare-earth transition-metal alloys, which are an exceptionally interesting material since they allow single-pulse all-optical switching [10]. The models will be presented in the same order as the equivalent descriptions for ferromagnets. First, the Weiss model is extended to multiple spin sublattices to cover the equilibrium properties of the magnetization. Then, we will discuss two descriptions of the spin dynamics. The first one is based on the M3TM [78], whereas the second is an extension of the *s*-*d* model [58, 87, 88]. Both implementations use the Weiss model for ferrimagnets as the equilibrium conditions.

To shortly address the equilibrium magnetization in ferrimagnets, the Weiss model is formulated for the two spin sublattices of a two-component $\mathrm{A}_x\mathrm{B}_{1-x}$ alloy. The first step is to determine the exchange splitting for the distinct spin systems A and B. Within a mean-field approach, the exchange splitting Δ_A and Δ_B are expressed as

$$\Delta_A = x\gamma_{AA}m_A + (1-x)\gamma_{AB}m_B, \tag{2.92}$$

$$\Delta_B = x\gamma_{BA}m_A + (1-x)\gamma_{BB}m_B. \tag{2.93}$$

We defined the coefficient $\gamma_{ij} = j_{ij}zD_{s,j}S_j$ in terms of exchange coupling constant j_{ij} and the number of nearest neighbors z. Furthermore, the number of spins per atom is defined as $D_{s,j} = \mu_{\text{at},j}/(2S_j)$, with μ_{at} the atomic magnetic moment in units of the Bohr magneton. The latter is introduced phenomenologically to address the fact that the spin per atom is generally not a half-integer, and is an essential parameter in the case of ferrimagnetic systems.

Obviously, the exchange splitting for a pure material ($x = 0$ or 1) should retrieve the single-component Curie temperature. It automatically follows that the intrasublattice coupling constant is given by $\gamma_{ii} = 3k_BT_{C,i}/(S_i+1)$. Additionally, the intersublattice constants are determined by the exchange coupling constant j_{ij}, which is treated as a free parameter. To illustrate the description for ferrimagnetic alloys, we determine the magnetization as a function of temperature for a typical rare-earth transition-metal alloy. For the transition metal, notated as component A, we use $T_C = 1000$ K, $S = 1/2$ and $\mu_{\text{at}} = 2.0$. For the rare-earth metal B, we use the typical values $T_C = 292$ K, $S = 7/2$ and $\mu_{\text{at}} = 7.0$, which roughly represent Gadolinium. Finally, we set the intersublattice exchange constant to $j_{AB} = -2.0$ meV. Figure 2.10 shows the result, indicating the element-specific magnetic moment as a function of temperature. The red line indicates the magnetic moment of the transition metal, whereas the blue line corresponds to the rare-earth component. The calculation was performed using a concentration of $x = 0.73$. In this example, the total magnetic moment (in green) is compensated around room temperature.

Now that the equilibrium description of the element-specific magnetization is introduced, we can move on to the dynamical model. The first description we discuss is the extension of the M3TM to multisublattices magnets.

2.7.1 THE M3TM FOR FERRIMAGNETIC ALLOYS

In this section,[5] we shortly discuss the model for laser-induced spin dynamics in ferrimagnetic materials based on the M3TM. This description was introduced by Schellekens et al. [78] and is a relatively straightforward extension of the original

---

[5] This section was presented in the Supplemental Material of Ref. [127]. The main text of Ref. [127] corresponds to Chapter 6 of this thesis.

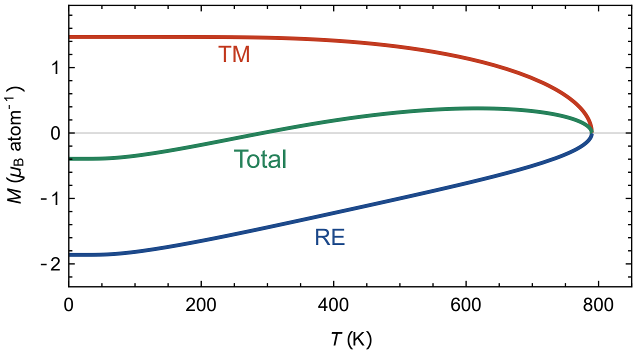

Figure 2.10: The element-specific magnetic moment as a function of the temperature of a ferrimagnetic alloy consisting of a typical transition-metal (red) and rare-earth (blue) component. The magnetic moment is calculated using the Weiss model for multisublattice magnets. Additionally, the green line indicates the total magnetic moment and shows that the compensation temperature is close to room temperature.

ferromagnetic model. The extension relies on two assumptions: (i) the demagnetization of the distinct spin sublattices is well described by the original M3TM, and (ii) an additional channel for intersublattice spin transfer is present that originates from exchange scattering processes.

As the name suggests, exchange scattering corresponds to the (spin-flip) electron-electron scattering processes that originate from the exchange interaction. The processes enable the mutual transfer of spin angular momentum between the sublattices. In the M3TM approximation, where electrons are treated as spinless, the Hamiltonian that describes intersublattice exchange scattering is given by [78]

$$\hat{H}_{\mathrm{ex},ij} = \sum_{\{\mathbf{k}\}} \sum_{v}^{ND_{\mathrm{s},i}} \sum_{w}^{ND_{\mathrm{s},j}} \left(\frac{j_{\mathrm{ex},ij}}{N^2}\right) c^{\dagger}_{\mathbf{k}'''} c^{\dagger}_{\mathbf{k}''} c_{\mathbf{k}'} c_{\mathbf{k}} (\hat{S}^{+}_{i,v} \hat{S}^{-}_{j,w} + \hat{S}^{-}_{i,v} \hat{S}^{+}_{j,w}), \tag{2.94}$$

where i and $j \neq i$ label the spin sublattices. The notation $\{\mathbf{k}\}$ indicates a summation over all appearing $\mathbf{k}$ vectors. Moreover, the indices v and w label the individual spins. Although $j_{\mathrm{ex},ij}$ is directly connected to the intersubalattice exchange coupling constant j_{ij}, we treat the former as a phenomenological parameter to compensate for the imperfection of the M3TM approximation. To further clarify the implementation of multisublattice magnets in the M3TM, a schematic overview is given in Fig. 2.12(b), indicating that the exchange scattering processes (in the gray box) mediate the intersublattice transfer of spin.

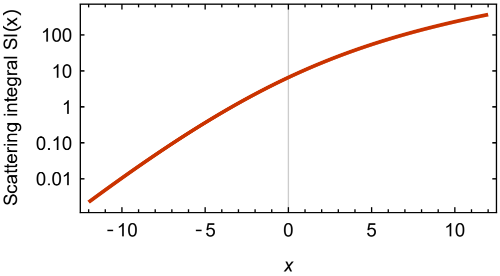

Figure 2.11: The scattering integral $\mathrm{SI}(x)$ plotted as a function of x.

In analogy with the previous calculations, Fermi's golden rule is used to determine the spin-transfer rate. In this case, one should take into account that the exchange scattering processes correspond to simultaneous (and opposite) transitions in the two spin subsystems. Hence, we define $\Gamma^{\pm\mp}_{ij,ss'}$, which corresponds to the rate at which in subsystem i transition $s \rightarrow s \pm 1$ occurs, accompanied by transition $s' \rightarrow s' \mp 1$ in subsystem j.[6] Fermi's golden rule yields [78]

$$\Gamma^{\pm\mp}_{ij,ss'} = \frac{2\pi}{\hbar} C_j D_{\mathrm{s},j} S^{\pm\mp}_{ij,ss'} \left(\frac{j^2_{\mathrm{ex},ij}}{N^4}\right) \sum_{\{\mathbf{k}\}} \delta(\epsilon_{\mathbf{k}} + \epsilon_{\mathbf{k}'} \mp \Delta_{ij} - \epsilon_{\mathbf{k}''} - \epsilon_{\mathbf{k}'''}) \qquad (2.95)$$
$$\times \left[f_{\mathbf{k}} f_{\mathbf{k}'} (1 - f_{\mathbf{k}''})(1 - f_{\mathbf{k}'''}) \right],$$

where we defined the coordination number $C_j = x \cdot z$, with z the number of nearest neighbors, and the relative exchange splitting $\Delta_{ij} = \Delta_i - \Delta_j$. Furthermore, $S^{\pm\mp}_{ij,ss'}$ results from the multiple spin ladder operators and is given by

$$S^{\pm\mp}_{ij,ss'} = (S_i(S_i + 1) - s(s \pm 1))(S_j(S_j + 1) - s'(s' \mp 1)). \qquad (2.96)$$

The expression in Eq. (2.95) is simplified by rewriting the summation over the momenta in terms of integrals over the energies. The transition rate $\Gamma^{\pm\mp}_{ij,ss'}$ is reformulated as

$$\Gamma^{\pm\mp}_{ij,ss'} = \frac{\eta_{ij} C_j T_e^3}{D_{\mathrm{s},i}} \mathrm{SI}(\mp\Delta_{ij}/k_B T_e) S^{\pm\mp}_{ij,ss'}, \qquad (2.97)$$

---

[6] s is here a shorthand notation for the previously used m_s.

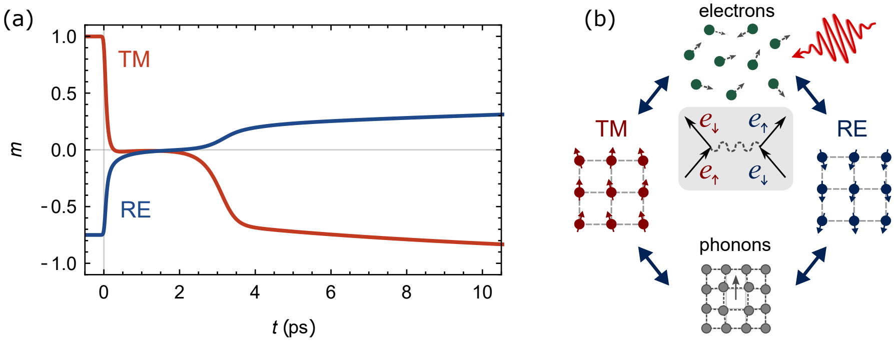

Figure 2.12: The element-specific magnetization dynamics of a rare-earth transition-metal alloy, which is calculated with the M3TM for multisublattice magnets. The red line indicates the normalized magnetization of the transition-metal component as a function of time after laser-pulse excitation at $t = 0$. The blue line corresponds to the normalized magnetization of the rare-earth metal. The presented figure is identical to Fig. 6.2(c). (b) Schematic overview of the M3TM for multisublattice magnets. Exchange scattering, as indicated in the gray box, mediates the transfer of spin angular momentum between the two distinct spin sublattices. Additionally, the individual sublattices transfer angular momentum to the lattice through Elliott-Yafet electron-phonon scattering processes.

where we defined the prefactor

$$\eta_{ij} = \frac{2\pi}{\hbar} j_{\mathrm{ex},ij}^2 D_F^4 D_{\mathrm{s},i} D_{\mathrm{s},j} k_B^3 \equiv \lambda_{ij} \frac{2\pi}{\hbar} j_{ij}^2 D_F^4 D_{\mathrm{s},i} D_{\mathrm{s},j} k_B^3. \tag{2.98}$$

Here, D_F is the density of states evaluated at the Fermi energy in units per energy per atom. In the second step, we introduced the dimensionless parameter λ_{ij}, that is determined by the ratio of $j_{ex,ij}$ and the intersublattice exchange coupling constant j_{ij}.

The scattering integral $\mathrm{SI}(\mp\Delta_{ij}/k_B T_e)$, which appears in Eq. (2.97), parametrizes the probability of an electron-electron scattering event to occur and is given by

$$\mathrm{SI}(\pm x) \equiv \int dx_1 dx_2 dx_3 (1 - f(x_1 + x_2 \pm x - x_3))(1 - f(x_3)) f(x_2) f(x_1), \tag{2.99}$$

where $f(x)$ is the Fermi-Dirac distribution. The function $\mathrm{SI}(x)$ is plotted in Fig. 2.11. Importantly, the scattering integral satisfies $\mathrm{SI}(x)/\mathrm{SI}(-x) = \exp(x)$. It yields that the exchange scattering rate vanishes in case the occupation probability of the spin levels is described by Boltzmann statistics.

Our main interest is calculating the element-specific magnetization dynamics driven by exchange scattering. In order to do so, we need to calculate the temporal derivative of the occupation probability $f_{i,s}$ of spin level s. To arrive at a compact expression, we first define

$$W^{\pm\mp}_{ij,ss'}(\Delta_{ij}) \quad = \quad \mathrm{SI}(\mp\Delta_{ij}/k_B T_e) S^{\pm\mp}_{ij,ss'} \ , \tag{2.100}$$

which corresponds to the dimensionless part of $\Gamma^{\pm\mp}_{ij,ss'}$. The time derivative of the occupation probability $f_{i,s}$ follows from collecting the rates of all the allowed spin transitions.[7] Subsequently, the normalized magnetization of sublattice i is determined by the ensemble average $m_i = (-1/S_i)\sum_{s=-S_i}^{S_i} s f_{i,s}$. Finally, the change of the magnetization m_i driven by exchange scattering is described by

$$\begin{aligned} \left.\frac{dm_i}{dt}\right|_{\mathrm{ex}} \quad = \quad & \frac{2\eta_{ij}C_j}{\mu_{\mathrm{at},i}} T_e^3 \Bigg[\sum_{s=-S_i+1}^{S_i} \sum_{s=-S_j}^{S_j-1} W^{-+}_{ij,ss'}(\Delta_{ij}) f_{i,s} f_{j,s'} \\ & - \sum_{s=-S_i}^{S_i-1} \sum_{s=-S_j+1}^{S_j} W^{+-}_{ij,ss'}(\Delta_{ij}) f_{i,s} f_{j,s'} \Bigg], \end{aligned} \tag{2.101}$$

where the definition $D_{\mathrm{s},i} = \mu_{\mathrm{at},i}/2S_i$ is used. To illustrate the physical meaning of Eq. (2.101), it is convenient to present the formula for two spin one-half subsystems $S_i = S_j = 1/2$. In that case, the exchange scattering results in

$$\left.\frac{dm_i}{dt}\right|_{\mathrm{ex}} = \frac{\eta_{ij}C_j}{2\mu_{\mathrm{at},i}} T_e^3 \left[\mathrm{SI}\left(\frac{\Delta_{ij}}{k_B T_e}\right)(1-m_i)(1+m_j) - \mathrm{SI}\left(-\frac{\Delta_{ij}}{k_B T_e}\right)(1+m_i)(1-m_j) \right]. \tag{2.102}$$

The two terms between the square brackets correspond to the opposite spin transitions, and the factors $(1 \mp m_i)(1 \pm m_j)$ determine the availability of the new spin states. The formula for an arbitrary spin quantum number, as given in Eq. (2.101), has a similar structure and includes the transition probabilities for all possible combinations of transitions. The full dynamics of the normalized magnetization is given by adding the contribution by exchange scattering to the original M3TM

$$\frac{dm_i}{dt} = \left.\frac{dm_i}{dt}\right|_{\mathrm{M3TM}} + \left.\frac{dm_i}{dt}\right|_{\mathrm{ex}}. \tag{2.103}$$

As an intuitive example, we modeled all-optical switching in a typical rare-earth transition-metal alloy. The result is shown in Fig. 2.12(a). Here, the red line indicates

---

[7] The full expression is given in the Supplemental Material of Ref. [127].

the transition-metal magnetization as a function of time after laser-pulse excitation at $t = 0$. The blue line describes the magnetization of the rare-earth component. The plot corresponds to a calculation that is presented in Chapter 6. There, the used system parameters are fully specified. Although the model simulates a successful all-optical switching process, the visible plateau near the ferromagnetic (FM) region deviates from the characteristic time-resolved measurements [11] (Introduction Fig. 1.7). We note here that the dynamics near the zero-crossing strongly depends on the parameters used in the calculation. Nevertheless, as shown later in the thesis, the model qualitatively agrees with the experiments in terms of the magnetic system requirements for successfully switching the magnetization with a single laser pulse.

Although this section focused on ferrimagnetic alloys, the introduced model can equivalently be applied to synthetic-ferrimagnetic multilayers. The latter material systems are addressed in Chapters 6 and 7. In these chapters, we will show that the switching mechanism in synthetic ferrimagnets has a nonlocal character. Nevertheless, the discussed framework does not allow to include spin currents within an itinerant spin system. In the following section, we shortly discuss the extension of the *s*-*d* model to ferrimagnetic systems. The latter allows to include the standard diffusive spin currents.

2.7.2 THE *s*-*d* MODEL FOR FERRIMAGNETIC ALLOYS

In this section, we present the extension of the *s*-*d* model to ferrimagnetic systems, as was introduced by Gridnev et al. [58]. Since all required mathematical steps are equivalent to the calculations for the ferromagnetic case, extending the model to ferrimagnets is a relatively straightforward task. In principle, it directly follows from a number of phenomenological arguments. A schematic overview of this approach is given in Fig. 2.13(b). It is assumed that the two magnetic sublattices indirectly exchange angular momentum through the interaction with a bath of itinerant spins. The spin sublattices are individually described by the *s*-*d* model. Additionally, the dynamics of the itinerant system is determined by the weighted sum of the spin-transfer rates of the local sublattices. From the angular momentum conservation of the *s*-*d* scattering processes, it automatically follows that the spin accumulation satisfies

$$D\frac{d\mu_s}{dt} = x(2S_A D_{s,\mathrm{A}})\frac{dm_\mathrm{A}}{dt}\bigg|_{sd} + (1-x)(2S_B D_{s,B})\frac{dm_\mathrm{B}}{dt}\bigg|_{sd} - \frac{D\mu_s}{\tau_s}, \tag{2.104}$$

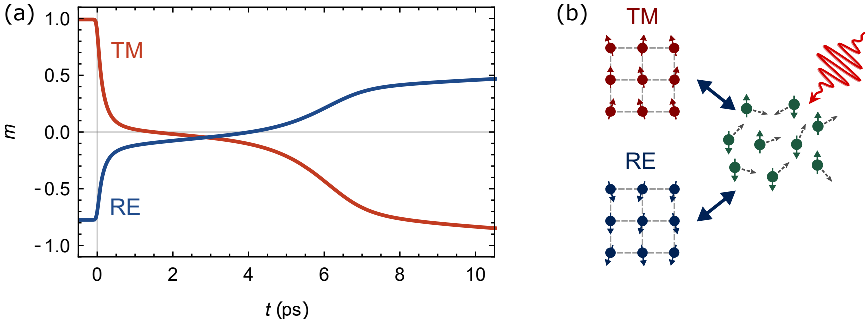

Figure 2.13: The element-specific magnetization dynamics of a rare-earth transition-metal alloy, which is calculated with the *s*-*d* model for ferrimagnetic alloys. The red line indicates the magnetization of the transition-metal component as a function of time after laser-pulse excitation at $t = 0$. The blue line corresponds to the magnetization of the rare-earth metal. (b) Schematic overview of the *s*-*d* model for ferrimagnets. The spin sublattices can indirectly exchange spin angular momentum through an *s*-*d* coupling to the electron bath.

where the first two terms on the right-hand side indicate the *s*-*d* model for the separate magnetic sublattices and are determined by the transition rates in Eq. (2.47).

Mediated by the itinerant spin system, the two magnetic sublattices indirectly exchange spin angular momentum. This channel of intersublattice spin transfer effectively allows the ferrimagnetic system to be switched by rapid heating [58]. To illustrate this, Fig. 2.13(a) presents a calculation of the element-specific magnetization dynamics in a rapidly heated rare-earth transition-metal alloy. The red line indicates the normalized magnetization of the transition-metal subsystem as a function of time. The blue line corresponds to the magnetization of the rare-earth component. In this calculation, the parameters for the ferrimagnetic system were chosen to be equal to the values used for Fig. 2.10. Additionally, the timescales that determine the efficiency of the spin-transfer rates were set to $\tau_{sd,\mathrm{Co}} = 0.1$ ps and $\tau_{sd,\mathrm{Gd}} = 1$ ps. The latter is very short compared to the experimental values for the demagnetization time of pure Gd [18]. It turns out that this enhanced Gd demagnetization rate is required to observe all-optical switching within this model. The choice of this parameter is highly nontrivial due to the orbital-specific demagnetization rates of $5d6s$ and $4f$ electrons [128], and because of the element-specific demagnetization time in a Gd-based alloy differs from the pure case [129]. It is needless to say that the specific time-resolved behavior is strongly affected by the choice of the system parameters. Nevertheless, the *s*-*d* model for ferrimagnets allows us to qualitatively investigate the interplay between the all-optical switching process and generated spin currents. This is particularly interesting for modeling magnetic multilayers that contain a ferrimagnetic component, where interlayer spin transport significantly influences the all-optical switching process [100, 101, 105, 130]. Some relevant preliminary calculations are presented in Chapter 8.

This brings us to the end of this theoretical background chapter, since all the models that are used in the remainder of the thesis are introduced. As will be shown, the presented descriptions of laser-induced spin dynamics qualitatively agree with the majority of the typical experiments. However, it is needless to say that there are some clear limitations. The latter will be pointed out in the main chapters and discussed in the outlook in Chapter 8.

3

s-d MODEL FOR LOCAL AND NONLOCAL SPIN DYNAMICS IN LASER-EXCITED MAGNETIC HETEROSTRUCTURES

We discuss a joint microscopic theory for the laser-induced magnetization dynamics and spin transport in magnetic heterostructures based on the s-d interaction. Angular momentum transfer is mediated by scattering of itinerant s electrons with the localized (d electron) spins. We use the corresponding rate equations and focus on a spin one-half d electron system, leading to a simplified analytical expression for the dynamics of the local magnetization that is coupled to an equation for the non-equilibrium spin accumulation of the s electrons. We show that this description converges to the microscopic three-temperature model in the limit of a strong s-d coupling. The equation for the spin accumulation is used to introduce diffusive spin transport. The presented numerical solutions show that during the laser-induced demagnetization in a ferromagnetic metal a short-lived spin accumulation is created that counteracts the demagnetization process. Moreover, the spin accumulation leads to the generation of a spin current at the interface of a ferromagnetic and nonmagnetic metal. Depending on the specific magnetic system, both local spin dissipation and interfacial spin transport are able to enhance the demagnetization rate by providing relaxation channels for the spin accumulation that is built up during demagnetization in the ferromagnetic material.[1]

---

[1] This chapter has been published in *Physical Review B* [131].

3.1 INTRODUCTION

Exciting magnetic systems with ultrashort laser pulses gives rise to fascinating physics. First, it was shown that a femtosecond laser pulse can quench the magnetization of a ferromagnetic thin film on a subpicosecond timescale [13]. Later, all-optical magnetization switching was discovered in GdFeCo alloys [10], which proved the high potential of using ultrashort laser pulses for future data-writing technologies. Moreover, it was demonstrated that the laser pulse generates a spin current [14, 15]. In noncollinear magnetic heterostructures the ultrafast generated spin current exerts a spin-transfer torque [64, 65], leading to the excitation of Terahertz standing spin waves [66, 67]. Understanding all these ultrafast phenomena paves the way towards faster magnetic data technologies, and bridges the boundaries between photonics, spintronics, and magnonics.

Despite the vast experimental developments within the field, the microscopic origin of the observed demagnetization rates is still heavily debated. Various microscopic processes have been proposed as being the dominant mechanism, such as (i) the coherent interaction between the photons and the spins [21, 22], (ii) spin-dependent transport of hot electrons [39], and (iii) local spin dynamics as triggered by laser heating or excitation [13, 18, 23, 24, 26, 31, 33, 35–38]. In the latter case, the models often rely on the assumption that heating of the electrons increases the amount of spin-flip scattering events, resulting in the transfer of angular momentum. An example of this type of models is the microscopic three-temperature model (M3TM) [18], where it is assumed that the magnetization dynamics is dominated by Elliott-Yafet electron-phonon scattering. Arguably, other types of scattering mechanisms can also account for the observed demagnetization rates, such as Elliott-Yafet electron-electron scattering [26] and electron-magnon scattering [31, 36]. The latter stems from the *s*-*d* interaction in ferromagnetic transition metals, that couples the local magnetic moments (*d* electrons) and free carriers (*s* electrons). Similar models were derived to describe the ultrafast magnetization dynamics in semiconductors [56] and ferrimagnetic alloys [58].

Another important question is what mechanism drives the optically induced spin currents in magnetic heterostructures. First, it could be directly related to the proposed superdiffusive spin currents created in the magnetic material [39, 73]. Secondly, the laser-induced thermal gradients can generate a spin current resulting from the spin-dependent Seebeck effect [74, 75]. Recently, it was proposed that the spin-polarized electrons are generated at a rate given by the temporal derivative of the magnetization [65]. Interestingly, this implies that the demagnetization and the generated spin current are driven by the same physical mechanism. The *s*-*d* interaction, which mediates angular momentum transfer between the local magnetic moments and itinerant electrons, is a principal candidate [36, 65, 72].

In this chapter, we discuss an extended *s*-*d* model for laser-induced magnetization dynamics that includes spin transport. The model describes that during demagnetization an out-of-equilibrium spin accumulation is created in the *s* electron system [36, 56], which leads to the generation of a spin current in magnetic heterostructures [65, 72]. We apply the *s*-*d* model to investigate the interplay between the local magnetization dynamics and spin transport in laser-excited magnetic heterostructures. The numerical solutions of the rate equations show a qualitative agreement with the experiments and support the view that the *s*-*d* interaction could be the main driving force of the observed ultrafast phenomena [36, 65, 72]. Furthermore, the crucial role of the spin accumulation is emphasized, namely (i) the generated spin accumulation has a negative feedback on the demagnetization process [36, 56] and (ii) this bottleneck can be removed by either local spin-flip processes or by electron spin transport. Hence, both local and nonlocal processes play a crucial role in the magnetization dynamics. Finally, we discuss the limit in which the *s*-*d* model becomes equivalent to the M3TM, and we conclude with an outlook.

We start with an overview of the derivation of the *s*-*d* model in Section 3.2 and we highlight the simplifications we use compared to the derivations reported in Ref. [36] and Ref. [56]. Importantly, we show that the *s*-*d* model can be written in a mathematical form analog to the M3TM, as was discussed in Sec. 2.4. In Section 3.3, we model the demagnetization experiments and discuss the role of the spin accumulation. We describe the laser-induced dynamics in a collinear magnetic heterostructure in Section 3.4. We explain how the different demagnetization rates of the parallel and antiparallel configurations can be understood from the *s*-*d* model. In Section 3.5, we describe a bilayer consisting of a ferromagnetic and nonmagnetic metallic layer. Here, we introduce diffusive spin transport, similar to the modeling as presented in [65, 71, 72]. We specifically address the interplay between the local magnetization dynamics and spin transport. We investigate the role of the layer thickness on the magnetization dynamics and we analyze the temporal profile of the injected spin current in the nonmagnetic layer.

3.2 MODEL FOR LOCAL SPIN DYNAMICS

The content of this section is equivalent to Section 2.4 of the theoretical background chapter, where we introduced the *s*-*d* model for ultrafast magnetization dynamics in transition metal ferromagnets. Hence, readers familiar with this model may skip this section and move to Section 3.3.

Here, we give a brief overview of the derivation of the *s*-*d* model. Although our approach is closely related to the derivation as presented in Ref. [36], it mathematically resembles the results for magnetic semiconductors [56]. We keep our notation consistent with these references and we highlight the modifications that are needed to reach the simplified *s*-*d* model that is used in the remainder of this chapter.

Analogous to Ref. [36], we define the ferromagnetic transition metal in terms of two separate electronic systems, corresponding to the 3*d* and 4*s* electrons. A schematic overview of the model is presented in Fig. 3.1(a). The *d* electrons are the main contributor to the magnetic properties of the system and are relatively localized. Therefore, we approximate the *d* electron system as a lattice of localized spins. At each lattice site there is only one spin and the atomic magnetic moment is given by $\mu_{\mathrm{at}} = 2S\mu_{\mathrm{B}}$, where μ_{B} is the Bohr magneton and S is the spin quantum number. We neglect the orbital angular momentum.

In this chapter, we describe the localized spin system within a Weiss mean-field approach, similar to the description used in the M3TM [18]. The Hamiltonian of the *d* electrons is expressed as

$$\hat{H}_d = \Delta \sum_j \hat{S}_j^{d,z}, \tag{3.1}$$

where $\hat{S}_j^{d,z}$ is the z component of the spin at lattice site j and Δ is the exchange splitting. Hence, each spin corresponds to a system of $2S+1$ energy levels split by energy Δ. Note that this description of the *d* electron system does not consider spin-wave excitations, which makes it different from the approach in Ref. [36].

The *s* electrons are described as a free electron gas. They are coupled to the localized spins through the on-site *s*-*d* interaction, given by [36]

$$\hat{H}_{sd} = J_{sd} V_{\mathrm{at}} \sum_j \hat{\mathbf{S}}_j^d \cdot \hat{\mathbf{s}}(\mathbf{r}_j). \tag{3.2}$$

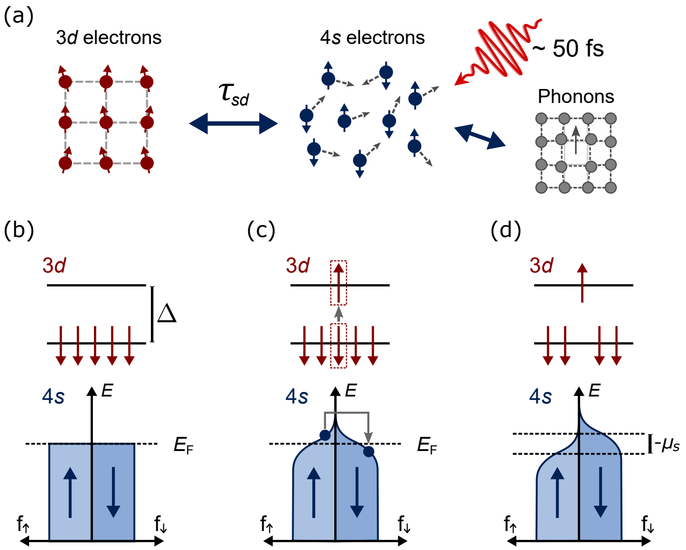

Figure 3.1: Schematic overview of the *s*-*d* model for ultrafast demagnetization [36, 56]. (a) The system is divided into a subsystem of localized 3*d* electrons and itinerant 4*s* electrons. The laser pulse heats up the *s* electrons. Angular momentum is transferred between the *s* and *d* subsystems by the *s*-*d* interaction. Secondly, angular momentum can dissipate out of the combined system by additional spin-flip processes in the *s* system, e.g., Elliott-Yafet electron-phonon scattering. Figures (b)-(d) schematically show the occupation of the energy levels in the *d* and *s* subsystems during the laser heating (for $S = 1/2$). Figure (b) indicates the ground state ($T_e = 0$ K). Figure (c) shows that the broadening of the Fermi-Dirac distribution allows spin-flip transitions around the Fermi level. This process is accompanied by a spin flip of a local *d* spin. The *s* electrons thermalize rapidly and a nonzero spin accumulation μ_s is created, as is indicated in Fig. (d).

Here, J_{sd} is the *s*-*d* exchange coupling constant, V_{at} is the atomic volume, $\hat{\mathbf{S}}_j^d$ is the spin operator of the spin at lattice site j, and $\hat{\mathbf{s}}(\mathbf{r}_j)$ is the spin density operator of the *s* electrons at position $\mathbf{r}_j$ of lattice site j. We express $\hat{\mathbf{s}}(\mathbf{r}_j)$ in terms of the electron creation and annihilation operators in momentum space. This yields [56]

$$\hat{H}_{sd} = \sum_j \sum_{\mathbf{k}\mathbf{k}'} \left[J^*_{j\mathbf{k}\mathbf{k}'} c^\dagger_{\mathbf{k}'\downarrow} c_{\mathbf{k}\uparrow} \hat{S}_j^{d+} + \text{h.c.} \right], \tag{3.3}$$

where the coupling strength is parametrized by the matrix element $J_{j\mathbf{k}\mathbf{k}'}$. $\hat{S}_j^{d\pm}$ corresponds to the spin ladder operator for the spin at lattice site j. The operator $c^\dagger_{\mathbf{k}\sigma}$ ($c_{\mathbf{k}\sigma}$) creates (annihilates) an *s* electron with momentum $\mathbf{k}$ and spin σ. In the transition from Eq. (3.2) to Eq. (3.3) the terms proportional to the z components are omitted and rewritten in terms of a mean-field energy shift in the Hamiltonian for the s electrons [36]. The similar energy shift in the d electron system (a shift of Δ) plays a minor role and is neglected.

Equation (3.3) describes the spin-flip scattering of s electrons with the localized spins, which mediates angular momentum transfer between the s and d electron systems, but conserves the total angular momentum. Hence, these scattering events change the total spin in the z direction of the d electron system. To calculate the resulting magnetization dynamics, we apply perturbation theory using the density matrix formalism. We only show the most important steps, for more details we refer to Ref. [56], where an equivalent calculation is presented for semiconductors. In contrast to Ref. [56], our system does include a direct (d-d) exchange interaction between the localized spins, as represented by Eq. (3.1).

First, we assume that the density matrix of the complete system can be factorized in terms of a density matrix $\hat{\rho}_C$ for the carriers (s electrons) and $\hat{\rho}_S$ for the localized spins (d electrons). Secondly, we assume that after excitation there is no coherence between the spins. In other words, the timescale at which the spins dephase is the shortest timescale within the system, such that the density matrix $\hat{\rho}_S$ is diagonal. The diagonal elements of $\hat{\rho}_S$ are given by the occupation numbers $\rho_{S,m_s m_s} = f_{m_s}$ for each energy level m_s of a single spin, where m_s corresponds to the z component of the spin. In this Boltzmann approach, the ensemble average of the spin in the z direction is given by $\langle \hat{S}^{d,z} \rangle = \sum_{m_s=-S}^{S} m_s f_{m_s}$.

In order to find the magnetization dynamics, we calculate the time derivative of all occupation numbers f_{m_s}. The mathematical description follows from the Liouville-von Neumann equation, and a coarse-grained description of the time evolution of the density operator [132]. The coarse-graining step size, interval δt, determines the time resolution of the model and should be sufficiently small compared to the observed demagnetization time τ_M. Moreover, we assume that the time interval δt satisfies the conditions for the Markov approximation, i.e., δt should be much larger than the correlation time of the electrons and the density matrix changes relatively slowly [35, 56]. Secondly, it is assumed that the time interval is much larger than the timescale associated with the energy transfer, in this case that yields $\delta t \gg \hbar/\Delta$ [35]. This is the standard limit underlying Fermi's golden rule, i.e., the condition leads to the transitions having a well-defined energy conservation represented by the Dirac delta function. Hence, we should have that $\hbar/\Delta \ll \delta t \ll \tau_M$. Since $\hbar/\Delta \sim 10$ fs (having $\Delta \sim k_B T_C$ and Curie temperature $T_C \sim 1000$ K) and τ_M is of the order of ~ 100 fs, the validity of this limit is not trivial. However, it is expected that the role of all the approximations is relatively weak and only affects the results quantitatively.

Finally, using the diagonality of the density matrix $\hat{\rho}_S$ and the explicit form of the interaction Hamiltonian $\hat{H}_{sd}$, the rate equation can be written as [56]

$$\begin{aligned}\frac{df_{m_s}}{dt} &= -(W_{m_s-1,m_s} + W_{m_s+1,m_s})f_{m_s} \\ &\quad +W_{m_s,m_s-1}f_{m_s-1} + W_{m_s,m_s+1}f_{m_s+1},\end{aligned} \tag{3.4}$$

where $W_{m_s\pm1,m_s}$ are the transition rates from level m_s to $m_s \pm 1$. The transition rates are calculated using Fermi's golden rule, analogous to the derivation of the M3TM [18]. We assume that the s electrons thermalize rapidly due to Coulomb scattering and can be described by Fermi-Dirac statistics. Here, the distributions for the spin up and spin down s electrons have a common temperature T_e, but are allowed to have a distinct chemical potential for which the difference is defined as the spin accumulation $\mu_s = \mu_\uparrow - \mu_\downarrow$ [36, 56]. In the limit that the Fermi energy is much larger than all other energy scales, the transition rate is given by [56, 58]

$$W_{m_s\pm1,m_s} = \frac{\pi}{2\hbar} J_{sd}^2 S_{m_s}^{\pm} D_\uparrow D_\downarrow (\Delta - \mu_s) \frac{\exp\left(\mp \dfrac{\Delta - \mu_s}{2k_B T_e}\right)}{2\sinh\left(\dfrac{\Delta - \mu_s}{2k_B T_e}\right)}. \tag{3.5}$$

Here, $S_{m_s}^{\pm} = S(S+1) - m_s(m_s \pm 1)$ and $D_{\uparrow,\downarrow}$ (in units $\mathrm{eV}^{-1}\mathrm{atom}^{-1}$) is the density of states at the Fermi level for the spin up and spin down s electrons, respectively. Equation (3.5) mathematically quantifies the amount of available phase space for transitions induced by the s-d interaction. Figures 3.1(b)-3.1(d) schematically show the changes to the occupation of the d and s electron states as a result of laser heating the system. Figure 3.1(c) shows that the thermal broadening of the Fermi-Dirac functions allows for transitions between the two spin directions of the s electrons, which is accompanied by a flip of a localized d electron spin. The s electrons thermalize rapidly and the new distributions have a shifted chemical potential, i.e., a nonzero spin accumulation is created, as is depicted in Fig. 3.1(d).

The dynamics of the spin accumulation μ_s can be derived analogously and directly follows from spin angular momentum conservation. Now we define the normalized magnetization $m_d = -\langle \hat{S}^{d,z} \rangle / S$ of the localized magnetic moments. In equilibrium, the experimentally detectable magnetization is dominated by m_d. This is not straightforward after excitation because of the induced exchange of angular momentum between the s and d electrons. In general, the magneto-optical signal in typical pump-probe experiments is a linear superposition of the contribution of the s and d electrons. For a $S = 1/2$ system we have $\Delta = 2k_B T_C m_d$, and the dynamics is described by the two equations

$$\frac{d\mu_s}{dt} = \rho_{sd}\frac{dm_d}{dt} - \frac{\mu_s}{\tau_s}, \tag{3.6}$$

$$\frac{dm_d}{dt} = \frac{1}{\tau_{sd}}\left(m_d - \frac{\mu_s}{2k_B T_C}\right)\left[1 - m_d \coth\left(\frac{2m_d k_B T_C - \mu_s}{2k_B T_e}\right)\right], \tag{3.7}$$

where we used the definition $\rho_{sd} = D^{-1} - J_{sd}/2$, with $D = 2D_\uparrow D_\downarrow/(D_\uparrow + D_\downarrow)$ from Ref. [36]. Note that the term proportional to J_{sd} results from the energy gap between the spin up and spin down s electrons arising from the s-d interaction (as was introduced in the transition from Eq. (3.2) to Eq. (3.3)), which can be both positive and negative depending on the sign of J_{sd}. Moreover, we defined $\tau_{sd}^{-1} = (\pi/\hbar)J_{sd}^2 D_\uparrow D_\downarrow k_B T_C$, which is closely related to the demagnetization rate. We introduced the phenomenological term proportional to τ_s^{-1}, which describes all spin-flip scattering processes that dissipate angular momentum out of the combined electronic system [36], e.g., this term includes Elliott-Yafet electron-phonon scattering.

Equation (3.7) clearly shows the similarities with the standard form of the equation for the longitudinal magnetization relaxation of a spin $S = 1/2$ system within a mean-field approach. For instance, in the limit $\tau_s \to 0$ the spin accumulation directly vanishes and the equilibrium condition is given by $m_d = \tanh(m_d T_C/T_e)$. In this limit, there is no net spin polarization, i.e., the s electrons can be considered as spinless, which is exactly the assumption underlying the M3TM [18]. We note that although this expression closely resembles the expression presented in Ref. [18], the prefactor corresponds to a completely different physical mechanism. More details about the relation with the M3TM will be discussed in Section 3.4.

Although we have a simple definition of the parameters ρ_{sd} and τ_{sd}, the estimation of these parameters is far from straightforward. We approximated the d and s electrons as two distinct systems, localized and itinerant electrons. In the real system there is no such clear separation because of s-d hybridization. Effectively, we separated the 'band-like' and 'local magnetic' properties of the combined electronic system (d and s), which makes it complex to estimate the relevant value of D.

Hence, it is convenient to treat both τ_{sd} and ρ_{sd} as effective parameters. In the upcoming sections, we interpret τ_{sd} as the experimentally retrieved demagnetization time and we choose the constant $\rho_{\mathrm{sd}} = 1$ eV. The exact values should be retrieved from carefully fitting the model to the experiments, which is beyond the scope of this theoretical paper.

Finally, D^{-1} ($D^{-1}_{\uparrow,\downarrow}$) scales with the width of the conduction band and is typically much larger than $J_{sd}/2$, i.e., we have $\rho_{sd} = D^{-1} - J_{sd}/2 \approx D^{-1}$. Then, we can define the magnetization of the total spin system (s and d electrons) as $m_{\mathrm{tot}} = m_d - \rho_{sd}^{-1}\mu_s$, which is conserved by the s-d interaction and will be used in the following analyses.

In the next section, we discuss the important role of the spin accumulation by describing the laser-induced demagnetization experiments using the numerical solutions of Eqs. (3.6)-(3.7).

3.3 ULTRAFAST DEMAGNETIZATION

In order to investigate the typical laser-induced dynamics of the local magnetization and spin accumulation specifically, we consider a system with magnetic parameters $\tau_{sd} = 0.2$ ps and $T_C = 1000$ K. To model the laser heating we define the temporal profile of the laser pulse as $P(t) = (P_0/(\sigma\sqrt{\pi}))\exp\left[-(t-t_0)^2/\sigma^2\right]$, where P_0 is the absorbed laser pulse energy density and σ determines the pulse duration, which is set to 50 fs. We use the standard two-temperature model to find the dynamics of the s electron temperature T_e and phonon temperature T_p [17]. The two-temperature model describes the equilibration of T_e and T_p by electron-phonon scattering. We include a heat dissipation term that transfers heat out of the phonon system on a timescale $\tau_D = 20$ ps. For the heat capacities and the electron-phonon coupling constant we use the values for Cobalt given in Ref. [18]. We calculate the dynamics of the magnetization and spin accumulation by solving Eqs. (3.6)-(3.7) numerically. We do this for multiple values of τ_{s}. The results are presented in Figs. 3.2(a)-(d).

Figure 3.2(a) shows the laser heating of the s electrons and the equilibration of the electron temperature with the phonon temperature. Figures 3.2(b)-(d) display the laser-induced dynamics of the spin systems for different values of the spin-flip scattering time τ_s, as indicated by the different line types. Figure 3.2(b) shows the magnetization of the d electrons m_d as a function of time. The temporal profile of the spin accumulation μ_s is presented in Fig. 3.2(c). Finally, Fig. 3.2(d) displays the

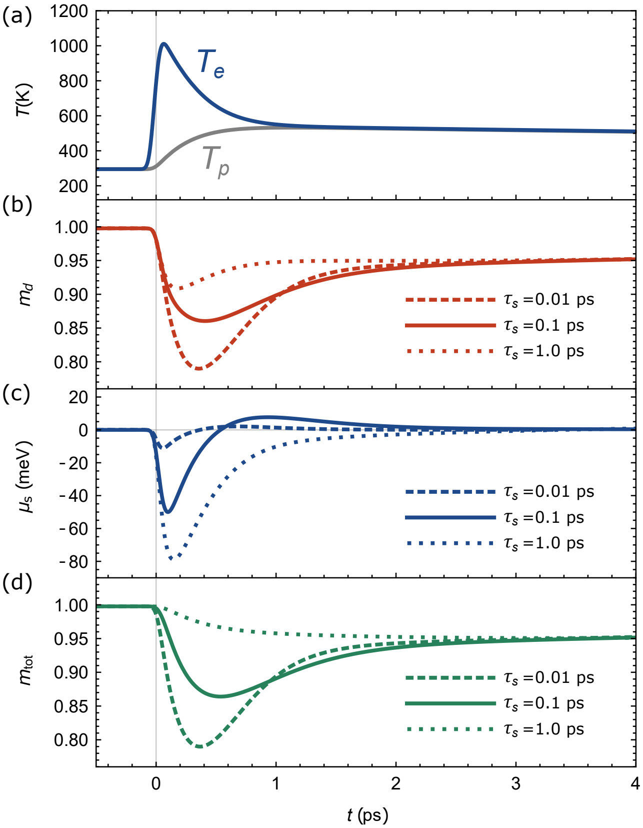

Figure 3.2: Ultrafast demagnetization described by the *s*-*d* model. Figure (a) shows the temporal profile of the *s* electron temperature T_e and phonon temperature T_p, after laser-pulse excitation at $t = 0$ with $P_0 = 12 \cdot 10^8$ Jm^{-3}. Figures (b)-(d) present the laser-induced dynamics of the spin systems, using $T_C = 1000$ K and $\tau_{sd} = 0.2$ ps. Here, the line types indicate the calculations for different values of τ_s, which are given in the figure. Figure (b) shows the resulting magnetization dynamics in the *d* electron system. Figure (c) shows the temporal profile of the spin accumulation μ_s, and Fig. (d) shows the dynamics of the total magnetization m_{tot}.

total magnetization m_{tot} as a function of time (m_{tot} is defined on page 74). Figures 3.2(b) and 3.2(d) clearly show that the demagnetization of m_d and m_{tot} is maximized for the smallest τ_s.

The calculations show that the creation of a spin accumulation has a negative feedback effect on the demagnetization (of both m_d and m_{tot}), i.e., the short-lived spin accumulation acts as a bottleneck [36, 56]. The bottleneck can be removed by the additional spin-flip relaxation processes in the *s* electron system, which happen at

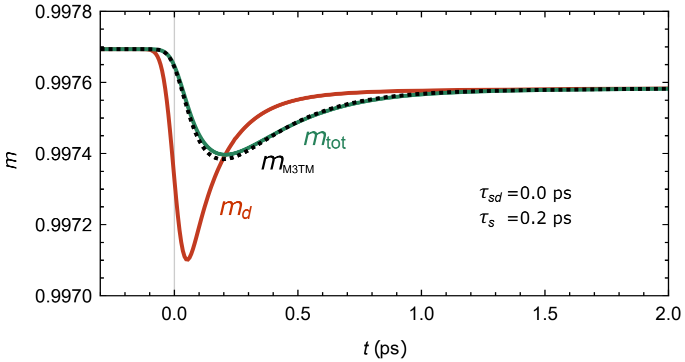

Figure 3.3: The *s*-*d* model in the limit of a strong *s*-*d* coupling ($\tau_{sd} \to 0$), compared to the microscopic three-temperature model (M3TM) [18]. The plot shows the magnetizations m_d (red) and m_{tot} (green) as a function of time after laser-pulse excitation at $t = 0$ with $P_0 = 0.1 \cdot 10^8\ \mathrm{Jm}^{-3}$ and $\sigma = 50$ fs. The remaining magnetic parameters are given by $T_C = 1000$ K and $\tau_s = 0.2$ ps. The dotted black line indicates the magnetization calculated with the basic M3TM (using demagnetization timescale $\tau_M = \tau_s = 0.2$ ps).

a rate given by τ_s^{-1}. This means that in the limit $\tau_{sd} \ll \tau_s$ the demagnetization rate strongly depends on τ_s. In the extreme case $\tau_{sd} \to 0$, which corresponds to an infinitely strong *s*-*d* interaction, m_d and μ_s are equilibrated instantaneously and their relation can be found by setting Eq. (3.7) equal to zero. Now the *d* and *s* electrons can be treated as a single spin system with magnetization m_{tot} of which the subsequent dynamics is governed by T_e and the additional spin-flip scattering processes of the *s* electrons. These additional scatterings include Elliott-Yafet electron-phonon scattering. Hence, in analogy with the M3TM [18], the system behaves as a single spin system with a characteristic demagnetization rate that is associated with Elliott-Yafet electron-phonon scattering. More specifically, in the low-fluence limit and having temperatures well below the Curie temperature, $m_{\mathrm{tot}}(t)$ converges to the magnetization dynamics from the M3TM, which is visualized in Fig. 3.3. Here, $m_d(t)$ and $m_{\mathrm{tot}}(t)$ follow from the *s*-*d* model using $P_0 = 0.1 \cdot 10^8\ \mathrm{Jm}^{-3}$ and $\tau_s = 0.2$ ps in the limit of a strong *s*-*d* coupling ($\tau_{sd} \to 0$). All other system parameters are kept equal to the calculations of Fig. 3.2. The dotted black line is the magnetization described by the M3TM for the same system, using the demagnetization timescale $\tau_M = \tau_s = 0.2$ ps, [2] which shows a clear overlap with the total magnetization m_{tot}.

---

[2] The timescale τ_M corresponds to the prefactor $\tau_M^{-1} = RT_p/T_C$ from the standard M3TM [18], and it taken as a constant.

On the other hand, in the limit $\tau_{sd} \gg \tau_s$ the spin accumulation relaxes efficiently and the bottleneck effect is negligible. In this limit, the magnetizations m_d and m_{tot} converge and their dynamics can be well described by Eq. (3.7) without the terms involving μ_s (similar to the limit $\tau_s \to 0$). Up to a prefactor, the magnetizations m_d and m_{tot} are now described by the same mathematical expression as in the M3TM. However, the physical origin of the ultrafast demagnetization is different.

In conclusion, in both regimes there is a clear relation with the M3TM. Nevertheless, in a real system it is expected that τ_{sd} and τ_s can be of the same order and a short-lived spin accumulation influences the magnetization dynamics. Finally, Fig. 3.2(c) shows that for a decreasing τ_s the spin accumulation becomes directly proportional to the temporal derivative of the magnetization m_d, as can be mathematically derived from Eq. (3.6) in the limit $\tau_s \to 0$. These typical curves for μ_s resemble the measurements in the experimental investigations of the optically generated spin currents at the interface of a ferromagnetic and nonmagnetic metal [65].

In the following sections, we investigate the role of spin transport on the demagnetization process.

3.4 F/N/F STRUCTURES: PARALLEL VERSUS ANTIPARALLEL

In the previous section, we showed that during laser-pulse excitation a spin accumulation is generated that counteracts the demagnetization process. In this section, we show that spin transport can act as an additional mechanism for removing this bottleneck effect. We model the experiments with collinear magnetic heterostructures [14, 16]. More specifically, we address the results presented in Ref. [14], in which a magnetic heterostructure is investigated that consists of two identical Co/Pt multilayers separated by a Ru spacer layer. The authors present a comparison of the demagnetization of the parallel and antiparallel aligned states of the heterostructure. The measurements showed that the antiparallel configuration has a larger demagnetization rate and amplitude, which can be explained by the generation of a spin current that enhances the demagnetization process. In the following, we will show that these results can be understood and reproduced by the presented *s*-*d* model.

Hence, we consider a system containing two identical ferromagnetic (F) layers with a nonmagnetic (N) layer in between. We further refer to this system as the F/N/F

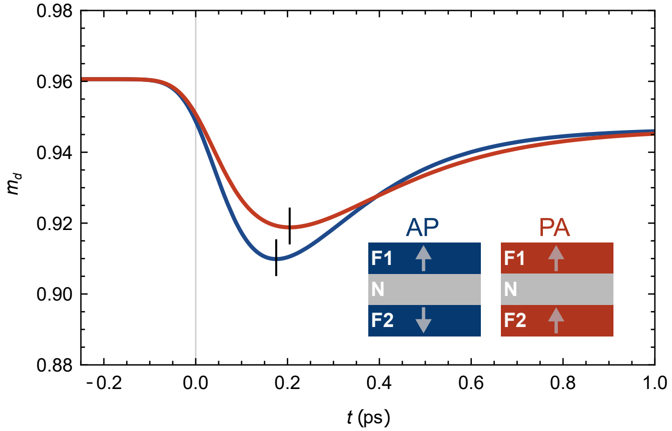

Figure 3.4: The laser-induced magnetization dynamics of the F/N/F structure in the antiparallel and parallel configurations, described by the s-d model. We used a low-energetic laser pulse with $P_0 = 1 \cdot 10^8$ Jm^{-3} and $\sigma = 70$ fs. The diagram shows the magnetization m_d of F layer 1 as a function of time. The color scheme indicates the specific configuration, as is indicated in the inset. The F layers have magnetic parameters $T_C = 600$ K, $\tau_{sd} = 0.1$ ps and $\tau_s = 0.02$ ps.

structure. We investigate the different laser-induced demagnetization rates for the parallel and antiparallel configurations of the F/N/F structure. The systems are schematically depicted in the inset of Fig. 3.4. By definition, F layer 1 is pointing up in both configurations, whereas F layer 2 is pointing in the up and down direction for the parallel and antiparallel configurations, respectively.

We assume all the layers to be very thin, such that we can take the temperature, magnetization, and spin accumulation homogeneous within each layer. We define a magnetization $m_{d,i}$ and $\mu_{s,i}$ for each F layer i. Because of the very small thickness of the N layer, we assume that the electron transport is in the ballistic regime. In that case, we can approximate that the spin transport in the nonmagnetic layer is purely driven by the difference in the spin accumulation of both F layers. Within these limits, the spin accumulations satisfy

$$\frac{d\mu_{s,i}}{dt} = \rho_{sd}\frac{dm_{d,i}}{dt} - \frac{\mu_{s,i}}{\tau_{s,i}} - \frac{\mu_{s,i} - \mu_{s,j}}{\tau_{\mathrm{B}}}, \tag{3.8}$$

where $i \neq j$ and $i, j \in \{1,2\}$. The last term, which is introduced phenomenologically, represents the spin transfer between the F layers driven by ballistic electron transport and enforces the spin accumulations to equilibrate. The prefactor is defined in terms of the timescale τ_B. We use that $\tau_B \sim 1$ fs based on the assumptions that the Fermi velocity is $v_F \sim 10^6$ ms^{-1} and the thickness of the N layer is $d_N \sim 1$ nm. Note that the transport term depends on the spin accumulation at the same time coordinate, i.e., the distinct F layers feel changes in the opposing layer instantaneously. In the real experiment there might be a small delay. However, we expect that this effect can be neglected in our calculations. Finally, we stress that this particular form of the transport term can only be used for two strictly identical F layers, as was the case in Ref. [14].

For the F layers we use the magnetic parameters $\tau_{\mathrm{sd}} = 0.1$ ps, $\tau_{\mathrm{s}} = 0.02$ ps and $T_C = 600$ K, which are approximated values corresponding to the Co/Pt multilayers used in the experiments [14]. Furthermore, we apply a low-energetic laser pulse with $P_0 = 1 \cdot 10^8$ Jm^{-3} and assume that the system is heated homogeneously. In this specific case, we set the pulse duration to $\sigma = 70$ fs [14]. For convenience, we still use the heat capacities and electron-phonon coupling constant of pure Cobalt [18].

The results are displayed in Fig. 3.4. The red and blue curves show the magnetization m_d of F layer 1 for the parallel and antiparallel configurations, respectively. It is verified that m_{tot} (not shown) behaves very similar. In agreement with the experiments, we observe a larger demagnetization rate and amplitude for the antiparallel configuration. This can be easily understood from the transport term in Eq. (3.8). In the parallel configuration we have $\mu_{s,1} = \mu_{s,2}$ at any time and the transport term vanishes. In contrast, for the antiparallel configuration we have $\mu_{s,1} = -\mu_{s,2}$, the transport does not vanish and behaves as an extra channel for angular momentum transfer. This extra channel assists the reduction of the spin accumulation, thereby leading to a larger demagnetization. Equivalently, in the antiparallel configuration the spin current in the nonmagnetic layer is nonzero and has exactly the correct polarization to enhance the demagnetization rates in both F layers. Finally, Fig. 3.4 also shows that the demagnetization curves of the two configurations converge at $t \sim 400$ fs, which is in agreement with the experiments [14].

In the next section, we analyze the temporal profile of the spin current generated in an F/N structure in the diffusive regime. Furthermore, we investigate the role of the thickness of the layers.

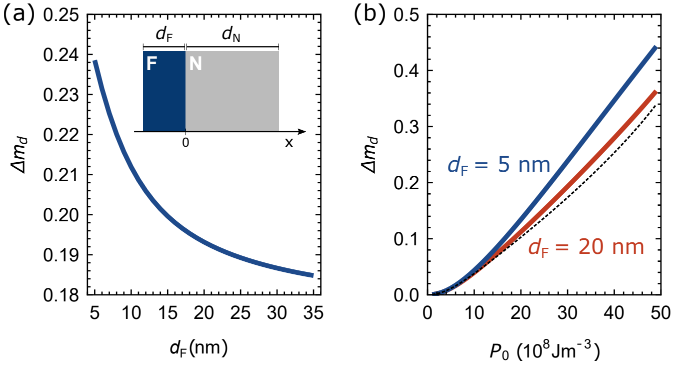

Figure 3.5: The laser-induced magnetization dynamics in an F/N structure. The magnetic parameters of the ferromagnetic layer are given by $\tau_{sd} = 0.3$ ps, $\tau_s = 0.2$ ps and $T_C = 1388$ K. (a) The maximum demagnetization Δm_d (averaged over the F layer) as a function of the ferromagnetic layer thickness d_F. The nonmagnetic layer thickness is set to $d_N = 200$ nm and we used $P_0 = 30 \cdot 10^8$ Jm^{-3}. The inset shows the system schematically. (b) The maximum demagnetization Δm_d as a function of P_0 for $d_F = 5$ nm (blue) and $d_F = 20$ nm (red). For both systems we have $d_N = 200$ nm. The black dashed line indicates the demagnetization of the bulk ferromagnet in the absence of an F/N interface ($d_F = \infty$ and $d_N = 0$).

3.5 F/N STRUCTURES: DIFFUSIVE SPIN TRANSPORT

Finally, we introduce diffusive spin transport in the simplified *s*-*d* model and we show that in magnetic heterostructures spin diffusion within the *s* electron system can significantly enhance the demagnetization rate. Here, we model a system consisting of a ferromagnetic (F) layer and a nonmagnetic (N) layer. In contrast to the similar approach reported in Refs. [65, 71, 72], we calculate the local magnetization dynamics dm_d/dt directly from the *s*-*d* model using Eq. (3.7), that serves as a source for spin-polarized *s* electrons via Eq. 3.6. Thereby, we can specifically address the mutual influence of the dynamics of the local magnetization m_d and spin accumulation μ_s, both as a function of position and time.

As indicated in the inset of Fig. 3.5(a), we define the thickness of the F layer and N layer as d_F and d_N, respectively. Spin transport is described in the diffusive regime, where both layers are treated on an equal footing [124]. For convenience, we assume that the system is heated homogeneously, i.e., there are no thermal gradients present. Hence, the demagnetization of the F layer is the only source of the spin current and there is no spin-dependent Seebeck effect included in this calculation.

It is assumed that the interface is transparent for spins, such that the spin accumulation is continuous at the interface. Imposing that there is no charge transport, the spin current density can be expressed as $j_s = -(\tilde{\sigma}/e^2)\partial\mu_s/\partial x$ [71, 124], with $\tilde{\sigma} = 2\sigma_\uparrow\sigma_\downarrow/(\sigma_\uparrow + \sigma_\downarrow)$ and $\sigma_{\uparrow,\downarrow}$ the spin-dependent electrical conductivity. Combining this with the continuity equations for spin up and spin down electrons [71, 126], gives that introducing diffusive spin transport in Eq. (3.6) leads to [71]

$$\frac{\partial\mu_s}{\partial t} - \frac{1}{\tilde{\nu}}\frac{\partial}{\partial x}\left[\frac{\tilde{\sigma}}{e^2}\frac{\partial\mu_s}{\partial x}\right] \quad = \quad \rho_{sd}\frac{\partial m_d}{\partial t} - \frac{\mu_s}{\tau_s}, \tag{3.9}$$

where all variables explicitly depend on the spatial coordinate x and we assumed that the system is homogeneous in the lateral directions. The interface is at $x = 0$. Here, $\tilde{\nu} = 2\nu_\uparrow\nu_\downarrow/(\nu_\uparrow + \nu_\downarrow)$ with $\nu_{\uparrow,\downarrow}$ the spin-dependent density of states in units per volume per energy ($\tilde{\nu} = D/V_{\text{at}}$). The N layer ($x > 0$) is characterised by $\sigma_\uparrow = \sigma_\downarrow$ and $\nu_\uparrow = \nu_\downarrow$, and the absence of the (s-d interaction) source term. Equation (3.9) is further simplified by imposing that $\tilde{\nu}$ is independent of x, where we have assumed that in the F layer $\nu_\uparrow \sim \nu_\downarrow$ and $\sigma_\uparrow \sim \sigma_\downarrow$. These choices are made for convenience and are consistent with the underlying assumptions of the s-d model, that the d electrons in the F layer do not contribute to the conductive properties of the material. In that case, Eq. (3.9) reduces to

$$\frac{\partial\mu_s}{\partial t} \quad = \quad \rho_{sd}\frac{\partial m_d}{\partial t} - \frac{\mu_s}{\tau_s} + \frac{\partial}{\partial x}\left[D_{\text{diff}}\frac{\partial\mu_s}{\partial x}\right], \tag{3.10}$$

with the diffusion coefficient $D_{\text{diff}} = \tilde{\sigma}/(\tilde{\nu}e^2)$ [71, 72]. Finally, we set the spin currents at the edges equal to zero $j_s(-d_F) = j_s(d_N) = 0$. Equation (3.10) is solved numerically, where we discretized the system using a finite difference method. Note that the spatial derivative of the diffusion coefficient D_{diff} is only nonzero at the interface. In these calculations, the F layer corresponds to pure Cobalt for which we use the diffusion coefficient $D_{\text{diff}} = 250\ \text{nm}^2\text{ps}^{-1}$[72]. Furthermore, we use $\tau_{sd} = 0.3$ ps and $\tau_s = 0.2$ ps. For the N layer we take $D_{\text{diff}} = 9500\ \text{nm}^2\text{ps}^{-1}$ and $\tau_s = 25$ ps, which correspond to the diffusion coefficient and spin-flip relaxation time for Copper [72].

Figure 3.5(a) shows a calculation of the F/N structure excited with a laser pulse with energy density $P_0 = 30 \cdot 10^8\ \text{Jm}^{-3}$ and pulse duration $\sigma = 50$ fs, where we used the heat capacities and electron-phonon coupling constant of Cobalt [18]. The diagram shows the maximum demagnetization $\Delta m_d = m_{d,0} - m_{d,\text{min}}$ (averaged over the F layer) as a function of the F layer thickness d_F, where $m_{d,0}$ is the initial (equilibrium) value of m_d, and $m_{d,\mathrm{min}}$ is the minimum of m_d after excitation. The thickness of the N layer is kept constant and set to $d_N = 200\,\mathrm{nm}$. It clearly shows that the demagnetization becomes larger when the F layer thickness decreases. Intuitively, the injection of spins into the nonmagnetic layers can enhance the demagnetization significantly as long as the F layer is relatively thin. This conclusion is corroborated by the results presented in Fig. 3.5(b), which shows the demagnetization Δm_d as a function of P_0. The results are plotted for $d_F = 5$ nm and $d_F = 20$ nm. The dashed line indicates the demagnetization of a bulk ferromagnet in the absence of an N layer ($d_F = \infty$ and $d_N = 0$). The calculations show that for a relatively thin F layer spin injection into the N layer can lead up to $\sim 30\%$ more demagnetization.

Now we discuss the dynamics of the injected spin current itself. We do this by calculating the spin accumulation at the outer edge of the N layer $\mu_s(d_N)$. The results are shown in Fig. 3.6, which displays the spin accumulation as a function of time for three different values of d_N that are given in the figure. The F layer thickness is kept constant at $d_F = 10\,\mathrm{nm}$. In agreement with the experimental investigations [65, 72], the diagram clearly shows that for an increasing d_N the minimum of $\mu_s(d_N)$ shifts in time and is reduced. This behavior can be understood from the diffusive character of the spin transport. Here, the temporal profile of $\mu_s(d_N)$ is highly sensitive to the specific material that composes the F layer and the corresponding effective parameters, as is expected from the experimental and numerical investigation using various materials for the F layer [72].

A more quantitative comparison with the experiments would require addressing spin transport beyond the diffusive regime and implementing a finite penetration depth of the laser pulse in the modeling. However, we focused our discussion on the dynamics that stems from the *s*-*d* interaction and we specifically investigate the role of μ_s independent of the thermal properties of the system. In that case, the model shows that in the presence of only the *s*-*d* interaction, the typical experimental observations can be explained and show a qualitative agreement [65, 72].

3.6 CONCLUSION AND DISCUSSION

In conclusion, we discussed a simplified *s*-*d* model that we used to describe laser-induced magnetization dynamics in magnetic heterostructures and to study the

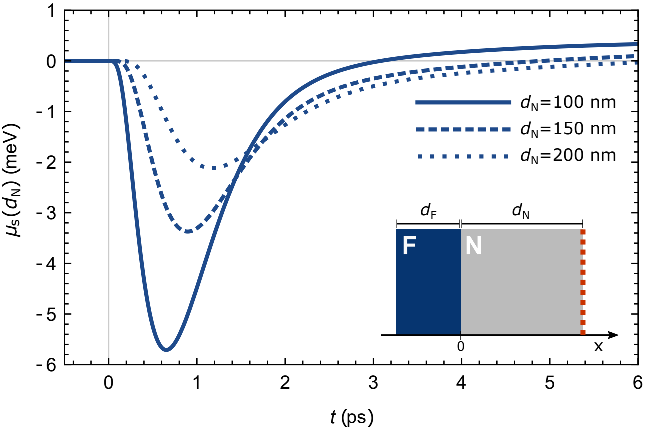

Figure 3.6: The diffusive spin current injected in the nonmagnetic (N) layer with thickness d_N, coupled to a ferromagnetic (F) layer with thickness d_F. The diagram shows the spin accumulation at the outer edge of the N layer (position $x = d_N$, indicated by the red dotted line in the inset) as a function of time. Furthermore, we set $P_0 = 20 \cdot 10^8$ Jm^{-3} and $\sigma = 50$ fs. The magnetic parameters are identical to the values used in Fig. 3.5. The line types indicate the results for three different values of d_N. The thickness of the F layer is kept constant and set to $d_F = 10$ nm.

interplay between local and nonlocal spin dynamics. The presented numerical calculations emphasize the critical role of the spin accumulation. During demagnetization a spin accumulation is created, which counteracts the demagnetization process. Both local spin-flip scatterings and spin transfer to a nonmagnetic layer can reduce this spin accumulation effectively and, depending on the system, can both play a dominant role in the characterization of the demagnetization rate. Importantly, the modeling shows that even in the absence of any other interaction, the *s*-*d* interaction could account for the typically observed ultrafast phenomena, such as being a driving force for laser-induced spin transport in magnetic heterostructures.

The presented analyses show that the simplified *s*-*d* model provides a versatile description of ultrafast magnetization dynamics, which converges to the M3TM for a strong *s*-*d* coupling and possesses the additional feature that spin transport can be included straightforwardly. However, one needs to keep in mind that the model is a simplified description of the underlying physics. As was earlier discussed, the *d* electrons are not perfectly localized. Moreover, the *d* electron spins are described using a Weiss model, i.e., spin-wave excitations are neglected. In a more complete description, the *d* electrons are described as a magnonic system and the *s*-*d* interaction corresponds to electron-magnon scattering [36]. That has the advantage that spin transport driven by magnon transport can be included, which is expected to give a nonnegligible contribution to the spin transport at the interface between a ferromagnetic and nonmagnetic metal [126]. In that case, the electronic and magnonic contribution to the spin transport can be treated on an equal footing by introducing a magnon chemical potential [118, 126], as will be discussed in Chapter 4. This description should allow for both chemical potential gradients and thermal gradients. For instance, thermal gradients can be induced by a finite penetration depth of the laser pulse and can drive a spin current via the electronic spin-dependent Seebeck effect [74, 75] and the magnonic spin Seebeck effect [133, 134]. Nevertheless, we expect that the dominant contributions to the dynamics can be well described by the simplified *s*-*d* model including spin transport and it provides a useful pathway to investigate the underlying physics.

4

MODELING ULTRAFAST DEMAGNETIZATION AND SPIN TRANSPORT: THE INTERPLAY OF SPIN-POLARIZED ELECTRONS AND THERMAL MAGNONS

We theoretically investigate laser-induced spin transport in metallic magnetic heterostructures using an effective spin transport description that treats itinerant electrons and thermal magnons on an equal footing. Electron-magnon scattering is included and taken as the driving force for ultrafast demagnetization. We assume that in the low-fluence limit the magnon system remains in a quasi-equilibrium, allowing a transient nonzero magnon chemical potential. In combination with the diffusive transport equations for the itinerant electrons, the description is used to chart the full spin dynamics within the heterostructure. In agreement with recent experiments, we find that in case the spin-current-receiving material includes an efficient spin dissipation channel, the interfacial spin current becomes directly proportional to the time derivative of the magnetization. Based on an analytical calculation, we discuss that other relations between the spin current and magnetization may arise in case the spin-current-receiving material displays inefficient spin-flip scattering. Finally, we discuss the role of (interfacial) magnon transport and show that, a priori, it cannot be neglected. However, its significance strongly depends on the system parameters.[1]

---

[1] This chapter has been published in *Physical Review B* [135].

4.1 Introduction

Rapidly heating magnetic heterostructures generates spin currents on ultrashort timescales [14, 15]. Their unique transient dynamics lead to fascinating physics in magnetic multilayers. For example, the spin current gives rise to the emission of THz electromagnetic radiation in magnetic heterostructures, resulting from the inverse spin Hall effect [68, 69]. Additionally, in noncollinear magnetic systems THz standing spin waves are excited by the spin-transfer torque [66, 67]. Moreover, the spin currents can play an assisting role in deterministic all-optical switching [100, 101, 103, 105, 130]. In other words, optically induced spin currents provide a versatile tool to manipulate magnetic systems on ultrashort timescales and pave the way towards future spintronic technologies.

Since the first experimental proof of subpicosecond demagnetization in laser-excited magnetic thin films [13], the physical origin of ultrafast spin dynamics remains a subject of heavy debate. Locally, possible mechanisms that drive ultrafast demagnetization are the direct coherent interactions between photons and spins [21, 22], and local spin dynamics as triggered by laser heating or excitation [13, 18, 23–26, 30–38]. The latter may involve an increased rate of various spin-flip scattering processes that eventually transfer angular momentum to the lattice degrees of freedom [54, 55]. Furthermore, nonlocal mechanisms can play a role, since spin angular momentum can be transported away from the ferromagnetic layer via the generated spin currents [14, 39, 62]. Different mechanisms have been proposed, such as superdiffusive spin transport [39, 73], and the spin-dependent Seebeck effect [74, 75].

In the last few years, multiple experimental and theoretical studies suggest that the local demagnetization and spin-current generation have the same physical origin [36, 65, 71, 72]. The main observation is that the rate at which spin-polarized electrons are generated is determined by the demagnetization rate [65]. This can be understood as being a result of electron-magnon scattering, which stems from the *s*-*d* interaction that couples local magnetic moments to itinerant spins [31, 36, 56, 58, 131]. Recent experiments support this view and show a direct proportionality between the spin current injected into a neighboring nonmagnetic layer and the temporal derivative of the magnetization [70, 136].

In this chapter, we investigate the relation between demagnetization and spin-current injection in rapidly heated magnetic heterostructures. We specifically address the role of thermal magnons and their interaction with electrons, and use a diffusive spin transport description that includes both spin-current carriers. It is assumed that electron-magnon scattering is the main driving force for ultrafast demagnetization. This scattering channel has been extensively investigated in theoretical studies [25, 31, 34, 36], and was phenomenologically introduced as a spin source in the electronic spin diffusion equation to model laser-induced spin transport [65, 71, 72]. Here, we additionally include magnon transport and it is treated on an equal footing with spin-dependent electron transport. This is achieved by allowing the magnon chemical potential to be nonzero [118]. The description has many similarities with the steady-state magnon transport calculations in magnetic insulators [118, 137, 138] and metallic heterostructures [126, 139]. Ref. [126] suggested that for thermally injected steady-state spin currents at metallic interfaces the magnonic contribution cannot be neglected a priori. Here, we develop this insight for the time-dependent scenario of rapidly heated magnetic heterostructures. Furthermore, we show that the interfacial spin current becomes directly proportional to the temporal derivative of the magnetization in the case the receiving material is an efficient spin sink. As we demonstrate analytically, other behavior is found when the latter displays inefficient spin-flip scattering.

This article starts with an overview of the used model in Section 4.2, specifically discussing the underlying assumptions. For a number of experimentally relevant cases, such as a Ni/Pt bilayer, we present numerical calculations for the local demagnetization and spin transport in Sections 4.3.1 and 4.3.2. In Section 4.3.3, we analytically derive the different relations between the interfacial spin current and the magnetization for the limiting cases of either efficient or inefficient spin dissipation in the spin-current-receiving material. Finally, we investigate the role of magnon transport and interfacial electron-magnon scattering in more detail.

4.2 Model

This section gives an overview of the diffusive model we use to investigate spin transport in rapidly heated magnetic heterostructures. Although other authors already presented the descriptions of spin-dependent electron transport [65, 71, 72, 107, 124, 140] and diffusive magnon transport [118, 137] separately, we here discuss them in a more integrated fashion. The presented overview strongly overlaps with the content of Sections 2.5 and 2.6 of the theoretical background chapter. Here, some additional details are presented, including the evaluated coupling constants and transport coefficients (Table 5.1), and the boundary conditions that specify the investigated magnetic heterostructure (Sec. 4.2.5). Since the later part of this chapter includes clear references to the essential formulas of the model section, readers familiar with the general description may skip this section and move to Section 4.3. Below, we start with reviewing the description of the thermal magnon system.

4.2.1 MAGNON DENSITY AND MAGNON ENERGY DENSITY

We define the magnonic system similar to Tveten et al. [36]. The standard Heisenberg model for a lattice of local spins, representing the relatively localized $3d$ electrons, is expressed in terms of bosonic creation and annihilation operators using the Holstein-Primakoff transformation [115]. Diagonalization by the use of Fourier transformations yields the magnon dispersion relation, which is approximated as being quadratic $\epsilon_q = \epsilon_0 + Aq^2$ [36]. Here, q is the magnitude of the magnon wave vector, ϵ_0 is the magnon gap and A is the spin-wave stiffness. The corresponding density of states is then given by $D(\epsilon) = \sqrt{\epsilon - \epsilon_0}/(4\pi^2 A^{3/2})$ [36, 116].

In contrast to Ref. [36], we assume the magnon system remains internally thermalized. As we only address the low-fluence limit, we argue that after the laser pulse excites the ferromagnet the magnon distribution function remains very similar to a Bose-Einstein function. On the ultrashort timescales that we are interested in, which can potentially be much shorter than the magnon lifetime, we should treat the magnon number as a (quasi-)conserved quantity. Then, the magnon number and total magnon energy compose two degrees of freedom. Hence, two parameters are needed to describe this system, the magnon temperature T_m and the magnon chemical potential μ_m. We stress that the chemical potential and temperature used here correspond to effective parameters, where effective refers to the fact that the magnon distribution function might slightly deviate from a Bose-Einstein distribution. The description is similar to Ref. [31], with the extension that it allows a nonzero chemical potential.

The magnon number density n_d and magnon energy density U_d are defined by the integrals [116]

$$n_d = \int_{\epsilon_0}^{\infty} d\epsilon D(\epsilon) n_{\mathrm{BE}}(\epsilon, \mu_m, T_m), \tag{4.1}$$

$$U_d = \int_{\epsilon_0}^{\infty} d\epsilon (\epsilon D(\epsilon)) n_{\mathrm{BE}}(\epsilon, \mu_m, T_m), \tag{4.2}$$

where $n_{\mathrm{BE}}(\epsilon, \mu_m, T_m)$ corresponds to the Bose-Einstein distribution

$$n_{\mathrm{BE}}(\epsilon, \mu_m, T_m) = \frac{1}{e^{(\epsilon-\mu_m)/(k_B T_m)} - 1}. \tag{4.3}$$

Note that in Eqs. (4.1)-(4.2), we extended the upper boundary of the energy integration to infinity, which is valid under the condition that the temperature remains much lower than the Curie temperature $T_m \ll T_C$. Now n_d and U_d can be expressed in terms of a polylogarithm [117]. We assume that deviations in the magnon temperature are small compared to the ambient temperature T_0, i.e., $(T_m - T_0) \ll T_0$. Furthermore, we assume $\mu_m/(k_B T_0) \ll 1$ and $\epsilon_0/(k_B T_0) \ll 1$. The polylogarithm can be expressed in terms of a series expansion for the given small factors. We eliminate the factors higher than linear order, and we stress that the mathematical expressions presented in the remainder of this section are only valid for small perturbations. Details about this approximation are given in Appendix 4.A (on page 110). Following this procedure, the temporal derivative of the magnon density and the magnon energy density are expressed as

$$\frac{\partial n_d}{\partial t} = C_{n,\mu}\dot{\mu}_m + C_{n,T}\dot{T}_m, \tag{4.4}$$

$$\frac{\partial U_d}{\partial t} = C_{U,\mu}\dot{\mu}_m + C_{U,T}\dot{T}_m. \tag{4.5}$$

The definitions of the prefactors are given in Table 4.1. The prefactor $C_{n,\mu}$ requires special attention, since it depends on the magnon chemical potential. As explained in Appendix 4.A, the latter is essential to describe the correct behavior as a function of chemical potential and is a direct consequence of the bosonic nature of magnons. As the chemical potential approaches the magnon gap, the magnon density grows increasingly strong, corresponding to the divergence of $C_{n,\mu}$. For physically relevant values of the magnon gap this effect is nonnegligible. Therefore, the model includes one nonlinear term arising from $C_{n,\mu}$.

4.2.2 SPIN AND ENERGY TRANSFER RATE BY ELECTRON-MAGNON SCATTERING

Here, we give expressions for the spin transfer and energy transfer between the magnonic system and the itinerant electron system, which are driven by electron-magnon scattering. Starting from the *s-d* Hamiltonian [36], the electron-magnon scattering rate is calculated using Fermi's golden rule [31, 36, 117]. It is assumed that the itinerant electron system is instantaneously thermalized and parametrized by the spin accumulation μ_s and electron temperature T_e. In the limit that the Fermi energy is the largest energy scale in the model, the angular momentum transfer rate I_{sd} (in units of $\hbar$) and energy density transfer rate U_{sd} can be expressed as [36, 116, 117]

$$\begin{aligned} I_{sd} &= \int_{\epsilon_0}^{\infty} d\epsilon \frac{\Gamma(\epsilon)}{\hbar} D(\epsilon)(\epsilon - \mu_s) \\ &\quad \times (n_{\mathrm{BE}}(\epsilon, \mu_s^F, T_e) - n_{\mathrm{BE}}(\epsilon, \mu_m, T_m)), \end{aligned} \tag{4.6}$$

$$\begin{aligned} U_{sd} &= \int_{\epsilon_0}^{\infty} d\epsilon \frac{\Gamma(\epsilon)}{\hbar} (\epsilon D(\epsilon))(\epsilon - \mu_s) \\ &\quad \times (n_{\mathrm{BE}}(\epsilon, \mu_s^F, T_e) - n_{\mathrm{BE}}(\epsilon, \mu_m, T_m)). \end{aligned} \tag{4.7}$$

For simplicity, the energy-dependent scattering rate coefficient $\Gamma(\epsilon)$ is assumed to be constant and replaced by the dimensionless effective coefficient Γ_0. The constant Γ_0 can be directly related to the effective Gilbert damping [116]. We note that the presented expressions for the scattering rate, such as Eqs. (4.6)-(4.7), require the electronic density of states to be approximately constant in the vicinity of the Fermi level. This approximation is not generally valid and may affect the dynamics [141]. However, in the linear regime corrections can be adopted in the effective prefactors, and therefore do not alter the dynamics discussed in this chapter.

Following the same procedure as simplifying the magnon densities, the transfer rates can be expressed as

$$I_{sd} = \frac{g_{n,\mu}}{\hbar}(\mu_s - \mu_m) + \frac{g_{n,T}}{\hbar}(T_e - T_m), \tag{4.8}$$

$$U_{sd} = \frac{g_{U,\mu}}{\hbar}(\mu_s - \mu_m) + \frac{g_{U,T}}{\hbar}(T_e - T_m). \tag{4.9}$$

The coupling constants are summarized again in Table 4.1, which are all expressed in terms of the scattering rate coefficient Γ_0, the spin-wave stiffness A, and the ambient temperature T_0. The factors $\zeta(z)$ and $\Gamma(z)$ correspond to the Riemann zeta function and Gamma function, respectively.

4.2.3 DIFFUSIVE MAGNON TRANSPORT

Here, we discuss the description of diffusive magnon transport. We follow exactly the same steps as the model for diffusive magnon transport in magnetic insulators [118, 137]. As discussed below, applying this in ferromagnetic metals requires some extra comments [126].

To treat the magnons within a local-density approximation it is needed that the characteristic length scale of the system, which in this case is the thickness of the ferromagnetic layer, is much larger than the thermal de Broglie wavelength. Up to a numerical prefactor the latter wavelength is of the order $\lambda_{\mathrm{th}} \sim (A/(k_B T_0))^{1/2}$ [118]. For Ni this estimate gives $\lambda_{\mathrm{th}} \sim 0.4$ nm at room temperature, using the numerical values listed in Table 4.2 (on page 110). Secondly, to be able to describe the transport as diffusive the magnon mean-free path $\lambda_{\mathrm{mfp}} \sim (A k_B T_0)^{1/2} \tau_{\mathrm{tr},m}/\hbar$ should be much smaller than the thickness of the ferromagnetic system. The magnon momentum relaxation time $\tau_{\mathrm{tr},m}$ is discussed below. For Ni we estimate that the mean-free path is of the order $\lambda_{\mathrm{mfp}} \sim 1.5$ nm. Despite that these requirements are only weakly satisfied for an ultrathin ferromagnetic layer, we assume that the qualitative behavior is predicted correctly by the diffusive magnon transport description.

Within these limits, the magnon current density and the magnon heat current density can be expressed as [118]

$$j_m = -\frac{\sigma_m}{e^2}\frac{\partial \mu_m}{\partial x} - \frac{L}{T_0}\frac{\partial T_m}{\partial x}, \tag{4.10}$$

$$j_{Q,m} = -L\frac{\partial \mu_m}{\partial x} - \kappa_m \frac{\partial T_m}{\partial x}, \tag{4.11}$$

where σ_m is the magnon conductivity, L is the spin Seebeck coefficient [133, 137], and κ_m is the magnon heat conductivity. The transport coefficients are given in Table 4.1. To a good approximation, all transport coefficients are linear in the magnon transport timescale $\tau_{\mathrm{tr},m}$, which corresponds to the magnon momentum relaxation time. This timescale is at least as short as the electron-magnon scattering time, which is naturally related to the observed demagnetization timescale. Therefore, the latter is an upper bound for $\tau_{\mathrm{tr},m}$. Since other contributing scattering processes

Table 4.1: Model coefficients expressed in terms of the magnon transport timescale $\tau_{\mathrm{tr},m}$, spin-wave stiffness A, and the bulk electron-magnon scattering rate coefficient Γ_0 [118]. The interfacial scattering rate coefficients can be found by the substitution $\Gamma_0 \to g_{\uparrow\downarrow}/(\pi s)$.

Symbol	Expression
$C_{n,\mu}$	$\frac{(k_B T_0)^{1/2}\Gamma(3/2)}{4\pi^2 A^{3/2}}\left(\Gamma(1/2)\left(\frac{\epsilon_0-\mu_m}{k_B T_0}\right)^{-1/2}+\zeta(1/2)\right)$
$C_{n,T}$	$\frac{(k_B T_0)^{1/2}\Gamma(3/2)}{4\pi^2 A^{3/2}}(3/2)\zeta(3/2)k_B$
$C_{U,\mu}$	$\frac{(k_B T_0)^{3/2}\Gamma(5/2)}{4\pi^2 A^{3/2}}\zeta(3/2)$
$C_{U,T}$	$\frac{(k_B T_0)^{3/2}\Gamma(5/2)}{4\pi^2 A^{3/2}}(5/2)\zeta(5/2)k_B$
σ_m	$\frac{e^2\tau_{\mathrm{tr},m}(k_B T_0)^{3/2}\Gamma(3/2)\zeta(3/2)}{2\pi^2\hbar^2 A^{1/2}}$
L	$\frac{\tau_{\mathrm{tr},m}(k_B T_0)^{5/2}(5/2)\Gamma(5/2)\zeta(5/2)}{3\pi^2\hbar^2 A^{1/2}}$
κ_m	$\frac{\tau_{\mathrm{tr},m}(k_B T_0)^{5/2}(7/2)\Gamma(7/2)\zeta(7/2)}{3\pi^2\hbar^2 A^{1/2}}k_B$
$g_{n,\mu}$	$\frac{\Gamma_0(k_B T_0)^{3/2}\Gamma(5/2)\zeta(3/2)}{4\pi^2 A^{3/2}}$
$g_{n,T}$	$\frac{\Gamma_0(k_B T_0)^{3/2}\Gamma(5/2)(5/2)\zeta(5/2)}{4\pi^2 A^{3/2}}k_B$
$g_{U,\mu}$	$\frac{\Gamma_0(k_B T_0)^{5/2}\Gamma(7/2)\zeta(5/2)}{4\pi^2 A^{3/2}}$
$g_{U,T}$	$\frac{\Gamma_0(k_B T_0)^{5/2}\Gamma(7/2)(7/2)\zeta(7/2)}{4\pi^2 A^{3/2}}k_B$

are expected to be less efficient, we assume in the remainder of this article that the timescale $\tau_{\mathrm{tr},m}$ is of the same order of magnitude as the demagnetization time. For instance, we use $\tau_{\mathrm{tr},m} = 0.1$ ps, corresponding to the typical order of magnitude of the demagnetization time in ferromagnetic transition metals.

To clarify the notation we give the continuity equation for the magnon density and magnon energy density

$$\frac{\partial n_d}{\partial t}+\frac{\partial j_m}{\partial x} = I_{sd}, \tag{4.12}$$

$$\frac{\partial U_d}{\partial t}+\frac{\partial j_{Q,m}}{\partial x} = U_{sd}. \tag{4.13}$$

Filling in Eqs. (4.4)-(4.5), Eqs. (4.8)-(4.9), and Eqs. (4.10)-(4.11), gives the full expressions that are used in the calculations presented in the later sections of this article. Now we move on to the electronic system.

4.2.4 THE CONTINUITY EQUATIONS FOR THE ELECTRONIC SYSTEM

We assume that the out-of-equilibrium spin density δn_s in the itinerant electron system can be parametrized by $\delta n_s = \tilde{\nu}_{\mathrm{F}} \mu_s^{\mathrm{F}}$, where $\tilde{\nu}_{\mathrm{F}} = 2\nu_\uparrow \nu_\downarrow/(\nu_\uparrow + \nu_\downarrow)$ is the spin-averaged density of states evaluated at the Fermi energy [2]. Expressed in terms of the spin accumulation, the continuity equations for the spin and energy in the ferromagnetic layer are given by [36, 71]

$$\tilde{\nu}_{\mathrm{F}} \frac{\partial \mu_s^{\mathrm{F}}}{\partial t} + \frac{\partial j_{s,e}^{\mathrm{F}}}{\partial x}, \quad = \quad -\frac{\tilde{\nu}_{\mathrm{F}} \mu_s^{\mathrm{F}}}{\tau_{s,\mathrm{F}}} - 2I_{sd}, \tag{4.14}$$

$$C_e \frac{\partial T_e^{\mathrm{F}}}{\partial t} + \frac{\partial j_{Q,e}^{\mathrm{F}}}{\partial x} \quad = \quad g_{ep}(T_p^{\mathrm{F}} - T_e^{\mathrm{F}}) - U_{sd} + P(t,x). \tag{4.15}$$

The spin current $j_{s,e}^{\mathrm{F}}$ and electronic heat current $j_{Q,e}^{\mathrm{F}}$ are given below. The term proportional to $\tau_{s,\mathrm{F}}^{-1}$, which is introduced phenomenologically [36], represents the additional spin-flip scattering processes. The latter includes Elliott-Yafet spin-flip scattering processes and is the main spin dissipation channel for the combined electronic and magnonic system [36]. C_e corresponds to the electron heat capacity, g_{ep} corresponds to the electron-phonon coupling constant and T_p^{F} corresponds to the phonon temperature. The function $P(t,x)$ represents the laser-excitation profile, which will be further specified when the calculations are presented.

Imposing that there is no charge transport, the electronic spin current $j_{s,e}^{\mathrm{F}}$ and heat current $j_{Q,e}^{\mathrm{F}}$ can be expressed as [71, 124]

$$j_{s,e}^{\mathrm{F}} \quad = \quad -\frac{\tilde{\sigma}}{e^2} \frac{\partial \mu_s^{\mathrm{F}}}{\partial x} - \frac{\tilde{\sigma}}{e^2} S_s \frac{\partial T_e^{\mathrm{F}}}{\partial x}, \tag{4.16}$$

$$j_{Q,e}^{\mathrm{F}} \quad = \quad -\frac{\tilde{\sigma}}{2e^2} \Pi_s \frac{\partial \mu_s^{\mathrm{F}}}{\partial x} - \kappa_e \frac{\partial T_e^{\mathrm{F}}}{\partial x}, \tag{4.17}$$

where $\tilde{\sigma} = 2\sigma_\uparrow \sigma_\downarrow/(\sigma_\uparrow + \sigma_\downarrow)$ is the spin-averaged electrical conductivity, S_s is the

---

[2] For convenience, we neglected the dynamic splitting of the spin up and spin down band due to changes in the magnon density [36]. As discussed in Ref. [36] and Sec. 2.5, this can be included straightforwardly by introducing the constant ρ_{sd} in the rate equations.

spin-dependent Seebeck coefficient [124], Π_s is the spin-dependent Peltier coefficient ($\Pi_s = T_0 S_s$), and κ_e is the electronic heat conductivity. The expressions for the dynamics of the electronic system within the nonmagnetic layer can be found by replacing all indices F → N and removing the spin-dependent quantities (including I_{sd} and U_{sd}).

Finally, for the phonon system we take a highly simplified approach. For convenience, phonon heat transport is not included. Furthermore, in the description for the local phonon temperature a heat sink is included that dissipates energy out of the phonon system within a timescale of 20 ps. The latter is introduced to make sure the system relaxes to its initial temperature on a reasonable timescale. We stress that the exact description of the phonon system does not play a direct role in the discussions presented in this chapter.

4.2.5 BOUNDARY CONDITIONS AND SYSTEM SPECIFICATIONS

Finally, we have to specify the boundary conditions. We define the ferromagnetic layer on the domain $x \in [-d_\mathrm{F}, 0]$, where d_F is the thickness of the ferromagnetic layer. At the left end of the system we impose insulating boundary conditions, setting all currents to zero.

$$j_m(-d_\mathrm{F}) = j_{Q,m}(-d_\mathrm{F}) \quad = \quad 0. \tag{4.18}$$

$$j^\mathrm{F}_{s,e}(-d_\mathrm{F}) = j^\mathrm{F}_{Q,e}(-d_\mathrm{F}) \quad = \quad 0. \tag{4.19}$$

Secondly, at the interface, which is positioned at $x = 0$, the total spin current and total heat current should be continuous.

$$j^\mathrm{F}_{s,e}(0) + 2j_m(0) \quad = \quad j^\mathrm{N}_{s,e}(0), \tag{4.20}$$

$$j^\mathrm{F}_{Q,e}(0) + j_{Q,m}(0) \quad = \quad j^\mathrm{N}_{Q,e}(0), \tag{4.21}$$

where the superscript N indicates the quantities in the nonmagnetic layer. The factor 2 arises from the fact that a magnon carries twice as much spin angular momentum as an electron. We write the interfacial electronic spin current and heat current as

$$j_{s,e}^{\mathrm{F}}(0) = \frac{g_1}{\hbar}(\mu_s^{\mathrm{F}} - \mu_s^{\mathrm{N}}) + \frac{g_1}{\hbar} S_s^i (T_e^{\mathrm{F}} - T_e^{\mathrm{N}}), \tag{4.22}$$

$$j_{Q,e}^{\mathrm{F}}(0) = \frac{g_1}{\hbar}\frac{T_0 S_s^i}{2}(\mu_s^{\mathrm{F}} - \mu_s^{\mathrm{N}}) + \kappa_e^i (T_e^{\mathrm{F}} - T_e^{\mathrm{N}}), \tag{4.23}$$

where the prefactor g_1 is determined by the interfacial electrical conductance [72] and all variables are evaluated at $x = 0$. The interfacial electronic heat conductivity is given by κ_e^i. The factor S_s^i corresponds to the spin-dependent Seebeck coefficient of the interface.

The interfacial magnon current and magnon heat current are determined by the interfacial electron-magnon scattering rate [36, 126]. The linearized expressions for the scattering rate can be found by replacing $\Gamma_0 \rightarrow g_{\uparrow\downarrow}/(\pi s)$ in Eqs. (4.8)-(4.9) [36, 116, 117], where $g_{\uparrow\downarrow}$ is the real part of the spin-mixing conductance and s is the saturation spin density. In other words, the interfacial magnon current $j_m(0)$ and magnon heat current $j_{Q,m}(0)$ are expressed as

$$j_m(0) = \frac{g_{n,\mu}^i}{\hbar}(\mu_m - \mu_s^{\mathrm{N}}) + \frac{g_{n,T}^i}{\hbar}(T_m - T_e^{\mathrm{N}}), \tag{4.24}$$

$$j_{Q,m}(0) = \frac{g_{U,\mu}^i}{\hbar}(\mu_m - \mu_s^{\mathrm{N}}) + \frac{g_{U,T}^i}{\hbar}(T_m - T_e^{\mathrm{N}}). \tag{4.25}$$

The second term in Eq. (4.24), proportional to $g_{n,T}^i$, corresponds to the interfacial spin Seebeck effect [134].

Finally, the nonmagnetic layer is defined on the domain $x \in [0, d_{\mathrm{N}}]$, where d_{N} is the thickness of the nonmagnetic layer. At the outer interface $x = d_{\mathrm{N}}$ we impose the boundary conditions

$$j_{s,e}^{\mathrm{N}}(d_{\mathrm{N}}) = \frac{g_2}{\hbar}\mu_s^{\mathrm{N}}(d_{\mathrm{N}}), \tag{4.26}$$

$$j_{Q,e}^{\mathrm{N}}(d_{\mathrm{N}}) = 0. \tag{4.27}$$

For convenience, we assume that this interface is a heat insulator. In contrast, we allow the interface to be permeable for spins. The latter is parametrized by the constant g_2. In case $g_2 \neq 0$, spins are allowed to leak out of the bilayer. It is assumed that the interface is connected to an ideal spin sink, which corresponds to a vanishing μ_s for $x > d_{\mathrm{N}}$ and yields Eq. (4.26). The latter could for example be realized by a secondary magnetic layer that is perpendicularly oriented to the other magnetic layer, as is the case in noncollinear magnetic heterostructures [136].

In the following, we will start with discussing the situation where $g_2 = 0$, corresponding to completely insulating boundary conditions. Later, we will investigate the situation $g_2 \neq 0$ in more detail.

4.3 RESULTS

In this section, we present the numerical solutions to the equations discussed in the previous sections. Specifically, Eqs. (4.12)-(4.13) are solved for the magnonic system in the ferromagnetic layer, and Eqs. (4.14)-(4.15) are solved for the electronic system throughout the complete heterostructure. Furthermore, the boundary conditions as discussed in Section 4.2.5 are imposed. First, we investigate the dynamics of the local thermodynamical parameters: temperatures, chemical potentials, and the magnetization.

4.3.1 TEMPERATURE, CHEMICAL POTENTIAL, AND MAGNETIZATION DYNAMICS

We start with calculating the laser-induced response of a Ni(5 nm)/Pt(3 nm) bilayer with insulating boundary conditions at the outer interfaces. Specifically, we first investigate the dynamics of the local thermodynamical parameters within the Ni layer. To model laser heating we assume that the spatial and temporal profile of the laser pulse can be approximated by

$$P(t,x) = \frac{P_0}{\sigma\sqrt{\pi}} \exp\left[-\frac{x+d_{\mathrm{F}}}{\tilde{\lambda}}\right] \exp\left[-\frac{t^2}{\sigma^2}\right], \tag{4.28}$$

where P_0 is the absorbed laser pulse energy density and σ determines the pulse duration, which is set to 70 fs. The laser pulse penetration depth is given by $\tilde{\lambda}$ and set to a typical value of $\tilde{\lambda} = 15$ nm. For simplicity, we assume that the laser pulse absorption in the Ni and Pt layer is equally efficient and we use $P_0 = 0.15 \times 10^8$ Jm^{-3}. All other system parameters are given in Table 4.2 and 4.3.

Figures 4.1(a)-(c) show the response of the magnetic bilayer to laser heating. All plotted variables are spatially averaged over the range of the ferromagnetic (Ni) layer. Figure 4.1(a) shows the rapid increase of the electron temperature T_e^{F} and the

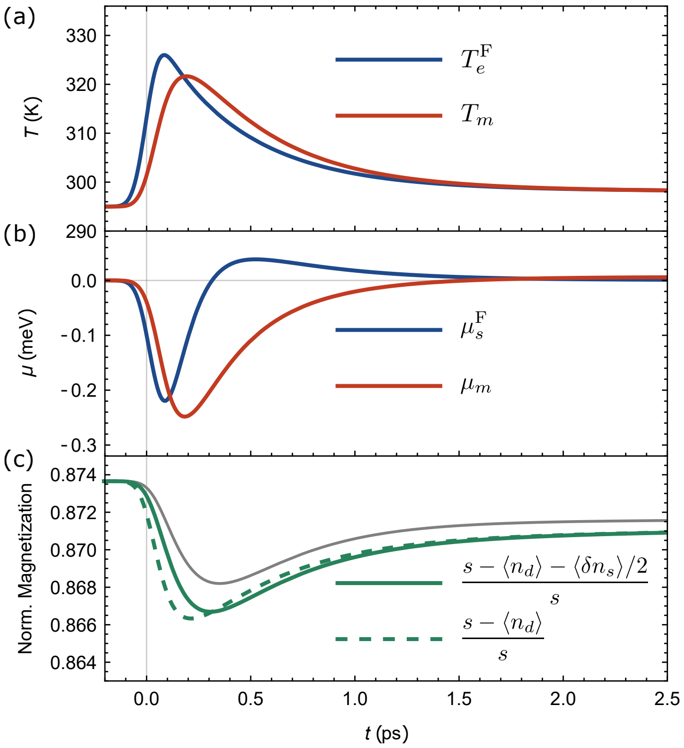

Figure 4.1: Laser-induced dynamics of the temperatures, chemical potentials, and magnetization within the Ni layer of a Ni(5 nm)/Pt(3 nm) bilayer. The quantities are plotted as a function of t after laser-pulse excitation at $t = 0$, and are spatially averaged over the ferromagnetic (Ni) layer. (a) The electron temperature (blue) and magnon temperature (red). (b) The spin accumulation (blue) and magnon chemical potential (red). (c) The normalized magnetization. The solid green line indicates the changes of the total spin density. The dashed green line indicates the case that only changes in magnon density are taken into account. The thin gray line represents the magnetization in the case of an isolated Ni layer, in the absence of a neighboring Pt layer.

response of the magnon temperature T_m driven by electron-magnon scattering. This transient behavior of the magnon temperature yields a rapid increase in the magnon density. Figure 4.1(b) displays the laser-induced dynamics of the spin accumulation (blue) and magnon chemical potential (red). The spin accumulation shows the typical bipolar behavior, in analogy with previous calculations and experimental observations of the generated spin-polarized electrons [65, 71, 72, 131]. The magnon chemical potential shows different behavior, it can be shown that this is related to the equilibration of the chemical potentials playing a minor role and the magnon chemical potential opposes the dynamics of the magnon temperature.

Finally, Fig. 4.1(c) shows the normalized magnetization as a function of time. The magnetization requires special attention. In this chapter, it is assumed that the magnetic signal measured in the experiments is determined by the total spin density. The magnetization is defined as

$$m = \frac{s - \langle n_d \rangle - \langle \delta n_s \rangle / 2}{s} = \frac{s - \langle n_{\mathrm{tot}} \rangle}{s}, \tag{4.29}$$

which is normalized with respect to the saturation spin density $s = S/a^3$, where S is the spin per atom (in units of $\hbar$) and a the lattice constant. The bracket notation indicates spatial averaging over the ferromagnetic layer.

The solid green curve in Fig. 4.1(c) shows the typical ultrafast demagnetization behavior and critically depends on the spin-flip scattering rate $\tau_{s,\mathrm{F}}$. Upon excitation, electron-magnon scattering generates a net change of the magnon density and spin density in the itinerant spin system. However, electron-magnon scattering conserves the total spin angular momentum. The Elliott-Yafet spin-flip processes originating from spin-orbit coupling enable changes of the total spin density and therefore demagnetization of the combined spin system [19, 34, 36, 43]. In the end, spin is efficiently transferred to the lattice, as was recently demonstrated experimentally [54, 55].

We stress that this interpretation of the magnetization remains a point of discussion and its relation to the magnetic signal in the experiments strongly depends on the probing method. Therefore, we have plotted the dynamics of the magnon density $\langle n_d \rangle$ separately. The latter is normalized with respect to the saturation spin density s and indicated by the dashed green line in Fig. 4.1(c), emphasizing the subpicosecond generation of magnons [46]. As will be discussed in the next section, the used interpretation of the magnetization, as being determined by the sum of the magnon density and the itinerant electron spin density, is strongly supported by the investigation of the relation between the interfacial spin current and the demagnetization rate.

Finally, the thin gray line in Fig. 4.1(c) represents the calculation of the magnetization in case the Pt layer is absent and spin can not be transported out of the Ni layer. The latter emphasizes that the demagnetization is primarily driven by local spin dissipation. However, in the presence of a nonmagnetic layer (solid green curve), interfacial spin transfer significantly contributes to the demagnetization rate.

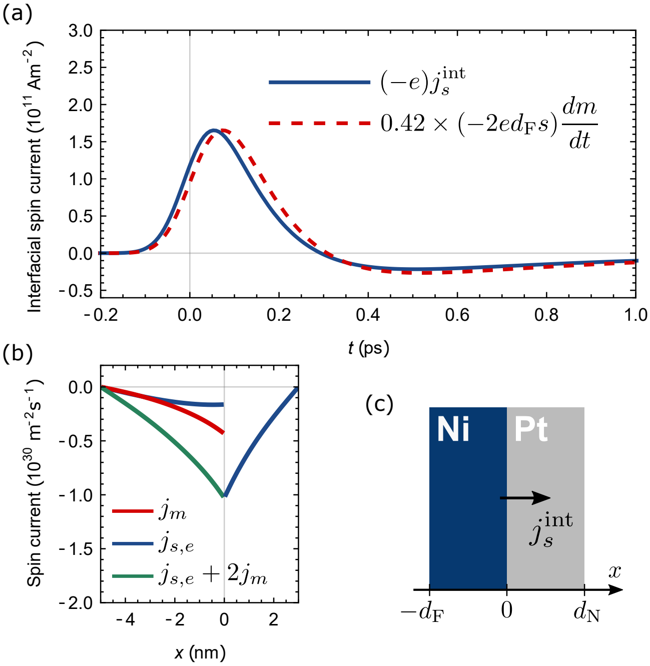

Figure 4.2: Laser-induced spin transport in a Ni(5 nm)/Pt(3 nm) bilayer with insulating boundary conditions. (a) The interfacial spin current (blue) as a function of time t after laser-pulse excitation at $t = 0$. The dashed red line indicates the temporal derivative of the magnetization, scaled by a prefactor that is fitted to the amplitude of the spin current. (b) Distinct spin current contributions as a function of spatial coordinate x, evaluated at $t = 0.05$ ps. Blue indicates the electronic contribution, red the magnonic contribution, and green the total. (c) Schematic overview of the system.

4.3.2 SPIN TRANSPORT IN MAGNETIC HETEROSTRUCTURES

In this section, we calculate the spin current that arises from laser exciting the magnetic heterostructure corresponding to the results of Fig. 4.1. As given by Eq. (4.20), we define the total interfacial spin current at $x = 0$ as $j_s^{\mathrm{int}} = j_{s,e}^{\mathrm{F}}(0) + 2j_m(0)$, where $j_{s,e}^{\mathrm{F}}(0)$ is the spin current carried by the conduction electrons and $j_m(0)$ is the interfacial magnon current. We again focus on a Ni(5 nm)/Pt(3 nm) bilayer with insulating boundary conditions, as schematically depicted in Fig. 4.2(c).

The blue line in Fig. 4.2(a) shows the results from calculating j_s^{int} by numerically solving the set of equations as presented in Section 4.2. The material parameters and description of the laser pulse are identical to the previous section. The result clearly shows the bipolar behavior of the interfacial spin current, yielding a transient oscillation within the THz regime. The red dashed curve indicates the temporal derivative of the magnetization, scaled by a prefactor that is fitted to the amplitude of the spin current. The comparison indicates a qualitative agreement with the experiments [70, 136], as a close relation is expected between the spin current injected into the nonmagnetic layer and the temporal derivative of magnetization. The visible phase shift is interesting in itself, but smaller than the temporal resolution of 40 fs in the experiment in Ref. [70].

Figure 4.2(b) shows the different contributions to the spin current as a function of position x, calculated at $t = 0.05$ ps. The figure suggests that for the used parameters magnon transport and spin-polarized electron transport comparably contribute to the total spin current within the bulk of the ferromagnet. One should keep in mind that their ratio strongly depends on the specific time instance and system parameters. The spin transport by electrons is mainly driven by bulk electron-magnon scattering, which generates negatively polarized spins that are transferred towards the receiving layer via spin diffusion. The negative magnon current in Fig. 4.2(b) indicates thermal magnons being created at the interface by electron-magnon scattering. Consequently, a flow of magnons towards the negative x direction is generated. The magnon current $j_m(0)$ is mainly determined by the temperature difference $T_m - T_e^{\mathrm{N}}$ at the interface, which corresponds to the interfacial spin Seebeck effect [134]. In contrast to our work, the latter is typically neglected in the models for spin transport in metallic magnetic heterostructures [71, 72].

In the following section, we investigate the relation between the interfacial spin current and the magnetization analytically and specifically address the role of (interfacial) magnon transport.

4.3.3 RELATION BETWEEN THE INTERFACIAL SPIN CURRENT AND DEMAGNETIZATION

In this section, we analytically investigate the relation between the interfacial spin current and the demagnetization. Integrating Eqs. (4.12) and (4.14) over the thickness of the ferromagnetic layer and adding up the results yields an expression for the interfacial spin current

$$j_s^{\mathrm{int}}(t) = -2d_{\mathrm{F}}\frac{d\langle n_{\mathrm{tot}}\rangle}{dt} - d_{\mathrm{F}}\frac{\langle \delta n_s\rangle}{\tau_{s,\mathrm{F}}}, \tag{4.30}$$

where the brackets indicate spatial averaging over the ferromagnetic layer. Equation (4.30) simply follows from spin angular momentum conservation, as the total spin density $\langle n_{\mathrm{tot}} \rangle$ can only be changed by either spin transport or local spin dissipation. In the limit where the latter is absent $\tau_{s,\mathrm{F}} \to \infty$, spin transport and demagnetization couple trivially. For the systems of interest, where we have a subpicosecond $\tau_{s,\mathrm{F}}$, a more cumbersome calculation is required to eliminate the local spin dissipation term from Eq. (4.30).

In order to do this, we solve the spin diffusion equation for the full heterostructure. In the frequency domain, we write

$$\begin{aligned} \frac{\partial^2 \mu_s^{\mathrm{F}}(\omega,x)}{\partial x^2} &= \kappa_{\mathrm{F}}(\omega)^2 \mu_s^{\mathrm{F}}(\omega,x) + \frac{2\tau_{s,\mathrm{F}} I_{sd}(\omega,x)}{\tilde{\nu}_{\mathrm{F}} l_{s,\mathrm{F}}^2}, && (4.31) \\ \frac{\partial^2 \mu_s^{\mathrm{N}}(\omega,x)}{\partial x^2} &= \kappa_{\mathrm{N}}(\omega)^2 \mu_s^{\mathrm{N}}(\omega,x), && (4.32) \end{aligned}$$

where we use the parameter $\kappa_{\mathrm{F}}(\omega) = l_{s,\mathrm{F}}^{-1}\sqrt{i\omega\tau_{s,\mathrm{F}}+1}$ for the ferromagnetic layer and $\kappa_{\mathrm{N}}(\omega) = l_{s,\mathrm{N}}^{-1}\sqrt{i\omega\tau_{s,\mathrm{N}}+1}$ for the nonmagnetic layer [142]. $l_{s,\mathrm{F}}$ and $l_{s,\mathrm{N}}$ correspond to the spin diffusion length of the ferromagnetic and nonmagnetic layer, respectively. The boundary conditions are identical to Section 4.2.5, but now expressed in the frequency domain. For convenience, we neglect the spin-dependent Seebeck effect (S_s and S_s^i) in this analytical calculation. The goal is to express the Fourier transform of the interfacial spin current

$$j_s^{\mathrm{int}}(\omega) = \frac{g_1}{\hbar}\left(\mu_{s,\mathrm{F}}(\omega,0) - \mu_{s,\mathrm{N}}(\omega,0)\right) + 2j_m(\omega,0), \tag{4.33}$$

in terms of the electron-magnon scattering rates, specifically, the bulk contribution $I_{sd}(\omega,x)$ and interfacial contribution $j_m(\omega,0)$. The resulting expression is given by

$$j_s^{\mathrm{int}}(\omega) = 2A(\omega) j_m(\omega,0) - 2d_{\mathrm{F}} B(\omega) \mathcal{I}_{sd}(\omega), \tag{4.34}$$

where $\mathcal{I}_{sd}(\omega)$ is

$$\mathcal{I}_{sd}(\omega) = \int_{-d_{\mathrm{F}}}^{0} dx' \, \frac{\kappa_{\mathrm{F}}(\omega)\cosh[(d_{\mathrm{F}}+x')\kappa_{\mathrm{F}}(\omega)]}{\sinh[d_{\mathrm{F}}\kappa_{\mathrm{F}}(\omega)]} I_{sd}(\omega,x'). \tag{4.35}$$

Furthermore, the function $A(\omega)$ is given by

$$A(\omega) = \frac{1 + \dfrac{\hbar \tilde{v}_{\mathrm{F}} d_{\mathrm{F}}}{g_1 \tau_{s,\mathrm{F}}} \left(\dfrac{l_{s,\mathrm{F}}^2 \kappa_{\mathrm{F}}(\omega)}{d_{\mathrm{F}}} \right) \tanh[\kappa_{\mathrm{F}}(\omega) d_{\mathrm{F}}]}{1 + \dfrac{\hbar \tilde{v}_{\mathrm{F}} d_{\mathrm{F}}}{g_1 \tau_{s,\mathrm{F}}} \left(\dfrac{l_{s,\mathrm{F}}^2 \kappa_{\mathrm{F}}(\omega)}{d_{\mathrm{F}}} \right) \tanh[\kappa_{\mathrm{F}}(\omega) d_{\mathrm{F}}] G_{\mathrm{N}}(\omega)}, \tag{4.36}$$

which can deviate from one (compared to Eq. (4.34)), indicating that the spin current driven by electron-magnon scattering at the interface is modified by spins flowing back into the ferromagnetic layer. Secondly, the bulk contribution depends on the function $B(\omega)$

$$B(\omega) = \frac{\left(\dfrac{1}{d_{\mathrm{F}} \kappa_{\mathrm{F}}(\omega)} \right) \tanh[\kappa_{\mathrm{F}}(\omega) d_{\mathrm{F}}]}{1 + \dfrac{\hbar \tilde{v}_{\mathrm{F}} d_{\mathrm{F}}}{g_1 \tau_{s,\mathrm{F}}} \left(\dfrac{l_{s,\mathrm{F}}^2 \kappa_{\mathrm{F}}(\omega)}{d_{\mathrm{F}}} \right) \tanh[\kappa_{\mathrm{F}}(\omega) d_{\mathrm{F}}] G_{\mathrm{N}}(\omega)}. \tag{4.37}$$

The function $G_{\mathrm{N}}(\omega)$ includes all the parameters that describe the properties of the nonmagnetic layer and the interfaces

$$G_{\mathrm{N}}(\omega) = 1 + \frac{g_1 + \dfrac{g_1 g_2 \tau_{s,\mathrm{N}}}{\hbar \tilde{v}_{\mathrm{N}} l_{s,\mathrm{N}}^2 \kappa_{\mathrm{N}}(\omega)} \tanh[\kappa_{\mathrm{N}}(\omega) d_{\mathrm{N}}]}{g_2 + \dfrac{\hbar \tilde{v}_{\mathrm{N}} l_{s,\mathrm{N}}^2 \kappa_{\mathrm{N}}(\omega)}{\tau_{s,\mathrm{N}}} \tanh[\kappa_{\mathrm{N}}(\omega) d_{\mathrm{N}}]}. \tag{4.38}$$

What remains is simplifying Eq. (4.34) and expressing it in terms of the total spin density $\langle n_{\mathrm{tot}}(\omega) \rangle$ and thereby the normalized magnetization m. For convenience, we first focus on the situation that interfacial electron-magnon scattering is absent.

BULK ELECTRON-MAGNON SCATTERING

Here, we set $j_m(\omega, 0) \to 0$. Hence, the interfacial spin current is given by the second term in Eq. (4.34). As is discussed in Appendix 4.B (on page 112) , a relevant approximation is that the function $\mathcal{I}_{sd}(\omega)$ closely resembles the spatial average $\langle I_{sd}(\omega) \rangle$. To eliminate $\langle I_{sd}(\omega) \rangle$ from Eq. (4.34), we make use of the continuity equations for n_d and δn_s spatially averaged over the ferromagnetic layer. In the absence of interfacial electron-magnon scattering this yields

$$\begin{aligned} i\omega\langle n_d(\omega)\rangle &= \langle I_{sd}(\omega)\rangle, && (4.39)\\ i\omega\langle \delta n_s(\omega)\rangle &= -2\langle I_{sd}(\omega)\rangle - \frac{\langle \delta n_s(\omega)\rangle}{\tau_{s,\mathrm{F}}} - \frac{j_s^{\mathrm{int}}(\omega)}{d_\mathrm{F}}. && (4.40)\end{aligned}$$

Using these equations the interfacial spin current can be expressed in terms of the Fourier transform of the total spin density

$$j_s^{\mathrm{int}}(\omega) = -2d_\mathrm{F}\widetilde{B}(\omega) \times (i\omega\langle n_{\mathrm{tot}}(\omega)\rangle), \tag{4.41}$$

where the new function $\widetilde{B}(\omega)$ is given by

$$\widetilde{B}(\omega) = \frac{B(\omega)(i\omega\tau_{s,F}+1)}{i\omega\tau_{s,F}B(\omega)+1}. \tag{4.42}$$

The function $\widetilde{B}(\omega)$ carries all information about the relation between the temporal evolution of the magnetization and the interfacial spin current. We investigate the Taylor expansion

$$\widetilde{B}(\omega) = B(0) + i\tau\omega + \mathcal{O}(\omega^2), \tag{4.43}$$

where we introduced the timescale $\tau = -i\widetilde{B}'(0)$.

We focus on a Ni(3.4 nm)/Cu(2.5 nm) bilayer, which is similar to the system used in the experiments of Ref. [136]. When the interface at $x = d_\mathrm{N}$ is permeable for spins ($g_2 \neq 0$) and connected to an ideal spin sink, we estimate $\tau_{g_2\neq 0} \sim 5.1 \times 10^{-16}$ s, when using the constants for Ni/Cu as presented in Table 4.2 and 4.3. For frequencies up to the THz regime it satisfies $\tau_{g_2\neq 0}\,\omega \ll B(0) \sim 0.52$, implying that $\widetilde{B}(\omega)$ is approximately independent of frequency and given by $B(0)$. Inverse Fourier transforming Eq. (4.41) yields

$$j_s^{\mathrm{int}}(t) = -2d_\mathrm{F}B(0) \times \frac{d\langle n_{\mathrm{tot}}\rangle}{dt}. \tag{4.44}$$

By definition $-(1/s)d\langle n_{\mathrm{tot}}\rangle/dt = dm/dt$. Using this substitution the interfacial spin current in terms of the normalized magnetization m is

$$j_s^{\mathrm{int}}(t) = \epsilon \times (2d_\mathrm{F}s)\frac{dm}{dt}, \tag{4.45}$$

where we defined the efficiency parameter $\epsilon = B(0)$. This expression is identical to the relation as reported in Ref. [136]. Contrasting behavior is found when we switch

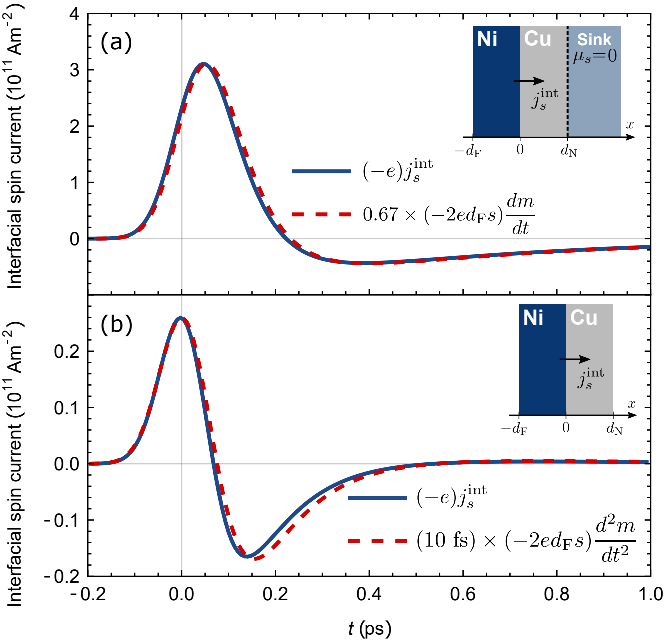

Figure 4.3: Laser-induced spin transport in a Ni(3.4 nm)/Cu(2.5 nm) bilayer for two types of boundary conditions at $x = d_{\rm N}$. (a) The interfacial spin current (blue) as a function of time t after laser-pulse excitation at $t = 0$, for an interface at $x = d_{\rm N}$ that is permeable for spins ($g_2 \neq 0$) and connected to an ideal spin sink. The dashed red line indicates the temporal derivative of the magnetization, scaled by a prefactor that is fitted to the amplitude of the spin current. (b) The interfacial spin current (blue) for insulating boundary conditions ($g_2 = 0$). The dashed red line indicates the second derivative of the magnetization, scaled to have the same amplitude as the spin current.

to $g_2 = 0$, when all spins are blocked at $x = d_{\rm N}$. A critical role is played by the function $G_{\rm N}(\omega)$, which under these conditions shows $G_{\rm N}(0) \gg 1$ and dominates the frequency dependence of $\widetilde{B}(\omega)$. Using that the Cu nonmagnetic layer satisfies $d_{\rm N}/l_{s,{\rm N}} \ll 1$, it follows that

$$\tau_{g_2=0} \approx B(0)^2 \frac{\tilde{v}_{\rm F} d_{\rm F} \tau_{s,{\rm N}}^2}{\tilde{v}_{\rm N} d_{\rm N} \tau_{s,{\rm F}}} \sim 7.0 \text{ fs}. \tag{4.46}$$

In combination with $B(0) \sim 4 \times 10^{-4}$, it typically satisfies $\tau_{g_2=0}\,\omega \gg B(0)$. Hence, in this specific case the first-order term of $\widetilde{B}(\omega)$ dominates. The spin current is now given by

$$j_s^{\rm int} = \tau_{g_2=0} \times (2d_{\rm F}s)\frac{d^2m}{dt^2}. \tag{4.47}$$

Rather than being proportional to dm/dt, the interfacial spin current is now approximately proportional to the second derivative of m. This behavior is a direct consequence of the large spin-flip scattering time $\tau_{s,\mathrm{N}} = 17$ ps of Cu [72]. In this case, an efficient spin dissipation channel is absent, resulting in an altered response of the spin accumulation in the nonmagnetic layer which affects the temporal behavior of the interfacial spin transport.

The clear distinction between the dynamics predicted by Eq. (4.45) and Eq. (4.47) for a Ni(3.4 nm)/Cu(2.5 nm) bilayer is depicted in Figs. 4.3(a)-(b). We here assumed that the laser pulse is only absorbed by the Ni layer and used $P_0 = 0.2 \times 10^8$ Jm^{-3}. The absorption by the Cu layer is neglected, since Cu has a relatively small imaginary component of the dielectric constant [71]. All remaining parameters are given in Table 4.2 and 4.3. Figure 4.3(a) shows the correspondence between the spin current (blue solid line) and the temporal derivative of the magnetization (red dashed line) in the case that the bilayer is connected to an ideal spin sink. There is no significant phase shift present, which is in agreement with the experiments in Ref. [136]. In Fig. 4.3(b) the spin sink is absent, and a close relation between the spin current (blue solid line) and the second derivative of the magnetization (red dashed line) is found. Note that the scaling factors given in the figure do not match the values calculated in the text, as the calculations presented in the figures include magnon transport, the spin-dependent Seebeck effect, and the full frequency dependence.

We observe that in case the receiving layer is an efficient spin sink, or is connected to an efficient spin sink, the interfacial spin current is directly proportional to the temporal derivative of m, as described by the relation Eq. (4.45). This is in agreement with the results of the previous section because Pt has a very short spin-flip scattering time of $\tau_{s,\mathrm{N}} \sim 0.02$ ps [143, 144]. In the opposite case, if the receiving material displays inefficient spin-flip scattering, other relations may arise. We stress that the behavior predicted by Eq. (4.47) strongly depends on the exact components of the heterostructure. As shown by the calculation, a Ni/Cu bilayer is an ideal system to demonstrate the latter limiting case, mainly because Cu has a very large spin-flip scattering timescale and a Ni/Cu interface has a relatively large electrical conductance [72]. To demonstrate this experimentally, two methods can potentially be used to probe the spin-current generation into the nonmagnetic layer. First, probing the THz electromagnetic radiation that results from the inverse spin Hall effect yields the temporal profile of the spin current [70]. However, due to the small spin Hall angle of Cu the signal is expected to be very small [145]. A second method is using the magneto-optical Kerr effect. In that case, the spin accumulation is probed instead of the spin current [65]. For insulating boundary conditions, the spin density that builds up in the nonmagnetic layer is given by

$$\langle \delta n_s(\omega) \rangle_{\mathrm{N}} = \frac{1}{d_{\mathrm{N}}} \frac{j_s^{\mathrm{int}}(\omega)}{i\omega + \tau_{s,\mathrm{N}}^{-1}}. \tag{4.48}$$

Here, the brackets indicate spatial averaging over the nonmagnetic layer. For Cu, with the large $\tau_{s,\mathrm{N}}$, the interfacial spin current and the build-up spin density differ by a factor $\sim i\omega$. Indicating that the optically probed signal will replicate the first derivative of the magnetization. Despite the difficulty of observing the behavior of Eq. (4.47), the analysis emphasizes that by modifying the properties of the nonmagnetic material the bandwidth of the spin current can be tuned [68, 143]. Although compositions other than Ni/Cu might not yield the ideal comparison as in Figs. 4.3(a)-(b), performing experiments for various nonmagnetic materials and probing both the magnetization and the spin current simultaneously, will yield valuable information.

In the analytical calculation presented in this section, we left out the interfacial electron-magnon scattering. In the following section, we specifically address its contribution to spin current injection and discuss the role of magnon transport.

INTERFACIAL ELECTRON-MAGNON SCATTERING AND MAGNON TRANSPORT

Magnon spin transport and magnon heat transport are directly coupled, which makes them complex to investigate analytically. Hence, this section presents a numerical analysis of the role of interfacial electron-magnon scattering and magnon transport.

The results are shown in Figs. 4.4(a)-(d), and correspond to a Ni(3.4 nm)/Cu(2.5 nm) bilayer connected to an ideal spin sink. The calculations include bulk electron-magnon scattering, interfacial electron-magnon scattering, and the spin-dependent Seebeck effect. The used system parameters are presented in Table 4.2 and 4.3. The phase diagram in Fig. 4.4(a) indicates the amplitude of the spin current, determined by its maximum value, as a function of the spin-mixing conductance $g_{\uparrow\downarrow}$ and the magnon transport timescale $\tau_{\mathrm{tr},m}$. The spin-mixing conductance, which is made dimensionless by dividing it by a factor $(\pi s d_{\mathrm{F}})$, determines the strength of the

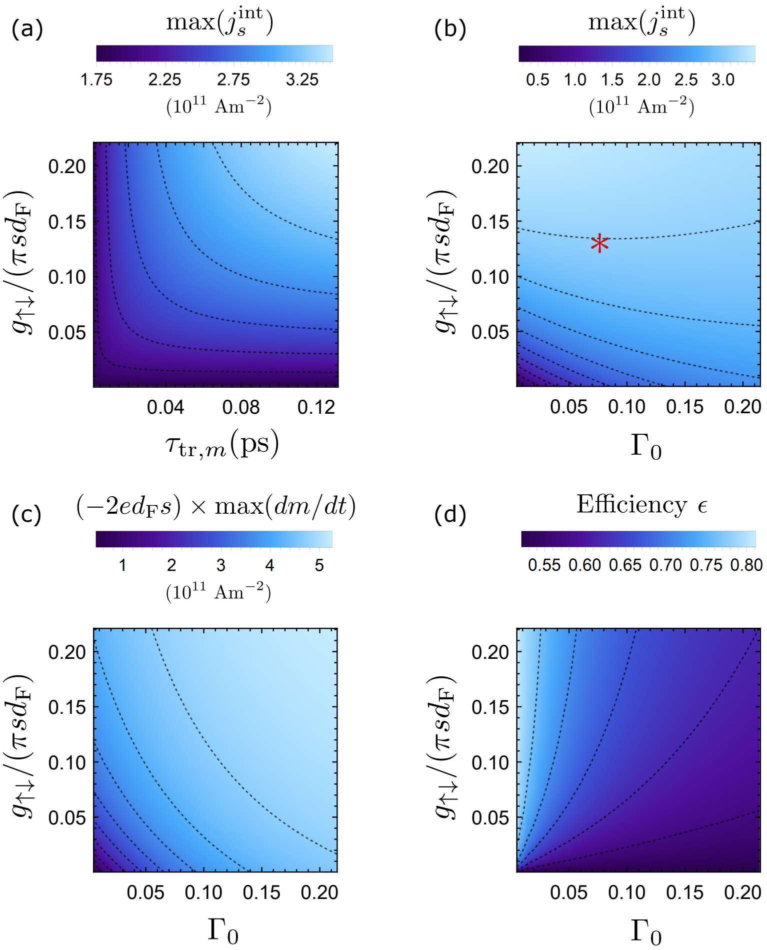

Figure 4.4: Phase diagrams that characterize the interfacial spin current in a Ni(3.4 nm)/Cu(2.5 nm) bilayer connected to an ideal spin sink. (a) Phase diagram of the amplitude of the interfacial spin current as a function of the spin-mixing conductance $g_{\uparrow\downarrow}$ (made dimensionless by dividing it by $(\pi s d_{\rm F})$) and the magnon transport timescale $\tau_{{\rm tr},m}$. (b)-(d) Phase diagrams as a function of the spin-mixing conductance $g_{\uparrow\downarrow}$ and the bulk electron-magnon scattering rate coefficient Γ_0, where $\tau_{{\rm tr},m} = 0.1$ ps is set constant. (b) The amplitude of the interfacial spin current. The red star indicates the values used in Fig. 4.3(a). (c) The amplitude of $(-2ed_{\rm F}s)dm/dt$. (d) The efficiency parameter ϵ, as defined in Eq. (4.45).

interfacial electron-magnon scattering and thereby the magnon spin current near the interface. The timescale $\tau_{{\rm tr},m}$ determines the effectiveness of magnon transport in the bulk. In order to have interfacial electron-magnon scattering significantly contribute to the total spin current, it is required to have efficient magnon transport in the bulk, as indicated by the light region in Fig. 4.4(a).

Figures 4.4(b)-(d) compare the contributions by bulk and interfacial electron-magnon scattering. These phase diagrams are plotted as a function of the spin-mixing conductance and the bulk electron-magnon scattering rate coefficient Γ_0. Here, the magnon transport timescale is set to $\tau_{\text{tr},m} = 0.1$ ps, similar to the calculations presented in the previous sections. The color scheme in Fig. 4.4(b) indicates the amplitude of the interfacial spin current. The figure emphasizes that including interfacial electron-magnon scattering boosts the amplitude of the spin current, however, the significance of the increase depends on the efficiency of the bulk electron-magnon scattering.

Figure 4.4(c) indicates the amplitude of dm/dt, given in the same units as the spin current. Intuitively, the demagnetization favors a simultaneously large interfacial and bulk electron-magnon scattering rate, since both contribute to the generation of thermal magnons. This does not linearly translate to a maximized spin current, as the relation between the spin current and demagnetization depends on which contribution dominates. The color scheme in Fig. 4.4(d) indicates the efficiency ϵ, as defined in Eq. (4.45). Keeping in mind the analytical calculation, the range of ϵ is approximately related to the values of prefactors $A(0)$ and $B(0)$ (see Eqs. (4.36)-(4.37)). In the case only interfacial electron-magnon scattering is present this yields $\epsilon \sim A(0) \sim 0.79$, whereas for the pure bulk scenario $\epsilon \sim B(0) \sim 0.52$. A small deviation compared to Fig. 4.4(d) arises as the numerical calculation includes the spin-dependent Seebeck effect and the full frequency dependence.

All calculations presented here imply that spin transport by magnons, which is typically neglected in the calculations of laser-induced spin transport in metallic magnetic heterostructures [71, 72], is relevant to include in the analyses [36]. Since magnon transport is driven by electron-magnon scattering at the interface, the ratio of Γ_0 and $g_{\uparrow\downarrow}/(\pi s d_{\text{F}})$ plays a decisive role [36]. Furthermore, constants that parametrize either bulk magnon transport or spin-polarized electron transport are essential. Their coupled dynamics complexifies the characterization of bulk spin transport, including the modification of the diffusion length scales [139]. On top of that, nonmagnetic system parameters that correspond to the thermal properties of the system do strongly affect the importance of magnon transport. For instance, the interfacial magnon current is mainly determined by the temperature difference $T_m - T_e^{\text{N}}$, which critically depends on the thermal and optical properties of the nonmagnetic layer. Further theoretical work is required to chart the essential dependencies on the properties of the heterostructure. Hence, we state that the role of interfacial electron-magnon scattering and, consequently, bulk magnon transport can not be neglected a priori [36]. It may play a significant role depending on the specific system components and properties. Nevertheless, bulk electron-magnon scattering always remains essential, as ultrafast demagnetization is observed in magnetic thin films regardless of the presence of a neighboring nonmagnetic metallic layer [61].

4.4 Conclusion and outlook

In conclusion, we modeled ultrafast demagnetization and spin transport in rapidly heated magnetic heterostructures, addressing the interplay of thermal magnons and itinerant spins. Within this model, the magnetization is determined by the total spin density of the two populations and ultrafast demagnetization is driven by the combination of electron-magnon scattering and additional spin-flip scattering processes originating from spin-orbit coupling. Secondly, electron-magnon scattering is a driving force of nonlocal spin transfer, for which we calculated the resulting spin transport by magnons and spin-polarized electrons within a diffusive description. It is shown that in the case the receiving material is an efficient spin sink, the interfacial spin current becomes directly proportional to the time derivative of the magnetization. Furthermore, we have discussed the role of interfacial electron-magnon scattering and magnon transport, and showed that they cannot be neglected a priori. However, their significance strongly depends on the material properties of the full magnetic heterostructure.

In this chapter, we focused on ultrathin magnetic heterostructures. To explore the role of bulk temperature gradients and identify characteristic length scales, a quantitative analysis over a larger range of thicknesses is required. Secondly, it will become interesting to go beyond the assumptions that the phononic system plays a minor role and behaves as an ideal spin sink. As recent experiments show that during the ultrafast demagnetization spin is transferred to the lattice [54, 55], and specifically circularly polarized phonons [55], it becomes obvious that a more complete description of the phononic system is needed. Moreover, it was already proposed that a coupling between magnons and phonons should be implemented within a three-temperature description [59]. Nevertheless, it is expected that the dominant physical concepts are captured within the assumptions of the presented model.

4.A EXPANSION OF THE POLYLOGARITHM

In this appendix, we present additional details regarding the calculations in the main sections. The starting point is the evaluation of the polylogarithm function. To evaluate the integrals that are needed for the description of the magnonic system, we make use of the following expression for the polylogarithm [117]

$$\mathrm{Li}_s(e^x) = \frac{1}{\Gamma(s)} \int_0^\infty dt \frac{t^{s-1}}{e^t/e^x - 1}. \tag{4.49}$$

As mentioned in Sec. 4.2.1, we assume the parameter x remains small. The polylogarithm can be written as a series expansion [138]

$$\mathrm{Li}_s(e^x) = \Gamma(1-s)(-x)^{s-1} + \sum_{k=0}^{\infty} \frac{\zeta(s-k)}{k!} x^k. \tag{4.50}$$

Since x remains small, we truncate this series for $k \geq 2$, which is the basis for the calculation of all coefficients presented in Table 4.1. As an example, we calculate the magnon density from Eq. (4.1)

$$n_d = \frac{(k_B T_m)^{3/2}}{4\pi^2 A^{3/2}} \Gamma(3/2) \mathrm{Li}_{3/2}\left(e^{(\mu-\epsilon_0)/(k_B T_m)}\right). \tag{4.51}$$

Table 4.2: Parameters that characterize the magnonic system in Ni.

symbol	meaning	estimate
T_0 (K)	ambient temperature	295
T_C (K) [1]	Curie temperature	628
$\tau_{\mathrm{tr},m}$ (ps) [a]	magnon momentum relaxation time	0.1
A (meVÅ^2) [b]	spin-wave stiffness	400
a (nm) [146]	lattice constant	0.35
S [c]	Spin per atom (in units $\hbar$)	$0.6 \times (1/2)$
Γ_0 [d]	e-m scattering rate coefficient	2×0.038
ϵ_0 (meV) [e]	magnon gap	0.05

[a] Discussed in the main text.

[b] Typical order of magnitude estimated by $A \sim 2k_B T_C S a^2$.

[c] Estimated from atomic magnetic moment given in [18].

[d] Using relation $\Gamma_0 = 2\alpha$ [116] and α of Ni [23].

[e] Typical order of magnitude from FMR frequency of ~ 10 GHz.

Applying the expansion up to first order in $\mu_m/(k_B T_m), \epsilon_0/(k_B T_m) \ll 1$ we have

$$\begin{aligned} n_d &= \frac{(k_B T_m)^{3/2}}{4\pi^2 A^{3/2}} \Gamma(3/2) \Bigg[\Gamma(-1/2) \left(\frac{\epsilon_0 - \mu_m}{k_B T_m} \right)^{1/2} \\ &\qquad + \zeta(3/2) - \zeta(1/2) \left(\frac{\epsilon_0 - \mu_m}{k_B T_m} \right) \Bigg]. \end{aligned} \tag{4.52}$$

If we now impose that we only have small changes of the magnon temperature compared to room temperature, $(T_m - T_0)/T_0 \ll 1$, and only collect the terms up to first order in small parameters we find

$$\begin{aligned} n_d &= \frac{(k_B T_0)^{3/2}}{4\pi^2 A^{3/2}} \Gamma(3/2) \\ &\quad \Bigg[\Gamma(-1/2) \left(\frac{\epsilon_0 - \mu_m}{k_B T_0} \right)^{1/2} + \zeta(3/2) \\ &\quad - \zeta(1/2) \left(\frac{\epsilon_0 - \mu_m}{k_B T_0} \right) + (3/2)\zeta(3/2) \frac{(T_m - T_0)}{T_0} \Bigg]. \end{aligned} \tag{4.53}$$

Evaluatimg this expression at the maximum temperature and chemical potential of the calculation in Sec. 4.3.1 (Fig. 4.1), it only differs approximately one per cent from the exact value Eq. (4.51). Taking the temporal derivative of n_d yields

$$\begin{aligned} \frac{\partial n_d}{\partial t} &= \frac{(k_B T_0)^{3/2}}{4\pi^2 A^{3/2}} \Gamma(3/2) \\ &\quad \Bigg[\left(\Gamma(1/2) \left(\frac{\epsilon_0 - \mu_m}{k_B T_0} \right)^{-1/2} + \zeta(1/2) \right) \frac{\dot{\mu}_m}{k_B T_0} \\ &\quad + (3/2)\zeta(3/2) \frac{\dot{T}_m}{T_0} \Bigg], \end{aligned} \tag{4.54}$$

which determines the coefficients $C_{n,\mu}$ and $C_{n,T}$, as defined in the main text and given in Table 4.1. When μ_m approaches the magnon gap ϵ_0, the first term in $C_{n,\mu}$ diverges, which originates from Bose-Einstein statistics. It is essential to include this nonlinear term in $C_{n,\mu}$ as otherwise we would find time traces of the magnon chemical potential that may largely exceed the magnon gap.

For all remaining coefficients in Table 4.1, the first term in the expansion Eq. (4.50) will only yield higher-order contributions. In that case the coefficients follow equivalently from the first-order Taylor expansion (the second term in Eq. (4.50)), where in the prefactors it is used that for sufficiently small ϵ_0 we approximate

$\mathrm{Li}_s(\exp(-\epsilon_0/(k_B T_0))) \sim \zeta(s)$. We stress that all expansion methods we use here remain a rough estimate. In order to retrieve valuable quantitative results from the magnonic calculation, it is essential to implement the full polylogarithm.

4.B NOTES ON THE APPROXIMATIONS IN THE ANALYTICAL CALCULATION

In Section 4.3.3 the bulk electron-magnon scattering rate, which is implemented in the spin diffusion equation as a source of spins, is simplified using the following considerations. We express the source $I_{sd}(\omega, x)$ in terms of a cosine expansion

$$I_{sd}(\omega, x) = \frac{I_{sd,0}(\omega)}{2} + \sum_{n=1}^{\infty} I_{sd,n}(\omega) \cos\left(\frac{n\pi x}{d_{\mathrm{F}}}\right), \tag{4.55}$$

where the coefficients $I_{sd,n}(\omega)$ are given by

$$I_{sd,n} = \frac{2}{d_{\mathrm{F}}} \int_{-d_{\mathrm{F}}}^{0} dx I_{sd}(\omega, x) \cos\left(\frac{n\pi x}{d_{\mathrm{F}}}\right). \tag{4.56}$$

Note that the zeroth mode corresponds to twice the spatial average $I_{sd,0}(\omega) = 2\langle I_{sd}(\omega)\rangle$. The higher-order modes are a measure of the spatial inhomogeneity of the source term. We want to express the function $\mathcal{I}_{sd}(\omega)$, as given in Eq. (4.35), in terms of the coefficients $I_{sd,n}(\omega)$. By performing the spatial integration we find

$$\mathcal{I}_{sd}(\omega) = \langle I_{sd}(\omega)\rangle + \sum_{n=1}^{\infty} \frac{I_{sd,n}(\omega)}{\left(\frac{n\pi}{d_{\mathrm{F}}\kappa_{\mathrm{F}}(\omega)}\right)^2 + 1}. \tag{4.57}$$

Hence, the $n \geq 1$ modes of $I_{sd}(\omega, x)$ are truncated by the denominator. In combination with the inhomogeneous modes remaining relatively small compared to the homogeneous mode, it turns out to be a relevant approximation to neglect all the terms in the summation in Eq. (4.57).

Table 4.3: Parameters for the electronic system of Ni, Pt, and Cu. Parameters that characterize the interface correspond to Ni/Cu and Ni/Pt.

symbol	Ni	Pt	Cu	Ref.
γ ($\mathrm{Jm^{-3}K^{-2}}$)	1077	721	100	[59, 71, 72]
C_p ($10^6\,\mathrm{Jm^{-3}K^{-1}}$)	3.6	2.85	3.45	[59, 71]
g_{ep} ($10^6\,\mathrm{Jm^{-3}K^{-1}ps^{-1}}$)	0.855	0.29	0.07	[59, 71]
$2\tilde{\nu}$ ($\mathrm{eV^{-1}nm^{-3}}$) [a]	272	137 [b]	26	[72, 140, 143]
$2\tilde{\sigma}$ ($10^6\,\mathrm{Sm^{-1}}$) [a]	7.1	6.6	39	[71, 72]
κ_e ($\mathrm{Wm^{-1}K^{-1}}$)	50	50	300	[71, 72]
S_s ($10^{-24}\,\mathrm{JK^{-1}}$) [c]	-0.3			
g_1 ($10^{19}\,\mathrm{m^{-2}}$) [d]		0.3	1.0	[71, 72]
g_2 ($10^{19}\,\mathrm{m^{-2}}$)			1.0	
κ_e^i ($10^9\,\mathrm{Wm^{-2}K^{-1}}$) [e]		10	40	[71, 72]
S_s^i ($10^{-24}\,\mathrm{JK^{-1}}$) [f]		-0.3	-0.3	
$g_{\uparrow\downarrow}$ ($10^{19}\,\mathrm{m^{-2}}$)		0.3	1.0	[142, 147]
τ_s (ps)	0.1	0.02	17	[72, 143, 144]

[a] We assume that the spin-averaged quantities $\tilde{\nu}$ and $\tilde{\sigma}$ are approximately given by the (total) electrical quantity divided by two.

[b] Calculated from the ratio of the conductivity and diffusion coefficient in [143].

[c] Using that the Seebeck coefficient scales as $(\pi^2/3)k_B(T_0/T_F)$, with Fermi temperature $T_F \sim 10^4$ K, the polarization $P_s \sim 0.2$, and sign of the spin-dependent Seebeck effect [124].

[d] Estimated from the electrical conductance given for Ni/Cu in [72] and [Co/Ni]/Pt in [71].

[e] Estimated from the electrical conductance and the Wiedemann-Franz law [72].

[f] Assumed to be equal to the bulk value.

4.C SYSTEM PARAMETERS

The system parameters that are used in the calculations presented in the main sections are summarized in Table 4.2 and Table 4.3. Table 4.2 shows the estimated parameters that characterize the magnonic system in Ni. Table 4.3 presents the parameters of the electronic system in Ni, Pt, and Cu. Furthermore, it includes the parameters that correspond to the interfaces.

5

SPIN-POLARIZED HOT ELECTRON TRANSPORT VERSUS SPIN PUMPING MEDIATED BY LOCAL HEATING

A 'toy model'—aimed at capturing the essential physics—is presented that jointly describes spin-polarized hot electron transport and spin pumping driven by local heating. These two processes both contribute to spin-current generation in laser-excited magnetic heterostructures. The model is used to compare the two contributions directly. The spin-polarized hot electron current is modeled as a first generation of hot electrons with a spin-dependent excitation and relaxation scheme. Upon decay, the excess energy of the hot electrons is transferred to a thermalized electron bath. The elevated electron temperature leads to an increased rate of electron-magnon scattering processes and yields a local accumulation of spin. This process is dubbed as spin pumping by local heating. The built-up spin accumulation is effectively driven out of the ferromagnetic system by (interfacial) electron transport. Within our model, the injected spin current is dominated by the contribution resulting from spin pumping, while the hot electron spin current remains relatively small. We derive that this observation is related to the ratio between the Fermi temperature and Curie temperature, and we show what other fundamental parameters play a role.[1]

---

[1] The work presented in this chapter is related to the research documented in the MSc thesis of K.A. de Mare [148]. This chapter has not been published in a physics journal yet.

5.1 INTRODUCTION

The generation of spin transport by femtosecond laser-pulse excitation paves the way towards ultrafast spintronic applications. Similar to subpicosecond quenching of the magnetization [13, 18, 21–26, 30–39, 54, 149], the physical origin of laser-induced spin transport is an unsolved quest and remains heavily debated after more than a decade of experimental and theoretical research [14, 15, 39, 65, 68, 69, 71, 73–75, 100, 101, 103, 105, 130, 131]. Nevertheless, it is clear that the manipulation of magnetic materials with femtosecond laser pulses is unique by being ultrafast and very efficient. Therefore, understanding the underlying physical mechanisms is interesting from both a fundamental and technological viewpoint.

There are two dominant theories on the physical origin of ultrafast spin currents. First, the laser pulse generates a population of highly energetic electrons that through spin-dependent excitation rates and mobilities yield a spin-polarized hot electron current. Including the generated cascades of secondary hot electrons, it is an efficient scheme of spin-current generation, as is described by the model for superdiffusive spin transport [39, 73]. The second theory is based on the notion that laser heating results in an increased rate of spin-flip scattering processes, including electron-magnon scattering. The latter generates a local spin accumulation [36, 65, 72], a process referred to as bulk spin pumping [72, 142], that effectively can be transported towards a neighboring nonmagnetic layer through spin diffusion. With the two major viewpoints in mind, the essential unanswered question is whether the generated spin current is a direct result of the excitation of hot electrons or is indirectly driven by heating and subsequent spin pumping.

In this chapter, we present a simplified phenomenological model—also referred to as 'toy model'—that jointly describes the generated hot electron spin currents and the spin currents driven by spin pumping. Hot electron transport is described by one generation of optically-excited electrons with spin-dependent excitation and decay rates. Within our approach, the hot electrons decay into an instantaneously thermalized electron bath, where the absorbed excess energy results in an increase of the electron temperature. The latter, and the coupling to a thermal magnon bath, is calculated explicitly. It gives an expression for the total built-up spin accumulation and the resulting spin current transported by the thermal electrons. The two contributions to the spin current are calculated equivalently at the interface of a ferromagnetic metal/nonmagnetic metal heterostructure. We show that the spin

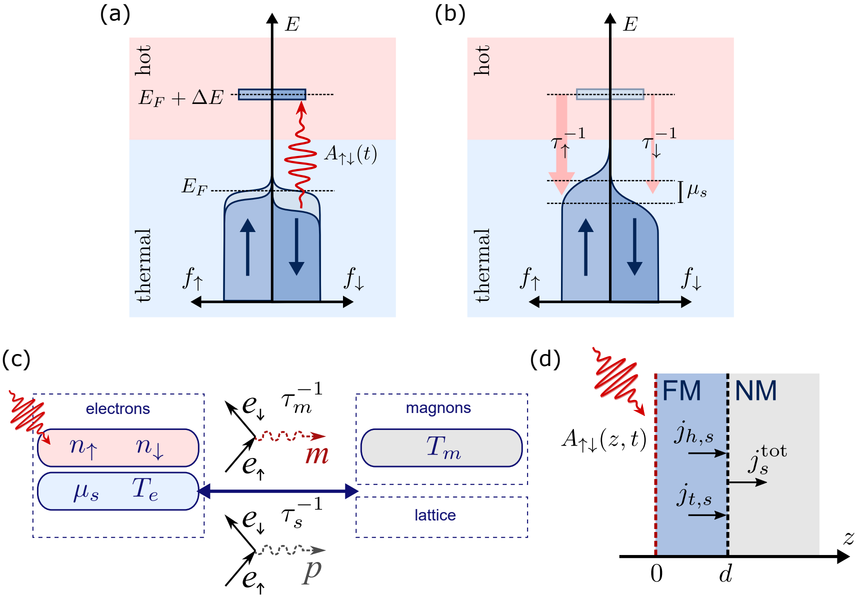

Figure 5.1: Schematic overview of the toy model. The system of electrons is composed of hot electrons and a bath of electrons that remains thermalized. (a) Excitation by a laser pulse yields a population of hot electrons and a reduction of the number of electrons in the thermal system. (b) The spin-dependent excitation and decay rates yield a net spin accumulation within the thermal system. (c) The decay processes are associated with an energy absorption of the thermal system, leading to an increased temperature T_e. Subsequent interactions among electrons, magnons, and the lattice, compose the full spin angular momentum flow. (d) Schematic overview of the modeled heterostructure, excited at position $z = 0$ by absorption profile $A_{\uparrow\downarrow}(t)$. The total interfacial spin current j_s^{tot} is the sum of the hot electron spin current $j_{h,s}$ and the spin current generated within the thermal electron system $j_{t,s}$.

current driven by spin pumping dominates and we derive that this observation is related to the ratio between the Fermi temperature and Curie temperature. Finally, we discuss the presence of spin-polarized screening currents and investigate their role.

5.2 Toy model for laser-induced hot electron dynamics

We start with defining two categories of electrons for each spin polarization separately. First, the electrons far above the Fermi level are defined as ‘hot’ electrons. Secondly, the electrons close to and far below the Fermi level are assumed to remain thermalized and are dubbed as ‘thermal’ electrons. We treat the thermal electron system as a single population of mobile electrons, representing hybridized 3*d* and 4*s* electrons in the transition metal ferromagnets, composed of the subsystems for majority spins (here defined as ↓) and minority spins (↑). A schematic overview is given in Figs. 5.1(a)-(b). Upon excitation, a (spin-polarized) population of thermal electrons is transferred to the higher energetic 'hot' state at energy ΔE above the Fermi level. In combination with the spin-dependent decay rates $\tau_{\uparrow\downarrow}^{-1}$, this leads to a shift of the spin-dependent chemical potential $\mu_s = \mu_\uparrow - \mu_\downarrow$. In other words, a spin accumulation is created. During the decay of the hot electrons, the excess energy ΔE is absorbed by the thermal system and leads effectively to an elevated electronic temperature T_e. The latter gives rise to the creation of thermal magnons and an additional change of the spin accumulation μ_s, as will be discussed in Sec. 5.3.

We first focus on the hot electron transport generated after excitation. We consider a (magnetic) metallic system described by spin-dependent electron distribution functions that remain homogeneous in the transverse plane but may vary along the longitudinal (out-of-plane) z direction. Furthermore, we assume that when hot electrons are excited they move in a random direction with a (spin-dependent) fixed speed $v_{\uparrow\downarrow}$ until they decay after time $\tau_{\uparrow\downarrow}$. The distribution function describing this hot electron system satisfies the Boltzmann equation

$$\frac{\partial n_{\uparrow\downarrow}(z,v,t)}{\partial t} + v\frac{\partial n_{\uparrow\downarrow}(z,v,t)}{\partial z} = A_{\uparrow\downarrow}(z,t) - \frac{n_{\uparrow\downarrow}(z,v,t)}{\tau_{\uparrow\downarrow}}, \tag{5.1}$$

where $n_{\uparrow\downarrow}(z,v,t)$ corresponds to the distribution function for hot electrons with up (↑) and down (↓) spin at position z with velocity component v along the z axis. The function $A_{\uparrow\downarrow}(z,t)$ describes the spatiotemporal profile of the laser-pulse absorption and is spin-dependent due to the different absorption coefficients for up and down spins. For simplicity, we assume that this source term is a Dirac delta function located at $z = 0$, having $A_{\uparrow\downarrow}(z,t) = A_{0,\uparrow\downarrow}(t)\delta(z)$ (see Fig. 5.1(d)), where $A_{0,\uparrow\downarrow}(t)$ is determined by the temporal profile of the laser pulse. Only focusing on this simplified example is relevant, since the response to a general spatial-dependent function can be calculated straightforwardly by performing a convolution [73]. Furthermore, we define the polarization coefficient $P_A = (A_{0,\uparrow}(0) - A_{0,\downarrow}(0))/(A_{0,\uparrow}(0) + A_{0,\downarrow}(0))$ such that $A_{0,\uparrow\downarrow}(t) = A_0(t)(1 \pm P_A)$, where $A_0(t)$ corresponds to the spin-averaged excitation profile.

Using Fourier transformation, we switch from the time domain to the frequency

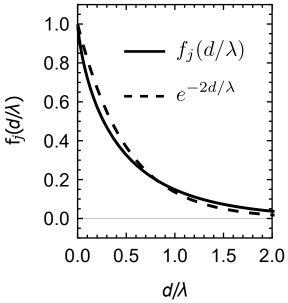

Figure 5.2: The function $f_j(d/\lambda)$, which describes the spatial decay of the hot electron spin current, plotted as a function of the normalized thickness d/λ (black solid line). The function is compared to the exponent of $-2d/\lambda$, represented by the dashed black line.

domain, which simplifies the following calculations because convolutions now correspond to a multiplication. We are interested in the dynamics in the region $z \geq 0$, where the solution to Eq. (5.1) is given by

$$n_{\uparrow\downarrow}(z,v,\omega) = \frac{A_0(\omega)(1 \pm P_A)}{v} \exp\left(-\frac{z}{v\tau_{\uparrow\downarrow}}(1 + i\omega\tau_{\uparrow\downarrow})\right)\theta(v). \tag{5.2}$$

The Heaviside theta function $\theta(v)$ makes sure that the solution does not diverge in the limit $z \to \infty$, meaning that only right-moving electrons are present. We assume that all hot electrons move in a random (positive) direction with a fixed speed $v_{\uparrow\downarrow}$. The number density of the electrons can then be written as

$$n_{\uparrow\downarrow}(z,\omega) = \frac{A_0(\omega)(1 \pm P_A)}{v_{\uparrow\downarrow}} f_n\left[\frac{z(1 + i\omega\tau_{\uparrow\downarrow})}{\lambda_{\uparrow\downarrow}}\right], \tag{5.3}$$

where the function $f_n(x)$ results from a surface integral over a positive hemisphere with radius $v_{\uparrow\downarrow}$ and we used $\lambda_{\uparrow\downarrow} = v_{\uparrow\downarrow}\tau_{\uparrow\downarrow}$. The proper normalization factors are defined within $A_0(\omega)$. Similarly, the current densities can be expressed as

$$j_{\uparrow\downarrow}(z,\omega) = A_0(\omega)(1 \pm P_A)\, f_j\left[\frac{z}{\lambda_{\uparrow\downarrow}}(1 + i\omega\tau_{\uparrow\downarrow})\right]. \tag{5.4}$$

Since the solutions follow from the Boltzmann equation, the functions $f_n(x)$ and $f_j(x)$ satisfy $f_j'(x) = -f_n(x)$. The function $f_j(x)$ is plotted in Fig. 5.2, showing its similarity with exponential decay. Keeping the latter in mind, the inverse Fourier transform of Eq. (5.4) approximately corresponds to an exponential decay with length scale $\lambda_{\uparrow\downarrow}/2$ and a phase shift $2z/v_{\uparrow\downarrow}$ compared to the temporal profile of the laser pulse.

Although we focus on a magnetic heterostructure in the following paragraphs, we assume for hot electron transport that the system is homogeneous, since we aim for a simple toy model. The hot electron current at the interface of the heterostructure is simply assumed to be equal to Eq. (5.4) being evaluated at $z = d$, where d is the thickness of the (imaginary) ferromagnetic layer (see Fig. 5.1(d) for a schematic overview). Moreover, in the following calculation we need the spatial average of $n_{\uparrow\downarrow}(z,\omega)$ over the domain $(0,d]$, notated simply as $n_{\uparrow\downarrow}(\omega)$, which is given by

$$\begin{aligned} n_{\uparrow\downarrow}(\omega) &= \frac{A_0(\omega)(1 \pm P_A)}{v_{\uparrow\downarrow}} \frac{1}{1+i\omega\tau_{\uparrow\downarrow}} \frac{\lambda_{\uparrow\downarrow}}{d} \\ &\quad \times \left(1 - f_j\left[\frac{z}{\lambda_{\uparrow\downarrow}}(1+i\omega\tau_{\uparrow\downarrow})\right]\right), \end{aligned} \tag{5.5}$$

using the relation between $f_n(x)$ and $f_j(x)$. For convenience, we define one more function that will become relevant in the second part of this chapter

$$\begin{aligned} F_{\pm}(\omega) &= \pm(1+P_A)\frac{1 - f_j\left[\frac{d}{\lambda_\uparrow}(1+i\omega\tau_\uparrow)\right]}{1+i\omega\tau_\uparrow} \\ &\quad +(1-P_A)\frac{1 - f_j\left[\frac{d}{\lambda_\downarrow}(1+i\omega\tau_\downarrow)\right]}{1+i\omega\tau_\downarrow}, \end{aligned} \tag{5.6}$$

where depending on the sign (±), the factor $F_{\pm}(\omega)$ represents phenomena related to the charge (+) or spin degree of freedom (−). For instance, $F_{+}(\omega)$ determines the total amount of hot electrons that decay within distance d and appears in the description for the local heating process (Sec. 5.3). Furthermore, $F_{-}(\omega)$ will determine the contribution to the hot electron spin current resulting from the spin-dependent decay rates (Sec. 5.4). We now have all ingredients to calculate the distinct contributions to the spin current, and to investigate the response of the thermal system to the hot electron dynamics.

5.3 Spin pumping mediated by local heating

In this section, we calculate the spin current that arises in the thermal electron bath and we express it in terms of the characteristic functions for the hot electron dynamics. The method can be separated into three steps. (i) The interfacial spin current within the thermal electron system is expressed in terms of the electron-magnon scattering rate. (ii) The scattering rate is parametrized by an electron temperature and a magnon temperature. (iii) The magnon temperature is eliminated and the electron temperature is expressed in terms of the hot electron functions defined in the previous section (such as $F_+(\omega)$ from Eq. (5.6)). Combining these three steps yields a simple expression for the thermal spin current that can directly be compared to the hot electron contribution.

Hence, the starting point is to express the interfacial spin current in terms of the bulk electron-magnon scattering rate. To find a simple description, we assume that the ferromagnetic system is much thinner than the spin-diffusion length, having $d \ll \lambda_{\mathrm{sf}}$.[2] Then by approximation, the spin density in the thermal electron system is parametrized by a spatial homogeneous spin accumulation μ_s. From the conservation of spin in the combined system, we write down the equation for the out-of-equilibrium spin density $\delta n_{t,s}$ of the thermalized electrons. In the frequency domain it is given by [36, 135]

$$\begin{aligned} i\omega\delta n_{t,s}(\omega) + \frac{j_{t,s}(\omega)}{d} &= -2I_{sd}(\omega) - 2P_A A_0(\omega) \\ &\quad + \frac{n_\uparrow(\omega)}{\tau_\uparrow} - \frac{n_\downarrow(\omega)}{\tau_\downarrow} - \frac{\delta n_{t,s}(\omega)}{\tau_s}, \end{aligned} \tag{5.7}$$

where $j_{t,s}(\omega)$ is the interfacial spin current generated in the thermal electron system. On the right-hand side, I_{sd} is determined by the rate of spin transfer per unit volume driven by electron-magnon scattering [36, 117], and was discussed in Chapter 4. The term proportional to P_A corresponds to the spin-dependent excitation of electrons which are transferred to the hot electron system. Moreover, the terms proportional to $\tau_{\uparrow\downarrow}^{-1}$ result from the decay of the hot electrons. In combination with the previous term (proportional to P_A), the latter will generate an additional spin current that will partially compensate the hot electron contribution. This 'backflow' spin current

---

[2] It should be noted that we keep the spin-flip scattering rate τ_s fixed, meaning that the limit $d \ll \lambda_{\mathbf{sf}}$ actually corresponds to assuming a very large conductivity. The expressions presented here are equivalent to the similar calculation in Section 4.3.3 for $d \ll \lambda_{\mathrm{sf}}$.

will be discussed below. Finally, the last term on the right-hand side of Eq. (5.7) corresponds to the additional channels of spin-flip scattering with corresponding timescale τ_s [36].

The out-of-equilibrium spin density is proportional to the spin accumulation $\delta n_{t,s} = \tilde{\nu}_F \mu_s$, where $\tilde{\nu}_F$ is the spin-averaged density of states evaluated at the Fermi energy. Analogously, the interfacial spin current carried by the thermal electrons is written as $j_{t,s}(\omega) = (g/\hbar)\mu_s(\omega)$, where g is a conductance for the spin current. Here, it is assumed that the neighboring nonmagnetic material is a good spin sink. By solving Eq. (5.7) for μ_s, and using the expressions for $n_\uparrow(\omega)$ and $n_\downarrow(\omega)$ as given in Eq. (5.5), the interfacial spin current becomes

$$j_{t,s}(\omega) = \frac{(-2d)I_{sd}}{1 + \frac{\tau_g}{\tau_s}(1 + i\omega\tau_s)} - \frac{2P_A A_0(\omega) + A_0(\omega)F_-(\omega)}{1 + \frac{\tau_g}{\tau_s}(1 + i\omega\tau_s)}, \tag{5.8}$$

where the timescale τ_g is defined as $\tau_g^{-1} = g/(\hbar\tilde{\nu}_F d)$ and determines the efficiency of the spin transfer into the nonmagnetic layer. This timescale is treated as an effective parameter to compensate for the fact that (diffusive) spin transport in the bulk is assumed to be instantaneous, as a result of the condition $d \ll \lambda_{\mathrm{sf}}$.

The first term in Eq. (5.8) corresponds to the spin current driven by the electron-magnon scattering in the bulk (spin pumping) [36, 72], and indirectly results from the local heating process. The second term is generated because the spin-dependent excitation and decay of hot electrons affect the net spin density in the thermal system, and corresponds to the previously mentioned backflow spin current. Although the latter is directly related to the hot electron dynamics, it should still be considered as a spin current contribution carried by thermal electrons.

To get an analytical expression for the thermal spin current in terms of the excitation profile $A_0(\omega)$, we have to find a simplified description for the electron-magnon scattering rate. In order to do so, we first calculate the dynamics of the electron temperature. In the frequency domain the change of the (spatially-averaged) electron temperature $\delta T_e(\omega)$ satisfies an equation of the form

$$i\omega\delta T_e(\omega) = \frac{\Delta E}{C_e}\left(\frac{n_\uparrow(\omega)}{\tau_\uparrow} + \frac{n_\downarrow(\omega)}{\tau_\downarrow}\right) - \frac{\delta T_e(\omega)}{\tau_e}, \tag{5.9}$$

where the factor proportional to τ_e^{-1} is introduced phenomenologically and includes all processes that drive heat out of the electron system in the ferromagnetic region (including heat lost at the interface). Furthermore, C_e is the electronic specific heat and ΔE is the photon energy of the laser pulse. It follows that the elevated electron temperature $\delta T_e(\omega)$ can be expressed as

$$\delta T_e(\omega) \quad = \quad \frac{\tau_e A_0(\omega)\Delta E}{dC_e(1+i\omega\tau_e)} F_+(\omega). \tag{5.10}$$

To calculate the spin current that results from the increase of the electron temperature, we have to determine the electron-magnon scattering rate I_{sd}. We take a simplified approach and assume that the density of magnons that is generated is given by $\delta n_d(\omega) = C_{n,T}\delta T_m(\omega)$, where $\delta T_m(\omega)$ is the Fourier transform of the change of the magnon temperature and the coefficient $C_{n,T}$ is given in Chapter 4 (Table 4.1 on page 92). The rate at which magnons are generated is given by

$$i\omega C_n \delta T_m(\omega) \quad = \quad I_{sd}(\omega) = \frac{C_{n,T}}{\tau_m}(\delta T_e(\omega) - \delta T_m(\omega)), \tag{5.11}$$

where the electron-magnon scattering rate is expressed in terms of the difference in magnon temperature and electron temperature, and is proportional to a corresponding (demagnetization) timescale τ_m. Combining Eq. (5.10) and Eq. (5.11) gives a closed expression for the electron-magnon scattering rate in terms of the functions that depend on the hot electron system. This yields

$$I_{sd}(\omega) \quad = \quad \frac{C_{n,T}\Delta E}{C_e}\frac{(i\omega\tau_e)A_0(\omega)F_+(\omega)}{d(1+i\omega\tau_e)(1+i\omega\tau_m)}. \tag{5.12}$$

Physically, the product describes the consecutive processes of heating the thermal electrons through the energy retrieved from decaying hot electrons (described by $F^+(\omega)$), and the subsequent generation of thermal magnons by an increase of the temperature. By substituting the expression for $I_{sd}(\omega)$ in Eq. (5.8), the spin current driven by electron-magnon scattering can be expressed in terms of the functions that describe the hot electron dynamics.

5.4 COMPARISON OF THE HOT AND THERMAL SPIN CURRENTS

In this section, we directly compare the distinct contributions to the interfacial spin current. First, the total interfacial spin current is written as

$$j_s^{\mathrm{tot}}(\omega) = j_{h,s}(\omega) + j_{t,s}^{\mathrm{sd}}(\omega) + j_{t,s}^{\mathrm{back}}(\omega), \tag{5.13}$$

where $j_{h,s}$ corresponds to the direct spin current carried by hot electrons and $j_{t,s}^{\mathrm{sd}}$ corresponds to the thermal contribution driven by spin pumping. The spin current $j_{t,s}^{\mathrm{back}}$ is equal to the second term on the right-hand side of Eq. (5.8), named after that it drives a backflow that partially compensates the hot electron contribution.

To derive a simple relation that parametrizes the ratio between the different contributions to the spin current, we make the following assumptions. First, we assume that the ferromagnetic layer is very thin such that τ_g satisfies $\tau_g\omega \ll 1$. Similarly, we assume that the decay rate of the hot electrons is very fast $\tau_{\uparrow\downarrow}\omega \ll 1$. This means that we model a laser pulse that has a duration $\sigma \gg \tau_g, \tau_{\uparrow\downarrow}$. In that scenario we find

$$\begin{aligned} j_{h,s}(\omega) &= 2P_A A_0(\omega) + A_0(\omega)F_-(0), && (5.14)\\ j_{t,s}^{\mathrm{sd}}(\omega) &= \frac{-2C_{n,T}\Delta E}{C_e(1+\tau_g/\tau_s)} \frac{(i\omega\tau_e)A_0(\omega)F_+(0)}{(1+i\omega\tau_e)(1+i\omega\tau_m)}, && (5.15)\\ j_{t,s}^{\mathrm{back}}(\omega) &= -\frac{2P_A A_0(\omega) + A_0(\omega)F_-(0)}{1+\tau_g/\tau_s}. && (5.16) \end{aligned}$$

Importantly, it shows that $j_{t,s}^{\mathrm{back}}$ is directly proportional to the hot electron contribution and has an opposite sign. To explicitly calculate the spin currents in the time domain we assume the following temporal profile of the laser pulse

$$A_0(t) = \frac{P_0 d}{\Delta E(\sigma\sqrt{\pi})} \exp\left(-t^2/\sigma^2\right), \tag{5.17}$$

where σ is the pulse duration, P_0 plays the role of an absorbed laser pulse energy density, and ΔE is the photon energy. Inverse Fourier transforming Eqs. (5.14)-(5.16) (and for Eq. (5.15) performing a convolution in the time domain) yields the temporal profiles of the distinct spin current contributions. Figure 5.4(a) shows the resulting interfacial spin current as a function of time after laser-pulse excitation at $t = 0$. The used system parameters are presented in Table 5.1, which represent a typical magnetic heterostructure consisting of transition metal ferromagnet and

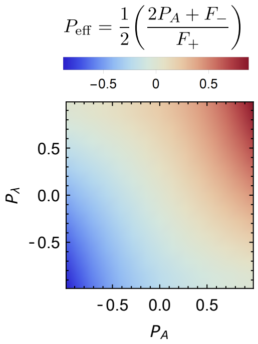

Figure 5.3: The effective polarization function P_{eff} (discussed below Eq. (5.18)) as a function of the polarization of the decay lengths P_λ and the polarization of the excitation P_A.

a nonmagnetic metal that is a good spin sink (such as Pt). In the figure, the gray line indicates the total spin current and the blue line shows the contribution by spin pumping. Furthermore, the red line represents the hot electron spin current and the dashed blue line the backflow spin current. The figure shows that for the used parameters the total spin current is dominated by the spin pumping contribution. The amplitude of the latter is approximately a factor ~ 5 times larger than the hot electron contribution. Moreover, including the backflow spin current yields that the hot electron spin current is almost completely compensated.

To further investigate the role of the several contributions to spin transport, it is convenient to calculate the ratio between $j_{t,s}^{\mathrm{sd}}$ and $j_{h,s}$ from Eq. (5.14) and Eq. (5.15). We define η as

$$\frac{\max(|j_{t,s}^{\mathrm{sd}}|)}{\max(|j_{h,s}|)} \equiv \eta \propto \frac{C_{n,T}\Delta E}{C_e\left(1 + \tau_g/\tau_s\right)}\left[\frac{-F_+(0)}{2P_A + F_-(0)}\right]. \tag{5.18}$$

Note that the exact ratio of the amplitudes also includes an additional prefactor determined by σ, τ_e and τ_m (not included in Eq. (5.18)). As is shown in Appendix 5.A, this additional factor typically scales as σ/τ_m, which in our example is of the order of one. The term between square brackets, on the right-hand side of Eq. (5.18), plays the role of an effective polarization P_{eff} of the hot electron current, and is determined by P_A and $P_\lambda = (\lambda_\uparrow - \lambda_\downarrow)/(\lambda_\uparrow + \lambda_\downarrow)$. This P_{eff} is plotted in Fig. 5.3 as a function of P_A and P_λ, for $d/\lambda = 0.3$ with $\lambda = (\lambda_\uparrow + \lambda_\downarrow)/2$. P_{eff} is shown to be a monotonic function of P_A and P_λ, which explains why it is interpreted as an effective polarization.

To express the ratio η in terms of fundamental parameters, we use that for a free electron gas the specific heat scales as $C_e \sim k_B(T/T_F)/a^3$ [108], where a is the lattice constant and T_F is the Fermi temperature. Furthermore, the magnon density coefficient $C_{n,T}$ scales as $C_{n,T} \sim (k_B T)^{1/2} A^{-3/2} k_B$ [135], where the spin-wave stiffness is proportional to the Curie temperature $A \sim k_B T_C a^2$. By implementing the numerical prefactors (including multiple factors of π) we estimate the order of magnitude of η and determine the crucial scaling factors

$$\eta \approx \left[\frac{2 * 10^{-2}}{(-P_{\text{eff}})} \frac{1}{1 + \tau_g/\tau_s} \right] \left(\frac{\Delta E}{k_B T} \right) \left(\frac{T_F}{T_C} \right) \sqrt{\frac{T}{T_C}}. \tag{5.19}$$

Although the factor between square brackets yields a number much smaller than one, this number is largely compensated by the remaining factors. Specifically, for a transition metal ferromagnet the Fermi temperature and Curie temperature typically differ an order of magnitude $(T_F/T_C) \sim 10$. Furthermore, for a ΔE of the order of electronvolts and a temperature close to room temperature we find the range $\Delta E/(k_B T) \sim 10^2$-$10^3$. Altogether, this implies that the contribution by spin pumping is generally large compared to the contribution by hot electron transport. In case the backflow is taken into account, the partial compensation of the hot electron spin current would lead to a change in the prefactor $(1 + \tau_g/\tau_s)^{-1} \rightarrow \tau_s/\tau_g$, resulting in an even larger η for $\tau_s > \tau_g$.

5.5 THE ROLE OF SPIN-POLARIZED SCREENING CURRENTS

Finally, we discuss the role of spin-polarized screening. It is generally assumed that screening of the charge degree of freedom happens on an extremely short timescale [71]. This corresponds to the approximation in the model that the system remains locally charge neutral and that the total charge current of the hot and thermal electrons is zero at all times. In the case of charge transport in the thermal electron system, the efficient screening approximation was already implemented throughout the previous sections (and chapters) and was briefly discussed in Sec. 2.6.1 when introducing spin diffusion. Additionally, in this chapter, we have the excited hot electrons that carry a nonzero charge current for which we analogously assume it is effectively screened through transport in the thermal electron system. Within the ferromagnetic region this results in an extra contribution to the spin

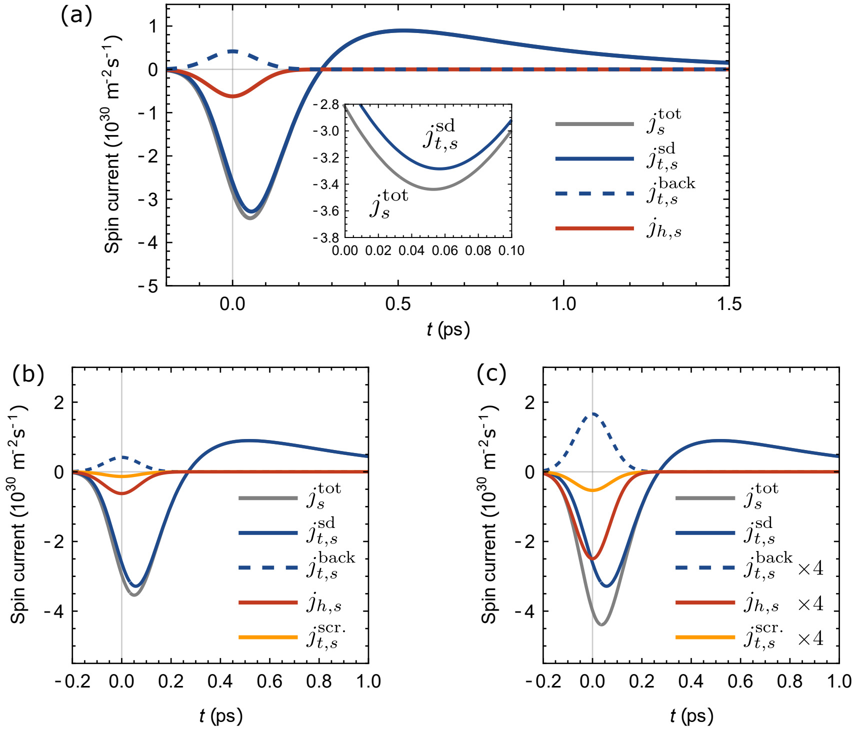

Figure 5.4: The interfacial spin current as a function of time after laser-pulse excitation. The gray line indicates the total spin current. Furthermore, the blue line indicates the contribution driven by electron-magnon scattering and the red line shows the hot electron spin current. Finally, the dashed blue line corresponds to the backflow current, as defined in the main text. (b) Similar calculation as (a), but now including a spin-polarized screening current indicated by the yellow line. (c) The contributions (indirectly) related to hot electron dynamics are multiplied by a factor of four to visually clarify the role of each contribution and to show the change of the total spin current (gray).

current since the present screening currents are subject to spin-dependent transport coefficients. Implementing spin-polarized screening currents within the toy model yields the following extension. First, charge neutrality requires the spin density of the thermalized system to satisfy

$$\delta n_s \quad = \quad \tilde{\nu}_F \mu_s - P_\nu (n_\uparrow + n_\downarrow), \tag{5.20}$$

where $P_\nu = (\nu_\uparrow - \nu_\downarrow)/(\nu_\uparrow + \nu_\downarrow)$ corresponds to the polarization of the density of states at the Fermi energy. Secondly, the absence of a net charge current requires that

$$j_{t,s} = \frac{g}{\hbar}\mu_s - P_g(j_\uparrow + j_\downarrow), \tag{5.21}$$

where we defined $P_g = (g_\uparrow - g_\downarrow)/(g_\uparrow + g_\downarrow)$. The conductance we used previously is given by the spin-averaged conductance $g = 2g_\uparrow g_\downarrow/(g_\uparrow + g_\downarrow)$. Implementing this within the previous scheme for the thermal electron system yields an extra contribution to the spin current

$$j^{\mathrm{scr.}}_{s,t}(\omega) = -P_g(j_\uparrow(\omega) + j_\downarrow(\omega))\frac{(\tau_g/\tau_s)}{1 + (\tau_g/\tau_s)}. \tag{5.22}$$

This is the spin-polarized screening current. Here, the term proportional to P_ν vanished due to the limit $\omega\tau_{\uparrow\downarrow} \ll 1$. The spin-polarized screening current is calculated for $P_g = 0.2$ and represented by the yellow curve in Fig. 5.4(b). Depending on the sign of P_g this contribution to the spin current either enhances or partially compensates the hot electron contribution. For illustrative purposes, Fig. 5.4(b) includes all other contributions to the spin current.

Additionally, we included Fig. 5.4(c). Here, we multiplied all terms (indirectly) related to the hot electron dynamics by a factor of four to emphasize the role of each separate contribution and to show the change of the total spin current (in gray). The figure emphasizes that in the case that the hot electron spin current is enhanced, for instance when taking into account multiple generations of hot electrons, the total spin current is significantly modified. Nevertheless, for the parameters used here, the spin current driven by spin pumping remains the dominant contribution.

5.6 CONCLUSION AND OUTLOOK

In conclusion, using a single simplified analytical model, we investigated the role of spin-polarized hot electron transport and spin transport driven by spin pumping in laser-excited magnetic heterostructures. This toy model yields that the spin current at the interface of the heterostructure is dominated by the thermal contribution initiated by local heating and subsequent spin pumping. We calculated the scaling factors that determine the ratio between the two contributions. As the latter depends on the fundamental parameters that describe the magnon system and thermal electron system, it could be expressed in terms of the Curie temperature, Fermi temperature, and laser-photon energy. This fundamental relation yields that the spin current driven by spin pumping is generally a significant contribution, and is dominant for the systems considered here.

An interesting extension to the toy model would be to implement multiple generations of hot electrons and calculate the resulting enhancement of the spin current. In that way, one reaches a description similar to the model for superdiffusive spin transport [39, 73]. Additionally, it would be interesting to implement the conceptual spin-polarized screening currents within the superdiffusive approach. Moreover, spin transport by thermal magnons and interfacial electron-magnon scattering processes are required to be investigated within this scheme [36, 135]. Nevertheless, it is expected that those extensions leave the presented scaling factors intact and spin pumping through local heating remains a dominant channel for spin-current generation.

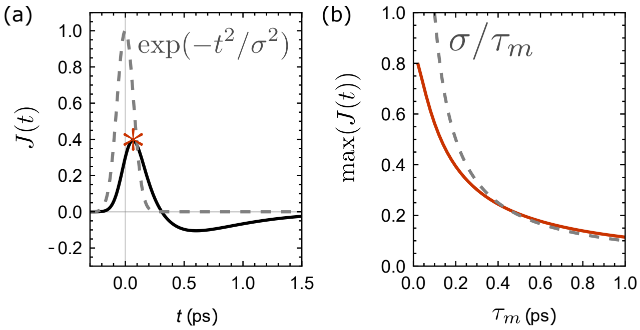

Figure 5.5: (a) Function $J(t)$ (solid black line) corresponds to the convolution of a Gaussian (dashed gray line) and the function $G(t)$ in the text. (b) The maximum of $J(t)$ plotted as a function of τ_m, compared to the function σ/τ_m.

5.A NOTES ON THE SPIN CURRENT DRIVEN BY SPIN PUMPING

In this appendix, we present some details regarding the temporal profile of the spin current induced by spin pumping. To calculate $j^{\mathrm{sd}}_{t,s}$, we have to perform an inverse Fourier transformation of the right-hand side of Eq. (5.15), including the function

$$G(\omega) \quad = \quad \frac{i\omega\tau_e}{(1+i\omega\tau_e)(1+i\omega\tau_m)}. \tag{5.23}$$

Disregarding the factors of 2π (which in the end all vanish), the function in the time domain is given by

$$G(t) \quad = \quad \frac{\tau_e}{\tau_e-\tau_m}\left(\frac{e^{-t/\tau_m}}{\tau_m}-\frac{e^{-t/\tau_e}}{\tau_e}\right)\theta(t). \tag{5.24}$$

The spin current is calculated by performing a convolution between $G(t)$ and the temporal profile of the laser pulse. To determine the scaling factor arising from this convolution we calculate

$$J(t) \quad = \quad \int dt' G(t-t')\exp\left(-\frac{t'^2}{\sigma^2}\right). \tag{5.25}$$

The extra scaling factor that should be added to Eq. (5.19) is given by the maximum of $J(t)$, as it corresponds to how much the (Gaussian) amplitude decreases after the convolution with $G(t)$ is performed. $J(t)$ is plotted in Fig. 5.5(a), together with the temporal profile of the Gaussian pulse. Here we used the values for σ, τ_m and τ_e

Table 5.1: Parameters used in the calculations presented in the main text. The chosen values represent a typical magnetic heterostructure consisting of transition metal ferromagnet and a nonmagnetic metal similar to Pt.

symbol	value	units
$\gamma = C_e/T_{\text{amb}}$ [59]	1077	$\text{Jm}^{-3}\text{K}^{-2}$
T_{amb}	300	K
ΔE	1	eV
P_0	$0.2 \cdot 10^8$	Jm^{-3}
σ	0.1	ps
A [a]	400	meVÅ^2
d	3	nm
λ [b]	10	nm
P_A [c]	-0.2	
P_λ [c]	-0.2	
τ_e [23]	0.45	ps
τ_m [23]	0.15	ps
τ_s [72]	0.1	ps
τ_g [d]	0.05	ps

[a] Used to calculate $C_{n,T}$ as given in Chapter 4.

[b] From a decay rate of 10 fs and a Fermi velocity of 1 nm fs^{-1}.

[c] A minus sign is present since we defined the spin down electrons as the majority spin population.

[d] Estimated using the values for g (Ni/Pt) and $\tilde{v}_F$ (Ni) from Chapter 4.

as given in Table 5.1. In the range $0.1 \text{ ps} < \tau_m \leq 1 \text{ ps}$, which is the typical order of magnitude for the demagnetization time of a ferromagnetic transition metal, the amplitude scales as σ/τ_m, as was mentioned in the main text. The ratio σ/τ_m is indicated by the dashed gray line in Fig. 5.5(b). Finally, we note that Table 5.1 presents the parameters used in the calculations.

6

COMPARING ALL-OPTICAL SWITCHING IN SYNTHETIC-FERRIMAGNETIC MULTILAYERS AND ALLOYS

We present an experimental and theoretical investigation of all-optical switching by single femtosecond laser pulses. Our experimental results demonstrate that, unlike rare earth-transition metal ferrimagnetic alloys, Pt/Co/[Ni/Co]$_N$/Gd can be switched in the absence of a magnetization compensation temperature, indicative for strikingly different switching conditions. In order to understand the underlying mechanism, we model the laser-induced magnetization dynamics in Co/Gd bilayers and GdCo alloys on an equal footing, using an extension of the microscopic three-temperature model to multiple magnetic sublattices and including exchange scattering. In agreement with our experimental observations, the model shows that Co/Gd bilayers can be switched for a thickness of the Co layer far away from compensating the total Co and Gd magnetic moment. We identify the switching mechanism in Co/Gd bilayers as a front of reversed Co magnetization that nucleates near the Co/Gd interface and propagates through the Co layer driven by exchange scattering.[1]

---

[1] This chapter has been published in *Physical Review B* [127]. The experiments were performed by M.L.M. Lalieu [150].

6.1 INTRODUCTION

Femtosecond laser pulses provide a unique tool to manipulate magnetic order on ultrashort timescales. A prime example of this is all-optical switching (AOS) of magnetization by a single pulse, as first observed in ferrimagnetic GdFeCo alloys using circularly polarized laser pulses [10]. Later, AOS was demonstrated in the same material by using a single linearly polarized laser pulse [11, 12], which indicated that GdFeCo can be switched with ultrafast heating as the only stimulus.

Deterministic AOS has a potential to be used in future magnetic memory devices, offering an ultrafast and energy-efficient way to write data. Helicity-dependent AOS by circularly polarized pulses has been demonstrated in a wide variety of materials [92, 151, 152]. However, in those cases the switch follows from a multiple-pulse mechanism. Purely thermal single-pulse AOS was only observed in a limited number of materials systems, all including rare earth (Gd)-transition metal alloys [11, 12, 93, 153]. Very recently, it was also demonstrated for the synthetic-ferrimagnetic layered structure [89], which allows for easy spintronic integration [99]. The fact that single-pulse AOS is observed in both ferrimagnetic alloys and synthetic-ferrimagnetic multilayers raises the questions to what extent the switching of these materials systems relies on the same physics, and what the specific conditions are for switching these materials systems.

In this chapter, we show that the conditions for single-pulse AOS in alloys (GdCo) and synthetic ferrimagnets (Co/Gd bilayers) are strikingly different. We experimentally demonstrate that single-pulse AOS in synthetic-ferrimagnetic Pt/FM/Gd is very robust, and can be achieved for a large range of the ferromagnetic (FM) layer thickness. The experiments indicate that the Pt/FM/Gd stacks can be switched in the absence of a compensation temperature. In contrast, for alloys it is believed that it is crucial to have a compensation temperature near ambient temperature, such that the magnetization of the sublattices is compensated significantly [93, 94].

We performed simulations in order to understand this contrasting behavior and to identify the underlying mechanisms. The general theoretical framework for AOS describes the dynamics of multiple magnetic sublattices which are coupled antiferromagnetically. The intersublattice exchange coupling plays a crucial role, transferring angular momentum between the sublattices [76]. Different approaches have been made to describe the spin dynamics of the magnetic sublattices, e.g., the atomistic Landau-Lifshitz-Gilbert equation [79, 81, 83–85] and the microscopic three-temperature model (M3TM) [18, 78]. Here, we use the latter microscopic description, in which it is assumed that angular momentum transfer between the sublattices is mediated by exchange scattering [78]. We derive an analytical expression for the magnetization dynamics resulting from the exchange scattering between (i) the sublattices in a GdCo alloy and (ii) the atomic monolayers in a Co/Gd bilayer. The model reproduces the distinct role of the compensation temperature. Moreover, it shows that the robustness of AOS in the Co/Gd bilayers can be explained by the nonlocal character of the switching mechanism, which we identify as a front of reversed Co magnetization that propagates away from the interface.

This chapter starts with a brief description of the experimental methods and results. After that, the theoretical framework will be introduced. For the sake of direct comparison, we focus our theoretical discussion on the magnetization dynamics in GdCo alloys and Co/Gd bilayers. We present phase diagrams that show qualitatively the switching conditions and point out the differences for both materials systems. Finally, the typical switching mechanism of the bilayers is explained explicitly.

6.2 Threshold fluence as a function of layer thickness

The experiments are performed using Si:B(substrate)/Ta(4)/Pt(4)/FM/Gd(3)/Pt(2) stacks (thickness in nm), which are deposited at room temperature using dc magnetron sputtering at 10^{-8} mbar base pressure. Here, Co(0.2)/[Ni(0.6)/Co(0.2)]$_N$ multilayers are used for the FM layer, with N repeats ranging from $N = 2$ to 5. Using polar magneto-optical Kerr effect measurements, a square hysteresis loop with 100% remanence was obtained for all samples, confirming the presence of a well-defined perpendicular magnetic anisotropy in the samples.

The response of the magnetization in the Pt/FM/Gd stacks to laser-pulse excitation was investigated using linearly polarized laser pulses with a central wavelength of 700 nm and a pulse duration of ≈ 100 fs. The measurements are performed at room temperature, and start by saturating the magnetization using an externally applied field. Then, the external field is turned off, and the sample is exposed to single laser pulses with varying pulse energies. The response of the magnetization to the laser-pulse excitation is measured in the steady state (i.e., long after the excitation)

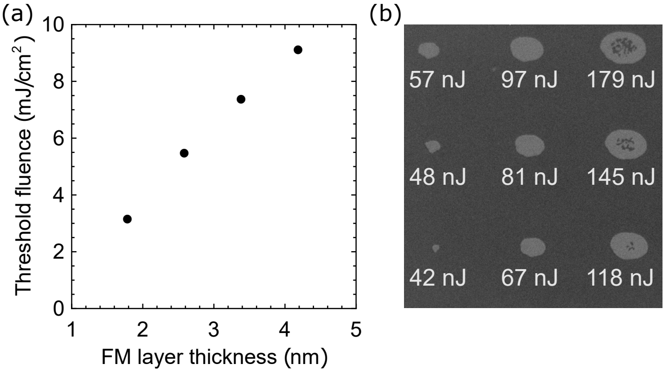

Figure 6.1: (a) Threshold fluence as a function of the FM layer thickness in a Pt/FM/Gd stack. The black dots are measured using an FM layer composed of Co(0.2)/[Ni(0.6)/Co(0.2)]$_N$ multilayers for $N = 2, 3, 4, 5$. The error margins are small compared to the scale of the figure. (b) A Kerr microscope image of the (initially saturated) Co/Ni sample with $N = 3$ after excitation with single linearly polarized laser pulses with different pulse energies.

using a magneto-optical Kerr microscope.

A typical result of the AOS measurement for the sample with $N = 3$ is presented in Fig. 6.1(b). The figure displays the Kerr image of the (initially saturated, dark) sample after excitation with single linearly polarized laser pulses with different pulse energies. The figure shows clear homogeneous domains with an opposite magnetization direction (light) being written by the laser pulses. Moreover, the domain size increases for increasing pulse energy, as is expected when using a Gaussian pulse shape. For the highest pulse energies a multidomain state is formed in the center region of the domain, where the lattice is heated above the Curie temperature [154].

The AOS-written domain size as a function of the pulse energy can be used to determine the threshold fluence [89, 155]. Figure 6.1(a) displays the threshold fluence as a function of the (total) thickness of the Co(0.2)/[Ni(0.6)/Co(0.2)]$_N$ multilayer. The results show that decreasing the thickness of the FM layer leads to a lower threshold fluence. This behavior is reproduced in the model calculations that are presented later. It can be partially explained by a decrease in the Curie temperature with film thickness in the thin-film limit, but it will be shown that also other processes are involved.

Remarkably, single-pulse AOS is seen for up to 5 repeats, corresponding to an FM layer thickness of 4.2 nm. For these relatively thick FM layers, the total magnetic moment of the FM layer is much larger than the induced magnetic moment in the Gd layer corresponding to approximately 1-2 atomic monolayers of fully saturated Gd [89], i.e., the system is far from compensated. Hence, the experiment indicates that the switching mechanism in the bilayers is independent of a possible compensation temperature. To understand the underlying mechanism, we developed a simplified model.

6.3 Modeling AOS in alloys and bilayers

In this section, we present the simplified model that is used to analogously describe AOS in GdCo alloys and Co/Gd bilayers. In the case of alloys, the model was introduced in Sec. 2.7.1. Here, we give an overview of the model for ferrimagnetic alloys, and present the extension to synthetic-ferrimagnetic (Co/Gd) bilayers.

Analogous to Schellekens et al. [78], we assume that separate spin subsystems are coupled to a single electron and phonon subsystem. Like in the basic M3TM [18], the electrons are treated as a spinless free electron gas and the phonons are described within the Debye model. It is assumed that both subsystems are internally thermalized, and that the electron temperature T_e and phonon temperature T_p are homogeneous. The spin specific heat is neglected. Femtosecond laser heating is modeled by adding an energy source to the electron subsystem. Heat diffusion to the substrate is added to the phonon subsystem as an energy dissipation term with timescale τ_D. The spin subsystems, labeled with index i, are treated within a Weiss mean-field approach. At each lattice site $D_{\mathrm{s},i} = \mu_{\mathrm{at},i}/2S_i$ spins are present, where $\mu_{\mathrm{at},i}$ is the atomic magnetic moment (in units of the Bohr magneton μ_B) and S_i is the spin quantum number.

For the $\mathrm{Gd}_{1-x}\mathrm{Co}_x$ alloys, we define a normalized magnetization m_i for each of the two sublattices. As depicted in the inset of Fig. 6.2(a), the exchange field experienced by each atom depends on the type of atom and the composition of its nearest neighbors. Hence, the exchange splitting is given by

$$\Delta_{\mathrm{Co}} = x\gamma_{\mathrm{Co\text{-}Co}} m_{\mathrm{Co}} + (1-x)\gamma_{\mathrm{Co\text{-}Gd}} m_{\mathrm{Gd}}, \tag{6.1}$$

$$\Delta_{\mathrm{Gd}} = x\gamma_{\mathrm{Gd\text{-}Co}} m_{\mathrm{Co}} + (1-x)\gamma_{\mathrm{Gd\text{-}Gd}} m_{\mathrm{Gd}}, \tag{6.2}$$

where we defined $\gamma_{ij} = j_{ij} z D_{\mathrm{s},j} S_j$ ($i,j \in \{\text{Co,Gd}\}$) in terms of the (intra- or intersublattice) exchange coupling constant j_{ij} and the number of nearest neighbors z. Note that $j_{\text{Co-Gd}}$ is negative and quantifies the strength of the antiferromagnetic coupling between the Co and Gd sublattices.

For the Co/Gd bilayers, we introduce a normalized magnetization m_i for each atomic monolayer i separately. Each layer only interacts with its adjacent layers. For simplicity, we assume that the separate layers lie in the (111) plane of an fcc lattice. This means that each atom has 6 nearest neighbors in the same layer and 3 nearest neighbors in each adjacent layer. Thus, the exchange splitting of layer i is

$$\Delta_i = \frac{\gamma_{i,i-1}}{4} m_{i-1} + \frac{\gamma_{i,i}}{2} m_i + \frac{\gamma_{i,i+1}}{4} m_{i+1}. \tag{6.3}$$

Note that the antiferromagnetic coupling, proportional to $j_{\text{Co-Gd}}$, is only experienced by the layers adjacent to the interface (see inset Fig. 6.2(b)).

We include two channels for angular momentum transfer. Elliott-Yafet spin-flip scattering mediates the transfer of angular momentum between the spin subsystems and the lattice [23]. An extension of the M3TM, which accounts for spin systems with arbitrary spin S, is derived to describe the resulting magnetization dynamics [18, 56].[2] Here, we take $S_{\text{Co}} = 1/2$ and $S_{\text{Gd}} = 7/2$, for which the Weiss model is well fitted to the experimental data for the magnetization as a function of temperature [1, 156]. Angular momentum transfer between the different spin subsystems is mediated by exchange scattering [78]. In this *e*-*e* scattering process, spins originating from different subsystems are flipped in the opposite direction. We use Fermi's golden rule to find an analytical expression for the magnetization dynamics resulting from the exchange scattering (see Chapter 2 Section 2.7.1). For $i \neq j$ we have

$$\begin{aligned} \left.\frac{dm_i}{dt}\right|_{\text{ex}} = \frac{2\eta_{ij}C_j}{\mu_{\text{at},i}} T_e^3 \Bigg[& \sum_{s=-S_i+1}^{S_i} \sum_{s'=-S_j}^{S_j-1} W^{-+}_{ij;ss'}(\Delta_i - \Delta_j) f_{i,s} f_{j,s'} \\ & - \sum_{s=-S_i}^{S_i-1} \sum_{s'=-S_j+1}^{S_j} W^{+-}_{ij;ss'}(\Delta_i - \Delta_j) f_{i,s} f_{j,s'} \Bigg]. \end{aligned} \tag{6.4}$$

The indices s and s' correspond to the z component of the spin and label the discrete energy levels. The average occupation of level s in spin subsystem i is given by $f_{i,s}$,

---

[2] Presented in Chapter 2 Section 2.3.4.

and $\Delta_i - \Delta_j$ is the energy difference between the initial and final spin configuration. The dimensionless function $W^{\pm\mp}_{ij;ss'}$ parametrizes the transition rate from level s to $s \pm 1$ in subsystem i and level s' to $s' \mp 1$ in subsystem j. The coordination number C_j counts the relative number of nearest neighbors that are part of spin subsystem j. For alloys C_j is given by $C_{\mathrm{Co}} = 12x$ and $C_{\mathrm{Gd}} = 12(1-x)$. For bilayers we have $C_j = 3$, the number of nearest neighbors in an adjacent layer. The constant η_{ij} is determined by the matrix element of the exchange scattering Hamiltonian (see Section 2.7.1), for which we assume that it is proportional to the exchange coupling constant. Hence, we write $\eta_{ij} \propto \lambda_{ij} j_{ij}^2$, where λ_{ij} is a dimensionless parameter. In the following discussions, we assume that $\lambda_{ij} = \lambda = 5$, which is chosen in order to retrieve realistic results from the simulations (e.g., for $\lambda = 1$ no switching is found). Results for different choices of λ and S_{Gd} are presented in the Supplemental Material of Ref. [127](The publication corresponding to this chapter). Note that for the bilayers, Eq. (6.4) should include terms for the interaction with both adjacent layers, i.e., $j = i+1$ and $j = i-1$, and the full expression is given by the sum of these two terms.

The temporal profile of the laser pulse is modeled by a Gaussian function $P(t) = (P_0/(\sigma\sqrt{\pi}))\mathrm{Exp}(-(t-t_0)^2/\sigma^2)$, where P_0 is the absorbed laser pulse energy density and σ is the pulse duration, which is set to 50 fs. We assume that the laser pulse heats up the system homogeneously, which is a valid approximation for the systems we model, e.g. Co/Gd bilayers containing up to 20 Co atomic monolayers. We note that for thicker systems the approximation becomes questionable, and a finite penetration depth should be incorporated into the modeling.

The laser-induced dynamics of $m_i(t)$ is calculated numerically. We assume that the spin subsystems are not necessarily in internal equilibrium, meaning that after excitation the ratio between $f_{i,s}$ and $f_{i,s\pm1}$ is not given by a Boltzmann distribution, and we need to solve a set of $2S_i + 1$ coupled differential equations for each spin subsystem i. The exact values for the material parameters, including the exchange coupling constants j_{ij}, are listed in Appendix 6.A (on page 143).

Two phase diagrams are constructed that display the occurrence of AOS as a function of the laser pulse energy P_0 and (i) the Co concentration x of a $\mathrm{Gd}_{1-x}\mathrm{Co}_x$ alloy, (ii) the number of Co monolayers for a Co/Gd bilayer (the Co thickness). We assume that the ambient temperature is equal to room temperature ($T_{\mathrm{amb}} = 295$ K). The result is shown in Fig. 6.2(a) and Fig. 6.2(b). The color scheme indicates whether the magnetization of the Co is reversed after relaxation, which is deter-

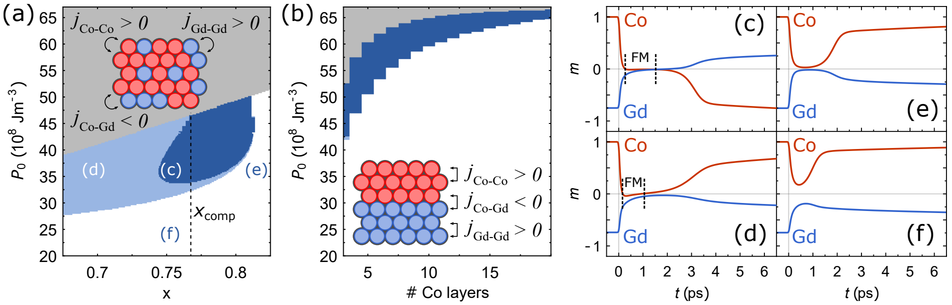

Figure 6.2: Phase diagram for AOS as a function of the laser pulse energy P_0 and (a) Co concentration x for a $Gd_{1-x}Co_x$ alloy, (b) the number of Co monolayers in a Co/Gd bilayer. The dark blue regions indicate a switch in the final state (c) and the white regions indicate no switch (e)-(f). Light blue indicates a transient ferromagnetic state, but no switch (d). The gray regions indicate that the phonon temperature T_p exceeds the Curie temperature T_C. The dashed line in figure (a) indicates the Co concentration x_{comp} for which the compensation temperature is equal to room temperature. The insets in (a) and (b) schematically show the modeled system, including the exchange parameters. Figure (c)-(f) display the element-specific magnetization dynamics in $Gd_{1-x}Co_x$ for different values for x and P_0, corresponding to the various regions in (a).

mined by calculating its sign at $t = 100$ ps. For the bilayers we take the average of the magnetization of the Co monolayers. Figure 6.2(c)-(f) are presented to clarify the meaning of the color scheme and show the corresponding element-specific magnetization dynamics for the alloys. In the phase diagrams, the dark blue regions indicate that the Co magnetization is reversed, meaning that AOS has occurred (Fig. 6.2(c)). The light blue regions indicate that there is a transient ferromagnetic state created, but after relaxation the magnetization is switched back to its initial direction (Fig. 6.2(d)). The white regions indicate that the magnetization relaxes to its initial direction, without a transient ferromagnetic state (Fig. 6.2(e)-(f)). The gray regions indicate that the maximum of the phonon temperature T_p exceeds the Curie temperature. In the experiments, this would likely result in the creation of a multidomain state [154].

The vertical dashed line in Fig. 6.2(a) indicates the compensation point $x_{\text{comp}} \sim 0.77$, the Co concentration for which the total magnetic moment of the alloy is zero at room temperature. The dark blue region shows that the alloys can only be switched in a limited range of the Co concentration, sufficiently close to the compensation point. Furthermore, the minimum threshold fluence is found to be close to the compensation point. These findings are in agreement with the experiments [94]. From the phase diagram we can conclude that in order to switch the alloy, a

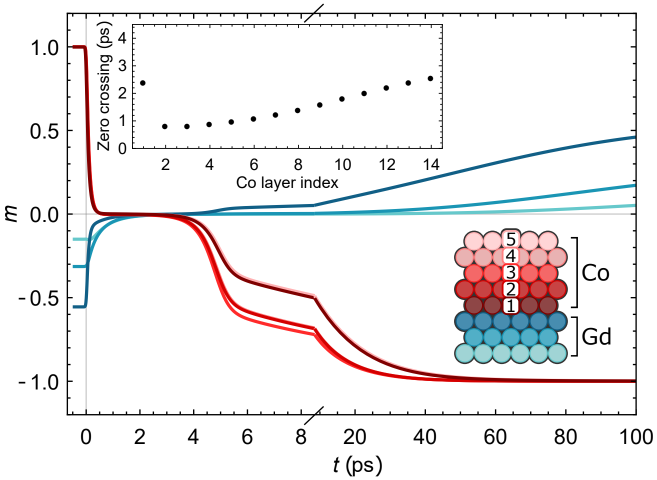

Figure 6.3: Laser-induced magnetization dynamics of all atomic monolayers in a Co/Gd bilayer consisting of 5 Co monolayers and 3 Gd monolayers for $P_0 = 55 \cdot 10^8$ Jm^{-3}. The inset shows the time at which the magnetization of each Co monolayer is reversed for a system of 14 Co layers and 3 Gd layers for $P_0 = 65 \cdot 10^8$ Jm^{-3} (index 1 corresponds to the Co layer adjacent to the interface).

significant magnetization compensation is necessary. Hence, the model yields that the magnetization compensation temperature plays a crucial role in switching the alloys.

A clear difference is found when we compare this to the situation for bilayers, Fig. 6.2(b). This phase diagram shows that the bilayers can be switched for a relatively large number of Co monolayers, even though the threshold fluence increases as a function of the number of Co monolayers. More specifically, even bilayers with 20 Co monolayers can be switched. For these bilayers, the ratio of the total Co and Gd magnetic moment is $\mu_{\text{Co}}/\mu_{\text{Gd}} \sim 4$ (at $T_{\text{amb}} = 295$ K), which is significantly far from compensation ($\mu_{\text{Co}}/\mu_{\text{Gd}} = 1$). In contrast, for the alloys switching only occurs in the range $\mu_{\text{Co}}/\mu_{\text{Gd}} \sim 0.9$ - 1.3. Note that for convenience we described the FM layer as pure Co, whereas in the experiments Co/Ni multilayers are used. Including the Co/Ni multilayers will not change the qualitative properties of the switching mechanism. Hence, the model agrees well with our experimental observation that shows single-pulse AOS in Pt/FM/Gd for relatively thick FM layers, and verifies that the magnetization compensation temperature does not play a crucial role in switching the synthetic ferrimagnets.

A more detailed analysis of the typical switching mechanism in the bilayers is presented in Fig. 6.3, which shows AOS in a system of 5 Co monolayers and 3 Gd monolayers. We plotted the normalized magnetization of the separate layers as a function of time after laser pulse excitation (at $t = 0$). The inset displays the time at which each Co monolayer reverses its magnetization direction, for a system of 14 Co layers and 3 Gd layers. The inset clearly shows that the Co layers are switched consecutively, starting with the Co layers near the Co/Gd interface. Triggered by the laser pulse, the switch is initiated near the interface due to exchange scattering between the adjacent Co and Gd monolayers. The dynamics of the first Co monolayer (Index 1 in Fig. 6.3) is strongly modified by the exchange field from the slowly demagnetizing Gd layer. Hence, the second Co monolayer is switched first. Subsequently, the switch propagates throughout the Co layer driven by exchange scattering between neighboring Co monolayers. This successive switching mechanism, with a front of reversed Co magnetization propagating away from the interface, can succeed independently of the number of Co monolayers and explains why the Co/Gd bilayer can be switched for a relatively large Co thickness.

6.4 CONCLUSION

To conclude, both the experiment and the theoretical model show that single-pulse AOS switching in synthetic-ferrimagnetic bilayers is independent of a possible compensation temperature, whereas in ferrimagnetic alloys the compensation temperature plays a crucial role. We identified the propagation of a switching front as the characteristic mechanism for AOS in the bilayers. These new insights show that single-pulse AOS in synthetic ferrimagnets is more robust than in ferrimagnetic alloys, and emphasize that Pt/FM/Gd synthetic ferrimagnets are a very promising candidate for integration of single-pulse AOS in future data storage devices.

6.A USED SYSTEM PARAMETERS

In this appendix, we discuss some additional details regarding the parameters used in the presented calculations, starting with the specification of the electron and phonon system. For simplicity, we assume that the electronic and phononic properties of the system are fully determined by the majority compound, i.e. Co, and described by a two-temperature model

$$\begin{aligned} \gamma T_e(t)\frac{dT_e(t)}{dt} &= g_{ep}(T_p(t) - T_e(t)) + P(t), && (6.5) \\ C_p\frac{dT_p}{dt} &= g_{ep}(T_e(t) - T_p(t)) + C_p\frac{T_{\text{amb}} - T_p(t)}{\tau_D}. && (6.6) \end{aligned}$$

where T_{amb} is the ambient temperature and τ_D is the timescale of the heat diffusion. For the simulations we set $T_{\text{amb}} = 295$ K and $\tau_D = 20$ ps. The other parameters for the electronic and phononic system are listed in Table 6.1.

For the magnetic parameters of the system, e.g. j_{ij} and γ_{ij}, we take the following approximations. The intrasublattice exchange coupling should be chosen in such a way that for pure Co or pure Gd the correct Curie temperature is retrieved from the Weiss model. Hence, we should have that

$$\begin{aligned} \gamma_{\text{Co-Co}} &= \frac{3k_B T_{C,\text{Co}}}{S_{\text{Co}} + 1}, && (6.7) \\ \gamma_{\text{Gd-Gd}} &= \frac{3k_B T_{C,\text{Gd}}}{S_{\text{Gd}} + 1}. && (6.8) \end{aligned}$$

The intrasublattice exchange coupling constants can then be found by using that

Table 6.1: Used parameters for the electron and phonon system [18].

symbol	value
D_F ($\text{eV}^{-1}\text{at}^{-1}$)	3
C_p ($\text{Jm}^{-3}\text{K}^{-1}$)	$4 \cdot 10^6$
g_{ep} ($\text{Jm}^{-3}\text{K}^{-1}\text{ps}^{-1}$)	$4.05 \cdot 10^6$
γ ($\text{Jm}^{-3}\text{K}^{-2}$)	$2.0 \cdot 10^3$
τ_D (ps)	20
σ (ps)	0.05

$\gamma_{ij} = zj_{ij}D_{s,j}S_j$. For $z = 12$ this leads to

$$j_{\text{Co-Co}} = \frac{3k_B T_{\text{C,Co}}}{12(S_{\text{Co}}+1)(\mu_{\text{at,Co}}/2)}, \tag{6.9}$$

$$j_{\text{Gd-Gd}} = \frac{3k_B T_{\text{C,Gd}}}{12(S_{\text{Gd}}+1)(\mu_{\text{at,Gd}}/2)}. \tag{6.10}$$

For the intersublattice exchange coupling constant $j_{\text{Co-Gd}}$, we assume that the ratio between $j_{\text{Co-Co}}$ and $j_{\text{Co-Gd}}$ is equal to the ratio used for Fe and Gd reported in [83]. This means that we use $j_{\text{Co-Co}}\mu^2_{\text{at,Co}} : j_{\text{Co-Gd}}\mu_{\text{at,Co}}\mu_{\text{at,Gd}} \sim -0.388$. Hence, we write

$$j_{\text{Co-Gd}} = -0.388 \times \frac{3k_B T_{\text{C,Co}}}{12(S_{\text{Co}}+1)(\mu_{\text{at,Gd}}/2)}. \tag{6.11}$$

From this, $\gamma_{\text{Co-Gd}}$ and $\gamma_{\text{Gd-Co}}$ can be easily calculated by using the definition $\gamma_{ij} = zj_{ij}D_{s,j}S_j$. Note that $\gamma_{\text{Co-Gd}}/\gamma_{\text{Gd-Co}} = \mu_{\text{at,Gd}}/\mu_{\text{at,Co}}$. This asymmetry is found to be important in how small the concentration range for switching the alloys is. The used magnetic system parameters are listed in Table 6.2.

6.B NOTES ON THE ZERO CROSSING TIMES

Figure 6.4 shows the time at which each separate Co monolayer is switched in a system of 14 Co monolayers and 3 Gd monolayers after laser pulse excitation at $t = 0$. It corresponds to the same system as the inset of Fig. 6.3. In contrast to the main text, the calculation presented here corresponds to $\lambda_{\text{Co-Co}} = \lambda_{\text{Co-Gd}} = \lambda_{\text{Gd-Gd}} = 5$. We observe a clearly different behavior of the Co monolayer adjacent to the interface compared to the results in the main text, which can be understood as follows. In our theory, we only include nearest-neighbor interactions. Hence, only the Co monolayer adjacent to the interface experiences an exchange field originating

Table 6.2: Magnetic parameters used in the calculations [1, 18].

symbol	Co	Gd
R (ps^{-1})	25.3	0.092
T_C (K)	1388	292
μ_{at} (μ_B)	1.72	7.55
S	1/2	7/2

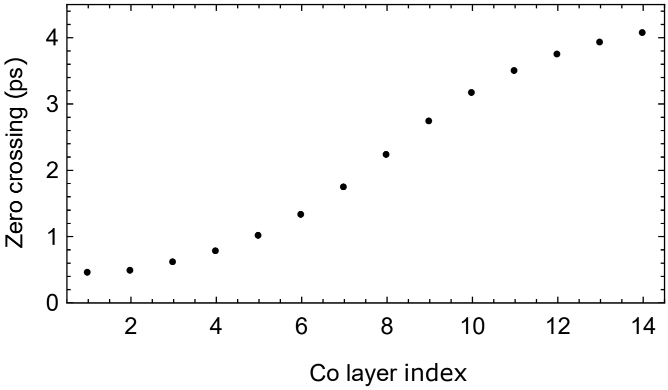

Figure 6.4: The time at which each Co monolayer is reversed (zero crossings) as a function of the Co layer index, in a system of 14 Co monolayers and 3 Gd monolayers. The figure shows the same situation as the inset of Figure 3 in the main text. However, here we used $\lambda_{\text{Co-Co}} = \lambda_{\text{Co-Gd}} = \lambda_{\text{Gd-Gd}} = 5$.

from the Gd layer. This exchange field opposes the demagnetization of the inner Co monolayer, eventually leading to a delayed demagnetization and switching of that Co monolayer. Comparing Fig. 6.4 ($\lambda_{\text{Co-Co}} = 5$) with Fig. 6.3 from the main text ($\lambda_{\text{Co-Co}} = 1$), clearly shows that increasing the exchange scattering rate $\eta_{\text{Co-Co}}$ leads to a faster switching mechanism ($\sim$ 2 times as fast). This again emphasizes that the exchange scattering between adjacent Co monolayers drives the switch throughout the Co layer.

7

THE ROLE OF INTERMIXING IN ALL-OPTICAL SWITCHING OF SYNTHETIC-FERRIMAGNETIC MULTILAYERS

We present a theoretical study of single-pulse all-optical switching (AOS) in synthetic-ferrimagnetic multilayers. Specifically, we investigate the role of interface intermixing in switching Co/Gd bilayers. We model the laser-induced magnetization dynamics in Co/Gd bilayers using the microscopic three-temperature model for layered magnetic systems. Exchange scattering is included, which mediates angular momentum transfer between the magnetic sublattices. In this chapter, each layer is represented by one atomic monolayer of a GdCo alloy with an arbitrary Co concentration, allowing Co/Gd bilayers with an intermixed interface to be modeled. Our results indicate that within the model intermixing of the Co/Gd interface reduces the threshold fluence for AOS significantly. We show that intermixing does not qualitatively affect the switching mechanism and leads to an increase of the propagation speed of the switching front. [1]

---

[1] This chapter has been published in AIP Advances [157].

7.1 Introduction

All-optical switching (AOS) refers to switching magnetization by femtosecond laser pulses and was first observed in ferrimagnetic GdFeCo alloys [10–12]. Single-pulse AOS has gained extensive attention due to the intriguing underlying physics and its potential for ultrafast data-writing technologies. Recently, it was demonstrated that not only alloys, but also Pt/Co/Gd stacks can be switched by the use of a single linearly polarized laser pulse [89]. This synthetic-ferrimagnetic multilayer has proven to be an ideal candidate for the integration of AOS in future magnetic memory devices [99]. Moreover, it has been shown that AOS in Pt/FM/Gd is very robust and can be achieved for a relatively large ferromagnetic (FM) layer thickness, i.e., the switching mechanism in synthetic-ferrimagnetic multilayers is independent of magnetization compensation (Chapter 6 and Ref. [127]).

The key ingredient of single-pulse AOS is that the material system contains multiple magnetic sublattices, coupled by an antiferromagnetic exchange interaction. The exchange coupling drives the magnetization reversal by transferring angular momentum between the sublattices [76]. This insight was corroborated by simulations using the atomistic Landau-Lifshitz-Gilbert equation [79, 81, 83–85]. An alternative approach was derived by extending the microscopic three-temperature model (M3TM) to multisublattice magnets [78]. The latter includes exchange scattering as the mechanism for angular momentum transfer between the sublattices. Very recently, we extended this model to describe single-pulse AOS in Co/Gd bilayers (Chapter 6 and Ref. [127]). Based on the simulations, it was concluded that the robustness of AOS in Pt/FM/Gd is caused by the nonlocal character of the switching mechanism. For example, the mechanism in Co/Gd bilayers can be understood as a front of reversed Co magnetization that, after laser-pulse excitation, nucleates at the Co/Gd interface and propagates through the Co layer driven by exchange scattering. An important question is to what extent the properties of the Co/Gd interface, e.g. the amount of intermixing, affect the switching mechanism within the model.

In this chapter, we show that intermixing reduces the threshold fluence for AOS in Co/Gd bilayers and leads to faster propagation of the switching front. We perform simulations of AOS in Co/Gd bilayers including an intermixed interface. In order to do this, we define each atomic monolayer in the Co/Gd bilayer as a GdCo alloy with an arbitrary Co concentration. By choosing the appropriate Co concentration for each monolayer, a Co/Gd bilayer including an intermixed (alloyed) interface is modeled. We use the M3TM including exchange scattering to describe the magnetization dynamics of the system [78, 127], which was discussed in Section 2.7.1 and used in Chapter 6. We present phase diagrams that show the reduced threshold fluence. Finally, we analyze the role of intermixing on the propagating switching mechanism by calculating the switching times for the individual atomic monolayers.

7.2 MODELING AOS OF INTERMIXED CO/GD BILAYERS

In the first part of this section, we discuss how the layered M3TM, which was introduced in Chapter 6, can be extended to describe synthetic-ferrimagnetic bilayers with an intermixed interface. Before discussing the extension, we shortly summarize the basic description.

To describe the system of interest, we introduce multiple spin subsystems that are all coupled to a single electron and phonon system [78]. We consider the same approximations as the basic M3TM [18], where the electrons are described as a spinless free electron gas and the phonons are treated within the Debye model. The electron and phonon systems are internally thermalized and the electron temperature T_e and phonon temperature T_p are homogeneous. The spin specific heat is neglected. The electron system contains an energy source term that represents the laser pulse. Heat diffusion to the substrate is included in the phonon system as an energy dissipation term. The spin subsystems are treated within a Weiss mean-field approach and all compose a magnetic sublattice with at each lattice site $D_\mathrm{s} = \mu_\mathrm{at}/2S$ spins, where μ_at is the atomic magnetic moment (in units of the Bohr magneton μ_B) and S is the spin quantum number.

We consider a system of N atomic monolayers. Each layer i corresponds to a two-dimensional $\mathrm{Gd}_{1-x_i}\mathrm{Co}_{x_i}$ alloy with Co concentration x_i. Hence, all the layers consist of two magnetic sublattices, one for each compound. We define $m_{\mathrm{Co},i}$ and $m_{\mathrm{Gd},i}$ as the normalized magnetization of a specific magnetic sublattice in layer i ($i \in [1, N]$). In the following, we only take into account nearest-neighbor interactions. First, we introduce the bulk exchange splitting for a $\mathrm{Gd}_{1-x_i}\mathrm{Co}_{x_i}$ alloy with Co concentration

x_i (see Chapter 6 or Ref. [127])

$$\begin{aligned}
\Delta^{\text{bulk}}_{\text{Co},i} &= x_i \gamma_{\text{Co-Co}} m_{\text{Co},i} + (1-x_i)\gamma_{\text{Co-Gd}} m_{\text{Gd},i}, & (7.1)\\
\Delta^{\text{bulk}}_{\text{Gd},i} &= x_i \gamma_{\text{Gd-Co}} m_{\text{Co}} + (1-x_i)\gamma_{\text{Gd-Gd}} m_{\text{Gd},i}, & (7.2)
\end{aligned}$$

where we defined $\gamma_{kl} = j_{kl} z D_{\text{s},l} S_l$ ($k,l \in \{\text{Co,Gd}\}$) in terms of the (intra- or inter-sublattice) exchange coupling constant j_{kl} and the number of nearest neighbors z.

To express the exchange splitting in the N layers of $\text{Gd}_{1-x_i}\text{Co}_{x_i}$, we assume that the separate layers lie in the (111) plane of an fcc lattice. In that case, each atom has 6 nearest neighbors in the same layer and 3 nearest neighbors in each adjacent layer. The exchange splitting for a specific compound in layer i is

$$\begin{aligned}
\Delta_{\text{Co},i} &= \frac{1}{4}\Delta^{\text{bulk}}_{\text{Co},i-1} + \frac{1}{2}\Delta^{\text{bulk}}_{\text{Co},i} + \frac{1}{4}\Delta^{\text{bulk}}_{\text{Co},i+1}, & (7.3)\\
\Delta_{\text{Gd},i} &= \frac{1}{4}\Delta^{\text{bulk}}_{\text{Gd},i-1} + \frac{1}{2}\Delta^{\text{bulk}}_{\text{Gd},i} + \frac{1}{4}\Delta^{\text{bulk}}_{\text{Gd},i+1}. & (7.4)
\end{aligned}$$

Note that for a homogeneous system (i.e., $x_i = x$ for all i) the exchange splitting reduces to the bulk value, Eqs. (7.1) and (7.2). For simplicity, we describe both the Co and Gd by a $S = 1/2$ system. Hence, all the spin subsystems correspond to a two-level system, split by the energy $\Delta_{\text{Co},i}$ or $\Delta_{\text{Gd},i}$. We note that the model can be easily extended to $S = 7/2$ for Gd, as was shown in Chapter 6.

In our model, the dynamics of the magnetic sublattices is driven by two interactions. First, Elliott-Yafet spin-flip scattering results in angular momentum transfer between the magnetic sublattices and the phonon system. The basic M3TM is used to describe the resulting magnetization dynamics [18]. Secondly, we include exchange scattering, which corresponds to electron-electron scattering with an opposing spin flip. Exchange scattering mediates angular momentum transfer between the different magnetic sublattices. The resulting magnetization dynamics is derived from Fermi's golden rule, using the exact same procedure as reported in Chapter 6.

The result is a system of coupled differential equations, which expresses $dm_{k,i}/dt$ for all compounds k and layers i. Each equation will contain terms for the angular momentum transfer (by exchange scattering) between (i) the two different compounds in the same layer, (ii) two different compounds in adjacent layers, and (iii) the same compound in adjacent layers. These terms will implicitly depend on the Co concentration of each layer via the coordination number, i.e., the number of

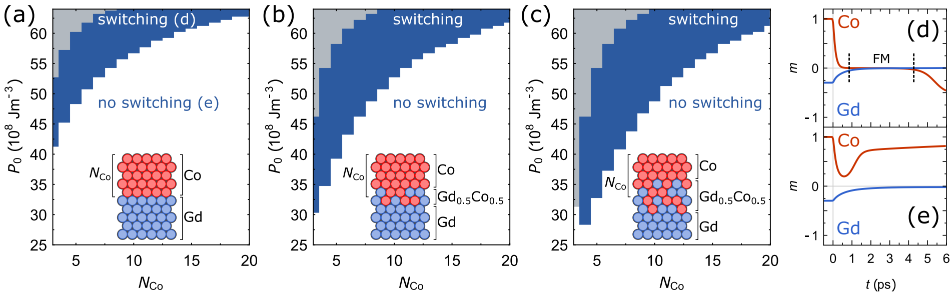

Figure 7.1: Phase diagrams for AOS as a function of the laser pulse energy P_0 and the number of Co monolayers N_{Co} in a Co/Gd bilayer. Figure (a) shows the phase diagram for an ideal Co/Gd bilayer, without intermixing at the Co/Gd interface (see inset Fig. (a)). Figure (b) shows the phase diagram for Co/Gd bilayers including intermixing, modeled by replacing the two layers adjacent to the interface with two layers of $\mathrm{Gd}_{0.5}\mathrm{Co}_{0.5}$ (see inset Fig. (b)). Figure (c) shows a similar phase diagram, but now the intermixing region is extended to four layers (see inset Fig. (c)). The blue regions indicate a switch in the final state and the white regions indicate no switch. Gray indicates that the phonon temperature T_p exceeds the Curie temperature T_C. The insets in (a)-(c) schematically show the modeled system. Figures (d) and (e) show the normalized magnetization of the Co and Gd layer as a function of time, in the case of switching (d) and no switching (e).

nearest neighbors of a specific compound and layer. The latter involves the same counting procedure as the derivation of the exchange splitting in Eqs. (7.3) and (7.4). Furthermore, all the exchange scattering terms depend on the corresponding matrix element of the exchange scattering Hamiltonian and the probability of an electron-electron scattering event to occur. For the mathematical description of these terms and a detailed discussion about the system parameters, we refer to Chapter 6 or Ref. [127].

The normalized magnetization $m_{k,i}(t)$ is calculated by solving the system of coupled differential equations numerically. In these simulations, the temporal profile of the laser pulse is given by $P(t) = (P_0/(\pi\sqrt{\sigma}))\mathrm{Exp}(-(t-t_0)^2/\sigma^2)$, where P_0 is the laser pulse energy density and σ is the pulse duration, which is set to 50 fs. Furthermore, the ambient temperature T_{amb} is set to 295 K.

We construct three phase diagrams that display the occurrence of AOS in Co/Gd bilayers as a function of the laser pulse energy P_0 and the number of Co monolayers N_{Co}. Figure 7.1(a) shows the phase diagram for an ideal Co/Gd bilayer, without intermixing of the Co/Gd interface. Figure 7.1(b) displays the phase diagram for an intermixed Co/Gd interface, described by replacing the two layers adjacent to the interface with a $\mathrm{Gd}_{0.5}\mathrm{Co}_{0.5}$ alloy. In Fig. 7.1(c), the intermixing region is further extended to four layers of $Gd_{0.5}Co_{0.5}$. Note that the definition of N_{Co} is unchanged (see insets Figs. 7.1(a)-(c)). The color scheme indicates whether the average magnetization of the Co layers is reversed after relaxation, which is determined by calculating its sign at $t = 100$ ps. Figures 7.1(d)-(e) show the dynamics of the normalized magnetization for an ideal Co/Gd bilayer, and are presented to clarify the color scheme of the phase diagrams. The blue regions indicate that AOS has occurred successfully, i.e., the magnetization is reversed (Fig. 7.1(d)). The white regions indicate that AOS has not occurred and the magnetization remained in its initial direction (Fig. 7.1(e)). The gray regions correspond to the situation where the phonon temperature T_p has exceeded the Curie temperature T_C. In the experiments this would likely result in the creation of a multidomain state [154].

Figure 7.1(a) clearly shows, as was discussed in Chapter 6, that the Co/Gd bilayers can be switched for a relatively large number of Co layers N_{Co}, i.e., for a large Co layer thickness. Moreover, the threshold fluence increases as a function of N_{Co}. The qualitative behavior observed in the phase diagram can be understood by the switching mechanism in the Co/Gd bilayers. First, the Co layers near the interface are switched, creating a front of reversed Co magnetization. Subsequently, the front propagates through the system driven by exchange scattering between adjacent layers. This propagating mechanism will continue until all Co layers are switched.

The phase diagram for the Co/Gd bilayers including intermixing shows the same qualitative behavior, as is depicted in Fig. 7.1(b). Interestingly, for relatively thin Co layers ($N_{Co} = 3$-5), the threshold fluence is reduced by $\sim 25\%$ compared to the system without intermixing. The reduction of the threshold fluence can be understood by (i) in the case of intermixing there is effectively more angular momentum transfer between Co and Gd sublattices, and (ii) a decrease of the Curie temperature T_C. Note that the observed value for the threshold fluence is now comparable to the value found in the simulations for the alloys (see Chapter 6 Fig. 6.2(a) on page 140).

Figure 7.1(c) shows that increasing the size of the intermixing region leads to a further reduction of the threshold fluence. However, no switching is observed for $N_{Co} = 3$. This can be understood from the fact that this particular system is very similar to a homogeneous $Gd_{0.5}Co_{0.5}$ alloy, which can not be switched because the total magnetic moment is not close to compensation.

Following the analysis of the phase diagrams, the question that arises is to what extent the intermixing of the Co/Gd interface influences the properties of the propagating switching mechanism. Figure 7.2(a) shows a detailed analysis of the switching mechanism in a system of 10 Co and 5 Gd layers. It displays the time at which each individual Co layer is reversed as a function of the layer index. The Co layers are labeled from 1 to 10, where the index 1 represents the Co layer adjacent to the Co/Gd interface. We consider the same three systems as in the phase diagrams (with $N_{\mathrm{Co}} = 10$), which are schematically presented in Figs. 7.2(b)-(d). Note that the layer indices are unchanged despite the addition of an intermixing region. In Fig. 7.2(a), the red dots represent an ideal Co/Gd bilayer, without intermixing (see Fig. 7.2(b)). The blue and yellow dots represent a Co/Gd bilayer with an intermixing region of two and four layers respectively (see Figs. 7.2(c)-(d)). Figure 7.2(a) shows that in all three systems the layers are switched consecutively starting with the layers near the interface, which defines the propagating switching mechanism. However, in the case of an ideal Co/Gd interface, the layer adjacent to the interface acts differently. As discussed in Chapter 6, in the approximation of only nearest-neighbor interactions, this is caused by the exchange field resulting from the slowly demagnetizing Gd layer [127]. This field slows down the demagnetization and reversal process of the inner Co layer due to the antiferromagnetic exchange coupling between Co and Gd. In the presence of intermixing, this effect is shifted to the unlabeled layers. Importantly, the blue and yellow dots clearly show that the propagating characteristics of the switching mechanism are maintained after including intermixing within the model.

To analyze the propagation speed of the switching front, we focus on the region from layer 3 to layer 10, which consists entirely of Co in all three systems (Figs. 7.2(b)-(d)). The propagation speed can be approximated from the interval between the switching times of layer 3 and 10 and the corresponding distance the switching front has traveled. Here, we take 0.2 nm for the thickness of one atomic monolayer of Co [89]. For the system without intermixing, the propagation speed is then given by approximately 2.1 km/s. For the systems including intermixing, we find a propagation speed of 3.9 km/s (Fig. 7.2(c)) and 6.6 km/s (Fig. 7.2(d)) respectively. Hence, intermixing of the Co/Gd interface increases the propagation speed of the switching front significantly. As noted before, intermixing leads to effectively more angular momentum transfer between the Co and Gd sublattices near the interface, increasing the magnetization gradient in the Co layer. This leads to a larger propagation speed of the switching front because the speed is related to the magnitude of the magnetization gradient.

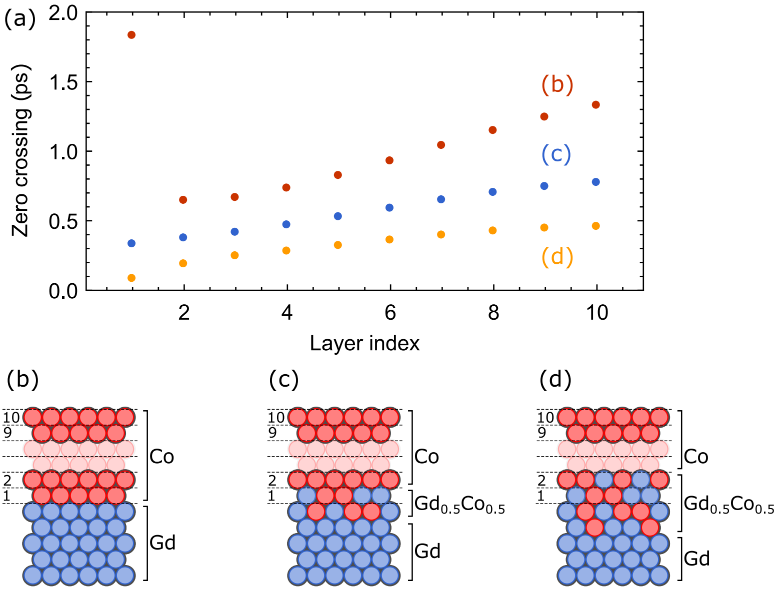

Figure 7.2: (a) The time at which each atomic Co monolayer is reversed for the systems indicated in Figures (b)-(d) and $P_0 = 60 \cdot 10^8 \text{Jm}^{-3}$. Figure (b) displays a system of 10 Co and 5 Gd atomic monolayers. The Co layers are numbered 1-10, where index 1 refers to the layer adjacent to the interface. Figures (c) and (d) show the systems including intermixing, with the Co/Gd interface replaced by two (c) and four (d) layers of $Gd_{0.5}Co_{0.5}$.

7.3 CONCLUSION

To conclude, within the model we considered in this paper, intermixing leads to a significant reduction of the threshold fluence for AOS compared to the ideal Co/Gd interface. Furthermore, intermixing does not affect the qualitative properties of the switching mechanism in Co/Gd bilayers. Quantitatively, intermixing increases the speed of propagation. Hence, previously reported statements about the switching mechanism in ideal Co/Gd bilayers can be generalized to bilayers including an intermixed Co/Gd interface.

8

ADDITIONAL RESEARCH AND OUTLOOK

In this final chapter, we present preliminary results regarding various applications of the previously discussed models. The aim of the presented calculations is to substantiate both the promises and limitations of the used theoretical methods. As a comprehensive example, the chapter opens with modeling laser-induced spin transport in ferrimagnetic systems. Specifically, we discuss spin-current-assisted all-optical switching in (synthetic-)ferrimagnetic multilayers. Furthermore, we model the excitation of standing spin waves with optically-generated spin currents and relate the results to recent experiments. Importantly, the sections only describe the calculations conceptually and do not specify the precise theoretical implementations. The latter is partially discussed in Appendix B, or is explained in the given references. The chapter ends with a general outlook on the field of ultrafast spintronics.

8.1 INTRODUCTION

In this final chapter, we present a collection of additional calculations using the models described in the previous chapters. The aim is to investigate several recently demonstrated phenomena that enlighten the full spectrum of ultrast magnetism. Furthermore, the presented preliminary calculations will elucidate both the utility and limitations of the proposed theoretical methods. The topics are chosen such that we can shortly address the connection with future applications. For that reason, the work mainly focuses on the laser-induced spin dynamics in magnetic heterostructures with a (synthetic-)ferrimagnetic component. Here, the interplay of all-optical switching and spin transport is of interest in relation to future opto-magnetic memory devices.

First, in Sec. 8.2 we show preliminary calculations regarding all-optical switching in GdFeCo/Cu/$[\mathrm{Co/Pt}]_N$ stacks, aiming to model the experimental results of Iihama and coworkers [100, 103, 104, 130]. There, a *ferro*magnetic layer is effectively reversed driven by the interlayer spin current generated by a *ferri*magnetic layer. This is particularly interesting in the context of implementing all-optical switching in future magnetic random-access memory, since a switchable ferromagnetic layer is advantageous for achieving the maximal readout capability within magnetic tunnel junctions [158].

In addition to reaching an efficient readout capability, another essential requirement is that all-optical switching should be transformed from a toggle mechanism to a fully deterministic writing process. Specifically, the magnetization direction of the written domain should be predetermined regardless of the initial state. Deterministic magnetization writing can be accomplished by introducing an additional magnetic reference layer. In line with the experiments of van Hees et al. [105] in rapidly-heated [Gd/Co]/Cu/FM multilayers, Sec. 8.3 presents calculations that elucidate the dependence of the switching threshold fluence on the magnetic orientation of the ferrimagnetic component and a reference ($[\mathrm{Co/Ni}]_N$) layer. As a result of this mechanism driven by interlayer spin transport, the laser fluence can be tuned to write a predetermined domain[105] .

In the examples above, the characteristic temporal behavior of the induced interlayer spin current plays a critical role. Similarly, in noncollinear magnetic heterostructures, the precise pulse shape of the interlayer spin current determines the ability and efficiency of exciting perpendicular standing spin waves in the receiving layer. In Sec. 8.4 we shortly discuss a simple analytical description that characterizes the excitation mechanism of the standing spin waves. The second part of this section includes a specific example related to the experiments of Lichtenberg et al. [159]. Here, the investigated noncollinear magnetic heterostructure includes a Co/Gd bilayer. The investigated standing spin waves are used to characterize the spin current that is generated within the ferrimagnetic region.

The abovementioned calculations partially agree with the results from the recent experimental works and clarify the underlying physical trends. Nevertheless, we observe clear limitations of the used simplified models in the case they are applied to a complex magnetic multilayer. The limitations are listed throughout this chapter.

Examples include the need for using atypical values for specific system parameters and the insufficiency of a pure diffusive treatment of laser-induced spin transport. The final section of the chapter, Sec. 8.5, puts the typical theoretical methods into a general perspective. Furthermore, it provides a brief outlook on the field of ultrafast magnetism and lists the most promising applications.

8.2 SWITCHING FERROMAGNETIC LAYERS WITH LASER-INDUCED SPIN CURRENTS

In this section, we model the laser-induced spin dynamics in GdFeCo/Cu/FM stacks, and relate the calculations to the experiments of Refs. [100, 104, 130], where the ultrafast switching of a ferromagnetic (FM) $[\mathrm{Co/Pt}]_N$ layer was demonstrated. A schematic overview of the system is given in Figs. 8.1(a)-(b). Here, we defined the parallel (PA) and antiparallel (AP) configurations of the initial magnetization direction in the FM layer and the transition-metal component of the GdFeCo alloy. The theoretical implementation of this complex magnetic structure is built up as follows. The ferromagnetic $[\mathrm{Co/Pt}]_N$ layer is approximated by a homogeneous material and described with the standard *s*-*d* model, as was previously used in Chapters 2 and 3. Furthermore, the ferrimagnetic GdFeCo component is described with the extension of the *s*-*d* model to ferrimagnetic alloys from Ref. [58], as was discussed in Sec. 2.7. In response to an increase of the electron temperature, this combined *s*-*d* model allows us to calculate the temporal behavior of the element-specific magnetization. Simultaneously, a spin accumulation will be generated within both magnetic regions and its nonzero gradient will result in interlayer spin transport. The latter is calculated through solving the spin diffusion equation within the full multilayer, in analogy with Sec. 3.5. In that way, up to a numerically practical length scale, we reach a spatially continuous model that jointly describes the local magnetization and the generated diffusive spin currents throughout the full magnetic stack. All used system parameters are given in Appendix B. Before presenting the results, we stress that the preliminary calculations required the use of some atypically valued system parameters to give a clear qualitative agreement with experiments. This limitation will be thoroughly discussed at the end of this section.

The presented calculations focus on determining the all-optical switching capability as a function of composition and absorbed laser-pulse energy. In that way, we

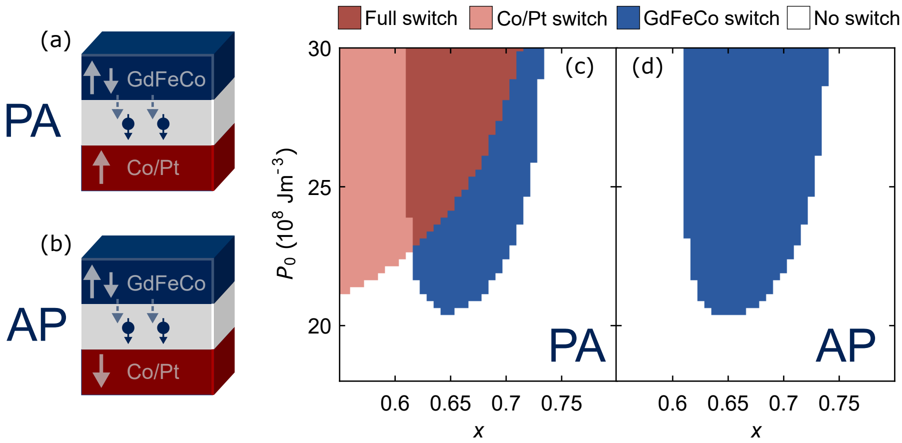

Figure 8.1: Modeling the laser-induced spin dynamics in GdFeCo/Cu/[Co/Pt]$_N$ multilayers. (a)-(b) Schematic overview of the magnetic multilayer and the generated interlayer spin current. In comparison, (a) and (b) indicate the parallel (PA) and antiparallel (AP) configurations between the FeCo and [Co/Pt]$_N$ magnetization direction. (c)-(d) Phase diagrams of the possible switched states, as a function of the FeCo concentration x and the absorbed laser-pulse energy density P_0. White indicates that none of the magnetic layers is switched. Furthermore, blue indicates that solely the GdFeCo is switched, whereas light red specifies a pure [Co/Pt]$_N$ switch. Finally, dark red corresponds to a complete switch.

can compare the modeling directly to the experiments of Ref. [130]. The results are presented in Figs. 8.1(c)-(d), where the two phase diagrams indicate the layer-specific switching capability as a function of the transition-metal concentration x of the Gd$_{1-x}$FeCo$_x$ layer and the absorbed laser-pulse energy density P_0. Figure 8.1(c) and (d), respectively, indicate the calculations for the initial parallel (c) and antiparallel (d) configurations. The color scheme specifies the switching of the distinct layers. White indicates that the magnetization direction within the full structure remains unchanged after equilibration. Blue indicates that only the alloy is successfully switched, whereas the light red region corresponds to the situation that only the FM layer magnetization is reversed. Finally, dark red indicates that both magnetic layers are simultaneously switched with a single pulse.

The phase diagram for the initial parallel configuration, as given in Fig. 8.1(c), is in a qualitative agreement with the experiments of Remy et al. [104, 130]. Importantly, it shows that all magnetic states of the multilayer can be reached by toggling the magnetization direction with a single laser pulse, indicated by the presence of a colored region for all components of the above-defined scheme. Additionally, the figure shows that the threshold fluence for a single-layer switch as a function of concentration, indicated by the top boundary of the white region, changes from being minimal for an FM layer switch (light red) to favoring a pure alloy switch (blue). The latter was quantitatively determined in Ref. [130]. Intuitively, switching of the FM layer favors a high Gd concentration, as the spin current generated in a Gd-rich ferrimagnetic alloy has the required polarization to be able to reverse the FM layer magnetization [102]. It is clear that this concept depends on the initial magnetic configuration of the multilayer. As it turns out, the modeling for the antiparallel configuration, as presented in Fig. 8.1(d), is not in full agreement with the experiments. The figure exclusively indicates the all-optical switching of the GdFeCo alloy, as represented by the blue region. Here, one might expect that at a high transition-metal concentration the spin current is sufficient to drive the switching of the FM layer, which was experimentally demonstrated in Ref. [104]. Although it is possible to observe this in the modeling by tuning the parameters, it does not appear under physically relevant conditions.

We again note that the shown phase diagrams correspond to preliminary calculations. A systemic effort to determine the best fitting choices for all system parameters has not been employed yet. Additionally, we observe two clear limitations of the used theoretical description. First, to observe a successful switch of the FM layer, it is required that its thickness is not much larger than the spin diffusion length. As the latter is expected to be of the order of ~ 1 nm for Co/Pt [72], we can not fully explain the switching of the 5 nm thick layers in the experiments [130]. To clarify, in the modeling we used a 1 nm thin $[\text{Co/Pt}]_N$ layer. This might be an indicator that one should implement superdiffusive spin currents to account for a larger penetration depth [39]. Second, in order to observe AOS in the ferrimagnetic alloy, it is needed to use a demagnetization time for the Gd that disagrees with the expected timescale [18], as was already noted in Sec. 2.7.2.

Although the calculations are not in full agreement with the experiments, the theoretical implementation using the *s*-*d* model provides a clear conceptual view of the ability to switch ferromagnetic materials through optically-generated spin transport. As noted in Sec. 8.1, the indication that picosecond switching is possible in ferromagnetic materials is a major step towards implementing all-optical switching in future opto-magnetic memory devices [153, 158]. It can either be accomplished through interlayer spin transport, as discussed here, or through a similar mechanism based on an interlayer exchange coupling [153].

In the following section, we investigate how the presence of a ferromagnetic reference layer manipulates the original switching mechanism for the ferrimagnetic component. Connecting it to the calculations above, the blue regions in the phase diagrams of Figs. 8.1(c)-(d) hardly show a difference in threshold fluence, indicating that in this system the ferromagnetic layer only weakly influences the AOS process of the ferrimagnetic alloy. In an optimized magnetic multilayer, the presence of an additional ferromagnetic layer has an advantageous effect on the all-optical switching capability of the ferrimagnetic region. The latter is the main topic of the following section, where we discuss spin-current-assisted all-optical switching in synthetic-ferrimagnetic multilayers.

8.3 SPIN-CURRENT-ASSISTED ALL-OPTICAL SWITCHING IN SYNTHETIC-FERRIMAGNETIC MULTILAYERS

In collinear magnetic heterostructures the demagnetization rates are enhanced if the magnetization of the individual ferromagnetic layers are aligned antiparallel. This was experimentally demonstrated by Malinowski et al. [14], and modeled in Sec. 3.4 of this thesis. A similar effect can be observed in case one of the layers is replaced by a ferrimagnetic component that allows helicity-independent all-optical switching. The remaining ferromagnetic layer, which is now dubbed as the 'reference layer', may assist or hinder the reversal of the ferrimagnet due to the generation of an interlayer spin current. Originally, this property was demonstrated in Gd/Co/Cu/[Co/Ni]$_N$ multilayers [105]. In this section, we model the time-resolved magnetization and verify that the description based on the *s*-*d* model qualitatively agrees with the experiments.

The magnetic system is modeled in analogy with the calculation presented in the previous section, where we have to specify two major changes. First, the ferrimagnetic region is implemented as an intermixed Co/Gd bilayer, where the width of the intermixed region is of the order of nanometers. Second, the reference layer is a relatively thick (5 nm) transition-metal ferromagnet. Schematic overviews of the modeled systems are given in Figs. 8.2(a)-(b), where we specify the parallel (PA) and antiparallel (AP) configurations between the top Co layer and the magnetization direction of the reference layer. Again, the set of system parameters is given in Appendix B. Additionally, the precise implementation of the intermixing region, which is modeled by a continuous step function for the concentration, is given in

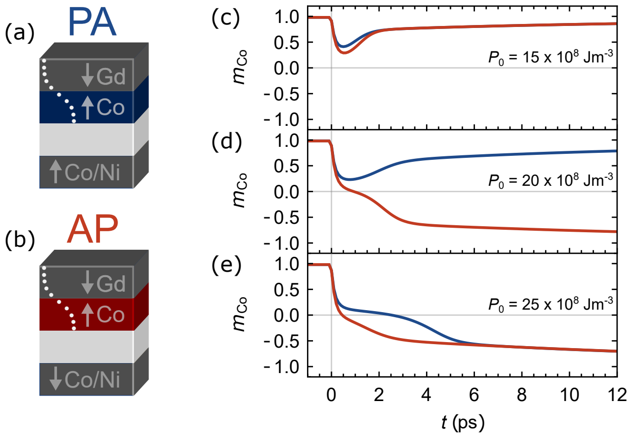

Figure 8.2: (a)-(b) Schematic overview of the multilayer system in case of a parallel (a) and antiparallel (b) configuration of the Co and reference [Co/Ni] layer. The white dots illustrate the typically used Co concentration profile in the intermixed Co/Gd bilayer. (c)-(e) The Co magnetization as a function of time after laser-pulse excitation at $t = 0$, plotted for varying absorbed laser-pulse energies P_0. The blue lines correspond to the parallel configuration (a), whereas the red lines correspond to the antiparallel configuration (b). Figure (d) illustrates that the interlayer spin current assists the all-optical switching process in the antiparallel configuration.

Ref. [159]. We note that the precise qualitative characteristics of the calculations below do not significantly depend on the implementation of intermixing.

To model the effect of interlayer spin transport on the all-optical switching of the synthetic-ferrimagnetic bilayer, we calculate the magnetization of the top Co layer as a function of time after laser-pulse excitation for the two distinct initial configurations. For increasing absorbed laser-pulse energy P_0, the results are given in Figs. 8.2(c)-(e), where the blue lines indicate the parallel configuration and the red lines indicate the antiparallel configuration. At low fluence, Fig. 8.2(c), the magnetization of the Co only demagnetizes for both configurations. Interestingly, for an intermediate magnitude of the absorbed energy, represented by Fig. 8.2(d), the Co magnetization switches in case the initial configuration with the reference layer is antiparallel. Finally, Fig. 8.2(e) shows the results for a high fluence and indicates the case that the Co magnetization switches regardless of the initial magnetic state of the multilayer. In analogy with the experiments of Ref. [105], the modeling shows that by tuning the laser fluence all-optical switching of the multilayer can be restricted to the antiparallel configuration. Using this, one can select a (double-)pulse scheme that writes a predetermined magnetic domain regardless of the initial state of the multilayer [105]. In that way, all-optical switching evolves from a toggle mechanism to a deterministic magnetization writing technique [105], which is desirable for applications.

Again, we stress that the presented calculations correspond to preliminary results and still require a more in-depth analysis. Obviously, the complex magnetic structures discussed here are tricky to implement on a physically consistent basis, especially due to a large number of unknown system parameters. Additionally, the numerical implementation is nontrivial. A technical dilemma arises, since the description of spin diffusion requires a continuous model, whereas to describe the local magnetization in the ferrimagnet an atomistic approach seems to be more relevant (as used in Chapters 6 and 7). Such a combined approach is only reliable in the case that all relevant length scales, including the spin diffusion length and the width of the intermixing region, are multiple orders of magnitude larger than the atomic spacing, which is not necessarily the case. Nevertheless, it is expected that the modeled qualitative behavior is realistic, as all imposed mathematical conditions are at least weakly satisfied.

In the context of the above spin-current-assisted all-optical switching process, one can imagine that the temporal shape of the interlayer spin current plays a critical role. Furthermore, in connection to the previous section, optical spin-current generation in Gd-based (synthetic-)ferrimagnets is an interesting concept from a technological perspective. Although it is possible to probe the generated spin transport in the two-component GdFeCo/Cu heterostructures, such as the experiments in Ref. [102], determining the interlayer spin currents in more complex magnetic multilayers is an unprecedented challenge.

One possibility is to indirectly characterize the optically-generated spin currents by focusing on noncollinear magnetic structures, and investigating the response of the transverse magnetization following the ultrafast spin-transfer torque [64–67]. As will be discussed in the following section, by probing the excited precessions one can partially deduce the pulse shape of the absorbed interlayer spin current [136, 159]. Before focusing on ferrimagnetic structures, we first present a simple analytical description of standing spin waves that provides a practical mathematical tool to investigate the excited magnetization dynamics.

8.4 THz STANDING SPIN WAVES IN NONCOLLINEAR MAGNETIC HETEROSTRUCTURES

In this section, we discuss the spin dynamics excited in noncollinear magnetic heterostructures by femtosecond laser-pulse excitation. This subject was shortly addressed in Sec. 1.3 by referring to the experimental demonstration of THz spin waves in Fig. 1.5(b). A schematic overview of the noncollinear magnetic heterostructure is given in Fig. 8.3(a), indicating the two perpendicularly magnetized layers and the interlayer spin current $j_s(t)$ that exerts the spin-transfer torque. In the following, we refer to the in-plane layer as the absorption layer, since it is our main interest, and the out-of-plane layer is dubbed as the generation layer. To model this combined spin system, we separate the theoretical problem into two steps. (i) The spin current from the generation layer is calculated with the *s*-*d* model including spin diffusion. Here, the (perpendicular) absorption layer is treated as an ideal spin sink and implemented within the boundary conditions. (ii) To describe the excited transverse magnetization dynamics in the generation layer, we use a linearized Landau-Lifshitz-Gilbert-Slonczewski equation with the spin current from (i) as an input function [7, 142]. As step (i) is already covered in Chapters 3 and 4, we here only discuss the implementation of step (ii).

The details of the implementation of step (ii) are presented in Appendix B. In summary, the model includes the effects of an (in-plane) external field, the exchange interaction, bulk Gilbert damping, interfacial spin pumping (at the FM/NM interface), and the anti-damping spin-transfer torque [7, 142]. Essentially, the latter is assumed to be driven by the externally generated spin current described by function $j_s(t)$ that is perpendicularly polarized. In the linear regime, assuming that the normalized transverse magnetization remains much smaller than one, this leads to a simple linear differential equation in terms of the out-of-plane spatial coordinate x and time t. In anticipation of that we investigate standing spin waves, the solution is expressed in terms of a cosine expansion, as schematically depicted by the white lines in Fig. 8.3(a). The amplitude of mode n, represented by dimensionless function $\delta m_{x,n}(t)$, can be expressed as a convolution

$$\delta m_{x,n}(t) \propto \mathrm{Re}\{(G_n * j_s)(t)\}. \tag{8.1}$$

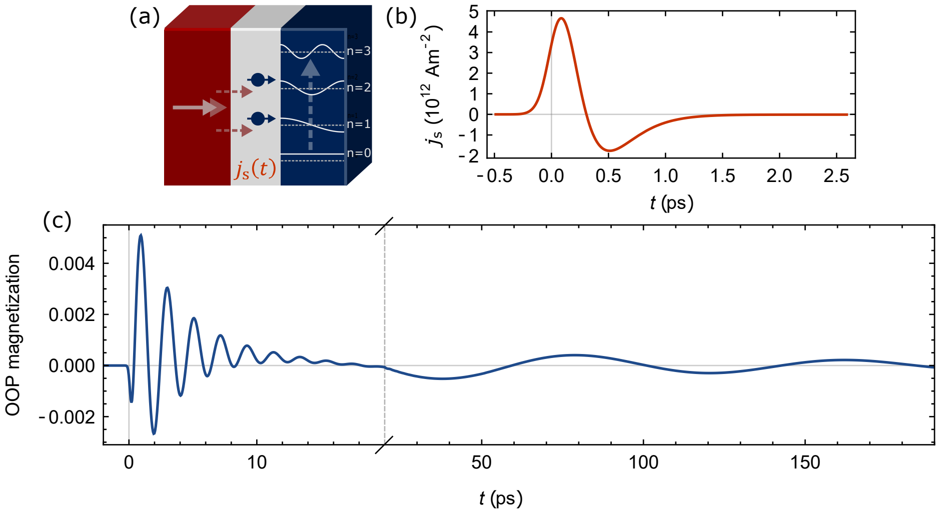

Figure 8.3: (a) Schematic overview of the excitation of transverse spin dynamics in a noncollinear magnetic heterostructure through laser-induced spin currents. The white lines in the in-plane (absorption) layer indicate the first four standing spin-wave modes. (b) The spin current $j_s(t)$ at interface of the (in-plane) absorption layer, plotted as a function of time after laser-pulse excitation at $t = 0$. (c) The (normalized) out-of-plane magnetization component of the absorption layer as a function of time. The plot includes the first normal mode ($\sim$ 0.5 THz) and the homogeneous mode (12 GHz).

The function $G_n(t)$ describes the response function of mode n, and is given by

$$G_n(t) \propto \theta(t) e^{i\omega_n(1+i\alpha_{\mathrm{eff},n})t}, \tag{8.2}$$

where it is assumed that the (mode-dependent) effective damping $\alpha_{\mathrm{eff},n}$ is much smaller than one. Intuitively, the response function describes a damped oscillation with frequency ω_n and effective damping $\alpha_{\mathrm{eff},n}$. The dispersion relation is given by $\omega_n = \omega_0 + A(n\pi/L)^2$, with ω_0 the angular FMR frequency, A the spin-wave stiffness, and L the thickness of the absorption layer.

Typically, in the experiments the out-of-plane magnetization is probed in the region near the outer edge of the absorption layer. Using the linearized approach discussed above, it is a straightforward task to model such a typical magnetic response. For an intuitive example, we use the spin current as given in Fig. 8.3(b), which followed from the *s*-*d* model for a standard transition-metal generation layer. Subsequently, Eq. (8.1) is used to determine the response of the transverse magnetization. The result for the zeroth and first normal modes is plotted in Fig. 8.3(c) as a function of time. Here, we used that the absorption layer is 5 nm thick and the FMR frequency is 12 GHz. Furthermore, the spin-wave stiffness is chosen such that the first normal mode has a frequency of $\sim$ 0.5 THz. All remaining parameters are set equal to the values given in Ref. [159]. For convenience, we did not include higher-order normal modes. The amplitude of these modes remains small and is damped out very rapidly. Nevertheless, as the exact result requires an infinite sum of modes, the plotted curve is incomplete near $t = 0$. With that in mind, the simple calculation qualitatively agrees with the magneto-optical signal from the experiments in Ref. [67], as was shown in Fig. 1.5(b).

To connect this approach to the previous sections, we replace the ferromagnetic generation layer with a synthetic-ferrimagnetic Co/Gd bilayer. A schematic overview of the system is given in Fig. 8.4(a). The recent experiments in Ref. [159] proposed that the excited transverse magnetization in the absorption layer, especially the phase of the excited oscillation, gives information about the interlayer spin current. To model this, we use the same approach as the previous section to describe the synthetic-ferrimagnet bilayer. Again, the generated spin current is calculated with the extended (ferrimagnetic) *s*-*d* model including diffusive spin transport, where the absorption layer is implemented as an ideal spin sink. In analogy to the discussion above, the absorbed spin current is substituted in Eq. (8.1). In this case, we only focus on the excited FMR mode ($n = 0$), and we perform the calculations for a varying thickness of the Gd layer. The details of the implementation of the Co/Gd bilayer, including the used definition of an effective Gd thickness t_{Gd} in an intermixed structure, are given in Ref. [159].

The results are presented in Figs. 8.4(b), where we plotted the excited homogeneous modes for $t_{\mathrm{Gd}} = 0$ (Pure Co, in red) and $t_{\mathrm{Gd}} = 2$ nm (in blue). The (vertical) dashed lines indicate a relative phase shift of approximately 120 degrees, which is in agreement with the experiments [159]. Figure 8.4(c) indicates the corresponding spin currents as a function of time, which explains the origin of the phase shift. The critical difference is that in the presence of a significant amount of Gd, the spin current is nonvanishing on a timescale beyond the picosecond regime. The latter results from the different magnetic properties of Gd compared to Co. For that reason, the phase shift corresponds to a minus sign change (180 degrees) due to the opposite magnetization of the Co and Gd, plus an additional phase shift determined by the long tail of the spin current. The phase shift as a function of thickness is given in Fig. 8.4(d), showing that the phase jump already occurs for a very small addition

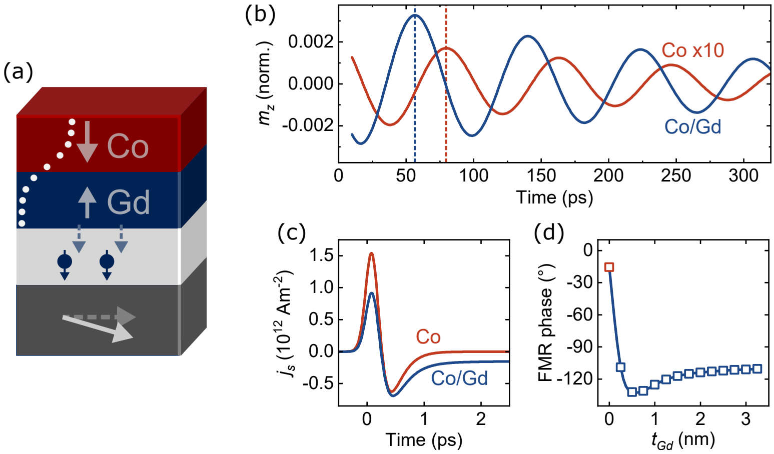

Figure 8.4: (a) Schematic overview of the multilayer that is investigated in Ref. [159]. The generated interlayer spin current excites a homogeneous magnetization precession in the in-plane absorption layer. (b) The excited FMR modes in the case that the out-of-plane magnetic region is pure Co (red), or a typical Co/Gd bilayer (Blue). A significant phase shift is observed, as indicated by the (vertical) dashed lines. (c) The interlayer spin current for a generation layer that consists of pure Co (red) or a Co/Gd bilayer (blue). The latter is nonvanishing beyond a few picoseconds. The absolute phase shift of the excited FMR mode as a function of the effective Gd layer thickness t_{Gd}.

of Gd. We note here that the specific horizontal scaling of the figure is strongly dependent on the precise implementation of the synthetic-ferrimagnetic layer.

In addition to the phase shift, a relatively large change in the amplitude is observed. This change is related to the Fourier component of the spin current evaluated at the FMR frequency. In the case of a pure Co generation layer, this low-frequency component is small, whereas in the presence of Gd the component becomes more apparent. Again, it is a result of the nonvanishing nature of the spin current at longer timescales. Here, a discrepancy with the experiments is present, as such a large amplitude difference is absent in the measured signals [159]. Additionally, in order to observe the typical absolute phase shift with a significant deviation from a pure sign change (180 degrees), it was critical to implement a demagnetization timescale for Gd of the order $\sim$ 20 ps. This is in contradiction with the previous sections, where it was required to use a short demagnetization rate for the Gd to observe all-optical switching. With that in mind, it is clear that a more in-depth analysis is required, to determine what additional parameters play a critical role.[1]

---

[1] One could give a long list of possible critical parameters in these complex synthetic-ferrimagnetic structures, including the density of states, the spin-flip scattering rate, the constant ρ_{sd} (Chapter 3), and

A possible critical step would be to investigate the correct implementation of spin transport within the Gd region. In the calculations above, it was assumed that within the full Co/Gd bilayer it could be described as diffusive spin transport with the system parameters of pure Co, which might strongly deviate from the actual spin transport properties of Gd.

From the calculation above, and the ones presented in the previous sections, we can make the following observation. On the one hand, the preliminary calculations were successful in qualitatively describing the observed physical phenomena. On the other hand, the modeling required making assumptions that could not be fully justified and needed the use of questionable values for multiple system parameters. In the following section, we will connect this observation to a general outlook on the field of femtomagnetism.

8.5 General outlook

With the ever-increasing need for faster and more efficient information technology devices, it is evident that it is required to find innovative techniques for the control and storage of binary data. More than 25 years of research in ultrafast magnetism proved that the use of femtosecond laser pulses and the smart engineering of magnetic materials provide a possible solution. The typical physical concepts in this context, such as laser-induced spin transport and all-optical switching, are all promising candidates for future applications. Nevertheless, it is clear that the full technological potential of ultrafast magnetism has not been completely explored yet. In this final section, we give a brief and general outlook on the future of femtomagnetism. For a specific outlook on the theoretical models, we refer to the main chapters.

Although the typical physical phenomena in ultrafast magnetism are not entirely understood, the experimental and technological possibilities have evolved at a fast pace. It is obvious that single-pulse all-optical switching (AOS) receives the most attention due to its evident relevance for future data-storage applications. Hence, a wide variety of recent studies focus on the optimization of magnetic material systems that allow single-pulse AOS. In relation to the previous sections, examples include the picosecond switching of ferromagnetic materials [100, 130, 153], and

---

much more.

the method for transforming AOS from a toggle mechanism to deterministic data writing [105]. Another critical observation is that the mechanism is not restricted to the use of ultrashort laser pulses, as it was shown that a rapid switching of magnetization can analogously be achieved by the use of picosecond electrical pulses [77, 160, 161]. In combination with the demonstration of AOS of magnetic tunnel junctions [162, 163], all the above steps pave the way towards the realization of the next generation of (opto-)magnetic random-access memory devices [158, 164].

Additionally, all-optical switching has clear relevance for the integration of femtomagnetism with photonics [99]. Using AOS, the information processed within a novel photonic integrated circuit can be stored indefinitely within a magnetic material, for instance, a magnetic racetrack that consists of a (synthetic-)ferrimagnetic material [9, 98, 99]. In combination with that magneto-optical effects allow determining the magnetization direction with light [165, 166], this provides a promising writing and reading scheme for data storage in integrated photonics.

It is needless to say that the technical relevance of femtomagnetism and ultrafast spintronics goes beyond all-optical switching. One very clear example is laser-induced spin transport in a magnetic heterostructure. Due to the inverse spin Hall effect, the transient optically-generated spin current indirectly results in the emission of THz radiation [68, 69, 167]. Finding new THz emitters is exceptionally interesting for applications, especially to optimize the bandwidth and efficiency compared to the traditional THz emitters [167, 168]. The examples go beyond information technology, as the use of THz radiation is suited for biomedical analysis tools, security imaging applications, and THz radars [167–170].

From a technological point of view, it is clear that the future of femtomagnetism and ultrafast spintronics is very bright. Because of the increasing complexity of the material systems that are optimal for opto-magnetic applications, the models that are required to interpret the underlying physics increase in difficulty. Although the work in this thesis exemplifies that a simplified analytical approach elucidates the various ultrafast phenomena, the calculations in this chapter indicated that the models start to lose accuracy when multiple concepts are jointly described. In this scenario, the advantages of a simplified model evaporate, and it becomes more appropriate to create a robust numerical implementation with fewer restrictions, that possibly includes physical mechanisms from contradicting theories. A relevant example could be the modeling of laser-induced spin transport, and the development of a joint description of the laser-excited superdiffusive spin currents and the spin transport driven by a locally generated spin accumulation. The hope is that such an approach creates a pathway to identify the dominant physics and helps to, at least partially, end the theoretical debates. Nevertheless, the critical challenge remains that it is difficult to experimentally distinguish the various contributions. To some extent, it is a characteristic of theoretical research in femtomagnetism, that there is surely no lack of theories to explain the observations, but the main challenge is to disentangle the contradicting interpretations.

To end this thesis with a positive note, we want to emphasize the fascinating phenomena that were explored with femtosecond laser-pulse excitation of magnetic materials. It remains truly remarkable that the laws of physics allow transferring magnetic information on the timescale of a trillionth of a second, and that a simple mechanism as rapid heating enables ultrafast magnetization switching. Although nobody can foresee the definitive technical relevance of femtomagnetism, or predict if the promising applications will ever become reality, it is obvious that it remains a progressive and blooming research field for the upcoming decades.

A

The Boltzmann equation and Fermi's golden rule

In this appendix, we discuss the Boltzmann equation and the implementation of Fermi's golden rule, which are repeatedly used in the main chapters. To derive this from first principles, we closely follow the mathematical steps from Ref. [132]. Furthermore, we extensively make use of the methods discussed in Refs. [35, 56, 111, 171].

A.1 Fermi's golden rule and transition rates

In the main text, the models require to calculate time derivatives of semiclassical distribution functions. This is related to calculating the evolution of the diagonal elements of a density matrix. Before diving into detail, we note that the equations in this section are directly taken from Ref. [132]. The starting point is the Liouville-von Neumann equation [132]

$$\frac{d\hat{\rho}}{dt} = \frac{1}{i\hbar}[\hat{H}, \hat{\rho}], \tag{A.1}$$

which describes the time evolution of the density matrix and directly follows from the Schrödinger equation. Here, the Hamiltonian is separated into two parts $\hat{H} = \hat{H}_0 + \hat{V}$, where $\hat{H}_0$ corresponds to the noninteracting Hamiltonian and $\hat{V}$ describes interactions. The goal is to express the dynamics of $\hat{\rho}$, as driven by perturbation $\hat{V}$, in terms of the occupation of the unperturbed eigenstates. In order to do so, the first step is to switch to the interaction picture, where the time evolution of $\hat{\rho}$ is strictly determined by the interaction Hamiltonian [132, 171]

$$\frac{d\hat{\rho}^i}{dt} = \frac{1}{i\hbar}[\hat{V}^i, \rho^i]. \tag{A.2}$$

By integration it follows that

$$\hat{\rho}^i(t) = \hat{\rho}^i(t_0) + \frac{1}{i\hbar}\int_{t_0}^{t} dt'[\hat{V}^i(t'), \hat{\rho}^i(t')], \tag{A.3}$$

where t_0 is the initial time. In principle, $\hat{\rho}^i(t)$ can now be calculated up to arbitrary order in the interaction strength through an iterative procedure [132]. A more practical approach is to substitute Eq. (A.3) in Eq. (A.2), and impose that $\hat{\rho}^i(t')$ changes relatively slow such that it can be replaced by $\hat{\rho}^i(t)$ in the integral. This is equivalent to the Markov approximation since it results in an expression that is local in time and does not depend on the history of $\rho(t)$. As discussed in the next section, the arguments for the Markov approximation become more sophisticated when we discuss the coupling of a spin system to an electron bath. Following Ref. [132], after imposing the Markov approximation and switching back to the Schrödinger picture one finds

$$\frac{d\hat{\rho}}{dt} = \hat{C} + \frac{1}{(i\hbar)^2}[\hat{V}, [\hat{\mathcal{K}}(t), \hat{\rho}(t)]]. \tag{A.4}$$

Here, $\hat{C}$ indicates the terms that describe the coherent evolution of the density matrix. Since we do not investigate the coherent dynamics in the research chapters of the thesis $\hat{C}$ is omitted in this overview.[1] Our main interest is the second term. Importantly, it includes the function $\mathcal{K}(t)$ [132]

$$\hat{\mathcal{K}}(t) = \int_0^{t-t_0} d\tau\, \hat{U}_0(\tau)\hat{V}\hat{U}_0^\dagger(\tau), \tag{A.5}$$

with $\hat{U}_0(\tau) = e^{-\hat{H}_0\tau/(i\hbar)}$ the time evolution operator for the noninteracting Hamiltonian. Using Eq. A.4 one can straightforwardly derive an expression for the dynamics of the semiclassical distribution function by substituting the diagonal density matrix $\hat{\rho} = \sum_\lambda f_\lambda |\lambda\rangle\langle\lambda|$ [132]. Here, $|\lambda\rangle$ indicate the eigenstates of the noninteracting Hamiltonian and the diagonal elements f_λ represent the occupation probabilities. This method results in the Boltzmann equation

$$\frac{df_\lambda}{dt} = \sum_{\lambda'}\left[W_{\lambda\lambda'}f_{\lambda'} - W_{\lambda\lambda'}f_\lambda\right], \tag{A.6}$$

---

[1] In Section 8.4 and Appendix B the coherent terms are essential, since they correspond to magnetization precession [35].

where the first term represents transitions into the state $|\lambda\rangle$ and the second term corresponds to the opposite transitions. The rates $W_{\lambda\lambda'}$ are given by

$$W_{\lambda\lambda'} = \frac{2\pi}{\hbar}|V_{\lambda\lambda'}|^2 \mathrm{Re}\{\mathcal{D}_{\lambda\lambda'}^{t-t_0}\}, \tag{A.7}$$

where $V_{\lambda\lambda'}$ is the corresponding matrix element of $\hat{V}$. Furthermore, the time-dependent function on the right-hand side is given by [132]

$$\mathcal{D}_{\lambda\lambda'}^{t-t_0} = \frac{1}{\pi\hbar}\int_0^{t-t_0} d\tau e^{-i(\epsilon_\lambda - \epsilon_{\lambda'})\tau/\hbar} \tag{A.8}$$

The standard way to arrive at Fermi's golden rule is to take the limit $t - t_0 \to \infty$, such that the Dirac delta function that imposes energy conservation appears

$$W_{\lambda\lambda'} = \frac{2\pi}{\hbar}|V_{\lambda\lambda'}|^2 \delta(\epsilon_\lambda - \epsilon_{\lambda'}). \tag{A.9}$$

This expression for the transition rate is the standard form of Fermi's golden rule. In the context of this thesis, it is required to formulate Fermi's golden rule for a system that is composed of multiple subsystems. The latter is the topic of the following section.

A.2 THE EXTENSION TO MULTIPLE (MANY-PARTICLE) SUBSYSTEMS

We focus on two coupled many-particle subsystems, labeled as system A and system B. The statistical state of the combined system is described by density matrix $\hat{\rho}$. The latter represents a mixture of many-particle states $|\lambda\rangle = |\{n_\alpha\}\rangle\,|\{n_\beta\}\rangle$, where $|\{n_\alpha\}\rangle$ is the collection of Fock states in system A. Here, n_α is the number of particles in the single-particle state α. The statistical state of system A is described by the reduced density matrix $\rho_A = \mathrm{tr}_B\{\hat{\rho}\}$, which results from tracing out system B. The goal is to determine the dynamics of ρ_A, in response to an interaction of the form

$$\hat{V} = \sum_\alpha \hat{A}_\alpha^+ \hat{B}_\alpha^- + \hat{A}_\alpha^- \hat{B}_\alpha^+, \tag{A.10}$$

where we notated $A_\alpha^+ (A_\alpha^-)$ as a ladder operator that increases (decreases) the number of particles with state α by one. First, we calculate the transition rates that determine the occupation of state α. The result follows from simplifying Eq. (A.4) and tracing out the nonrelevant degrees of freedom. Using this method, one can find the temporal derivative of the probability f_{n_α} of having n_α particles in state α.[2] The latter is related to the diagonal elements of the density matrix $\hat{\rho}_A$. The result is written in the typical form

$$\begin{aligned} \frac{df_{A,n_\alpha}}{dt} &= -(W^-_{\alpha;n_\alpha-1,n_\alpha} + W^+_{\alpha;n_\alpha+1,n_\alpha}) f_{A,n_\alpha} \\ &\quad + W^+_{\alpha;n_\alpha,n_\alpha-1} f_{A,n_\alpha-1} + W^-_{\alpha;n_\alpha,n_\alpha+1} f_{A,n_\alpha+1}. \end{aligned} \tag{A.11}$$

Here, the transition rate is written as

$$W^\pm_{\alpha;n_\alpha\pm1,n_\alpha} = \frac{2\pi}{\hbar} |(\hat{A}^\pm_\alpha)_{n_\alpha\pm1,n_\alpha}|^2 C^\pm_\infty(\epsilon_\alpha), \tag{A.12}$$

where we notated the matrix element $(\hat{A}^\pm_\alpha)_{n_\alpha\pm1,n_\alpha} = \langle n_\alpha \pm 1| \hat{A}^\pm_\alpha |n_\alpha\rangle$. In contrast to the simple case of Eq. (A.6), where $W_{\lambda\lambda'} = W_{\lambda'\lambda}$, in the reduced representation we generally have $W^\pm_{n_\alpha\pm1,n_\alpha} \neq W^\mp_{n_\alpha,n_\alpha\pm1}$ [132]. Importantly, we defined the function [111]

$$C^\pm_\infty(\epsilon_\alpha) = \frac{1}{2\pi\hbar} \int_{-\infty}^{\infty} d\tau \, e^{\mp i\epsilon_\alpha\tau/\hbar} C^\pm_{B,\alpha}(\tau), \tag{A.13}$$

which depends on a correlation function

$$C^\pm_{B,\alpha}(\tau) = \mathrm{tr}_B\{\hat{B}^\pm_\alpha \hat{B}^\mp_\alpha(\tau)\hat{\rho}_B\} = \langle \hat{B}^\pm_\alpha \hat{B}^\mp_\alpha(\tau)\rangle_B. \tag{A.14}$$

The bounds of the integral over τ were set to $\pm\infty$ because $C^\pm_{B,\alpha}(\tau)$ is assumed to decay rapidly on a timescale τ_c [171]. In other words, we have used that $t - t_0 \gg \tau_c$. The assumption of a short correlation time is equivalent to the Markov approximation, as it yields the memorylessness of the bath (system B).

A.3 NOTES ON THE SPIN-FLIP IMPURITY SCATTERING RATE

In this appendix, we present additional details regarding the calculation of the spin-flip scattering rate driven by impurity scattering, as was calculated in Sec. 2.3.2. Within the approximations of the microscopic three-temperature model, the interaction Hamiltonian has the form

---

[2] f_{n_α} has a similar meaning to the f_{m_s} in the main text. Obviously, f_{n_α} is not the most practical function to describe the statistical state of subsystems. A more formal approach is presented in Section A.4.

$$\hat{H} = \frac{\lambda}{N} \sum_j \sum_{\mathbf{k}\mathbf{k}'} \hat{S}_j^+ c_{\mathbf{k}'}^\dagger c_{\mathbf{k}} + \hat{S}_j^- c_{\mathbf{k}}^\dagger c_{\mathbf{k}'}. \tag{A.15}$$

We are interested in the transition rate of spin states from level m_s to $m_s \pm 1$. The result can be found by substituting $\hat{A}^\pm = \hat{S}^\pm$ and $\hat{B}^- = (\lambda/N) \sum_{\mathbf{k}\mathbf{k}'} c_{\mathbf{k}}^\dagger c_{\mathbf{k}'}$ (and $\hat{B}^+$ by its hermitian conjugate) in Eqs. (A.12)-(A.14). First, the correlation function in Eq. (A.14) is written out, which yields a complex exponential that is a function of $\epsilon_{\mathbf{k}} - \epsilon_{\mathbf{k}'}$. Second, the result is substituted in Eq. (A.13). Here, the infinite integral bounds make the expression equivalent to a Dirac delta function that imposes energy conservation, similar to the standard derivation of Fermi's golden rule. Finally, substitution in Eq. (A.12) gives the transition rate [56, 111]

$$W^\pm_{m_s\pm1,m_s} = \frac{2\pi}{\hbar} \lambda^2 S^\pm_{m_s} \frac{1}{N^2} \sum_{\mathbf{k}\mathbf{k}'} \delta(\epsilon_{\mathbf{k}} \mp \Delta - \epsilon_{\mathbf{k}'}) \langle c_{\mathbf{k}}^\dagger c_{\mathbf{k}'} c_{\mathbf{k}'}^\dagger c_{\mathbf{k}} \rangle_C. \tag{A.16}$$

Here, the ensemble average $\langle \ldots \rangle_C = \mathrm{tr}\{\ldots \rho_C\}$ is calculated for the carrier system with density matrix $\hat{\rho}_C$. Furthermore, the prefactor dependent on m_s is given by $S^\pm_{m_s} = S(S+1) - m_s(m_s \pm 1)$. For the calculations in the main text, it is required to express Eq. (A.16) in terms of distribution functions. The latter is given by $f_{\mathbf{k}} = \langle c_{\mathbf{k}}^\dagger c_{\mathbf{k}} \rangle_C$. Importantly, the term on the right-hand side of Eq. (A.16) can be expressed in terms of a product of two distribution functions [56]. In that way, we retrieve the following expression for the transition rate [56]

$$W^\pm_{m_s\pm1,m_s} = \frac{2\pi}{\hbar} \lambda^2 S^\pm_{m_s} \frac{1}{N^2} \sum_{\mathbf{k}\mathbf{k}'} \delta(\epsilon_{\mathbf{k}} \mp \Delta - \epsilon_{\mathbf{k}'}) f_{\mathbf{k}} (1 - f_{\mathbf{k}'}), \tag{A.17}$$

which was used in Sec. 2.3.2. We note that the extension to the *s*-*d* model, where the spin polarization of the electrons is taken into account, is very straightforward and not discussed in this appendix.

A.4 NOTES ON THE ELECTRON-MAGNON SCATTERING RATE

In this final part of Appendix A, we discuss the background of the formula for the time derivative of the magnon density, as was given in Eq. (2.69). The formula follows from calculating the expectation value of the number operator $a_{\mathbf{q}}^\dagger a_{\mathbf{q}}$, defined as the occupation number $n_{\mathbf{q}}$

$$n_{\mathbf{q}} = \langle a^\dagger_{\mathbf{q}} a_{\mathbf{q}} \rangle = \mathrm{tr}\{\hat{\rho}\, a^\dagger_{\mathbf{q}} a_{\mathbf{q}}\}. \tag{A.18}$$

Similarly, the distribution function $f_{\mathbf{k}\sigma}$ for electrons with momentum $\mathbf{k}$ and spin σ is

$$f_{\mathbf{k}\sigma} = \langle c^\dagger_{\mathbf{k}\sigma} c_{\mathbf{k}\sigma} \rangle = \mathrm{tr}\{\hat{\rho}\, c^\dagger_{\mathbf{k}\sigma} c_{\mathbf{k}\sigma}\}. \tag{A.19}$$

The goal is to derive an expression for the time derivative of $n_{\mathbf{q}}$. This can be found by using Eq. (A.4). Under the conditions given in the previous sections, it is straightforward to show that the result can be written as [112]

$$\begin{aligned} \frac{dn_{\mathbf{q}}}{dt} &= \frac{2\pi}{\hbar}\sum_{\mathbf{kk}'} |V_{\mathbf{kk}'\mathbf{q}}|^2 \delta(\epsilon_{\mathbf{k}\uparrow} - \epsilon_{\mathbf{k}'\downarrow} - \epsilon_{\mathbf{q}})\mathrm{tr}\{\hat{\rho}\, c^\dagger_{\mathbf{k}\uparrow} c_{\mathbf{k}'\downarrow} c^\dagger_{\mathbf{k}'\downarrow} c_{\mathbf{k}\uparrow} a_{\mathbf{q}} a^\dagger_{\mathbf{q}}\} \\ &\quad -\frac{2\pi}{\hbar}\sum_{\mathbf{kk}'} |V_{\mathbf{kk}'\mathbf{q}}|^2 \delta(\epsilon_{\mathbf{k}\uparrow} - \epsilon_{\mathbf{k}'\downarrow} - \epsilon_{\mathbf{q}})\mathrm{tr}\{\hat{\rho}\, c^\dagger_{\mathbf{k}'\downarrow} c_{\mathbf{k}\uparrow} c^\dagger_{\mathbf{k}\uparrow} c_{\mathbf{k}'\downarrow} a^\dagger_{\mathbf{q}} a_{\mathbf{q}}\}, \end{aligned} \tag{A.20}$$

By substituting the definitions of $n_{\mathbf{q}}$ and $f_{\mathbf{k}\sigma}$, one arrives at [36, 112, 117]

$$\begin{aligned} \frac{dn_{\mathbf{q}}}{dt} &= \frac{2\pi}{\hbar}\sum_{\mathbf{kk}'} |V_{\mathbf{kk}'\mathbf{q}}|^2 \delta(\epsilon_{\mathbf{k}\uparrow} - \epsilon_{\mathbf{k}'\downarrow} - \epsilon_{\mathbf{q}}) f_{\mathbf{k}\uparrow}(1 - f_{\mathbf{k}'\downarrow})(1 + n_{\mathbf{q}}) \\ &\quad -\frac{2\pi}{\hbar}\sum_{\mathbf{kk}'} |V_{\mathbf{kk}'\mathbf{q}}|^2 \delta(\epsilon_{\mathbf{k}\uparrow} - \epsilon_{\mathbf{k}'\downarrow} - \epsilon_{\mathbf{q}}) f_{\mathbf{k}'\downarrow}(1 - f_{\mathbf{k}\uparrow}) n_{\mathbf{q}}. \end{aligned} \tag{A.21}$$

Finally, the expression in Eq. (2.70), in terms of magnon density n_d, is found by summing over the momenta $\mathbf{q}$.

B

Details on the additional calculations

In this appendix, we present extra notes regarding the additional research from Chapter 8. The appendix consists of two parts. First, we derive an analytical description of standing waves, which was used for the calculations presented in Section 8.4. Second, we give an overview of the material parameters we used for the magnetic multilayers modeled in Sections 8.2 and 8.3.

B.1 An analytical description of standing spin waves

In this section, we perform an analytical calculation that results in a simple description of standing spin waves. Specifically, the spin waves that are excited in a noncollinear magnetic heterostructure as discussed in Sec. 8.4 and schematically depicted in Fig. 8.3. Within the absorption layer, the magnetization is described by the Landau-Lifshitz-Gilbert-Slonczewski equation, including an additional damping torque corresponding to spin pumping [7, 142]. The equation is expressed in terms of unit vector $\mathbf{n}$, which corresponds to the direction of the local spin density $\mathbf{n} = \mathbf{s}/s$ with s the saturation spin density (in units $\hbar$ per volume), and is given by [116, 142, 172, 173]

$$\frac{\partial \mathbf{n}}{\partial t} = \frac{A}{\hbar}\mathbf{n} \times \partial_x^2 \mathbf{n} - \omega_0 \mathbf{n} \times \hat{z} - \alpha\, \mathbf{n} \times \frac{\partial \mathbf{n}}{\partial t} + \boldsymbol{\tau}_{\mathrm{STT}} + \boldsymbol{\tau}_{\mathrm{sp}}, \tag{B.1}$$

where A corresponds to the spin-wave stiffness, ω_0 is the angular FMR frequency, and α is the bulk Gilbert damping. The incoming spins are assumed to be absorbed at the interface (defined as $x = 0$), giving the following expression for the exerted spin-transfer torque

$$\boldsymbol{\tau}_{\text{STT}} = \frac{\delta(x)}{s}\mathbf{n} \times \mathbf{j}_s^{\text{ext}} \times \mathbf{n}. \tag{B.2}$$

Here, $\mathbf{j}_s^{\text{ext}}$ corresponds to the spin current that is pumped out of the generation layer. For simplicity, we assume that the generation mechanism, and thereby $\mathbf{j}_s^{\text{ext}}$, is independent of the transverse spin dynamics in the absorption layer. We write

$$\mathbf{j}_s^{\text{ext}} = \frac{g_{\uparrow\downarrow}}{4\pi\hbar}\mu_{s,x}(t)\hat{x}, \tag{B.3}$$

where $\mu_{s,x}(t)$ is the transverse component of the spin accumulation at the interface and is in this analysis assumed to be a given function. Furthermore, spin pumping results in an additional (local) contribution to the damping [142]

$$\boldsymbol{\tau}_{\text{sp}} = -\delta(x)\frac{g_{\uparrow\downarrow}}{4\pi s}\mathbf{n} \times \partial_t\mathbf{n}. \tag{B.4}$$

By realizing that Eq. (B.1) can be written in the form of the continuity equation [172], the first term on the right-hand side corresponds to the divergence of the spin current

$$\mathbf{j}_s = -\frac{sA}{\hbar}\mathbf{n} \times \partial_x\mathbf{n}. \tag{B.5}$$

It should be noted that the terms proportional to a Dirac delta function ($\boldsymbol{\tau}_{\text{sp}}$ and $\boldsymbol{\tau}_{\text{STT}}$) then simply fix the boundary conditions at the interfaces $x = 0$ and $x = L$

$$\mathbf{j}_s(0) = -\frac{g_{\uparrow\downarrow}}{4\pi}\mathbf{n} \times \partial_t\mathbf{n}\big|_{x=0} + \mathbf{n} \times \mathbf{j}_s^{\text{ext}} \times \mathbf{n}\big|_{x=0}, \tag{B.6}$$

$$\mathbf{j}_s(L) = 0. \tag{B.7}$$

To calculate the spin waves excited by $\mathbf{j}_s^{\text{ext}}$, we simplify the problem by linearizing Eq. (B.1) using $\mathbf{n} = (\delta n_x, \delta n_y, -1)$ and defining the transverse magnetization parameter $\psi = \delta n_x + i\delta n_y$. In the bulk, the transverse magnetization dynamics is then described by the equation

$$-i(1 - i\alpha)\partial_t\psi = \Big[-\frac{A}{\hbar}\partial_x^2 + \omega_0\Big]\psi. \tag{B.8}$$

Similarly, the boundary conditions Eqs. (B.6)-(B.7) can be expressed in terms of ψ. It is straightforward to solve this problem analytically. The result is written as a cosine expansion

$$\psi(x,t) \quad = \quad \frac{\phi_0(t)}{2} + \sum_{n=1}^{\infty} \phi_n(t) \cos\Big(\frac{n\pi x}{L}\Big), \tag{B.9}$$

where each function $\phi_n(t)$ describes the temporal behavior of the n^{th} mode of the standing spin wave. In the end, the function $\phi_n(t)$ is expressed in terms of a convolution

$$\phi_n(t) \quad = \quad \frac{g_{\uparrow\downarrow}}{4\pi s L\hbar}\Big(\mu_{s,x} * G_n\Big), \tag{B.10}$$

where $G_n(t)$ is the Green's function that determines the dynamics of mode n. As long as the effective damping is much smaller than one, the Green's function is given by

$$G_n(t) \quad = \quad \theta(t)\exp(i\omega_n(1+i\alpha_{\text{eff},n})t), \tag{B.11}$$

where ω_n corresponds to the frequency of the n^{th} mode

$$\omega_n \quad = \quad \omega_0 + \frac{A}{\hbar}\left(\frac{n\pi}{L}\right)^2, \tag{B.12}$$

and the effective damping is given by

$$\alpha_{\text{eff},n} = \begin{cases} \alpha + \dfrac{g_{\uparrow\downarrow}}{4\pi s L}, & \text{if } n = 0 \\[2ex] \alpha + 2\dfrac{g_{\uparrow\downarrow}}{4\pi s L}, & \text{if } n \geq 1 \end{cases} \tag{B.13}$$

To derive Eqs. (B.11)-(B.13), we have implicitly assumed that $|\alpha_{\text{eff},n}|^2 \ll 1$. The factor two indicates that the inhomogeneous modes ($n \geq 1$) are damped twice as hard by interfacial spin pumping. The latter is a standard result and can be derived within various approaches [174, 175]. As a final remark, we note the close connection between the function $\phi_n(t)$ and the Fourier components of the spin accumulation. When we assume that $\mu_{s,x}(t)$ decays on a timescale given by τ, and we impose that $\tau \ll (\alpha_{\text{eff},n}\omega_n)^{-1}$, we have

$$\phi_n(t) \quad \propto \quad \mu_{s,x}(\omega_n)\exp(i\omega_n(1+i\alpha_{\text{eff},n})t). \tag{B.14}$$

In theory, the relation shows that the amplitude of the spin-wave modes can be used to map the Fourier transform of the absorbed spin accumulation.

Table B.1: System parameters used for the calculations in Secs. 8.2 and 8.3. The parameters of Section 8.4 are given in Ref. [159].

symbol	meaning	value
T_{amb}	ambient temperature	295 K
γ	electronic heat capacity parameter	2000 $\mathrm{Jm}^{-3}\mathrm{K}^{-2}$
C_p	phonon heat capacity	$4 \cdot 10^6$ $\mathrm{Jm}^{-3}\mathrm{K}^{-1}$
σ	pulse duration	0.05 ps
τ_D	heat dissipation timescale	20 ps
a	lattice spacing	0.25 nm
$T_{\mathrm{C,TM}}$	TM Curie temperature	1000 K
$T_{\mathrm{C,RE}}$	RE Curie temperature	292 K
S_{TM}	TM spin quantum number	1/2
S_{RE}	RE spin quantum number	7/2
$\mu_{\mathrm{at,TM}}$	TM atomic magnetic moment	2.0 μ_B
$\mu_{\mathrm{at,RE}}$	RE atomic magnetic moment	7.0 μ_B
ρ_{sd}	*s*-*d* coefficient [36, 131]	1.0 eV
$\tau_{sd,\mathrm{TM}}$	TM *s*-*d* scattering time	0.1 ps
$\tau_{sd,\mathrm{RE}}$	RE *s*-*d* scattering time	1.0 ps
τ_s	spin-flip scattering time (ferrimagnetic region)	0.2 ps
$\tau_{s,\mathrm{N}}$	spin-flip scattering time (nonmagnetic region)[72]	17 ps
σ	conductivity (magnetic region) [72]	$6.7 \cdot 10^6$ Sm^{-1}
σ_N	conductivity (spacer layer)[72]	$39 \cdot 10^6$ Sm^{-1}
D	spin diffusion coefficient (magnetic region)[72]	250 $\mathrm{nm}^2\mathrm{ps}^{-1}$
D_N	spin diffusion coefficient (spacer layer)[72]	9500 $\mathrm{nm}^2\mathrm{ps}^{-1}$
g	interfacial conductance parameter	$0.4 \cdot 10^{19}$ m^{-2}
$j_{\mathrm{Co-Gd}}$	interatomic exchange constant [76]	2.0 meV
$\tau_{sd,\mathrm{Co/Pt}}$	Co/Pt *s*-*d* scattering time	0.1 ps
$\tau_{s,\mathrm{Co/Pt}}$	Co/Pt spin-flip scattering time	0.02 ps
$\tau_{sd,\mathrm{Co/Ni}}$	Co/Ni *s*-*d* scattering time	0.1 ps
$\tau_{s,\mathrm{Co/Ni}}$	Co/Ni spin-flip scattering time	0.2 ps

B.2 SYSTEM PARAMETERS USED FOR THE PRELIMINARY CALCULATIONS

In this appendix, we present a few details regarding the modeling in Secs. 8.2 and 8.3. Table B.1 includes the list of all system parameters used in the calculations. As an additional remark, we note that in the calculations of Sec. 8.2 we modeled the laser-pulse absorption using $P_{0,\mathrm{Co/Pt}} = (1/2)P_{0,\mathrm{GdFeCo}}$. This was required as otherwise the phonon temperature exceeds the Curie temperature and the model becomes irrelevant. The resulting heat transport, which only has an indirect effect on the spin dynamics, is not included in the example calculations.

SUMMARY

In this thesis, we study and develop theoretical models that combine concepts from femtomagnetism and ultrafast spintronics. Femtomagnetism refers to the research field that focuses on the control of magnetic order with femtosecond laser pulses. The field emerged in the late nineties when it was discovered that upon laser-pulse excitation the magnetization of a ferromagnetic thin film is quenched on a subpicosecond timescale. The field gained a boost in 2007, when it was demonstrated that laser pulses can be used to switch the magnetization direction in ferrimagnetic materials, a phenomenon dubbed as all-optical switching (AOS). The discovery of AOS proved that femtomagnetism might lead to the development of innovative data-writing technologies. Another key observation is that laser-pulse excitation induces spin transport and provides an efficient tool to inject spin currents into adjacent metallic layers, paving the way towards ultrafast spintronic applications.

Despite the vast experimental developments in the field, identifying the physical origin of the observed phenomena remains a subject of heavy debate. In this thesis, we build on the theoretical fundaments that have been developed over the past decades and present new insights regarding the mechanisms underlying ultrafast magnetism.

In the first research chapter of the thesis, Chapter 3, we discuss a joint description of ultrafast demagnetization and laser-induced spin transport. By connecting the *s*-*d* model for the local spin dynamics to the diffusive description of spin transport, we were able to model the typical experiments within a single microscopic model. The calculations emphasize the plausibility that the demagnetization and generated spin current have the same physical origin. In Chapter 4, we extend this theory by including magnons, wave-like spin excitations that contribute to spin transport, and show that the role of magnons is nonnegligible. We put the theory into context by comparing it with recent experimental observations that the temporal behavior of the generated spin current is directly proportional to the derivative of the

magnetization. In Chapter 5, we present a toy model that allows us to compare two competing contributions to laser-induced spin transport. First, it includes the spin-polarized transport of hot electrons that are directly excited by the laser pulse. Second, the model describes the spin current driven by local heating. An analytical investigation is presented which supports the view that the contribution driven by local heating, specifically, the spin current that originates from the interaction between magnons and electrons, is expected to be dominant.

In the last two research chapters of the thesis, Chapters 6 and 7, we focus on modeling AOS. Motivated by the experimental demonstration of AOS in Co/Gd bilayers, we developed a model that simulates AOS in those synthetic-ferrimagnetic systems. Based on the calculations presented in Chapter 6, we identify the switching mechanism as a front of reversed Co magnetization that nucleates near the Co/Gd interface and propagates through the bilayer to establish the full switch. The latter mechanism makes AOS in synthetic ferrimagnets very robust in comparison to other switchable systems. Finally, in Chapter 7, we discuss the role of intermixing of the Co/Gd interface and show calculations that predict that intermixing enhances the AOS process and leads to a lower threshold fluence.

CURRICULUM VITAE

Maarten Beens was born on December 25th, 1993 in Kampen, The Netherlands. After finishing high school at the Ichthus College Kampen in 2012, Maarten started his bachelor Physics and Astronomy at Utrecht University. In the final semester, he worked on a theoretical graduation project about the current-driven motion of skyrmions in antiferromagnets and gained his first experience in theoretical spintronics. After that, Maarten obtained his Bachelor of Science degree *cum laude* in the summer of 2015.

Maarten continued his studies at Utrecht University and obtained his Master of Science degree in Theoretical Physics in 2017. The graduation project, which was performed at the Institute for Theoretical Physics (Utrecht) under the supervision of prof.dr. R.A. Duine, focused on the theoretical description of thermally-driven spin transport in magnetic heterostructures.

In the meantime, Maarten followed one semester of MSc-level courses on medical physics at the Delft University of Technology. The topics included medical imaging, pattern recognition, and radiological health physics. In September 2018, Maarten started his PhD project in the group Physics of Nanostructures at the Eindhoven University of Technology. The main goal was to develop a theoretical description of laser-induced spin transport. The results are presented in this thesis.

PUBLICATIONS

H Velkov, O. Gomonay, **M. Beens**, G. Schwiete, A. Brataas, J Sinova, and R.A. Duine, *Phenomenology of current-induced skyrmion motion in antiferromagnets,* New Journal of Physics, **18**, 075016 (2016)

M. Beens, J.P. Heremans, Y. Tserkovnyak, and R.A. Duine, *Magnons versus electrons in thermal spin transport through metallic interfaces,* Journal of Physics D: Applied Physics, **51**, 394002 (2018)

M. Beens, M.L.M. Lalieu, A.J.M. Deenen, R.A. Duine, and B. Koopmans, *Comparing all-optical switching in synthetic-ferrimagnetic multilayers and alloys,* Phys. Rev. B **100**, 220409(R) (2019)

M. Beens, M.L.M. Lalieu, R.A. Duine, and B. Koopmans, *The role of intermixing in all-optical switching of synthetic-ferrimagnetic multilayers,* AIP Advances **9**, 125133 (2019)

M. Beens, R.A. Duine, and B. Koopmans, *s-d model for local and nonlocal spin dynamics in laser-excited magnetic heterostructures,* Phys. Rev. B **102**, 054442 (2020)

T. Lichtenberg, **M. Beens**, M.H. Jansen, R.A. Duine, and B.Koopmans, *Probing optical spin currents using terahertz spin waves in noncollinear magnetic bilayers,* Phys. Rev. B **105**, 144416 (2022)

M. Beens, R.A. Duine, and B. Koopmans, *Modeling ultrafast demagnetization and spin transport: The interplay of spin-polarized electrons and thermal magnons,* Phys. Rev. B **105**, 144420 (2022)

T. Ferté, **M. Beens**, G. Malinowski, K. Holldack, R. Abrudan, F. Radu, T. Kachel, M. Hehn, C. Boeglin, B. Koopmans, and N. Bergeard, *Laser induced ultrafast Gd 4f spin dynamics in* $Co_{100-x}Gd_x$ *alloys by means of time-resolved XMCD,* submitted.

T. Lichtenberg, Y.L.W. van Hees, **M. Beens**, J. Levels, R. Lavrijsen, R.A. Duine, and B. Koopmans, *Probing laser-induced spin-current generation in synthetic ferrimagnets using spin waves,* submitted.

P. Li, J.W. van der Jagt, **M. Beens**, J. Hintermayr, R. Bruikman, B. Barcones, M. Verheijen, R. Juge, R. Lavrijsen, D. Ravelosona, and B. Koopmans, *Enhancing all-optical switching of magnetization by* He^+ *ion irradiation,* submitted.

M. Beens, K.A. de Mare, R.A. Duine, and B. Koopmans, *Spin-polarized hot electron transport versus spin pumping mediated by local heating,* submitted.

ACKNOWLEDGEMENTS

The job's finished! Writing this thesis was not possible without the help of many colleagues and I want to use this acknowledgements section to thank all the people involved.

Starting with my promotors, Bert and Rembert. It was an honor to have you both as my supervisors. Bert, your endless enthusiasm for physics is very inspiring and helped me a lot to keep motivated. Besides that, the research in this thesis would not be close as successful without your inexhaustive input and ideas. Rembert, thanks to you I could get this position in Eindhoven and I am very grateful that you helped me with that. Your way of supervising, ability to explain complex problems in a simple manner, and sense of humor, made all those years a fun experience.

Furthermore, I want to thank the entire FNA research group. The (former) PhD students and Postdocs, Adrien, Ani, Casper, Ece, Fanny, Hamed, Jianing, Julian, Juriaan, Lorenzo, Luding, Marcos, Maria, Mariëlle, Mariia, Mark dJ, Mark L, Mark P, Michał, Pingzhi, Thomas B, Thomas K, Tom, Tunç, Youri, and Zilu. The regular staff, Bart, Bert, Diana, Gerrie, Henk, Jeroen, Karin, Reinoud, and Rembert. Arriving in Eindhoven and joining FNA felt like a warm welcome, which is very nice when you move to an entirely new city. Furthermore, the social activities were very fun, such as the parties, the group outings, and all the dinners and drinks with my fellow PhD students. On top of that, the scientific trips to Nancy, Lisbon, Las Vegas, and Warsaw, were very nice experiences to share with all of you. Thank you, Casper, Shannen, and Youri, the road trip in the USA was a once-in-a-lifetime experience that I will remember as the best weeks of my PhD years.

Moreover, I want to thank the students who did their master or bachelor projects in collaboration with me. Tjacco en Steven, ondanks dat jullie onderzoek niet helemaal aansloot bij het onderwerp van mijn thesis, was het erg leerzaam om bij te dragen aan jullie master project. Ik wens jullie het allerbeste met jullie PhD project

in Nijmegen en Mainz. Koen, de resultaten van jouw master project waren erg verhelderend en ik wil je bedanken voor je enorme bijdrage aan het werk in hoofdstuk 5 van deze thesis. Thijs en Jules, ook jullie projecten hebben een belangrijke bijdrage geleverd aan het werk in deze thesis, dankjewel daarvoor.

I would like to thank the defense committee members, Peter Bobbert, Oksana Chubykalo-Fesenko, Johan Mentink, and Georg Woltersdorf. It is a great honor that you are present at my defense and I want to thank you all for the useful feedback on my thesis. Finally, I want to thank Quentin Remy and his colleagues in Nancy for the valuable discussions and the experimental data, which contributed to the work in Chapter 8.

Tenslotte wil ik mijn familie bedanken. Het is fijn dat ik nog steeds kan terugvallen op mijn thuisbasis in Kampen en altijd bij jullie terecht kan voor advies of gewoon voor de gezelligheid.

Maarten Beens
Eindhoven, August 2022

REFERENCES

[1] J.M.D. Coey, *Magnetism and Magnetic Materials* (Cambridge University Press, Cambridge, UK, 2009).

[2] W.D. Callister and D.G. Rethwisch, *Materials science and engineering: an introduction* (John Wiley and Sons, 2020).

[3] W. Heisenberg, Z. Phys. **49**, 619 (1928).

[4] A.J. Schellekens, *Manipulating spins* (PhD Thesis, Eindhoven University of Technology, 2014).

[5] M. N. Baibich, J. M. Broto, A. Fert, F. Nguyen Van Dau, F. Petroff, P. Etienne, G. Creuzet, A. Friederich, and J. Chazelas, Phys. Rev. Lett. **61**, 2472 (1988).

[6] G. Binasch, P. Grünberg, F. Saurenbach, and W. Zinn, Phys. Rev. B **39**, 4828(R) (1989).

[7] J.C. Slonczewski, Journal of Magnetism and Magnetic Materials **159**, L1 (1996).

[8] L. Berger, Phys. Rev. B **54**, 9353 (1996).

[9] S. S. Parkin, M. Hayashi, and L. Thomas, Science **320**, 190 (2008).

[10] C.D. Stanciu, F. Hansteen, A.V. Kimel, A. Kirilyuk, A. Tsukamoto, A. Itoh, and Th. Rasing, Phys. Rev. Lett. **99**, 047601 (2007).

[11] I. Radu, K. Vahaplar, C. Stamm, T. Kachel, N. Pontius, H.A. Dürr, T.A. Ostler, J. Barker, R.F.L. Evans, R.W. Chantrell, A. Tsukamoto, A. Itoh, A. Kirilyuk, Th. Rasing, and A.V. Kimel, Nature **472**, 205 (2011).

[12] T.A. Ostler, J. Barker, R.F.L. Evans, R.W. Chantrell, U. Atxitia, O. Chubykalo-Fesenko, S. El Moussaoui, L. Le Guyader, E. Mengotti, L.J. Heyderman, F.

Nolting, A. Tsukamoto, A. Itoh, D. Afanasiev, B.A. Ivanov, A.M. Kalashnikova, K. Vahaplar, J. Mentink, A. Kirilyuk, Th. Rasing, and A.V. Kimel, Nat. Commun. **3**, 666 (2012).

[13] E. Beaurepaire, J.-C. Merle, A. Daunois, and J.-Y. Bigot, Phys. Rev. Lett. **76**, 4250 (1996).

[14] G. Malinowski, F. Dalla Longa, J.H.H. Rietjens, P.V. Paluskar, R. Huijink, H.J.M. Swagten, and B. Koopmans, Nat. Phys. **4**, 855 (2008).

[15] A. Melnikov, I. Razdolski, T.O. Wehling, E.Th. Papaioannou, V. Roddatis, P. Fumagalli, O. Aktsipetrov, A.I. Lichtenstein, and U. Bovensiepen, Phys. Rev. Lett. **107**, 076601 (2011).

[16] D. Rudolf, C. La-O-Vorakiat, M. Battiato, R. Adam, J.M. Shaw, E. Turgut, P. Maldonado, S. Mathias, P. Grychtol, H.T. Nembach, T.J. Silva, M. Aeschlimann, H.C. Kapteyn, M.M. Murnane, C.M. Schneider, and P.M. Oppeneer, Nat. Commun. **3**, 1 (2012).

[17] S.I. Anisimov, B.L. Kapeliovich, and T.L. Perelman, Zh. Eksp. Teor. Fiz **66**, 375 (1974).

[18] B. Koopmans, G. Malinowski, F. Dalla Longa, D. Steiauf, M. Fähnle, T. Roth, M. Cinchetti, and M. Aeschlimann, Nat. Mat. **9**, 259 (2010).

[19] C. Illg, M. Haag, and M. Fähnle, Phys. Rev. B **88**, 214404 (2013).

[20] M.L.M. Lalieu and B. Koopmans, in *Handbook of Magnetism and Magnetic Materials* (Springer, 2021) pp. 477–547.

[21] G.P. Zhang and W. Hübner, Phys. Rev. Lett. **85**, 3025 (2000).

[22] J.-Y. Bigot, M. Vomir, and E. Beaurepaire, Nat. Phys. **5**, 515 (2009).

[23] B. Koopmans, J.J.M. Ruigrok, F. Dalla Longa, and W.J.M. de Jonge, Phys. Rev. Lett. **95**, 267207 (2005).

[24] N. Kazantseva, U. Nowak, R.W. Chantrell, J. Hohlfeld, and A. Rebei, Europhys. Lett. **81**, 27004 (2007).

[25] E. Carpene, E. Mancini, C. Dallera, M. Brenna, E. Puppin, and S. De Silvestri, Phys. Rev. B **78**, 174422 (2008).

[26] M. Krauß, T. Roth, S. Alebrand, D. Steil, M. Cinchetti, M. Aeschlimann, and H.C. Schneider, Phys. Rev. B **80**, 180407(R) (2009).

[27] U. Atxitia, O. Chubykalo-Fesenko, J. Walowski, A. Mann, and M. Münzenberg, Phys. Rev. B **81**, 174401 (2010).

[28] M. Fähnle and C. Illg, Journal of Physics: Condensed Matter **23**, 493201 (2011).

[29] B.Y. Mueller, T. Roth, M. Cinchetti, M. Aeschlimann, and B. Rethfeld, New Journal of Physics **13**, 123010 (2011).

[30] U. Atxitia and O. Chubykalo-Fesenko, Phys. Rev. B **84**, 144414 (2011).

[31] A. Manchon, Q. Li, L. Xu, and S. Zhang, Phys. Rev. B **85**, 064408 (2012).

[32] B.Y. Mueller, A. Baral, S. Vollmar, M. Cinchetti, M. Aeschlimann, H.C. Schneider, and B. Rethfeld, Phys. Rev. Lett. **111**, 167204 (2013).

[33] B.Y. Mueller and B. Rethfeld, Phys. Rev. B **90**, 144420 (2014).

[34] M. Haag, C. Illg, and M. Fähnle, Phys. Rev. B **90**, 014417 (2014).

[35] P. Nieves, D. Serantes, U. Atxitia, and O. Chubykalo-Fesenko, Phys. Rev. B **90**, 104428 (2014).

[36] E.G. Tveten, A. Brataas, and Y. Tserkovnyak, Phys. Rev. B **92**, 180412(R) (2015).

[37] K. Krieger, J.K. Dewhurst, P. Elliott, S. Sharma, and E.K.U. Gross, Journal of chemical theory and computation **11**, 4870 (2015).

[38] W. Töws and G.M. Pastor, Phys. Rev. Lett. **115**, 217204 (2015).

[39] M. Battiato, K. Carva, and P. M. Oppeneer, Phys. Rev. Lett. **105**, 027203 (2010).

[40] F. Dalla Longa, J.T. Kohlhepp, W.J.M. de Jonge, and B. Koopmans, Phys. Rev. B **75**, 224431 (2007).

[41] R.F.L. Evans, W.J. Fan, P. Chureemart, T.A. Ostler, M.O.A. Ellis, and R.W. Chantrell, Journal of Physics: Condensed Matter **26**, 103202 (2014).

[42] A.B. Schmidt, M. Pickel, M. Donath, P. Buczek, A. Ernst, V.P. Zhukov, P.M. Echenique, L.M. Sandratskii, E.V. Chulkov, and M. Weinelt, Phys. Rev. Lett. **105**, 197401 (2010).

[43] M. Fähnle, C. Illg, M. Haag, and N. Teeny, Acta Phys. Pol. A **127**, 170 (2015).

[44] S. Essert and H.C. Schneider, Phys. Rev. B **84**, 224405 (2011).

[45] S. Eich, M. Plötzing, M. Rollinger, S. Emmerich, R. Adam, C. Chen, H.C. Kapteyn, M.M. Murnane, L. Plucinski, D. Steil, B. Stadtmüller, M. Cinchetti, M. Aeschlimann, C.M. Schneider, and S. Mathias, Science Advances **3**, e1602094 (2017).

[46] E. Turgut, D. Zusin, D. Legut, K. Carva, R. Knut, J.M. Shaw, C. Chen, Z. Tao, H.T. Nembach, T.J. Silva, S. Mathias, M. Aeschlimann, P.M. Oppeneer, H.C. Kapteyn, M.M. Murnane, and P. Grychtol, Phys. Rev. B **94**, 220408(R) (2016).

[47] R.J. Elliott, Physical Review **96**, 266 (1954).

[48] Y. Yafet, *Solid State Physics* (Academic, 1963).

[49] D. Steiauf and M. Fähnle, Phys. Rev. B **79**, 140401(R) (2009).

[50] D. Steiauf, C. Illg, and M. Fähnle, Journal of magnetism and magnetic materials **322**, L5 (2010).

[51] K. Carva, M. Battiato, and P.M. Oppeneer, Phys. Rev. Lett. **107**, 207201 (2011).

[52] K. Carva, M. Battiato, D. Legut, and P.M. Oppeneer, Phys. Rev. B **87**, 184425 (2013).

[53] K. Leckron, S. Vollmar, and H.C. Schneider, Phys. Rev. B **96**, 140408(R) (2017).

[54] C. Dornes, Y. Acremann, M. Savoini, M. Kubli, M.J. Neugebauer, E. Abreu, L. Huber, G. Lantz, C.A.F. Vaz, H. Lemke, E.M. Bothschafter, M. Porer, V. Esposito, L. Rettig, M. Buzzi, A. Alberca, Y.W. Windsor, P. Beaud, U. Staub, D. Zhu, S. Song, J.M. Glownia, and S.L. Johnson, Nature **565**, 209 (2019).

[55] S.R. Tauchert, M. Volkov, D. Ehberger, D. Kazenwadel, M. Evers, H. Lange, A. Donges, A. Book, W. Kreuzpaintner, U. Nowak, and P. Baum, Nature **602**, 73 (2022).

[56] Ł. Cywiński and L.J. Sham, Phys. Rev. B **76**, 045205 (2007).

[57] V.N. Gridnev, Phys. Rev. B **88**, 014405 (2013).

[58] V.N. Gridnev, Journal of Physics: Condensed Matter **28**, 476007 (2016).

[59] K. Kang and G.-M. Choi, Journal of Magnetism and Magnetic Materials **514**, 167156 (2020).

[60] M. Hofherr, P. Maldonado, O. Schmitt, M. Berritta, U. Bierbrauer, S. Sadashivaiah, A.J. Schellekens, B. Koopmans, D. Steil, M. Cinchetti, B. Stadtmüller, P.M. Oppeneer, S. Mathias, and M. Aeschlimann, Phys. Rev. B **96**, 100403(R) (2017).

[61] A.J. Schellekens, W. Verhoeven, T.N. Vader, and B. Koopmans, Applied Physics Letters **102**, 252408 (2013).

[62] E. Turgut, C. La-o-vorakiat, J.M. Shaw, P. Grychtol, H.T. Nembach, D. Rudolf, R. Adam, M. Aeschlimann, C.M. Schneider, T.J. Silva, M.M. Murnane, H.C. Kapteyn, and S. Mathias, Phys. Rev. Lett. **110**, 197201 (2013).

[63] J. Wieczorek, A. Eschenlohr, B. Weidtmann, M. Rösner, N. Bergeard, A. Tarasevitch, T.O. Wehling, and U. Bovensiepen, Phys. Rev. B **92**, 174410 (2015).

[64] A.J. Schellekens, K.C. Kuiper, R.R.J.C. De Wit, and B. Koopmans, Nat. Commun. **5**, 4333 (2014).

[65] G.-M. Choi, B.-C. Min, K.-J. Lee, and D.G. Cahill, Nat. Commun. **5**, 4334 (2014).

[66] I. Razdolski, A. Alekhin, N. Ilin, J.P Meyburg, V. Roddatis, D. Diesing, U. Bovensiepen, and A. Melnikov, Nat. Commun. **8**, 15007 (2017).

[67] M.L.M. Lalieu, P.L.J. Helgers, and B. Koopmans, Phys. Rev. B **96**, 014417 (2017).

[68] T. Kampfrath, M. Battiato, P. Maldonado, G. Eilers, J. Nötzold, S. Mährlein, V. Zbarsky, F. Freimuth, Y. Mokrousov, S. Blügel, M. Wolf, I. Radu, P.M. Oppeneer, and M. Münzenberg, Nature Nanotechnology **8**, 256 (2013).

[69] T.S. Seifert, S. Jaiswal, J. Barker, S.T. Weber, I. Razdolski, J. Cramer, O. Gueckstock, S.F. Maehrlein, L. Nadvornik, S. Watanabe, C. Ciccarelli, A. Melnikov, G. Jakob, M. Münzenberg, S.T.B. Goennenwein, G. Woltersdorf, B. Rethfeld, P.W. Brouwer, M. Wolf, M. Kläui, and T. Kampfrath, Nat. Commun. **9**, 2899 (2018).

[70] S.M. Rouzegar, L. Brandt, L. Nadvornik, D.A. Reiss, A.L. Chekhov, O. Gueckstock, C. In, M. Wolf, T.S. Seifert, P.W. Brouwer, G. Woltersdorf, and T. Kampfrath, arXiv:2103.11710 .

[71] J. Kimling and D.G. Cahill, Phys. Rev. B **95**, 014402 (2017).

[72] I.-H. Shin, B.-C. Min, B.-K. Ju, and G.-M. Choi, Japanese Journal of Applied Physics **57**, 090307 (2018).

[73] M. Battiato, K. Carva, and P.M. Oppeneer, Phys. Rev. B **86**, 024404 (2012).

[74] G.-M. Choi, C.-H. Moon, B.-C. Min, K.-J. Lee, and D.G. Cahill, Nat. Phys. **11**, 576 (2015).

[75] A. Alekhin, I. Razdolski, N. Ilin, J.P. Meyburg, D. Diesing, V. Roddatis, I. Rungger, M. Stamenova, S. Sanvito, U. Bovensiepen, and A. Melnikov, Phys. Rev. Lett. **119**, 017202 (2017).

[76] J.H. Mentink, J. Hellsvik, D.V. Afanasiev, B.A. Ivanov, A. Kirilyuk, A.V. Kimel, O. Eriksson, M.I. Katsnelson, and Th. Rasing, Phys. Rev. Lett. **108**, 057202 (2012).

[77] C.S. Davies, T. Janssen, J.H. Mentink, A. Tsukamoto, A.V. Kimel, A.F.G. van der Meer, A. Stupakiewicz, and A. Kirilyuk, Phys. Rev. Applied **13**, 024064 (2020).

[78] A.J. Schellekens and B. Koopmans, Phys. Rev. B **87**, 020407(R) (2013).

[79] T.A. Ostler, R.F.L. Evans, R.W. Chantrell, U. Atxitia, O. Chubykalo-Fesenko, I. Radu, R. Abrudan, F. Radu, A. Tsukamoto, A. Itoh, A. Kirilyuk, Th. Rasing, and A.V. Kimel, Phys. Rev. B **84**, 024407 (2011).

[80] S. Wienholdt, D. Hinzke, K. Carva, P.M. Oppeneer, and U. Nowak, Phys. Rev. B **88**, 020406(R) (2013).

[81] J. Barker, U. Atxitia, T.A. Ostler, O. Hovorka, O. Chubykalo-Fesenko, and R.W. Chantrell, Scientific reports **3**, 3262 (2013).

[82] R.F.L. Evans, T.A. Ostler, R.W. Chantrell, I. Radu, and T. Rasing, Applied Physics Letters **104**, 082410 (2014).

[83] S. Gerlach, L. Oroszlany, D. Hinzke, S. Sievering, S. Wienholdt, L. Szunyogh, and U. Nowak, Phys. Rev. B **95**, 224435 (2017).

[84] U. Atxitia and T.A. Ostler, Appl. Phys. Lett. **113**, 062402 (2018).

[85] U. Atxitia, P. Nieves, and O. Chubykalo-Fesenko, Phys. Rev. B **86**, 104414 (2012).

[86] U. Atxitia, T.A. Ostler, J. Barker, R.F.L. Evans, R.W. Chantrell, and O. Chubykalo-Fesenko, Phys. Rev. B **87**, 224417 (2013).

[87] V.N. Gridnev, Phys. Rev. B **98**, 014427 (2018).

[88] V.N. Gridnev, Phys. Rev. B **100**, 174405 (2019).

[89] M.L.M. Lalieu, M.J.G. Peeters, S.R.R. Haenen, R. Lavrijsen, and B. Koopmans, Phys. Rev. B **96**, 220411(R) (2017).

[90] L. Avilés-Félix, A. Olivier, G. Li, C.S. Davies, L. Álvaro-Gómez, M. Rubio-Roy, S. Auffret, A. Kirilyuk, A.V. Kimel, T. Rasing, L.D. Buda-Prejbeanu, R.C. Sousa, B. Dieny, and I.L. Prejbeanu, Scientific Reports **10**, 5211 (2020).

[91] C. Banerjee, N. Teichert, K.E. Siewierska, Z. Gercsi, G.Y.P. Atcheson, P. Stamenov, K. Rode, J.M.D. Coey, and J. Besbas, Nature Commun. **11**, 4444 (2020).

[92] S. Mangin, M. Gottwald, C.-H. Lambert, D. Steil, V. Uhlíř, L. Pang, M. Hehn, S. Alebrand, M. Cinchetti, G. Malinowski, Y. Fainman, M. Aeschlimann, and E.E. Fullerton, Nat. Mat. **13**, 286 (2014).

[93] L. Le Guyader, S. El Moussaoui, M. Buzzi, M. Savoini, A. Tsukamoto, A. Itoh, A. Kirilyuk, Th. Rasing, F. Nolting, and A.V. Kimel, Phys. Rev. B **93**, 134402 (2016).

[94] Y. Xu, M. Deb, G. Malinowski, M. Hehn, W. Zhao, and S. Mangin, Advanced Materials **29**, 1703474 (2017).

[95] T.-M. Liu, T. Wang, A.H. Reid, M. Savoini, X. Wu, B. Koene, P. Granitzka, C.E. Graves, D.J. Higley, Z. Chen, G. Razinskas, M. Hantschmann, A. Scherz, J. Stöhr, A. Tsukamoto, B. Hecht, A.V. Kimel, A. Kirilyuk, T. Rasing, and H.A. Dürr, Nano Letters **15**, 6862 (2015).

[96] L. Caretta, M. Mann, F. Büttner, K. Ueda, B. Pfau, C.M. Günther, P. Hessing, A. Churikova, C. Klose, M. Schneider, D. Engel, C. Marcus, D. Bono, K. Bagschik, S. Eisebitt, and G.S.D. Beach, Nature Nanotechnology **13**, 1154 (2018).

[97] K. Cai, Z. Zhu, J.M. Lee, R. Mishra, L. Ren, S.D. Pollard, P. He, G. Liang, K.L. Teo, and H. Yang, Nature Electronics **3**, 37 (2020).

[98] P. Li, T.J. Kools, R. Lavrijsen, and B. Koopmans, arXiv:2204.11595 .

[99] M.L.M. Lalieu, R. Lavrijsen, and B. Koopmans, Nat. Commun. **10**, 110 (2019).

[100] S. Iihama, Y. Xu, M. Deb, G. Malinowski, M. Hehn, J. Gorchon, E.E. Fullerton, and S. Mangin, Advanced Materials **30**, 1804004 (2018).

[101] S. Iihama, Q. Remy, J. Igarashi, G. Malinowski, M. Hehn, and S. Mangin, Journal of the Physical Society of Japan **90**, 081009 (2021).

[102] G.-M. Choi and B.-C. Min, Phys. Rev. B **97**, 014410 (2018).

[103] J. Igarashi, Q. Remy, S. Iihama, G. Malinowski, M. Hehn, J. Gorchon, J. Hohlfeld, S. Fukami, H. Ohno, and S. Mangin, Nano Letters **20**, 8654 (2020).

[104] Q. Remy, *Ultrafast spin dynamics and transport in magnetic metallic heterostructures* (PhD Thesis, Université de Lorraine, Nancy, 2021).

[105] Y.L.W. van Hees, P. van de Meugheuvel, B. Koopmans, and R. Lavrijsen, Nat. Commun. **11**, 3835 (2020).

[106] G.E.P. Box, Journal of the American Statistical Association **71**, 791 (1976).

[107] T. Valet and A. Fert, Phys. Rev. B **48**, 7099 (1993).

[108] N.W. Ashcroft and N.D. Mermin, *Solid State Physics* (Holt, Rinehart and Winston, 1976).

[109] F. Dalla Longa, *Laser-induced magnetization dynamics: an ultrafast journey among spins and light pulses* (PhD Thesis, Eindhoven University of Technology, 2008).

[110] T. Roth, A.J. Schellekens, S. Alebrand, O. Schmitt, D. Steil, B. Koopmans, M. Cinchetti, and M. Aeschlimann, Phys. Rev. X **2**, 021006 (2012).

[111] Ł. Cywiński, *Magnetization dynamics and spin diffusion in semiconductors and metals* (PhD Thesis, UC San Diego, 2007).

[112] E.G. Tveten, *Manipulating Spins in Antiferromagnets with External Forces* (PhD Thesis, Norwegian University of Science and Technology, 2016).

[113] S.A. Bender and Y. Tserkovnyak, Phys. Rev. B **91**, 140402(R) (2015).

[114] S.M. Rezende, *Fundamentals of Magnonics* (Springer Nature Switzerland, 2020).

[115] T. Holstein and H. Primakoff, Phys. Rev. **58**, 1098 (1940).

[116] S.A. Bender, R.A. Duine, A. Brataas, and Y. Tserkovnyak, Phys. Rev. B **90**, 094409 (2014).

[117] S.A. Bender, R.A. Duine, and Y. Tserkovnyak, Phys. Rev. Lett. **108**, 246601 (2012).

[118] L.J. Cornelissen, K.J.H. Peters, G.E.W. Bauer, R.A. Duine, and B.J. van Wees, Phys. Rev. B **94**, 014412 (2016).

[119] S.O. Demokritov, V.E. Demidov, O. Dzyapko, G.A. Melkov, A.A. Serga, B. Hillebrands, and A.N. Slavin, Nature **443**, 430 (2006).

[120] M. Schneider, T. Braecher, D. Breitbach, V. Lauer, P. Pirro, D.A. Bozhko, H.Y. Musiienko-Shmarova, B. Heinz, Q. Wang, T. Meyer, F. Heussner, S. Keller, E.Th. Papaioannou, B. Lägel, T. Löber, C. Dubs, A.N. Slavin, V.S. Tiberkevich, A.A. Serga, B. Hillebrands, and A.V. Chumak, Nature Nanotechnology **15**, 457 (2020).

[121] L.J. Cornelissen, *Magnon spin transport in magnetic insulators* (PhD Thesis, University of Groningen, 2018).

[122] M. Lundstrom, *Fundamentals of carrier transport* (Cambridge University Press, 2010).

[123] J. Singh, *Electronic and optoelectronic properties of semiconductor structures* (Cambridge University Press, 2007).

[124] A. Slachter, F.L. Bakker, J.-P. Adam, and B.J. van Wees, Nat. Phys. **6**, 879 (2010).

[125] A. Slachter, *Thermal spin transport and spin transfer torque in ferromagnetic/non-magnetic nanoscale devices* (PhD Thesis, University of Groningen, 2011).

[126] M. Beens, J.P. Heremans, Y. Tserkovnyak, and R.A. Duine, Journal of Physics D: Applied Physics **51**, 394002 (2018).

[127] M. Beens, M.L.M. Lalieu, A.J.M. Deenen, R.A. Duine, and B. Koopmans, Phys. Rev. B **100**, 220409(R) (2019).

[128] B. Frietsch, J. Bowlan, R. Carley, M. Teichmann, S. Wienholdt, D. Hinzke, U. Nowak, K. Carva, P.M. Oppeneer, and M. Weinelt, Nat. Commun. **6**, 8262 (2015).

[129] T. Ferté, M. Beens, G. Malinowski, K. Holldack, R. Abrudan, F. Radu, T. Kachel, M. Hehn, C. Boeglin, B. Koopmans, and N. Bergeard, *in preparation* (2022).

[130] Q. Remy, J. Igarashi, S. Iihama, G. Malinowski, M. Hehn, J. Gorchon, J. Hohlfeld, S. Fukami, H. Ohno, and S. Mangin, Advanced Science **7**, 2001996 (2020).

[131] M. Beens, R.A. Duine, and B. Koopmans, Phys. Rev. B **102**, 054442 (2020).

[132] R.C. Iotti, E. Ciancio, and F. Rossi, Phys. Rev. B **72**, 125347 (2005).

[133] K. Uchida, J. Xiao, H. Adachi, J. Ohe, S. Takahashi, J. Ieda, T. Ota, Y. Kajiwara, H. Umezawa, H. Kawai, G.E.W. Bauer, S. Maekawa, and E. Saitoh, Nat. Mat. **9**, 894 (2010).

[134] J. Xiao, G.E.W. Bauer, K.-C. Uchida, E. Saitoh, and S. Maekawa, Phys. Rev. B **81**, 214418 (2010).

[135] M. Beens, R.A. Duine, and B. Koopmans, Phys. Rev. B **105**, 144420 (2022).

[136] T. Lichtenberg, M. Beens, M.H. Jansen, R.A. Duine, and B. Koopmans, Phys. Rev. B **105**, 144416 (2022).

[137] S.M. Rezende, R.L. Rodríguez-Suárez, R.O. Cunha, A.R. Rodrigues, F.L.A. Machado, G.A. Fonseca Guerra, J.C. Lopez Ortiz, and A. Azevedo, Phys. Rev. B **89**, 014416 (2014).

[138] V. Basso, E. Ferraro, and M. Piazzi, Phys. Rev. B **94**, 144422 (2016).

[139] Y. Cheng, K. Chen, and S. Zhang, Phys. Rev. B **96**, 024449 (2017).

[140] K.-H. Ko and G.-M. Choi, Journal of Magnetism and Magnetic Materials **510**, 166945 (2020).

[141] J. Ren, Phys. Rev. B **88**, 220406(R) (2013).

[142] Y. Tserkovnyak, A. Brataas, G.E.W. Bauer, and B.I. Halperin, Reviews of Modern Physics **77**, 1375 (2005).

[143] T.H. Dang, J. Hawecker, E. Rongione, G. Baez Flores, D.Q. To, J.C. Rojas-Sanchez, H. Nong, J. Mangeney, J. Tignon, F. Godel, S. Collin, P. Seneor, M. Bibes, A. Fert, M. Anane, J.-M. George, L. Vila, M. Cosset-Cheneau, D. Dolfi,

R. Lebrun, P. Bortolotti, K. Belashchenko, S. Dhillon, and H. Jaffrès, Applied Physics Reviews **7**, 041409 (2020).

[144] R. Freeman, A. Zholud, Z. Dun, H. Zhou, and S. Urazhdin, Phys. Rev. Lett. **120**, 067204 (2018).

[145] H.L. Wang, C.H. Du, Y. Pu, R. Adur, P.C. Hammel, and F.Y. Yang, Phys. Rev. Lett. **112**, 197201 (2014).

[146] W.P. Davey, Phys. Rev. **25**, 753 (1925).

[147] T. Yoshino, K. Ando, K. Harii, H. Nakayama, Y. Kajiwara, and E. Saitoh, Journal of Physics: Conference Series **266**, 012115 (2011).

[148] K.A. de Mare, *Ultrafast spin dynamics* (MSc Thesis, Eindhoven University of Technology, 2021).

[149] S.R. Tauchert, M. Volkov, D. Ehberger, D. Kazenwadel, M. Evers, H. Lange, A. Donges, A. Book, W. Kreuzpaintner, U. Nowak, and P. Baum, arXiv:2106.04189 .

[150] M.L.M. Lalieu, *Femtomagnetism meets spintronics and magnonics* (PhD Thesis, Eindhoven University of Technology, 2019).

[151] M.S. El Hadri, P. Pirro, C.-H. Lambert, S. Petit-Watelot, Y. Quessab, M. Hehn, F. Montaigne, G. Malinowski, and S. Mangin, Phys. Rev. B **94**, 064412 (2016).

[152] R. Medapalli, D. Afanasiev, D. Kim, Y. Quessab, S. Manna, S. Montoya, A. Kirilyuk, Th. Rasing, A.V. Kimel, and E.E. Fullerton, Phys. Rev. B **96**, 224421 (2017).

[153] J. Gorchon, C.-H. Lambert, Y. Yang, A. Pattabi, R.B. Wilson, S. Salahuddin, and J. Bokor, Appl. Phys. Lett. **111**, 042401 (2017).

[154] J. Gorchon, R.B. Wilson, Y. Yang, A. Pattabi, J.Y. Chen, L. He, J.P. Wang, M. Li, and J. Bokor, Phys. Rev. B **94**, 184406 (2016).

[155] J.M. Liu, Opt. Lett. **7**, 196 (1982).

[156] B.D. Cullity and C.D. Graham, *Introduction to Magnetic Materials* (Wiley, 1972).

[157] M. Beens, M.L.M. Lalieu, R.A. Duine, and B. Koopmans, AIP Advances **9**, 125133 (2019).

[158] D. Polley, A. Pattabi, J. Chatterjee, S. Mondal, K. Jhuria, H. Singh, J. Gorchon, and J. Bokor, Applied Physics Letters **120**, 140501 (2022).

[159] T. Lichtenberg, Y.L.W. van Hees, M. Beens, J. Levels, R. Lavrijsen, R.A. Duine, and B. Koopmans, *in preparation* (2022).

[160] Y. Yang, R.B. Wilson, J. Gorchon, C.-H. Lambert, S. Salahuddin, and J. Bokor, Science Advances **3**, e1603117 (2017).

[161] R.B. Wilson, J. Gorchon, Y. Yang, C.-H. Lambert, S. Salahuddin, and J. Bokor, Phys. Rev. B **95**, 180409(R) (2017).

[162] J.-Y. Chen, L. He, J.-P. Wang, and M. Li, Phys. Rev. Applied **7**, 021001 (2017).

[163] L. Wang, H. Cheng, P. Li, Y. Liu, Y.L.W. van Hees, R. Lavrijsen, X. Lin, K. Cao, B. Koopmans, and W. Zhao, arXiv:2011.03612 .

[164] A.V. Kimel and M. Li, Nature Reviews Materials **4**, 189 (2019).

[165] F.E. Demirer, C. van den Bomen, R. Lavrijsen, J.J.G.M. van der Tol, and B. Koopmans, Applied Sciences **10**, 8267 (2020).

[166] F.E. Demirer, Y. Baron, S. Reniers, D. Pustakhod, R. Lavrijsen, J.J.G.M. van der Tol, and B. Koopmans, Nanophotonics (2022).

[167] T.S. Seifert, L. Cheng, Z. Wei, T. Kampfrath, and J. Qi, Appl. Phys. Lett. **120**, 180401 (2022).

[168] W. Wu, C. Yaw Ameyaw, M.F. Doty, and M.B. Jungfleisch, Journal of Applied Physics **130**, 091101 (2021).

[169] J.F. Federici, B. Schulkin, F. Huang, D. Gary, R. Barat, F. Oliveira, and D. Zimdars, Semiconductor Science and Technology **20**, S266 (2005).

[170] G. Yao and Y. Pi, EURASIP Journal on Wireless Communications and Networking **2014**, 10 (2014).

[171] T. Albash, S. Boixo, D.A. Lidar, and P. Zanardi, New Journal of Physics **14**, 123016 (2012).

[172] Y. Tserkovnyak, E.M. Hankiewicz, and G. Vignale, Phys. Rev. B **79**, 094415 (2009).

[173] B. Flebus, *Collective spin and heat transport through magnetic systems* (PhD Thesis, Utrecht University, 2017).

[174] A. Kapelrud and A. Brataas, Phys. Rev. Lett. **111**, 097602 (2013).

[175] M.L.M. Lalieu, R. Lavrijsen, R.A. Duine, and B. Koopmans, Phys. Rev. B **99**, 184439 (2019).